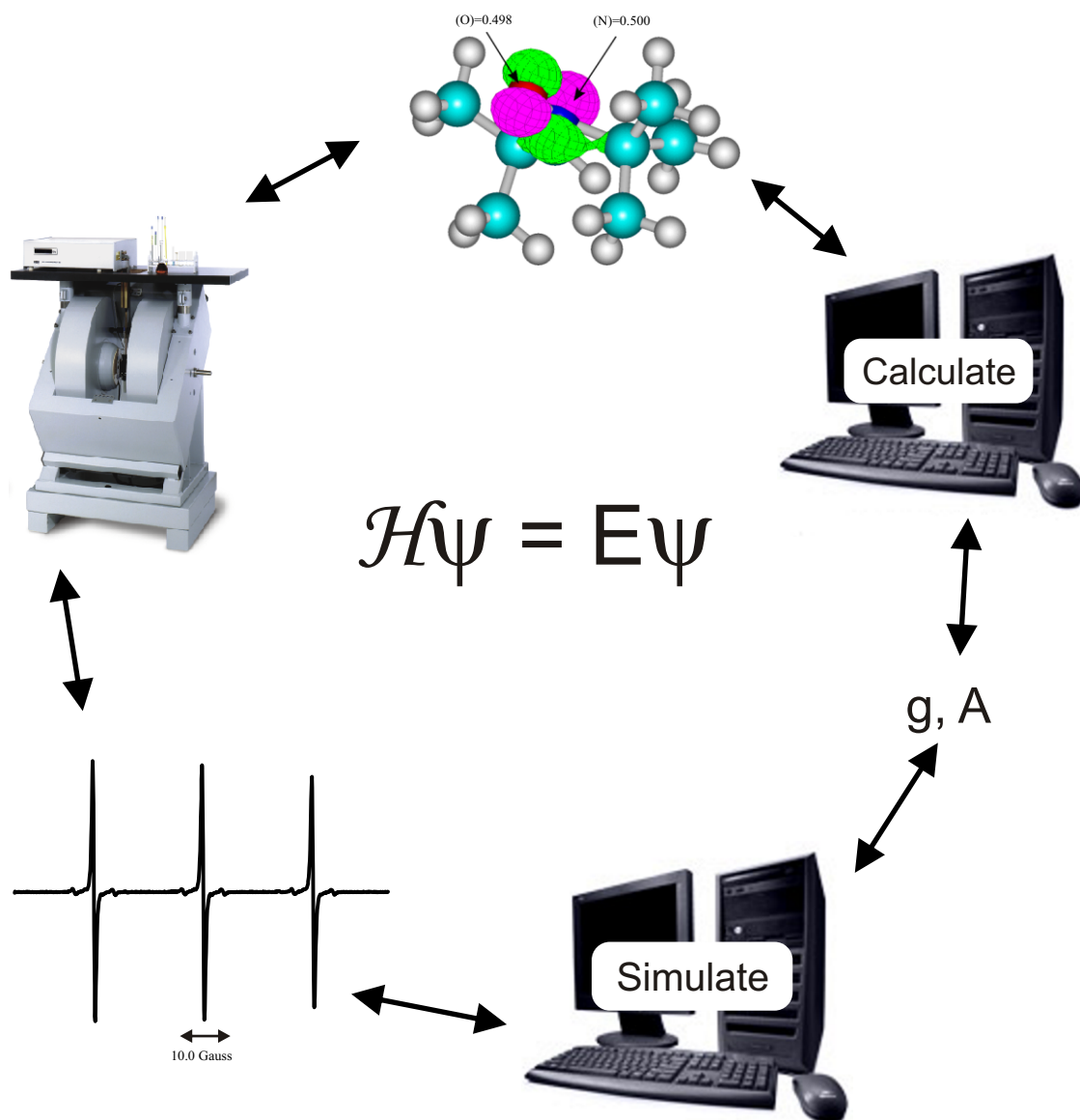


29th International EPR Symposium

# Calculation of EPR Parameters and Spectra Workshop



July 23, 2006



# Table of Contents

Introduction to the Workshop on Calculation  
of EPR Parameters and Spectra

The Calculation of the  $g$  and Hyperfine Tensors  
of Paramagnetic Molecules and Organic Free Radicals

Introduction to Calculations of  $g$  and  $A$   
Values for Transition Metal Complexes

Introduction to CW EPR Simulation

Introduction to Molecular Sophe  
The Next Generation of Computer  
Simulation Software

Appendix A. Methods and Basis Sets



# Introduction to the Workshop on Calculation of EPR Parameters and Spectra

Gareth R. Eaton, University of Denver  
July 2006

## Goals of this Workshop

This Workshop, prior to the 29<sup>th</sup> International EPR Symposium, provides an introduction to computations of g values and hyperfine couplings and simulation of EPR spectra. Computations are making increasingly important contributions to guiding and interpreting EPR experimentation. Such computations are not yet part of the fabric of routine EPR. We hope the Workshop will stimulate new work in this field.

## The series of Workshops

1987 Workshop on the Future of EPR  
1992 Workshop on the Future of EPR  
1999 First Pulsed EPR Workshop  
2000 Workshop on Pulsed EPR  
2001 Multifrequency EPR Workshop  
2002 Workshop on EPR of Aqueous Samples  
2003 Workshop on Measuring Electron-Electron Distances by EPR  
2004 Workshop on EPR Imaging  
2005 Workshop on Selecting an EPR Resonator  
2006 Workshop on Computation of EPR Parameters and Spectra

Publications related to the 1987 and 1992 Workshops on the future of EPR:

1. The Future of EPR Instrumentation, G. R. Eaton and S. S. Eaton, *Spectroscopy* **3**, 34-36 (1988).
2. Workshop on the Future of EPR (ESR) Instrumentation - Denver, Colorado, August 7, 1987, G. R. Eaton and S. S. Eaton, *Bull. Magn. Reson.* **10**, 3-21 (1988).
3. EPR Imaging: Progress and Prospects, G. R. Eaton and S. S. Eaton, *Bull. Magn. Reson.* **10**, 22-31 (1988).
4. The Future of Electron Paramagnetic Resonance Spectroscopy, S. S. Eaton and G. R. Eaton, *Spectroscopy*, **8** 20-27 (1993).
5. The Future of Electron Paramagnetic Resonance Spectroscopy, S. S. Eaton and G. R. Eaton, *Bull. Magn. Reson.* **16**, 149-192 (1995).

The materials distributed at several past Workshops (pulsed, multifrequency, aqueous samples, imaging, and distances) are available on line:

<http://www.bruker-biospin.com/brukerepr/symposium.htm>

The subject of this Workshop is part of an enormous intellectual landscape. This Workshop has to focus on a small portion, yet strive to give an entree to this aspect of EPR. To keep within practical bounds for a Workshop, we minimize emphasis on topics

such as simulation of DEER (see 2003 Workshop on Measuring Electron-Electron Distances by EPR), ESEEM (see 1999 and 2000 Pulsed EPR Workshops) or ENDOR.

There is separately a large literature of computer analysis of overlapping spectra, especially applied to kinetics of multiple species studied by EPR. See, for example, Keszler and Hogg (2005) and Chang et al. (2005). This topic is beyond the scope of this Workshop.

To forecast where we want to take these topics today, consider the spin density calculation shown in Figure 1. Ideally, the quantum mechanical calculation leads to a set of hyperfine constants and g value that fit the observed EPR spectrum.

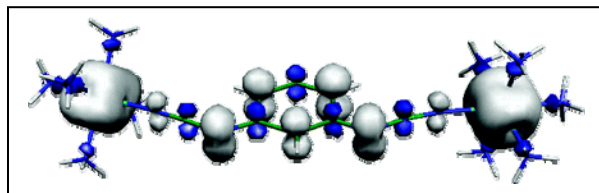


Figure 1. Computed spin density in a copper-copper dimer with a long bridge (picture from Ruiz et al., 2003).

The computations needed for g-values and hyperfine couplings are not fully developed yet, so there is need to continually refine the calculations by testing them against experimental results, in the way sketched in Figure 2.

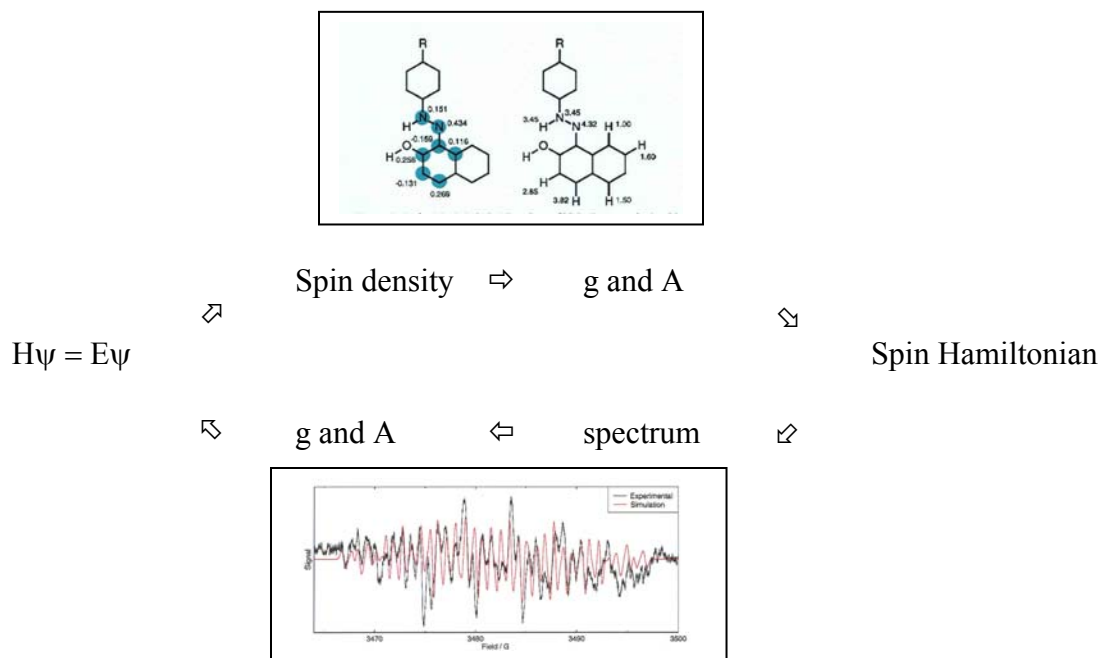


Figure 2. Schematic of the use of quantum mechanical calculations of g values and hyperfine couplings to simulate spectra, and the use of best fit spectral parameters to feed back to refinement of the computational methods (pictures from Abbott et al. 2005).

## Section 1. Examples of Simulations of EPR Spectra

### Introduction

It is inherent in the nature of EPR spectra that except for a few cases in which all lines are fully resolved, simulation of the CW EPR spectra has been an important part of spectral interpretation since early in the history of EPR. What is relatively new is the ready availability of instrumentation at multiple RF/microwave frequencies to perform many of the more than one hundred types of CW, pulsed, and multiple resonance EPR measurements (Eaton and Eaton 1997). This puts demands on computer simulation much greater than just having a program that computes to second order and incorporates g- and a-anisotropy. For a long time, high-resolution EPR spectra of simple organic radicals such as semiquinones have been used qualitatively as demonstrations of the correlation of hyperfine splittings with electron spin density distributions estimated by HMO theory (see, for example, Beck and Nibler, 1989). In the past few years quantum-mechanical calculations have improved to the point that not only can g-values and hyperfine splittings be calculated in reasonable agreement with experiment, but the ability to perform some such calculations is incorporated into commercially available computer programs. Thus, experiments that can now be performed on commercial spectrometers, plus a few high-field instruments, provide previously unavailable information about spin systems, and simulations of both CW and pulsed EPR experiments can now be performed with a high degree of confidence (and speed). Understanding of g-values and hyperfine constants is emerging at a computational level comparable to that used for calculating structure and reactivity of molecules. This convergence provides EPR with unprecedented conceptual power. The purpose of this Workshop on Computational EPR is to stimulate wider use of these new tools.

From a computational point of view, the key issue is which parameters can be considered isotropically averaged and which anisotropies have to be considered explicitly. Also of central importance is dynamics, including spin dynamics, molecular tumbling, and intramolecular motions. High-spin systems and even-spin systems, and multi-resonance experiments, present additional challenges, both experimentally and computationally. Even with the recent advances, there is as yet no ability to compute electron spin relaxation times from first principles. Further, very few computer programs use actual electron spin relaxation times in spectral simulations. Incorporation of realistic solvent interaction with radicals when computing g and a values is at a nascent stage, with many opportunities for new insights. Although there remain many hurdles, computation has already opened new vistas in EPR spectroscopy.

A reasonably complete assignment and interpretation of an EPR spectrum should be based on a simulation of that spectrum. Comparison of the simulation with experiment tests whether the terms used in the simulation include those most important to the physical phenomena that determine the shape of the spectrum. The computer power available on the desktop today provides both an opportunity and an obligation to perform simulations at least to the level of sophistication permitted by simulation programs commercially available or readily available from other labs. The following examples of

EPR spectra are selected to illustrate the range of complexity of spin Hamiltonians involved, and illustrate some of the successful simulations. One should always be aware that a simulation may not be unambiguous. It may require simultaneous simulation of experimental EPR spectra at multiple RF/microwave frequencies (and associated magnetic fields) to find the actual parameters. As a simple, but defining, example, consider that that 6-line spectrum observed for  $Mn^{2+}$  in fluid solution and in many crystalline solids can be simulated with no knowledge of or restriction on the zero-field splitting parameters D and E. Only in special cases can the five sets of zero-field split lines be observed at X-band. However, high-field/high frequency EPR (subsequently in these notes, simply HF EPR) can provide direct measurements of D and E. Even then, the sign of D may not be available unless measurements are done at two properly selected low temperatures.

From very early in the development of EPR, various research groups wrote computer programs for the simulation of the spectra of organic radicals and metal complexes. Although initially many of these programs calculated line positions to only first order, the ready availability of significant computer power even in a notebook computer makes it routine to incorporate second order Breit-Rabi shifts and details of line shapes. The SimFonia-WinEPR package written by Ralph Weber and available from Bruker BioSpin makes this level of simulation available to a wide range of users. Incorporating effects of intermediate and slow motion on line shapes still requires specialized programs, such as those by Freed and Budil (see, for example, Schneider and Freed, 1989). Until recently, most simulations of time-domain spectra were for analysis of, e.g., ESEEM and DEER. However, first-principles simulation of the effects of microwave pulses on spins has become available in programs such as EasySpin (Stoll 2003). The most ambitious effort for simulation of EPR spectra is the family of programs by Graeme Hanson that are evolving from Sophe (Chapter 5 in Lund and Shiotani, 2003). The version called XSophe is available from and supported by Bruker BioSpin. The version now under development will include simulations of fluid solution and rigid lattice CW spectra with few limits on the spin multiplicity or the number of nuclei interacting with the electron, and also simulations of time domain spectra. In simulating complex EPR spectra, computed g and hyperfine could be very useful starting points for the simulations (Mattar, 2005).

### **The Literature of Simulation of EPR Spectra**

There is a vast literature about simulation of EPR spectra. Most of the early literature is cited in the reviews of early use of computers in EPR by Van Camp and Heiss (1981) and Kirste (1994), which supplement the information in this booklet. Pilbrow (1996) and Weil (1999) also recently reviewed aspects of the simulation problem. Relaxation times are very much shorter for electron spins than for nuclear spins under most common circumstances, so many of the NMR experiments with elaborate multiple pulse sequences are not feasible in EPR. However, the fundamental principles of the spin physics are basically the same, and descriptions of the effects of pulse sequences in NMR are transferable to EPR. Some useful leading references about the effects of pulses on nuclear and electron spins include the following: the program GAMMA (Smith et al. 1994; Shane et al. 1998), pulsed EPR (Kevan and Bowman, 1990), 2D ESE (Eviatar et al.

1995), HYSCORE (Szosenfogel and Goldfarb 1998), multiple echo sequences with imperfect pulses (Kingsley, 1998), spectral rotation (Hornak and Freed, 1986), multiple-pulse NMR (Turner, 1989), phase cycling (Jerschow and Müller 1998), ESEEM (Reijerse and Keijzers, 1987; Benetis and Westerling, 1990; Benetis and Nordh, 1995; Jeschke and Schweiger, 2001; Madi et al., 2002; Stoll and Schweiger, 2003; Jeschke web site; Kulik and Dzuba 2004), EasySpin (Stoll and Schweiger, 2006; Stoll web site, Epel web site), field-swept pulsed EPR (Drew et al. 2001).

### **The Scope of Simulations of EPR Spectra**

A full simulation has to account for all of the terms in the spin Hamiltonian over the full range of the parameters listed in the next section.

$$H = \beta_e B^T \cdot g \cdot \hat{S} + \hat{S}^T \cdot D \cdot \hat{S} + \hat{S} \cdot A \cdot \hat{I} - g_n \beta_n B^T \cdot \hat{I} \quad (\text{from Weil et al., page 104})$$

**The scope of spectral simulation parameter space** is only hinted at by the following list:

Fluid solution with hyperfine splitting

Magnetic field dependence - the Breit-Rabi effect

Intermediate tumbling

Powder spectrum

Single crystal

Liquid crystal, partial orientation

$S > 1/2$

$S = 1$  Triplet

$S > 1/2$  large D

High-field  $S > 1/2$

Parallel mode

Spin-spin interaction - exchange and dipolar

AB quartets

Half-field transition

Nitroxyl-nitroxyl

Metal-nitroxyl

Pulsed (DEER)

Rapid scan spectra

Pulsed EPR – many experiments including ESEEM, DEER, HYSCORE

Making programs efficient, powerful, and flexible involves insightful choices of ways to interpolate and extrapolate, methods of distributions of parameters, various grids for powder spectra, etc. There are so many regimes to simulate that programs usually are optimized for one or another regime, and a suite of programs is needed to encompass all of the experimentally accessible range of spin and lattice dynamics, CW and pulse, saturation and passage effects,  $S = 1/2$  and  $S > 1/2$ , temperature, magnetic field and microwave frequency.

Even with all of this sophistication, few CW simulation programs incorporate fundamentals of relaxation times, distributions of microwave  $B_1$  over the sample, etc.

### Selected Examples of CW EPR Spectra

Each of the selected spectra includes a simulation for which details are given in the cited paper.

#### *High-resolution, rapidly tumbling, essentially first order*

One of the most familiar EPR samples is  $\alpha,\alpha'$ -diphenyl- $\beta$ -picryl hydrazyl (DPPH), although usually it is used as a solid, in which strong exchange interactions narrow the signal to a single, slightly anisotropic, line a little more than a gauss wide at X-band. In dilute, de-oxygenated, low-viscosity solution, one can observe an enormous number of lines, as in the figure. Dalal et al. (1973) simulated the CW spectrum for DPPH using hyperfine couplings measured by ENDOR. The simulation is convincing, but does not look exactly like the experimental spectrum. The problem is probably that 100 kHz magnetic field modulation was used in recording the spectrum, so the lines are broadened, and computer simulation programs available thirty years ago could not deal with modulation sidebands.

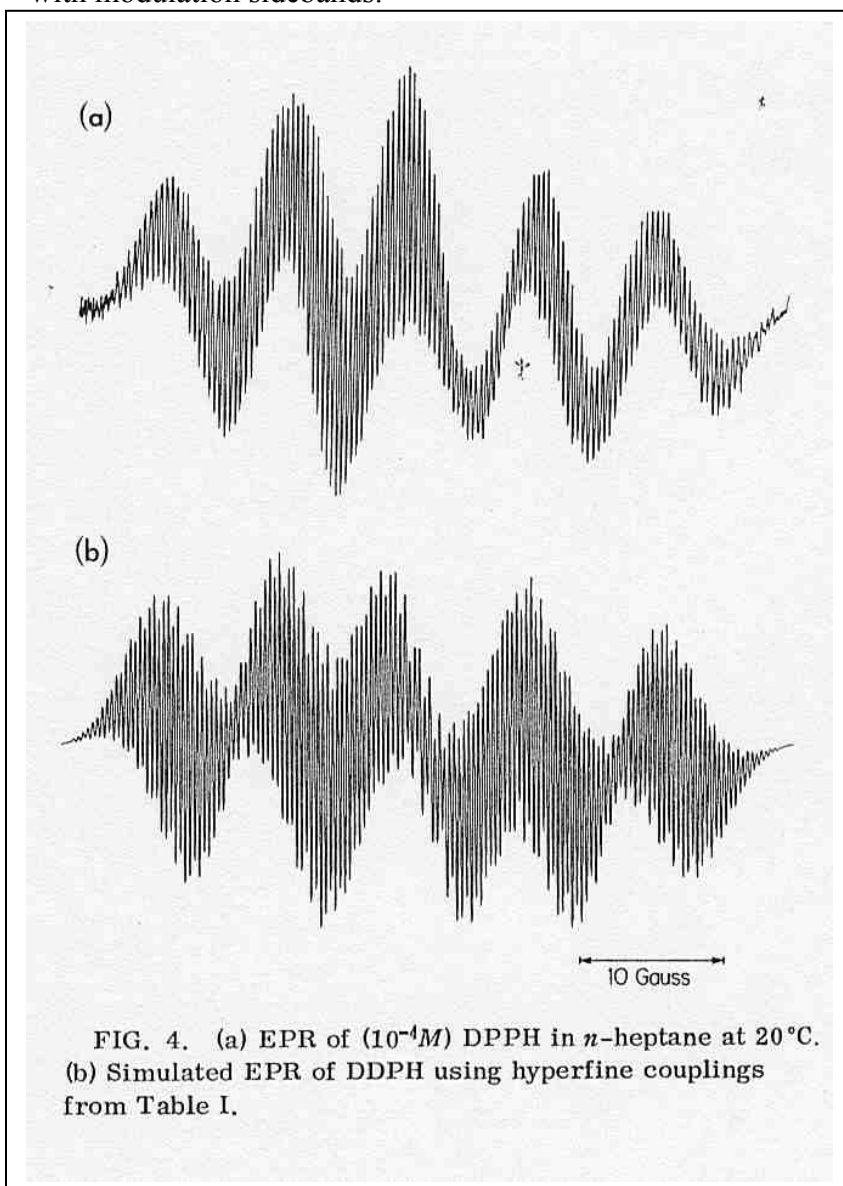


Figure 3. X-band spectrum of DPPH, with simulation. (Dalal et al. 1973)

### *Second order effects*

The commonly-used X-band frequency is high enough that second order shifts (Breit-Rabi effect) are not very important unless the hyperfine coupling is very large. (See Weil, Bolton and Wertz, pages 73, 116, 455). However, at low frequencies used for in vivo studies, even the N hyperfine in nitroxyl radicals is large enough relative to the electron Zeeman energy to result in unequal spacing between hyperfine components.

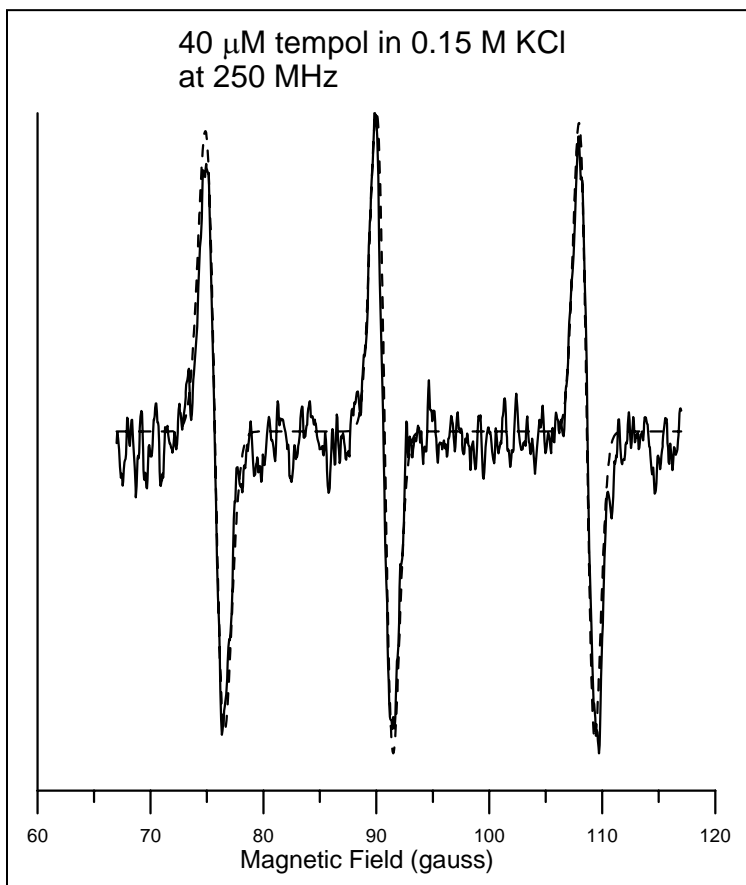


Figure 4. Tempol in 0.15 M aqueous KCl solution at 260 MHz (ca. 90 G), with simulation using a program that includes the second order shifts due to the Breit-Rabi effect. Although the  $3\ ^{14}\text{N}$  hyperfine lines of a nitroxyl radical are nearly equally spaced at X-band and higher frequencies, they are unequally spaced at lower frequencies.

### *Intermediate tumbling*

Long ago (McConnell, Kivelson, Rogers and Pake 1956-1966) it was shown that hyperfine-split EPR signals depend on the nuclear spin quantum number according to the approximate equation:

$$\Delta H = \frac{2}{\gamma\sqrt{3}T_2} = A + Bm_I + Cm_I^2$$

This equation assumes that there is no unresolved nuclear hyperfine, and that the derivative spectrum is recorded. This equation, in various forms, is the basis for estimating tumbling correlation times for nitroxyl radicals from ratios of peak heights.

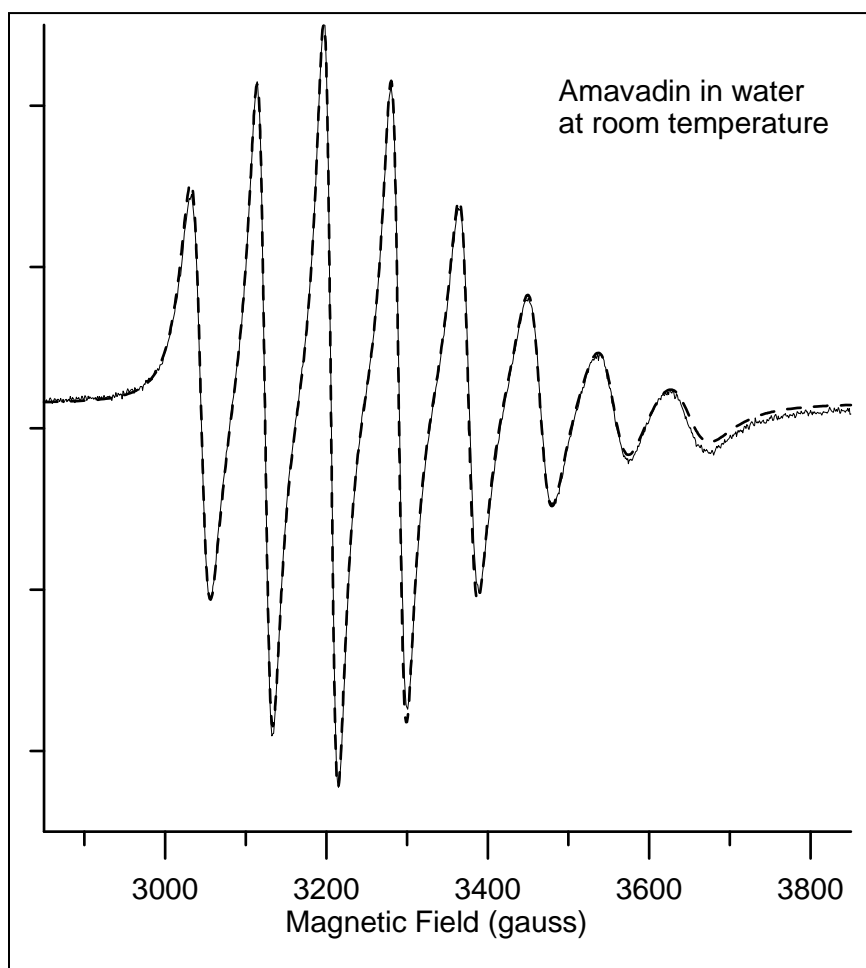


Figure 5 This dependence of line width on nuclear spin was used to simulate the CW spectrum of a vanadyl complex in water at room temperature (sample of amivadin was provided by Prof. Debbie Crans, Colorado State University).

More sophisticated programs are available to simulate the CW spectra of the very important nitroxyl radicals in order to estimate rates of motion of the radical.

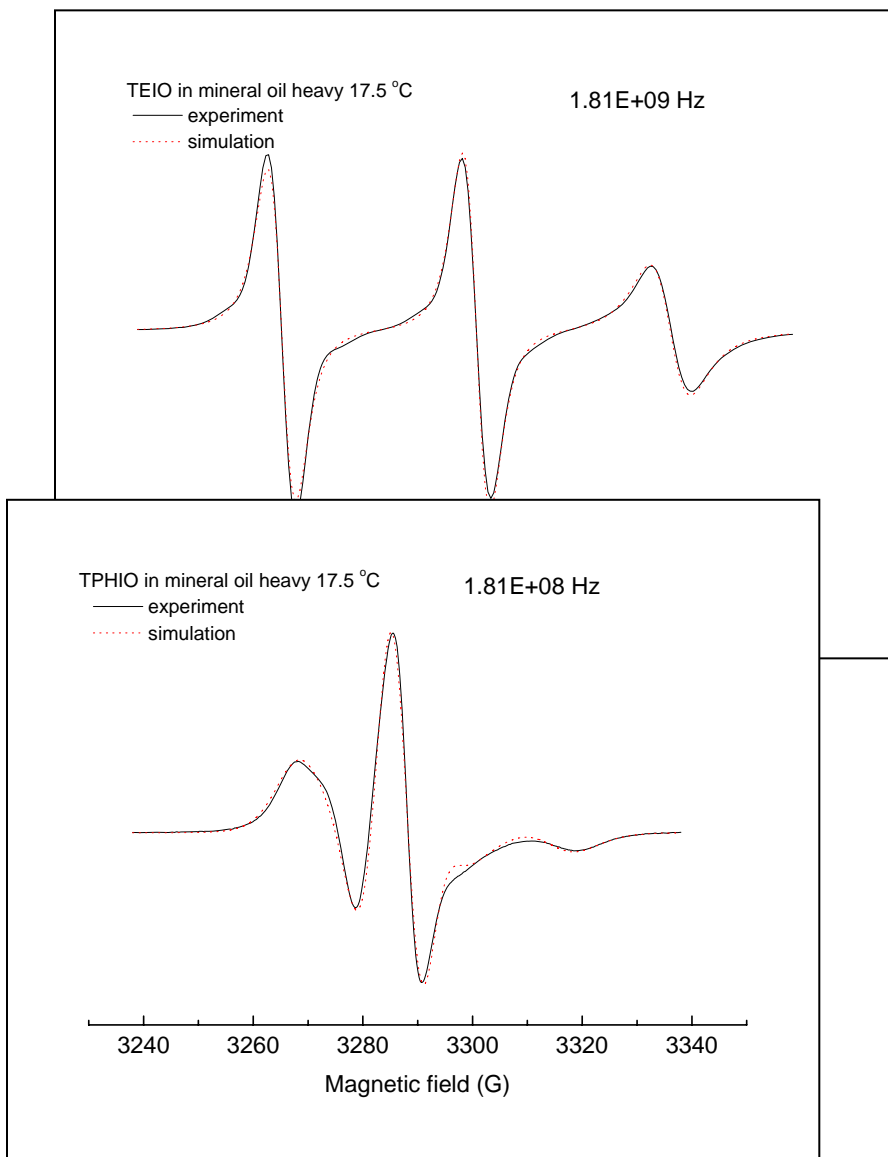
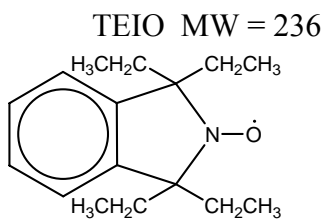
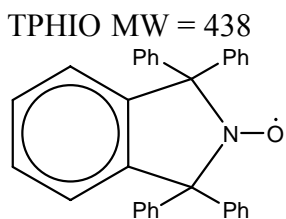


Figure 6. Intermediate tumbling of nitroxyl radicals, with simulation using the NLSL program provided by Budil. The radicals are



The radicals were provided by Steven E. Bottle, Queensland University of Technology.

Molecular dynamics effects are discussed by Schneider and Freed (1989), Budil et al. (1996), Freed (2005), Marsh et al. (2005), Beth and Hustedt (2005).

### Powder spectrum

The anisotropies that are largely averaged by motion in solution contribute to broad spectra, such as sketched in Figure 7:

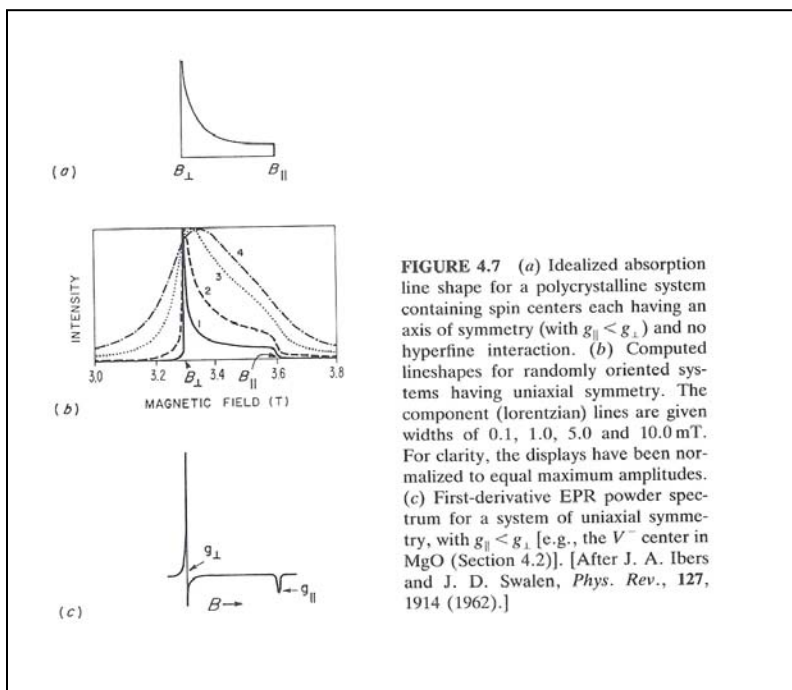


Figure 7. Contribution of anisotropic  $g$  values to powder spectral line shapes. Anisotropic hyperfine couplings have similar effect. (from Weil et al. 1994)

$S > 1/2$

Spectra of species with  $S > 1/2$  are a challenge to simulate, and even to acquire.

$S > 1/2$  Fe

Gaffney and Silverstone (1998) showed that for  $S > \frac{1}{2}$  the looping transitions that occur in field-swept spectra near avoided crossings can be simulated by cubic approximations to the transition frequencies. The resonance fields form a surface in B space. One set of such patterns was reproduced on the cover of an issue of Journal of Magnetic Resonance.

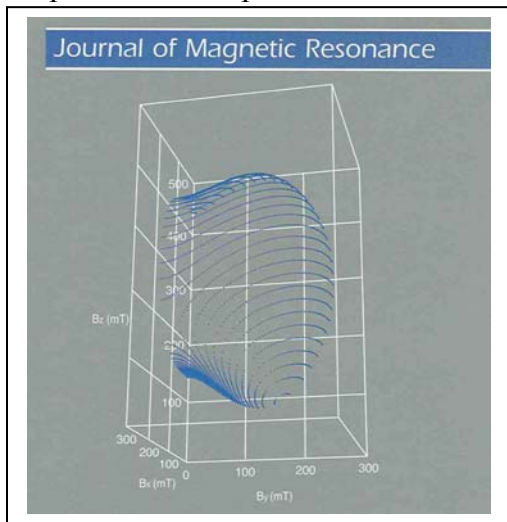


Figure 8. For  $S > \frac{1}{2}$  some transitions in field-swept spectra near avoided crossings form loops in B space. (Gaffney and Silverstone 1998)

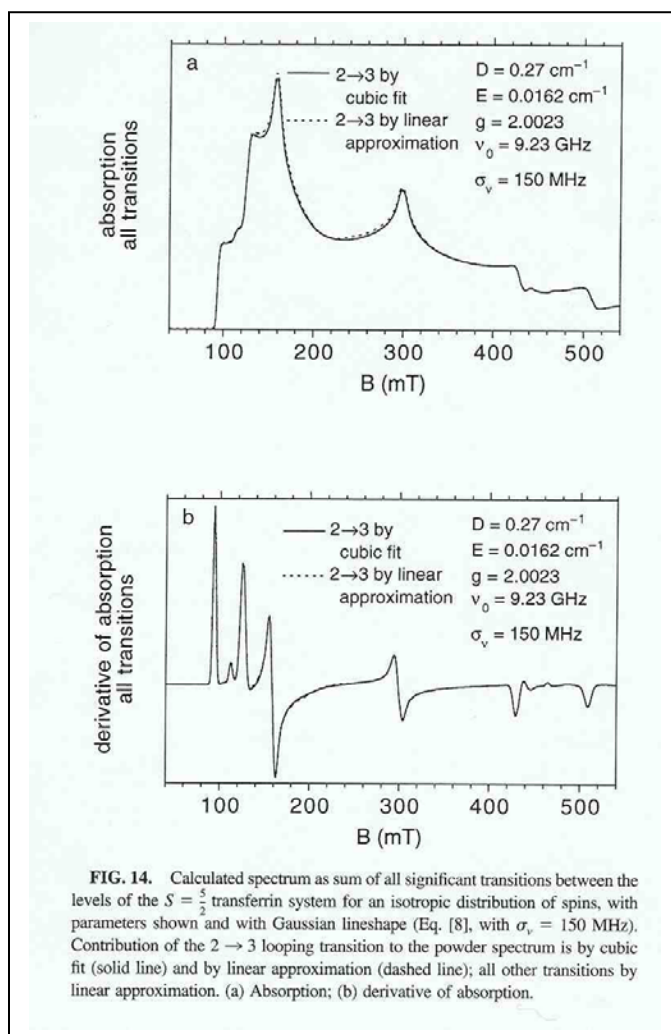


Figure 9. Calculated spectra for  $S = 5/2$  Fe(III) in transferrin. (Gaffney and Silverstone 1998)

### A Puzzle

If one were shown the spectrum in Figure 10 with no knowledge of the sample, it would be a great puzzle.

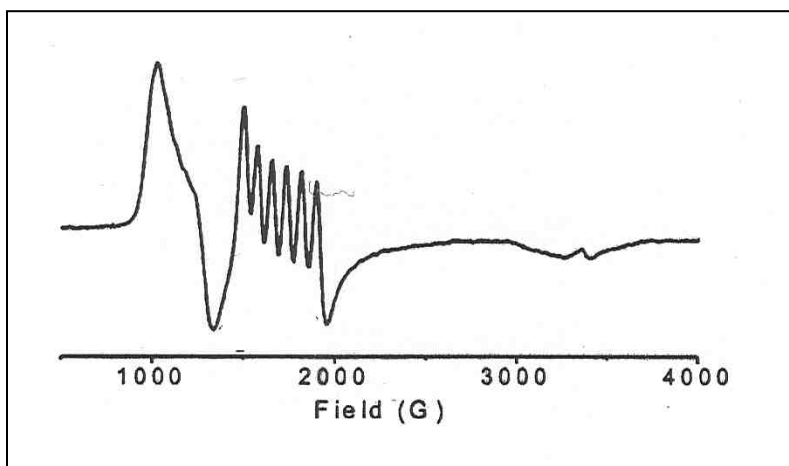


Figure 10. Zhong et al. (2006) obtained this spectrum at 77 K for the compound shown in Figure 11, with the metal oxidation states Mn(III) ( $d^4$ ) and Cu(II) ( $d^9$ ).

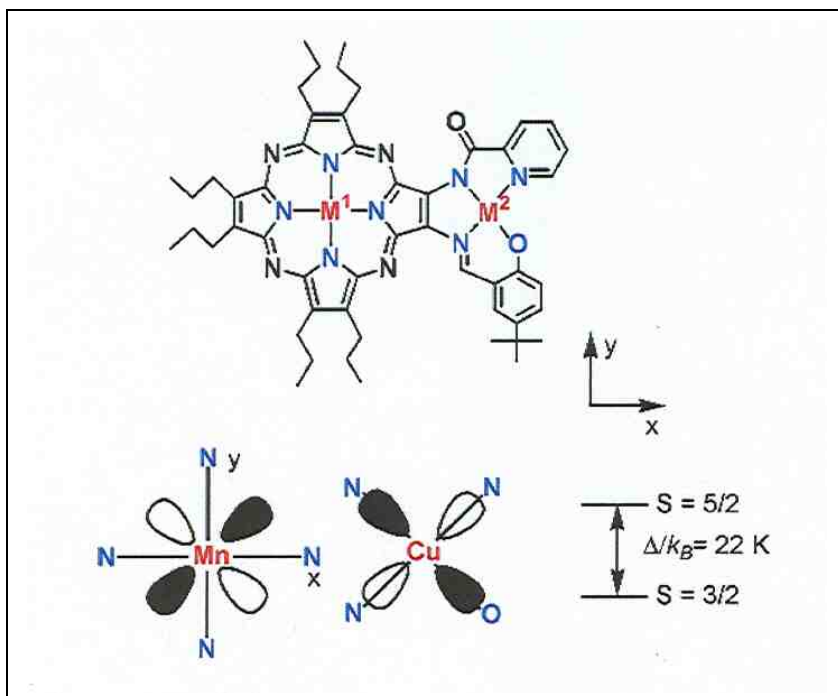


Figure 11. A complex containing two different metals interacting with one another. The spectrum in Figures 10 and 12 are for the case of Mn(II) and Cu(II). (Zhong et al. 2006)

Coupling between the Mn and Cu spins yields net spins of  $S = 3/2$  and  $S = 5/2$ . The two spin manifolds turned out to be separated by about 22 K, so both are populated at 77 K, and the spectrum is assigned as shown in Figure 12.

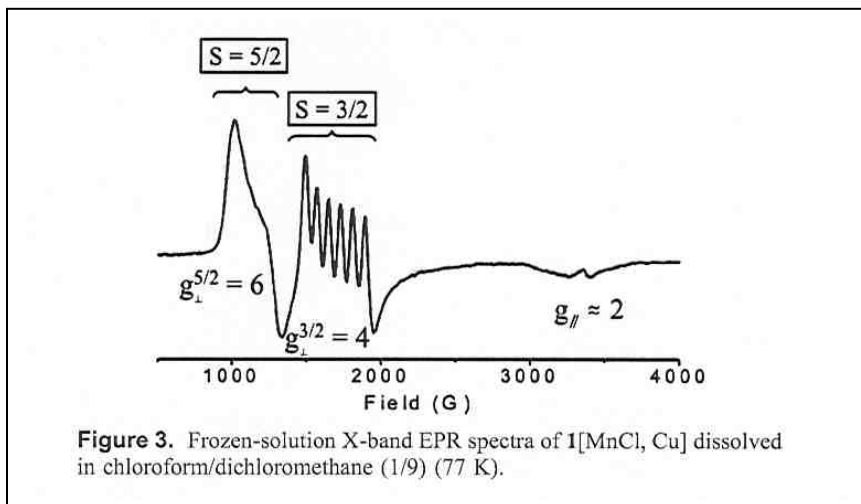


Figure 12. The Mn nuclear hyperfine (80 G) is well-resolved on the  $g = 4$  signal for the  $S = 3/2$  manifold. (Zhong et al. 2006)

### Frequency dependence of EPR spectra

There are two major impacts on CW EPR spectra of obtaining spectra at different magnetic field strengths (and associated RF/microwave/IR frequencies). Spectra become more first-order, and thus inherently easier to interpret the higher the magnetic field. The Breit-Rabi effect results in unequal spacings between hyperfine components when the hyperfine coupling is a significant fraction of the Zeeman field. The second major effect is that when zero-field splittings (ZFS) are larger than the Zeeman energy, the some transitions will not be observed. Using high field and high frequency makes it possible to observe these transitions. Figure 4 contained an example of the Breit-Rabi effect on nitroxyl radical spectra at 250 MHz, and the following examples illustrate the dependence of CW spectra on frequency and magnetic field.

The first example is a set of spectra of a copper(II) complex at 5 different microwave frequencies at Q-band and below. This is an illustration of the appearance and even observability of hyperfine splittings as a function of magnetic field.

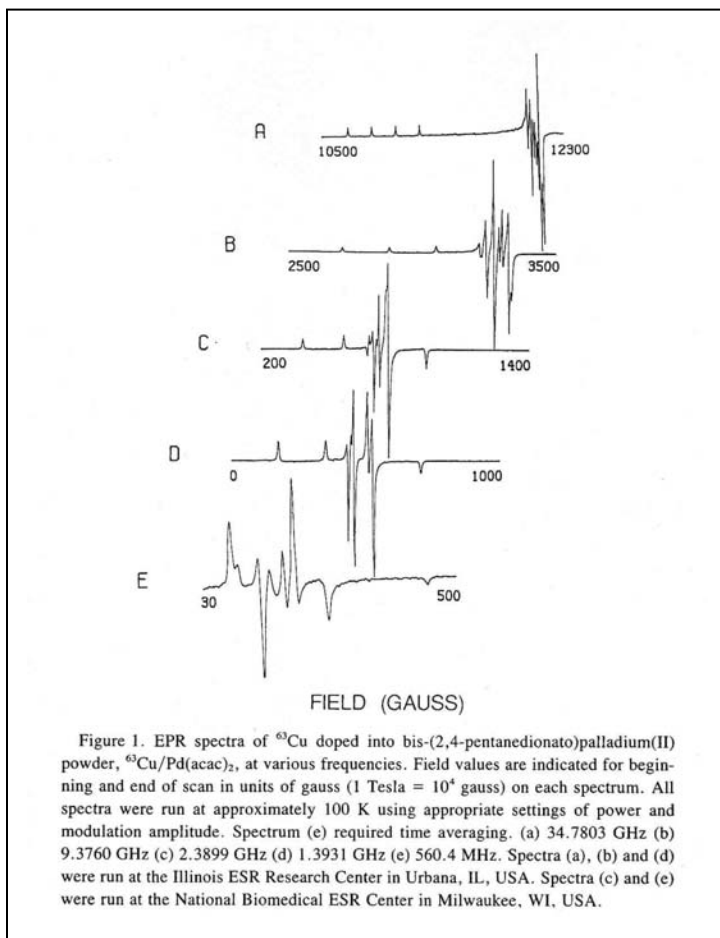


Figure 13. Powder spectra of the Cu(II) complex of 2,4-pentanedione (acac) doped into the Pd complex. Everyone would recognize the X-band spectrum of copper(II) in B, but interpretation of the lower-frequency spectra is less obvious upon visual inspection. A simulation program has to be able to match all of these spectra (from Belford et al.1987).

Similarly, the top spectrum in Figure 14 is easily recognized as vanadyl based on the 8 lines of varying height, but the lower spectrum requires prior knowledge of the sample and the microwave frequency.

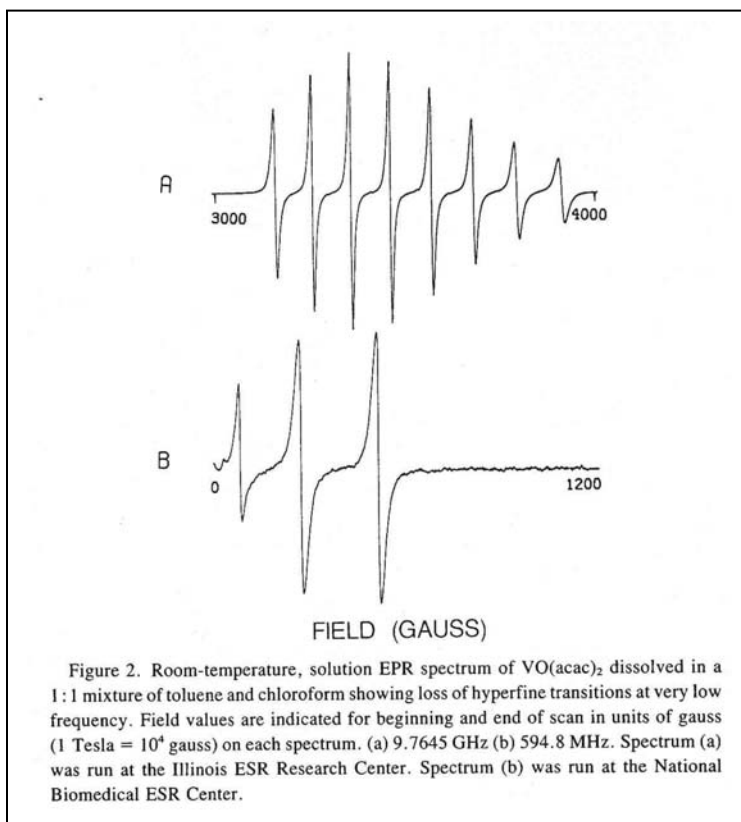


Figure 14. Comparison of X-band and ca. 600 MHz spectra of VO(acac)<sub>2</sub> in fluid solution. (Belford et al. 1987)

### EPR transitions that cannot be observed at X-band

For some spin systems, there are EPR transitions that cannot be observed at X-band. In these cases, simulation is useful to predict where transitions could occur, and hence the magnetic field and frequency required to detect them. The Figure 15 shows 95 and 285 GHz spectra, with simulations, for d<sup>4</sup> Cr(II) (Dobe et al. 2004).

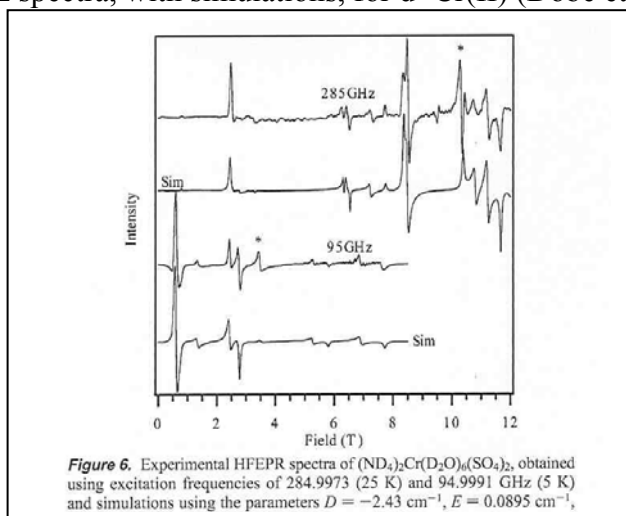


Figure 15. High-field, high-frequency CW EPR spectra of Cr(II),  $d^4$ . With ZFS  $D = -2.43 \text{ cm}^{-1}$ , no spectrum would be observed at X-band. (Dobe et al. 2004)

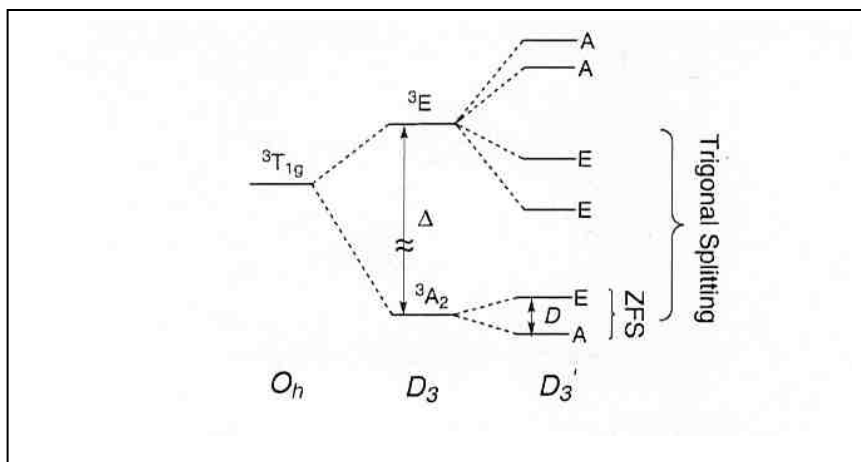


Figure 16. Energy level diagram for V(III) is  $d^2$  (Beaulac et al. 2006).

**Table 2.** Resonant Field Positions for HF-EPR Data Obtained for  $[\text{V}(\text{urea})_6](\text{ClO}_4)_3$  at 5 K and Spin Hamiltonian Parameters Derived from a Least-Squares Fit to the Observed Data

frequency (GHz)	obsd field (G)	calcd field (G)	difference obsd - calcd
189.9982	90 221	90 596	-375
189.9982	114 970	114 946	23
229.9988	32 074	31 706	367
229.9988	51 543	51 585	-42
229.9988	107 320	107 179	141
344.9982	51 085	51 688	-603
344.9982	83 698	83 611	87
344.9982	101 450	101 699	-249
379.9964	73 272	73 217	55
379.9964	98 063	98 076	-13
379.9964	116 142	116 041	101

param	value
$g_x$	1.848(2)
$g_y$	1.832(4)
$g_z$	1.946(7)
$D$	$6.00(2) \text{ cm}^{-1}$
$E$	$0.573(6) \text{ cm}^{-1}$

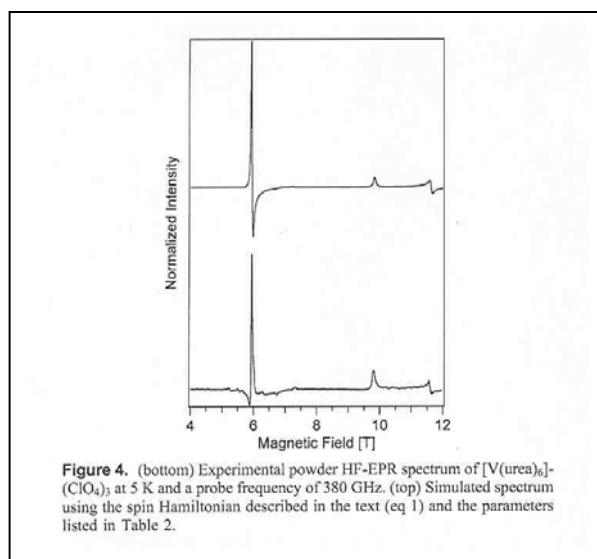


Figure 17. The field/frequency required to observe the EPR spectrum depends on the magnitude of the ZFS. For the V(III) hexa-urea complex,  $D = 6 \text{ cm}^{-1}$ , so a large magnetic field is needed.

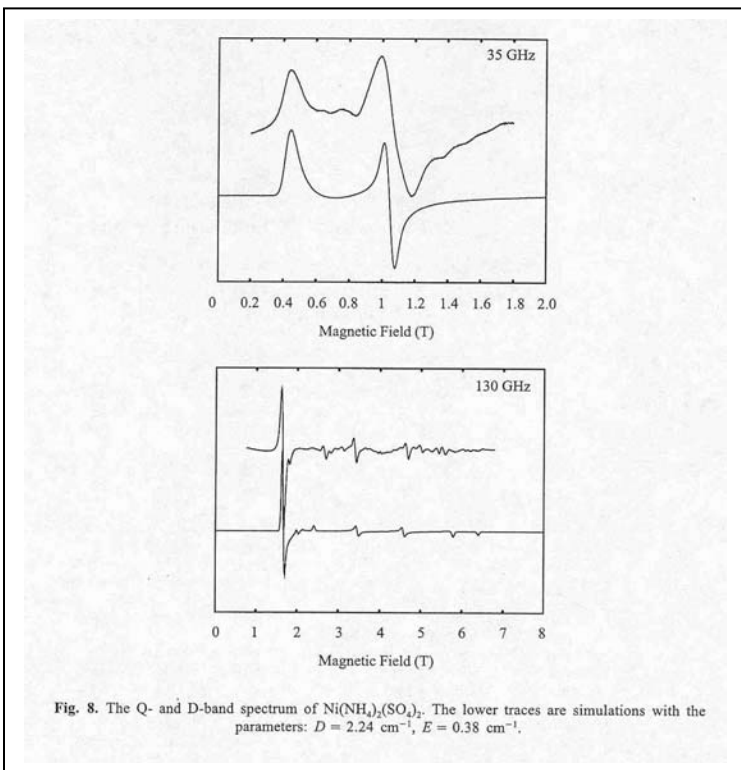


Figure 18.  $d^8$  Ni(II) is another challenging spin system to simulate. As shown, high-field, high-frequency spectra are important. (from Reijerse et al. 1998).

### Mn(II)

Mn(II),  $d^5$ , can always be seen in X-band and Q-band EPR because it has transition between  $S = \pm \frac{1}{2}$  states. However, as sketched in the diagram from Mantel et al. (2004), there are 5 possible EPR transitions, each split into 6 lines by the Mn nuclear spin, and then further split by nuclei in ligands. Anisotropies in  $g$  or hyperfine further complicate the spectra, whether in solution or in solids. Simulations of Mn(II) spectra have to take all of these possibilities into account. One rarely sees all of the 30 transitions predicted for Mn(II). One case in which they are observed is the oriented single crystal spectrum in figure 19.

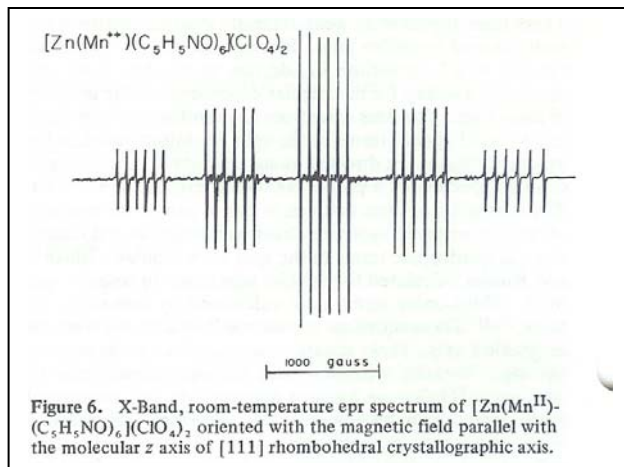


Figure 19. Oriented single crystal of  $[\text{Zn}(\text{Mn}(\text{II}))(\text{C}_5\text{H}_5\text{NO})_6](\text{ClO}_4)_2$  in which the 6 Mn hyperfine lines are observed for each of the 5 components of the  $S = 5/2$  spin system. (from O'Conner and Carlin 1975)

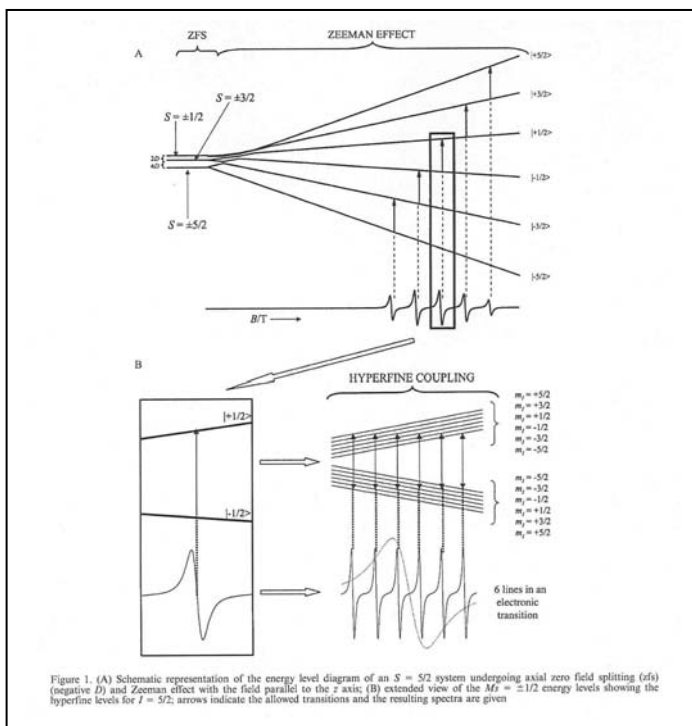


Figure 20. Schematic of Mn(II) energy level splittings. (Mantel et al. 2004).

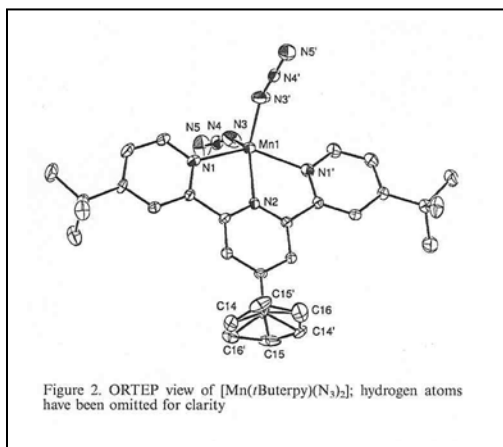


Figure 21. For the Mn(II) complex shown in this figure, EPR spectra were recorded at 5K and 10K at 285 GHz. (Mantel et al. 2004).

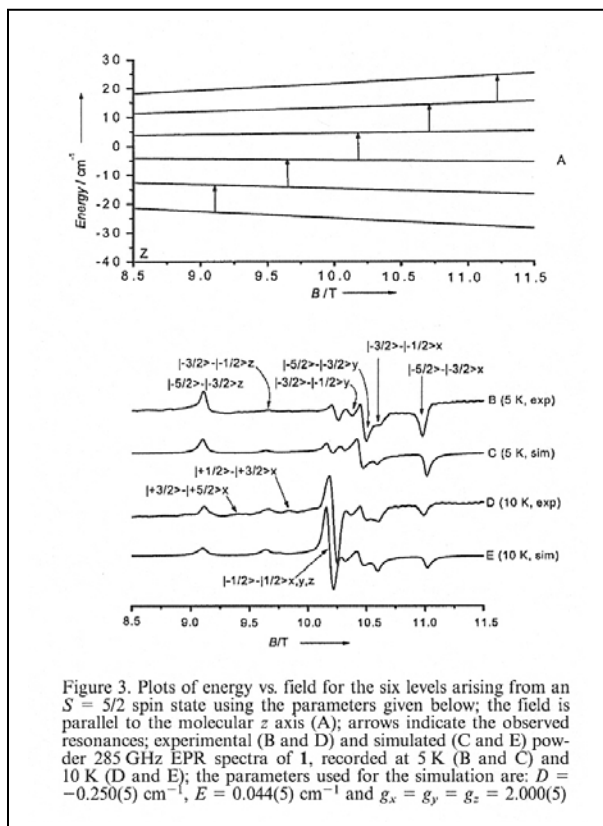


Figure 22. Transitions to which the peaks are assigned are labeled on the spectra. (Mantel et al. 2004).

Since at low temperatures only the lowest Zeeman levels are populated, the lowest-field peak (ca. 9.11 T) was assigned to the  $|5/2, -5/2\rangle$  to  $|5/2, -3/2\rangle$  transition. This implies that  $D$  is negative. The separation from the center of the spectrum is  $4D/g_z\beta$ , implying that  $D = 0.25 \text{ cm}^{-1}$  (Mantel et al. 2004).

Mn(III),  $d^4$  ( $S = 2$ ), also has some interesting challenges.

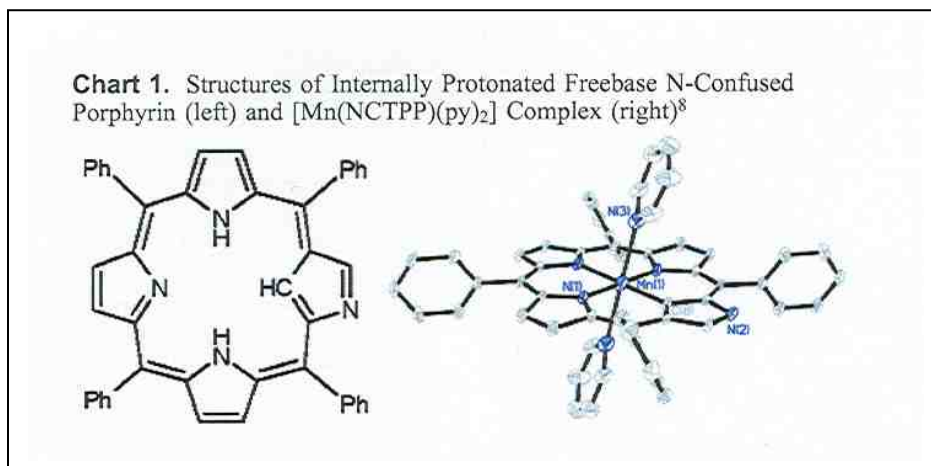


Figure 23. Harvey et al. (2005) showed the resonance field vs. microwave frequency for this spin system for the N-confused Mn porphyrin shown in the figure. The ZFS is large enough that no EPR signal is observed at X-band.

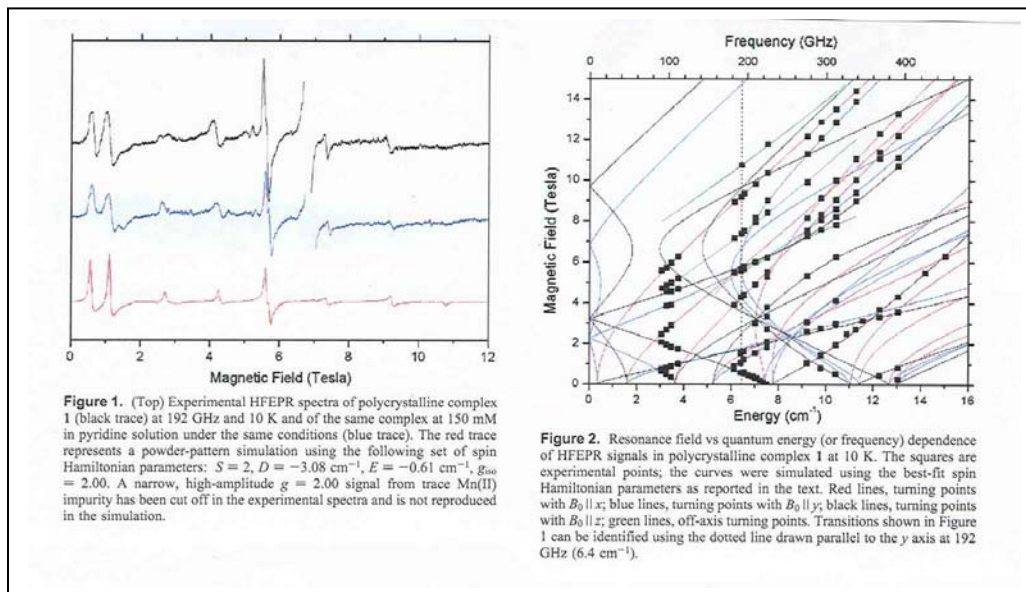


Figure 24. Multifrequency EPR spectra of the polycrystalline solid were measured and used to fit terms in a Hamiltonian of the form:

$$H = \beta B \cdot g \cdot S + D[S_z^2 - S(S+1)/3] + E(S_x^2 - S_y^2) + 4\text{th order ZFS terms}$$

The 4<sup>th</sup> order ZFS terms were "zero within statistical error."

More information about magnetic-field-dependence of EPR is in the booklet for the 2001 Workshop.

## Computer Simulation Programs

Most computer simulation programs are locally-written to solve a particular problem. Many of these are mentioned in the reviews cited, and currently-maintained programs are often mentioned on the web sites of EPR laboratories.

A few pulsed EPR simulation and analysis programs are available, such as GAMMA (Smith et al. 1994; Shane et al. 1998), EasySpin (Stoll, Epel) and the DEER programs by Jeschke. The most extensive set of CW EPR simulation programs is Sophe, written by Graeme Hanson. An outline of its features is in the following figure (from Hanson in Lund book). It is being extended to pulsed EPR, as described in detail separately by Graeme Hanson in this booklet. Additional leading references about pulsed EPR were cited above, and in the section by Graeme Hanson.

### Experiments

Continuous Wave EPR Spectra displayed in XeprView.  
Energy level diagrams, transition surfaces and transition roadmaps displayed in Netscape.  
Homotopy will be available in version 2.x of XSophe.  
Pulsed EPR spectra will be available as an additional component of version 2.x of XSophe.

### Spin Systems

Isolated and magnetically coupled spin systems.  
An unlimited number of electron and nuclear spins is supported with nuclei having multiple isotopes.

### Spin Hamiltonian Interactions

2<sup>nd</sup> order Fine Structure Interaction, 4<sup>th</sup> and 6<sup>th</sup> order corrections [S.D.S, B4, B6].<sup>8</sup>

Isotropic and Anisotropic Electron Zeeman [  $g\beta\mathbf{B}\cdot\mathbf{S}$ ,  $\beta\mathbf{B}\cdot\mathbf{g}\cdot\mathbf{S}$  ].

Isotropic and Anisotropic Hyperfine [  $a\mathbf{S}\cdot\mathbf{I}$ ,  $\mathbf{S}\cdot\mathbf{A}\cdot\mathbf{I}$  ].

Nuclear Zeeman Interaction for nuclei [  $g_N\beta_N\mathbf{B}\cdot\mathbf{I}$  ].

Quadrupole [  $\mathbf{I}\cdot\mathbf{P}\cdot\mathbf{I}$  ].

Isotropic Exchange [  $J_{mn}\mathbf{S}_m\cdot\mathbf{S}_n$  ].

Anisotropic Exchange (dipole dipole coupling) [  $\mathbf{S}_m\cdot\mathbf{J}\cdot\mathbf{S}_n$  ].

### Continuous Wave EPR Spectra

Spectra types:

Solution, randomly orientated and single crystal.

Symmetries:

Isotropic, axial, orthorhombic, monoclinic and triclinic.

Multidimensional spectra:

Variable temperature, multifrequency and the simulation of single crystal spectra in a plane.

### Methods

Matrix diagonalization - mosaic misorientation linewidth model.

Sophe Interpolation.

### Optimisation (Direct Methods)

Methods:

Hooke and Jeeves.

Quadratic variation of Hooke and Jeeves.

Simplex.

Two Simulated Annealing methods.

Spectral Comparison:

Raw data and Fourier transform.

## **Vision for the Future**

The long-term goal, and the reason for combining calculations of  $g$  and hyperfine and simulations of CW and pulsed EPR spectra all in one Workshop is the merger of these. Our vision is that one would hypothesize the species being observed, compute from first principles the  $g$ -value and hyperfine couplings, including the effect of solvent, use these to simulate the EPR spectrum, and compare with the observed spectrum. Computed hyperfine couplings and  $g$ -values, compared with the best-fit simulation will possibly identify the species, allow assignments without some of the isotopic substitutions that other wise would be necessary, and feed back to the computational models to improve the

basis sets for future use. The quantum mechanical calculations are improving rapidly, and the EPR simulation programs are improving rapidly, so we may see the practical implementation of this vision in the near future.

A greater challenge is to compute solvent-motion-induced modulation of zero field splittings and modulation of spin-orbit interactions with sufficient accuracy to predict electron spin relaxation times. In principle, it should be possible to use molecular dynamics calculations together with quantum mechanical estimates of dependence of spin-orbit interactions on molecular geometry to compute the dynamics of electron spin-lattice relaxation.

## **Section 2. Some Calculations of $g$ and $a$ values of radicals and metals**

We now turn to the quantum mechanical calculation of  $g$ -values and hyperfine couplings. The first summary relates to organic radicals. This is followed by calculations for transition metal complexes. Since the intent here is to provide references to examples that illustrate the fundamentals to be presented later in this booklet by Saba Mattar and Sarah Larsen, most of the information is provided in tabular form. In most cases, only one or two (hopefully representative) numerical values are extracted from papers that often contain detailed comparisons of multiple levels of computation and comparisons of basis sets.

### **Literature Search**

This brief introduction mentions a few leading references from the past several years. It is in no way comprehensive or exhaustive. Papers cited contain much more information than is even hinted at here. The goal of this introduction is to show a few of the types of molecules for which  $g$ -values or hyperfine couplings have been computed, and roughly the quality of agreement between experiment and theory attainable. No attempt has been made to give credit for “first” papers in either fundamental theory or applications. Most papers selected for inclusion in this summary were published in 2000 or later. Earlier papers can be found via the papers cited in these and in the reviews cited.

### **Introduction**

For many years educators have used the HMO interpretation of the EPR spectra of the naphthalene radical anion (McKelvey 1987) or the benzosemiquinone radical anion (Beck and Nibler, 1989) as an experimental demonstration of quantum mechanics for undergraduate students. In recent years various quantum mechanical calculational packages, such as Gaussian and ADF, have been shown to reproduce experimental molecular structures and energetics with good fidelity, and these programs now include capabilities to calculate  $g$  values and hyperfine couplings for open-shell molecules.

“One of the most challenging tasks in computational chemistry is the accurate calculation of the isotropic hyperfine components” Mattar and Stephens (2000). They performed the first such calculation for the commonly-used nitroxide free radical, tempone.

Background introduction and state-of-the-art applications are in the book by Weinhold and Landis (2005), the volumes edited by Lund and Shiotani (2003), by Kaupp, Bühl, and Malkin (2004), and the review by Improta and Barone (2004). The Amsterdam Density Functional 2005 was reviewed by Bomble (2006).

### **Selected Results for Organic Radicals**

Most of the examples selected here are for nitroxyl and semiquinone radicals.

The calculation of  $g$  values appears to generally agree better with experiment than the calculation of hyperfine values. Calculation of  $g$  values for organic radicals has been to within better than 1 part per thousand of the experimental value for many radicals. Mattar et al. (2006) found that UB1LYP and UPBE0 give nearly equivalent results, and there is little advantage in enlarging the basis set from EPR-II to aug-cc-pVTZ.

Mattar and A. D. Stephens (2000) state “the unrestricted UB1LYP HDF method provides us with electronic spin densities of sufficient quality to be able to directly compare the experimental and computed  $a^{\text{iso}}$  values. In the case of TEMPONE, which is a representative of spin labels, the agreement between theory and experiment is very good. This is only achieved if the effects of solvent, vibrational averaging of the NO1 bending mode and rapid interconversion of the twisted ring conformers are taken into account.”

For DTBN the calculated isotropic N hyperfine is in close agreement with experiment for several solvents (Mattar and Stephens, 2001). The largest discrepancy is for water. When using the PCM model, the calculated value is 16.28 G. When a supermolecule of DTBN and one H<sub>2</sub>O is optimized, the hyperfine increases to 16.78, in closer agreement with the experimental value of 17.16 G.

For nitroxyl radicals, Improta and Barone (2004) summarized (their table 5) the strong dependence (up to about a factor of two) of the computed N hyperfine coupling on the out of plane angle. Plato et al., computed that deviation from planarity of a nitroxyl radical strongly affects the slope of a plot of  $g_{xx}$  vs. nitrogen  $A_{zz}$ .

Specific hydrogen-bonding to the NO groups was explored by Engström et al. (2001) using 1 or 2 water or methanol molecules. The ROHF method was judged to exaggerate the effects of H-bonding. Owenius et al. (2001) compared experiment and theory for MTSSL in several solvents, and concluded that DFT gave more accurate results than ROHF methods.

Pavone et al. (2004) summarize prior calculations as showing that the polarizable continuum model (PCM) leads to good results for radicals in non-hydrogen-bonding solvents, but that inclusion of explicit water molecules together with the PCM is needed in the case of hydrogen-bonding solvents.

Ikryannikova et al. (2004) concluded that a cluster of >40 molecules of water is required around a nitroxyl radical to model a complete aqueous shell.

Further examples of the importance of solvation in the calculation of hyperfine is given in Mattar et al. 2004, where the calculated hyperfine couplings of 1,4-dihydro-9,10-anthrasemiquinone are closer to the experimental values when methanol and DMSO are included than are the gas-phase calculations. Improta and Barone (2004) also review methods for computing solvent effects on hyperfine couplings. They conclude “A combined PBE0/QCISD approach can further extend the reliability of the computational model to species such as nitroxides for which conventional and hybrid density functionals are not sufficiently accurate.”

Computations for perdeutero-tempone and tempo-palmitate show that the effects of solvent are local, with similar effects for the rather different molecules (Benzi et al., 2005). Solvent have stronger effect on the  $g_{xx}$  component of the  $g$  tensor than on the  $yy$  and  $zz$  components. Solvent effects on the N hyperfine are larger than the effect on  $g$ .

Barone and coworkers ( D’Amore et al, 2003; Cimino et al., 2006) state that all density functionals underestimate the absolute value of  $A_N$  in nitroxides, but quadratic configuration interaction approach coupled with purposely tailored basis sets provides accurate results. They obtained good agreement with experiment for solvents hydrogen-bonded to the nitroxyl.

Stipa (2006) compared 15 levels of DFT theory with experimental values for a dipyrindinium radical. Triple  $\zeta$  basis sets gave the poorest agreement with experiment. Several models for solvent-solute interaction were tried, but without much improvement in agreement. The best average agreement was with IPCM solvent model, PBE0 functional and 6-31G(d) basis set. The  $g$ -factor agreement was very good.

Kaup and coworkers ((Kacprzak et al. 2006) use B3LYP for hyperfine calculations “in combination with ... EPR II basis set (which was specifically designed for hyperfine calculations).” They state that “It is well known that gradient-corrected functionals such as BP86 underestimate the spin polarization in  $\pi$  radicals and thus provide less accurate hyperfine couplings.” A second order perturbation approach “has been demonstrated to provide unprecedented accuracy in calculations of  $g$ -tensors for organic radicals.” This paper analyzed in detail the effect on many hyperfine couplings of hydrogen bonding to the semiquinone in the  $Q_H$  site in quinol oxidase. Many computations were compared for different models.

Singel and coworkers (Boulet et al. 2000) showed that comparison of different levels of calculation result in ambiguous assignments of couplings, and that in the case of apogalactose radical the determination of hyperfine couplings may require detailed accounting of the protein environment, and not just a dielectric continuum model.

Computational results are getting good enough to guide interpretation of experimental results. For example, Saracino et al. (2002) computed the  $pK_a$  for 2,2,5,5-Tetramethyl-3-

carboxypyrrolidine, and, finding it in disagreement with the value in the literature, remeasured the pKa and found it to be closer to the computed value. The assignments of splittings in the EPR spectrum of the protonated radical obtained by reduction of the dye called Orange II were based on computed spin densities and hyperfine couplings (Abbott et al., 2005).

It appears that for organic radicals, including those with atoms as heavy as S, g-values can be computed within experimental accuracy with the most sophisticated calculations, including solvent effects. Hyperfine couplings of protons often can be calculated in reasonably close agreement with experiment, but couplings to N, especially in flexible ring systems such as those in nitroxyl radicals, are rarely in agreement with experiment.

Trends in computed hyperfine couplings among sets of radicals or among solvent environments for a given radical are generally better than the absolute values. The above papers and several others are in the Tables for quick review. Each of the papers cited contains much more information than was sampled for these summary tables.

**Table 1: 5- and 6-membered ring nitroxides**

radical	level of calculation	solvent	g expt.	g calc.	A <sub>N</sub> (G) expt.	A <sub>N</sub> calc.	reference
tempone <sup>1</sup>	UB1LYP, Barone triple- $\zeta$ EPR-III	yes, 1 PCM <sup>2</sup>			16.1 16.27	15.1	Mattar 2000
DTBN	UB1LYP, Barone triple- $\zeta$ EPR-III	UAHF-PCM			17.16	16.78	Mattar and Stephens 2001
DTBN	B3LYP BP86 6-31G(d,p)	PCM;super molecules; several solvents	$\Delta g$ 3241 ppm <sup>4</sup>	3192, 3344			Rinkevicius et al. 2004
diphenyl nitroxide	B3LYP BP86 6-31G(d,p)	PCM;super molecules; several solvents	$\Delta g$ 2761 ppm <sup>4</sup>	2773, 2933			Rinkevicius et al. 2004
pyrrolidine <sup>3</sup>	ROHF/cc-pVDZ AMFI	H <sub>2</sub> O H-bonding		2.0076 2.0061 2.0022			Engström et al. 2001
MTSSL	B3LYP/EPR-II BP86/IGLO-II	H <sub>2</sub> O H-bonding	2.00800 2.00586 2.00199	2.00750 2.00554 2.00213	16.12	11.25	Owenius et al. 2001
pyrrolidine <sup>3</sup>	Perdew86 IGLO-II				15.9	7.2	Engström 2002
carboxyproxyl carboxytempo	PBE0 6-31G(d)	several; results for 2 H <sub>2</sub> O			16.05 17.06	16.12 16.74	Saracino et al. 2002
(CH <sub>3</sub> ) <sub>2</sub> NO	6-31+G(d) PBE0 + MD	gas phase; water				13.3 15.3	Pavone et al., 2004
H <sub>2</sub> NO	BP86 ZORA-	32 H <sub>2</sub> O	2.0057	2.0080	27.1	17.8	Neugebauer

	QZ4P				(gas) 35.9 (H <sub>2</sub> O)	13.6	et al. 2005
tempo-palmitate	PBE1PBE 6-31G	n-pentyl cyano- biphenyl	$g_{xx}$ 2.00975	2.00837	$a_{zz}$ 19.13	18.18	Benzi et al. 2005
tempo	PBE0/QCISD 6-31+G(d,p) EPR-II	PCM phenol, benzylic alcohol			16.58 15.91	16.34 15.89	Cimino et al. 2006

Notes to the table:

1. twisted boat conformer
2. Tomasi's PCM method places the radical in a cavity in a continuum of dielectric constant 78.3
3. An analog of MTSL was used as a model: 2,2,5,5-tetramethyl pyrrolidinyl-1-oxyl
4. The values selected are for solvation by 2 water molecules.

**Table 2: Imidazoline nitroxyls**

radical	level of calculation	solvent	g expt.	g calc.	$A_N$ (G) expt.	$A_N$ calc.	reference
imidazo-line	PRIRODA DFT	41 H <sub>2</sub> O			15.8	13.5	Ikryannikova 2004
imidazo-line	B1LYP EPR-II	H <sub>2</sub> O			8.25 <sup>@</sup>	6.94	Matteo et al., 1999
CH <sub>3</sub> -Im <sup>&amp;</sup> imidazoline <sup>#</sup>	B1LYP	PCM			7.6 7.9	5.7 7.3	Adamo et al. 1999

<sup>@</sup> poorer agreement for C coupling.

<sup>&</sup> 2-methyl-4,4,5,5-tetramethylimidazoline-1-oxyl-3-oxide

<sup>#</sup> 2-(2-imidazolyl)-4,4,5,5-tetramethylimidazoline-1-oxyl-3-oxide

**Table 3: Other organic radicals**

radical	level of calculation	solvent	g expt.	g calc.	A expt. (G)	A calc.	reference
pyrimidine bases e.g., uracil	B3LYP 9 basis sets, e.g., 6-31+G(d,p)	up to 10 H <sub>2</sub> O			N1 0 N3 4.08	-0.02 4.1	Naumov et al. 2003
di-pyridinium*	B3LYP PBE0 many levels		2.00308	2.00302	N 0.648	N 0.180 to 0.726	Stipa 2006
allyl	B3LYP/DZP'	none			H1 -39.0	-39.5	Adamo et al. 1995
RH <sub>β</sub> C <sub>β</sub> =C <sub>α</sub> H <sub>α</sub> E and Z isomers	B1LYP 6-311+G(2df,p)				H 15.7 C 107 F 101	17.2 112 102	Jaszewski and Jeziarska 2001
H <sub>2</sub> CNO·	ROHF UCCD UQCISD(T) 6-311G(d,p)				<sup>14</sup> N 33.7	26.3 to 30.2	Jaszewski and Jeziarska 2001
iminoxy radicals C <sub>6</sub> H <sub>5</sub> COC(NO)H E	B1LYP EPR-III	none	2.0042		N 31.4 H <sub>α</sub> 27.6	30.8	Tabaka and Jeziarska

isomer						H <sub>γ</sub> 0.3	29.05 0.78	2004
cysteine-linked tyrosyl o-methylthiocresol	B3LYP MPWP86 6-31G(d)					42 and 24 MHz	ca. 0 to 16 MHz	Boulet et al. 2000
1,4-benzosemiquinone anion	B3P86/[632 41] B3LYP 6-31G(d)					<sup>1</sup> H - 2.18	-2.42	Boesch and Wheeler 1997
p-fluoranil semiquinone anion	B3P86/[632 41] B3LYP 6-31G(d)					<sup>19</sup> F 4.05	<sup>19</sup> F 2.54	Boesch and Wheeler 1997
p-fluoranil semiquinone anion	B1LYP EPR-III					<sup>19</sup> F 4.05	<sup>19</sup> F 3.2	Mattar et al. 2002
2,3,5,6-tetramethoxy- 1,4-benzosemiquinone	UB1LYP	1 MeOH				average = 0.0445	-0.0134	Mattar et al. 2002
semiquinones, H- bonding and substituent effects	BP86 DZVP BII BIII	H <sub>2</sub> O propanol	Δg 2684 ppm	2350				Kaupp et al 2002
p-benzo-semiquinone, H-bonding effects	B3LYP EPR-II	H <sub>2</sub> O MeOH	2.0047	2.0049		<sup>2</sup> H 0.03	-0.02	Sinnecker et al. 2004
semiquinone <sup>#</sup>	BP86	H- bonding analyzed						Kacprzak et al. 2006
dihydroantra- semiquinone	UB1LYP UAHF- PCM	MeOH DMSO				2.69  0.70	2.343 - 0.88	Mattar et al. 2004
1,4-benzo-semiquinone	UB1LYP UPBE0	4 MeOH	2.0047	2.0049		2.39	-2.448	Mattar 2004
CH <sub>3</sub> -SS <sup>•</sup>	ROHF CASSCF cc-pVDZ B3LYP		2.053 2.026 2.000	2.063 2.028 2.002		<sup>1</sup> H 10	9	Engström et al. 2000
4,5- bis(trifluoromethyl)- 1,3,2-dithazol-2-yl	B1LYP		2.0020 2.0004 2.0124	2.0030 2.0133		<sup>14</sup> N 11.3 <sup>19</sup> F 0.69	11.28 0.676	Mattar and Stephens 2000
1,3,2-dithiazolyl	UB1LYP UPBE0 aug-cc-pVTZ	toluene	2.00697	2.00691				Mattar 2005
thiopheno-1,3,2- dithiazolyl	UB1LYP UPBE0 aug-cc-pVTZ	THF CH <sub>2</sub> Cl <sub>2</sub>	2.0065	2.00699				Mattar et al. 2006

\* 1,1'-dimethyl-2,2'-dicyano-4,4'-bipyridinium bis-methylsulphate; 15 different levels of computation were compared with experiment.

<sup>#</sup> the Q<sub>H</sub> site of quinol oxidase

### Other potentially relevant papers about calculations.

Some of the calculations listed in the tables used the PBE0 model, which was described by Adamo and Barone (1999).

Yagi et al., (2001) calculated the n-π\* transition energies for (CH<sub>3</sub>)<sub>2</sub>NO. ROHF-SCI calculation yielded 25,461 in H<sub>2</sub>O and the experimental value is 23,753. As pointed out by Engström et al. (2001), the dominant contribution to g<sub>xx</sub> is due to the n-π\* transition excitation, and this is affected by H-bonding.

The polarizable continuum model (PCM) is commonly used for solvation of radicals. Cossi et al. (2002) describe how to use this model at several different levels. Neugebauer et al. (2005) discuss several models of solvent effects on calculations of  $g$  and hyperfine values for  $\text{H}_2\text{NO}$ , and show the dependence of hyperfine on out-of-plane bending and on the solvation model.

Neese (2001) presented a method that “is among the most accurate so far developed models for the prediction of  $g$  values.” Neyman et al. (2002) present “a novel scheme to calculate  $g$ -tensors of doublet-state systems within a density functional method” and compute  $g$  tensors for several small molecules.

### **Selected Results for Calculations of $g$ and $a$ Values of Metals**

Over the past few years there has been dramatically increased use of quantum mechanical methods to compute structure and electronic energy levels of transition metal complexes. Computational results are in good enough agreement with experiment for many heavy elements that they are being used to explicate, for example, catalytic pathways. The hardest problems are those involving 3d transition metals, which are just the cases most commonly studied by EPR. However, even for 3d elements it is becoming possible to compute the parameters most often measured in CW EPR – the  $g$ -value and the hyperfine splittings. In the following paragraphs and table, we present a few examples gleaned from the literature of the past few years to show what is possible with computer programs now available. The discrepancies between experiment and theory constitute a prediction of enhancements in theory that you can anticipate in the near future.

In addition to the books and reviews cited for organic radicals, see the review by Ruiz et al. (2005) on spin distribution in transition metal complexes.

If an electron in a 4s orbital significantly contributes to a singly-occupied molecular orbital (SOMO) then many functionals will give a good estimate of the metal hyperfine coupling. However, if the spin density at the metal arises largely from spin polarization it is much more difficult to compute the experimental hyperfine coupling (Munzarová et al. 2000).

Even systems as large and complex as the FeMo cluster of nitrogenase have been calculated (Lovell et al., 2001). Kaupp and coworkers (Arbuznikov et al., 2002) compared many functionals for 11 main group compounds and 10 3d and 4d transition metal complexes. They concluded that “the accurate evaluation of the EPR parameters for 3d transition metal complexes remains a challenge.” Neese (2003) computed hyperfine couplings for a large number of metal complexes using B3LYP and BP86, obtaining results within 5 to 10% of experimental in many cases. No solvent was included, but many of the complexes were coordinatively saturated. A couple of examples from this paper are in the table.

Neese (2001) described a method for computing  $g$  values and compared it with experiment for several metal complexes. As is common in many papers presenting computer  $g$  values, the reported value is the shift of  $g$  from the free-electron  $g$  value, in ppm. For a total of 11 Ti, V, Cr, Ni, and Cu complexes, Neese computed an average signed  $g$  shift error of -11.2, 1.2 and 8.0 ppm for BP, B3LYP, and PBE0, respectively. More commonly, though, the  $g$ -values of metal complexes, relative to the free-electron  $g$ , are reported in parts per thousand (ppt), whereas those of organic radicals are reported in parts per million (ppm).

Daul (2004) proposed a new DFT-based ligand field model and applied it to tetrahedral and octahedral complexes.

Jaszewski and Jezierska (2001) confirmed by DFT calculation the assignment of the largest proton hyperfine coupling to the  $\beta$ -hydrogens of cysteine-112 in azurin. However, even the largest basis set used with UB1LYP was not sufficient to get good agreement with experiment for the copper hyperfine or the degree of delocalization of the copper  $d$  orbital onto the sulfur.

Saladino and Larsen (2003) found that isotropic Cu hyperfine was calculated more accurately by SR UKS methods, but that the anisotropic components were calculated more accurately with SO + SR ROKS methods. Some of the results were attributed to cancellation of errors. The experimental values for the  $VO^{2+}$  complexes were for solid state materials, so “better than 10-15% agreement with experimental  $A$  values is not expected.” These papers contain many results, and only one arbitrarily selected value is listed in the table as an indication of the accuracy achieved. The best values for the  $VO^{2+}$   $A_{iso}$  was achieved using BHPW91.

A rather different situation is presented by benzenedithiolato metal complexes (Ray et al., 2005). Some oxidation states of these species can be written formally as having, for example, Cu(III) and a diamagnetic ligand, or Cu(II) and a free radical ligand. The DFT calculations describe the unpaired electron as ligand-based with mixture with a metal  $d_{xy}$  orbital.

Garipov et al. (2006) conclude that the 6-311G(2d,p) basis set is not accurate for Cu(II) hyperfine estimates. Hyperfine tensor components agree fairly well at the PBE/BS2 level.

Many of the computations are for  $d^1$  complexes. Aquino and Rodriguez (2005) computed zero-field splitting (ZFS) for the Fe(IV)-oxo moiety, achieving  $D = 28.17$  and  $28.67 \text{ cm}^{-1}$ , in good agreement with the experimental value of  $29 \pm 3 \text{ cm}^{-1}$ . Takeda et al. (2005) computed the spin-orbit coupling (SOC) contribution to ZFS for triplet benzene, naphthalene, carbene, and silylene, triplet  $O_2$ , and some single-molecule magnets. The SOC contribution is small in several cases, and extremely dependent on bond angle in the case of carbene and silylene. For a Mn(III)-Cu(II) molecule, the agreement with experiment was close when UBLYP and UPW91 were used, but UB3LYP underestimated the  $D$  value.

EPR has been a major tool for finding the distribution of electron spin density in metal complexes of non-innocent ligands. In many cases in which the ligands are known to support multiple oxidation states (e.g., quinone, semiquinone, hydroquinone), it can become very difficult to describe the oxidation state, and hence the electronic states, of the metal and ligands. Remenyi and Kaupp (2005) address this question for Ru complexes of quinonoid ligands using DFT computations. In one case, for example, a cationic complex is described as  $d^5$  Ru(III) with a neutral ligand, but the “anionic complexes turn out to be approximately halfway between a  $d^6$ -Ru<sup>II</sup>/semiquinone and a  $d^5$ -Ru<sup>III</sup>/catecholate formulation.” Reasonable agreement of g-tensors was achieved. Similarly, should (diiminepyridine)Al(CH<sub>3</sub>)<sub>2</sub> be classified as Al(II) or an Al(III) complex of an organic ligand? Scott et al. (2005) computed g and hyperfine values at the B3LYP and P86 level and concluded that the unpaired electron is largely in the ligand  $\pi^*$  orbital. The DFT calculations also showed that a splitting due to 6 equivalent H should be assigned to the two imine methyls and not to the two methyls bonded to the Al.

DFT was used to support the interpretation of HYSCORE spectra of a rhodium-aminyl complex (Maire et al., 2006). The calculated spin density was 41% on Rh and 28% on each of two N, which was consistent with the hyperfine values measured by ENDOR and HYSCORE.

One of the major problems in calculating magnetic parameters of transition metal complexes is to achieve a proper description of core and valence shell spin polarization without introducing appreciable spin contamination (Sojka and Pietrzyk, 2004). Honziček et al. (2004) summarized prior results as follows:

- (i) “gradient-corrected functionals tend to overestimate important core-shell spin polarization
- (ii) exact exchange mixing improves the agreement with experimental HFC tensor, however, in some cases spin contamination leads to deterioration of results.”

Kaupp and coworkers (Frantz et al. 2002) published the following summary: “Previous studies of g-tensors for transition metal complexes have indicated that the use of gradient-corrected (GGA) or local (LDA) density functionals underestimates the g-shift values significantly. It is possible to partly correct these deficiencies by admixture of Hartree-Fock exchange in hybrid functionals. In contrast, for organic radicals, GGA or LDA functionals tend to slightly overestimate the g-shifts, and hybrid functionals do not appear to change this situation.”

The table contains just enough information about the content of the paper to whet your appetite to consume the paper.

**Table 4: Transition metal complexes** (A in MHz unless other wise stated)

metal complex	level of calculation	$g_{\parallel}$ expt.	$G_{\parallel}$ calc.	$A_{\text{iso}}$ expt.	$A_{\text{iso}}$ calc.	reference
21 metal complexes [Cr(CO) <sub>4</sub> ] <sup>+</sup>	B3LYP, BP86, etc. CCSD			41.5	21.9 to	Munzarová and Kaupp 1999

	CCSD(T)				40.4	
9 metal complexes Co(CO) <sub>4</sub>	B-EXX(L)-PW91	$\Delta g_{\parallel}$ 3.6 $\Delta g_{\perp}$ 127.6	4 to 16.6 78.9 to 100			Arbuznikov and Kaupp 2004
20 d <sup>1</sup> metal porphyrins e.g., ClPCrO	VWN LDA	$\Delta g_{\parallel}$ -16 ppt	-10			Patchkovskii and Ziegler 2000
FeMo <sup>I</sup> cofactor	spin-unrestricted broken symmetry			11.7	8.8 to 15.1	Lovell et al., 2001
azurin	UB1LYP multiple basis sets			H <sub><math>\beta</math></sub> Cys112 28 MHz	45.5	Jaszewski and Jezierska 2001
11 main group, 10 3d and 4d	meta-GGA; B3PW91		plot of many g shifts		plot of many hyperfine couplings	Arbuznikov et al., 2002
3d <sup>3</sup> in SrTiO <sub>3</sub> Cr <sup>3+</sup> Mn <sup>4+</sup> Fe <sup>5+</sup>	SO	$\Delta g$ -0.0243 -0.0083 0.0108	-0.0240 -0.0092 0.0109			Zheng and Wu 2005
Mn(H <sub>2</sub> O) <sub>6</sub> <sup>2+</sup> S = 5/2	B3LYP BP86			-165	-245	Neese 2003
Cr(H <sub>2</sub> O) <sub>6</sub> <sup>3+</sup> S = 3/2	B3LYP BP86			35	55	Neese 2003
V(H <sub>2</sub> O) <sub>6</sub> <sup>2+</sup> S = 3/2	B3LYP BP86			-172	-247	Neese 2003
5 Cu complexes Cu(NH <sub>3</sub> ) <sub>4</sub> <sup>2+</sup>	B3LYP PWP1					Neese 2001
Cu(quin)	BLYP, BP86, BPW91			-238	-214 to 112	Saladino and Larsen 2003
Cu(ox) <sub>2</sub> <sup>2-</sup>	same			-180	-228 to 93	Saladino and Larsen 2003
Cu(acac) <sub>2</sub>	same			-231	-225 to 95	Saladino and Larsen 2003
Cu(L-alaO) <sub>2</sub>	same			-222	-206 to 91	Saladino and Larsen 2003
Cu(NH <sub>3</sub> ) <sub>4</sub> <sup>2+</sup>	SORCI BP B3LYP	$g_{\parallel}$ 2.241 $g_{\perp}$ 2.041	SORCI 2.045 2.055	A <sub><math>\parallel</math></sub> -586 A <sub><math>\perp</math></sub> -68	-591 3	Neese 2004
Cu dimer <sup>4</sup>	BP86 TZV B3LYP EPR-II			N <sub>ax</sub> 14.5, 14.5, 26.5 N <sub>eq</sub> 5.5, 5.5, 7	14.3, 14.3, 31.5 5.1, 5.2, 9.8	Kababya et al. 2006
VO Schiff base complexes	B3PW91 BHPW91	-30	-33.8 and -16.8	-274.4	-183 to -299.6	Munzarová and Kaupp 2001
VO <sup>2+</sup> + imidazole	relativistic; many levels				dependence on	Saladino and Larsen 2005

					dihedral angle	
VO(H <sub>2</sub> O) <sub>5</sub> <sup>2+</sup>	9 density functionals	1.933	1.923	-324	-415 to -21	Saladino and Larsen 2003, 2005
VO(H <sub>2</sub> O) <sub>5</sub> <sup>2+</sup>	B3LYP	1.939	1.9495	-324	-293	Baute et al. 2005
VO(mal) <sub>2</sub> <sup>2-</sup>	9 density functionals	1.942	1.957	-299	-297 to -2	Saladino and Larsen 2003
VO(acac) <sub>2</sub>	same	1.945	1.928	-307	-319 to -8	Saladino and Larsen 2003
VO(gly) <sub>2</sub>	same	1.950	1.957	-275	-288 to 19	Saladino and Larsen 2003
VO(ox) <sub>2</sub> <sup>2-</sup>	same	1.941	1.945	-295	-300 to -1	Saladino and Larsen 2003
Oxovanadium complexes with axial anionic ligands	B3LYP, B3LYP			-279	-196 (B3LYP) -256 (B3LYP)	Aznar, et al. 2004
VO(H <sub>2</sub> O) <sub>5</sub> <sup>2+</sup> and other vanadyl complexes	B3LYP, INDO/S	1.978	1.983 (B3LYP) 1.987 (INDO/S)	-182 cm <sup>-1</sup>	-165 cm <sup>-1</sup> (B3LYP)	Paine et al. 2004
vanadocene complexes	BHPB86			-207.2	-219.3	Honziček et al. 2004
Cr(V) complex	B3LYP ZORA	1.996	1.993	35	23.1	Kapre et al. 2006
[M(L)(L') M= Ni, Pd, Pt  Au(III)L <sub>2</sub>	ZORA-B3LYP	2.05 2.03 2.06  2.07	2.07 2.04 2.06  2.04	320, 278, 227 < line width	-302, -210, -129 -16, -21, -17	Ray et al. 2005
Cu(II) complex <sup>2</sup>	PBE/BS1 B3LYP/BS3	Δg = 0.0715	0.0502	-79	-62.4 to -101.2	Garipov et al. 2006
Cu(II) complex <sup>3</sup>	B3LYP 6-31G*	g <sub>⊥</sub> 2.041 g <sub>∥</sub> 2.191	2.041 2.134	A <sub>x</sub> 26.5 A <sub>z</sub> 200	-9.7 -204	Comba et al. 2006
Rh aminyl	ZORA RPBE			11.1	12	Maire et al. 2006
CuNO on catalyst	B3LYP 6-311G(d) BPW9/LanL2 DZ			Cu 158.5 cm <sup>-1</sup>	158.7	Sojka and Pietrzyk 2004

1. The example is for a particular spin state of the Mo<sup>4+</sup> 6Fe<sup>2+</sup> Fe<sup>3+</sup> FeMoco cluster.
2. Cu(II) complexes with N-phosphoryl thioureas
3. tris-macrocyclic complex with 4 N donors for each Cu
4. binuclear copper azacryptate

For multi-spin systems the calculation of zero-field splittings (ZFS) is a major challenge. One of the simplest systems for comparison of experiment with theory of ZFS is CH<sub>2</sub>.

Petrenko et al. (2002) calculated at the B3LYP level of theory for the triplet-optimized geometry,  $D = 0.8897 \text{ cm}^{-1}$  and  $E = -0.052 \text{ cm}^{-1}$ , which should be compared with experimental values of  $D = 0.7567 \text{ cm}^{-1}$  and  $|E| = 0.0461 \text{ cm}^{-1}$ . In the case of  $\text{CH}_2$  it is reasonable to assume that most of the ZFS will be due to spin-spin interactions, but for heavier main-group and transition metal compounds, spin-orbit interactions could also make important contributions.

## References

- L. C. Abbott, S. N. Batchelor, J. Oakes, B. C. Gilbert, A. C. Whitwood, J. R. L. Smith, and J. N. Moore, Experimental and Computational Studies of Structure and Bonding in Parent and reduced Forms of the Azo Dye Orange II. *J. Phys. Chem. A* **109**, 2894-2905 (2005).
- C. Adamo, V. Barone, and A. Fortunelli, Validation of self-consistent hybrid density functionals for the study of structural and electronic characteristics of organic  $\pi$  radicals. *J. Chem. Phys.* **102**, 384-393 (1995).
- C. Adamo, A. di Matteo, P. Rey, and V. Barone, Tuning of Structural and Magnetic Properties of Nitronyl Nitroxides by the Environment. A Combined Experimental and Computational Study. *J. Phys. Chem. A* **103**, 3481-3488 (1999).
- C. Adamo and V. Barone, Toward reliable density functional methods without adjustable parameters. *J. Chem. Phys.* **110**, 6158-6170 (1999).
- F. Aquino and J. H. Rodriguez, First-principle computation of zero-field splittings: Application to a high valent Fe(IV)-oxo model of nonheme iron proteins. *J. Chem. Phys.* **123**, 204902 (2005).
- A. V. Arbuznikov, M. Kaupp, V. G. Malkin, R. Reviakine, and O. L. Malkina, Validation study of meta-GGA functionals and of a model exchange-correlation potential in density functional calculations of EPR parameters. *Phys. Chem. Chem. Phys.* **4**, 5467-5474 (2002).
- A. V. Arbuznikov and M. Kaupp, Unrestricted open-shell Kohn-Sham scheme with local hybrid exchange-correlation potentials: improved calculation of electronic g-tensors for transition-metal complexes. *Chem. Phys. Lett.* **391**, 16-21 (2004).
- C. P. Aznar, Y. Deligiannakis, E.J. Tolis, T. Kabanos, M. Brynda, and D. Britt, ESE-ENDOR study and DFT calculations on oxovanadium compounds: Effect of axial anionic ligands on the V-51 nuclear quadrupolar coupling constant. *J. Phys. Chem. A*, **108**, 4310-4321 (2004).
- D. Baute and D. Goldfarb, The 17O hyperfine interaction in (VO)-O-17((H2O)-O-17)(5)(2+) and Mn ((H2O)-O-17)(6)(2+) determined by high field ENDOR aided by DFT calculations. *J. Phys. Chem. A*, **109**, 7865-7871 (2005).

- R. Beaulac, P. L. W. Tregenna-Piggott, A.-L. Barra, H. Weihe, D. Luneau, and C. Reber, The Electronic Ground State of  $[V(\text{urea})_6]^{3+}$  Probed by NIR Luminescence, Electronic Raman, and High-Field EPR Spectroscopies. *Inorg. Chem.* **45**, 3399-3407 (2006).
- R. Beck and J. W. Nibler, ESR Studies and HMO Calculations on Benzosemiquinone Radical Anions. *J. Chem. Ed.* **66**, 263-266 (1989).
- R. L. Belford, R. B. Clarkson, J. B. Cornelius, K. S. Rothenberger, M. J. Nilges, and M. D. Timken, EPR Over Three Decades of Frequency: Radiofrequency to Infrared. *Electronic Magnetic Resonance of the Solid State*. J. A. Weil, M. K. Bowman, J. R. Morton, K. F. Preston, eds. Canadian Society for Chemistry, Ottawa, Canada, 1987.
- N. P. Benetis and J. Westerling, Nonperturbative Simulation of Two-Pulse Electron Spin-Echo-Envelope Modulation Spectra. Comparison with Experimental Single-Crystal Spectra. *J. Magn. Reson.* **86**, 97-109 (1990).
- N. P. Benetis and U. E. Nordh, Non-secular simulation of frequency domain two-pulse powder ESEEM signals in multinuclear systems. *Chem. Phys.* **200**, 107-118 (1995).
- C. Benzi, M. Cossi, and V. Barone, Accurate prediction of electron-paramagnetic resonance tensors for spin probes dissolved in liquid crystals. *J. Chem. Phys.* **123**, 194909 (2005).
- A. H. Beth and E. J. Hustedt, Saturation Transfer EPR. *Biol Magn. Reson.* **24**, 369-407 (2005).
- S. E. Boesch and R. A. Wheeler,  $\pi$ -Donor Substituent Effects on Calculated Structures, Spin Properties, and Vibrations of Radical Anions of p-Chloranil, p-Fluoranil, and p-Benzoquinone. *J. Phys. Chem. A* **101**, 8351-8359 (1997).
- Y. J. Bomble, review of Amsterdam Density Functional 2005, *J. Am. Chem. Soc.* **128**, 3103 (2006).
- A. M. Boulet, E. D. Walter, D. A. Schwartz, G. J. Gerfen, P. R. Callis, and D. J. Singel, Electronic structure and hyperfine interactions in thioether-substituted tyrosyl radicals. *Chem. Phys. Lett.* **331**, 108-114 (2000).
- D. E. Budil, S. Lee, S. Saxena, and J. H. Freed, Nonlinear-Least\_squares Analysis of Slow-Motion EPR spectra in One and Two Dimensions Using a Modified Levenberg-Marquardt Algorithm. *J. Magn. Reson. A* **120**, 155-189 (1996).
- P. Cimino, M. Pavone, and V. Barone, Structural, thermodynamic, and magnetic properties of adducts between TEMPO radical and alcohols in solution: New insights from DFT and discrete-continuum solvent models. *Chem. Phys. Lett.* **419**, 106-110 (2006).

P. Comba, Y. D. Lampeka, A. I. Prikhod'ko, and G. Rajaraman, Determination of the Solution Structures of Melamine-Based Bis- and Tris-Macrocyclic Ligand Copper(II) Complexes. *Inorg. Chem.* **45**, 3632-3638 (2006).

M. Cossi, G. Scalmani, N. Rega, and V. Barone, New developments in the polarizable continuum model for quantum mechanical and classical calculations on molecules in solution. *J. Chem. Phys.* **117**, 43-54 (2002).

N. S. Dalal, D. E. Kennedy, and C. A. McDowell, Electron paramagnetic resonance (EPR) and electron-nuclear double resonance (ENDOR) of hyperfine interactions in solutions of  $\alpha, \alpha'$ -diphenyl- $\beta$ -picryl hydrazyl (DPPH). *J. Chem. Phys.* **59**, 3403-3410 (1973).

M. D'Amore, R. Improta, and V. Barone, Conformational Behavior and Magnetic Properties of a Nitroxide Amino Acid Derivative in Vacuo and in Aqueous Solution. *J. Phys. Chem. A* **107**, 6264-6269 (2003).

C. A. Daul, Modelling Properties of Molecules with open d- or f-Shells Using Density Functional Theory. *Chimia* **58**, 316-320 (2004).

C. Dobe, C. Noble, G. Carver, P. L. W. Tregenna-Piggott, G. J. McINTyre, A.-L. Barra, A. Neels, S. Janssen, and F. Juranyi, Electronic and Molecular Structure of High-Spin  $d^4$  Complexes: Experimental and Theoretical Study of the  $[\text{Cr}(\text{D}_2\text{O})_6]^{2+}$  Cation in Tutton's Salts. *J. Am. Chem. Soc.* **126**, 16639-16652 (2004).

S. C. Drew, J. R. Pilbrow, P. J. Newman, and D. R. MacFarlane, Field-swept pulsed electron paramagnetic resonance of  $\text{Cr}^{3+}$ -doped ZBLAN fluoride glass. *J. Phys. D: Appl. Phys.* **34**, 2987-2994 (2001).

S. S. Eaton and G. R. Eaton, EPR Methodologies – Ways of Looking at Electron Spins. EPR Newsletter Summer/Fall 1997, pages 15-18.

M. Engström, O. Vahtras, and H. Ågren, MCSCF and DFT calculations of EPR parameters of sulfur centered radicals. *Chem. Phys. Lett.* **328**, 483-491 (2000).

M. Engström, R. Owenius, and O. Vahtras, Ab initio g-tensor calculations of hydrogen bond effects on a nitroxide spin label. *Chem. Phys. Lett.* **338**, 407-413 (2001).

M. Engström, J. Vaara, B. Schimmelpfennig, and H. Ågren, Density Functional Theory Calculations of Electron Paramagnetic Resonance Parameters of a Nitroxide Spin Label in Tissue Factor and Factor VIIa Protein Complex. *J. Phys. Chem. B* **106**, 12354-12360 (2002).

Boris Epel, Kazan Viewer for Matlab, and  
Boris Epel, Igor Gromov and Stefan Stoll, SpecMan, the shell for pulse EPR experiments

<http://www.geocities.com/boep777/> (accessed 07/04/06)

H. Eviatar, Y. K. Levine, and D. I. Hoult, The Simulation of Two-Dimensional Electron Spin-Echo Experiments on Liquid-Crystalline Systems Using Stochastic Trajectories of Molecular Motion. *J. Magn. Reson. A* **117**, 41-52 (1995).

S. Frantz, H. Hartmann, N. Doslik, M. Wanner, W. Kaim, H.-J. Kümmerer, G. Denninger, A.L. Barra, C. Duboc-Toia, J. Fiedler, I. Ciofini, C. Urban, and M. Kaupp, Multifrequency EPR Study and Density Functional g-Tensor Calculations of Persistent Organorhenium Radical Complexes. *J. Am. Chem. Soc.* **124**, 10563-10571 (2002).

J. H. Freed, ESR and Molecular Dynamics, *Biol. Magn. Reson.* **24**, 239-268 (2005).

B. J. Gaffney and H. J. Silverstone, Simulation Methods for Looping Transitions. *J. Magn. Res.* **134**, 57-66 (1998).

R. R. Garipov, V. G. Shtyrin, D. A. Safin, Y. I. Zyavkina, F. D. Sokolov, A. L. Konkin, A. V. Aganov, and A. V. Zakharov, Combined EPR and DFT study of the copper(II) complexes with N-phosphoryl thioureas. *Chem. Phys.* **320**, 59-74 (2006).

G. R. Hanson, XSophe-Sophe-XeprView. A computer simulation software suite (v. 1.1.3) for the analysis of continuous wave EPR spectra. *J. Inorg. Biochem.* **98**, 903-916 (2004).

J. D. Harvey, C. J. Ziegler, J. Telser, A. Ozarowski, and J. Krzystek, High-Frequency and -Field EPR Investigation of a Manganese(III) N-Confused Porphyrin Complex, [Mn(NCTPP)(py)<sub>2</sub>]. *Inorg. Chem.* **44**, 4451-4453 (2005).

J. Honzíček, J. Vinklárek, and P. Nactigall, A density functional study of EPR hyperfine coupling of vanadocene(IV) complexes. *Chem. Phys.* **305**, 291-298 (2004).

J. P. Hornak and J. H. Freed, Spectral Rotation in Pulsed EPR Spectroscopy. *J. Magn. Reson.* **67**, 501-518 (1986).

L. N. Ikryannikova, L. Yu. Ustynyuk, and A. N. Tikhonov, DFT Study of Nitroxide Radicals. 1. Effects of Solvent on Structural and Electronic Characteristics of 4-Amino-2,2,5,5-tetramethyl-3-imidazoline-N-oxyl. *J. Phys. Chem. A* **108**, 4759-4768 (2004).

R. Improta and V. Barone, Interplay of Electronic, Environmental, and Vibrational Effects in Determining the Hyperfine Coupling Constants of Organic Free Radicals. *Chem. Rev.* **104**, 1231-1253 (2004).

A. R. Jaszewski and J. Jezierska, An ab initio approach to the structure and EPR parameters of formyldiminoxy radical. *Chem. Phys. Lett.* **334**, 136-144 (2001).

- A. R. Jaszewski and J. Jezierska, Hybrid density functional studies on the EPR parameters of heterosubstituted vinyl radicals: substituent effect on the isotropic hyperfine couplings with  $^1\text{H}$  and  $^{13}\text{C}$  nuclei. *Chem. Phys. Lett.* **340**, 581-590 (2001).
- A. R. Jaszewski and J. Jezierska, Hybrid density functional approach to the isotropic and anisotropic couplings with  $^{14}\text{N}$  and  $^1\text{H}$  nuclei in the blue copper proteins. *Chem. Phys. Lett.* **343**, 571-580 (2001).
- A. Jerschow and N. Müller, Efficient Simulation of Coherence Transfer Pathway Selection by Phase Cycling and Pulsed Field Gradients in NMR. *J. Magn. Reson.* **134**, 17-29 (1998).
- G. Jeschke and A. Schweiger, Principles of Pulse Electron Paramagnetic Resonance, Oxford, 2001.
- G. Jeschke web site <http://www.mpip-mainz.mpg.de/~jeschke/>
- S. Kacprzak, M. Kaupp, and F. MacMillan, Protein-Cofactor Interaction and EPR Parameters for the  $\text{Q}_\text{H}$  Quinone Binding Site of Quinol Oxidase. A Density Functional Study. *J. Am. Chem. Soc.* **128**, 5659- 5671 (2006).
- R. Kapre, K. Ray, I. Sylvestre, T. Weyhermüller, S. D. George, F. Neese, and K. Wieghardt. Molecular and Electronic Structures of Oxo-bis(benzene-1,2-dithiolato)chromate(V) Monoanions. A Combined Experimental and Density Functional Study. *Inorg. Chem.* **45**, 3499-3509 (2006).
- M. Kaupp, M. Bühl, and V. G. Malkin, Calculation of NMR and EPR Parameters. Wiley-VCH, Weinheim, 2004.
- M. Kaupp, C. Remenyi, J. Vaara, O. L. Malkina, and V. G. Malkin, Density Functional Calculations of Electronic g-Tensors for Semiquinone Radical Anions. The Role of Hydrogen Bonding and Substituent Effects. *J. Am. Chem. Soc.* **124**, 2709- (2002)
- L. Kevan and M. K. Bowman, Modern Pulsed and Continuous-Wave Electron Spin Resonance. Wiley, 1990.
- P. B. Kingsley, Signal Intensities and  $T_1$  Calculations in Multiple-Echo Sequences with Imperfect Pulses. *Concepts Magn. Reson.* **11**, 29-49 (1999).
- B. Kirste, Computer Techniques. Chapter II in *Handbook of Electron Spin Resonance*, C. P. Poole Jr. and H. A. Farach, eds., AIP Press, New York, 1994.
- L. V. Kulik and S. A. Dzuba, Electron Spin Echo Study of Molecular Structure and Dynamics: New Approaches Based on Spontaneous Fluctuations of Magnetic Interactions. *J. Structural Chem.* **45**, 298-314 (2004) (translation from Russian)

- T. Lovell, J. Li, T. Liu, D. A. Case, and L. Noodleman, FeMo Cofactor of Nitrogenase: A Density Functional Study of States  $M^N$ ,  $M^{OX}$ ,  $M^R$ , and  $M^I$ . *J. Am. Chem. Soc.* **123**, 12392-12410 (2001).
- A. Lund and M. Shiotani, eds., EPR of Free Radicals in Solids. Trends in Methods and Applications. Kluwer Academic Publishers, Dordrecht, 2003.
- R. D. McKelvey, Huckel MO Theory and Electron Spin Resonance in the Spectroscopy Course. *J. Chem. Ed.* **64**, 497-498 (1987).
- Z. L. Madi, S. Van Doorslaer, and A. Schweiger, Numerical Simulation of One- and Two-Dimensional ESEEM Experiments. *J. Magn. Reson.* **154**, 181-191 (2002).
- P. Maire, M. Königsmann, A. Sreekanth, J. Harmer, A. Schweiger, and H. Grützmacher, A Tetracoordinated Rhodium Aminyl Radical Complex. *J. Am. Chem. Soc.* **128**, 6578-6580 (2006).
- C. Mantel, C. Philouze, M-N. Collomb, and C. Duboc, Investigation of a Neat versus Magnetically Diluted Powdered Mononuclear  $Mn^{II}$  Complex by High-Field and High-Frequency EPR Spectroscopy. *Eur. J. Inorg. Chem.* 3880-3886 (2004).
- D. Marsh, L. Horváth, T. Páli, and V. A. Livshits, Saturation Transfer Spectroscopy of Biological Membranes, *Biol. Magn. Reson.* **24**, 309-367 (2005).
- S. M. Mattar and A. D. Stephens, UB1LYP hybrid density functional studies of the 2,2,6,6-tetramethyl-4-piperidone-oxyl (TEMPO) hyperfine tensors. *Chem. Phys. Lett.* **319**, 601-610 (2000).
- S. M. Mattar and A. D. Stephens, Magnetic Inequivalency, Electron Paramagnetic Resonance, Electronic Structure, Optimal Geometry, and Electronic Spectra of the 4,5-Bis(trifluoromethyl)-1,3,2-dithazol-2-yl Radical. *J. Phys. Chem. A* **104**, 3718-3732 (2000).
- S. M. Mattar and A. D. Stephens, Solvent dependence of the di-tert-butyl nitroxide (DTBN) hyperfine tensors: an experimental and computational study. *Chem. Phys. Lett.* **347**, 189-198 (2001).
- S. M. Mattar, A. D. Stephens, and A. H. Emwas, Generation and spectroscopic characteristics of the 2,3,5,6-tetramethoxy-1,4-benzosemiquinone reactive intermediate. *Chem. Phys. Lett.* **352**, 39-47 (2002).
- S. M. Mattar, Role of the Solvent in Computing the 1,4-Benzosemiquinone g-Tensor by the Coupled-Perturbed Kohn-Sham Hybrid Density Functional Method. *J. Phys. Chem. B* **108**, 9449-9455 (2004).

S. M. Mattar, g-Tensor calculations of bicyclic 1,3,2-dithiazolyl radicals using the coupled-perturbed Kohn-Sham UB1LYP and UPBE0 hybrid density functionals. *Chem. Phys. Lett.* **405**, 382-388 (2005).

S. M. Mattar, A. H. Emwas, and L. A. Calhoun, Spectroscopic Studies of the Intermediates in the Conversion of 1,4,11,12-Tetrahydro-9,10-anthraquinone to 9,10-Anthraquinone by Reaction with Oxygen under Basic Conditions. *J. Phys. Chem. A* **108**, 11545-11553 (2004).

S. M. Mattar, J. Sanford, and A. D. Goodfellow, g Tensor computation of the thiopheno-1,3,2-dithiazolyl radical by the coupled-perturbed Kohn-Sham hybrid density functional method. *Chem. Phys. Lett.* **418**, 30-35 (2006).

A. di Matteo, C. Adamo, M. Cossi, V. Barone, and P. Rey, Intrinsic and environmental effects in the physico-chemical properties of nitroxides. The case of 2-phenyl-4,4,5,5-tetramethyl-4,5-dihydro-1H-imidazol-1-oxyl-3-oxide. *Chem. Phys. Lett.* **310**, 159-165 (1999).

M. L. Munzarová and M. Kaupp, A Density Functional Study of EPR Parameters for Vanadyl Complexes Containing Schiff Base Ligands. *J. Phys. Chem. B* **105**, 12644-12652 (2001).

M. L. Munzarová and M. Kaupp, A Critical Validation of Density Functional and Coupled-Cluster Approaches for the Calculation of EPR Hyperfine Coupling Constants in Transition Metal Complexes. *J. Phys. Chem. A* **103**, 9966-9983 (1999).

M. L. Munzarová, P. Kubáček, and M. Kaupp, Mechanisms of EPR Hyperfine Coupling in Transition Metal Complexes. *J. Am. Chem. Soc.* **122**, 11900-11913 (2000).

S. Naumov, J. Reinhold, and D. Beckert, Investigation of the molecular structure of the radical anions of some pyrimidine-type bases in aqueous solution by comparison of calculated hyperfine coupling constants with EPR results. *Phys. Chem. Chem. Phys.* **5**, 64-72 (2003).

F. Neese, Prediction of electron paramagnetic resonance g values using coupled perturbed Hartree-Fock and Kohn-Sham theory. *J. Chem. Phys.* **115**, 11080-11096 (2001).

F. Neese, Prediction of electron paramagnetic resonance g values using coupled perturbed Hartree-Fock and Kohn-Sham theory. *J. Chem. Phys.* **115**, 11080-11096 (2001).

F. Neese, Theoretical Study of Ligand Superhyperfine Structure. Application to Cu(II) Complexes. *J. Phys. Chem. A* **105**, 4290-4299 (2001).

- F. Neese, Metal and ligand hyperfine couplings in transition metal complexes: The effect of spin-orbit coupling as studied by coupled perturbed Kohn-Sham theory. *J. Chem. Phys.* **118**, 3939-3948 (2003).
- J. Neugebauer, M. J. Louwrese, P. Belanzoni, T. A. Wesolowski, and E. J. Baerends, Modeling solvent effects on electron-spin-resonance hyperfine couplings by frozen-density embedding. *J. Chem. Phys.* **123**, 114101 (2005).
- K. M. Neyman, D. I. Ganyushin, A. V. Matveev, and V. A. Nasluzov, Calculation of Electronic g-Tensors Using a Relativistic Density Functional Douglas-Kroll Method. *J. Phys. Chem. A* **106**, 5022-5030 (2002).
- C. J. O'Conner and R. L. Carlin, Electron Paramagnetic Resonance Investigation of Crystal Field, Nuclear Quadrupole, and Structural Properties of Two Manganese(II) Compounds. *Inorg. Chem.* **14**, 291-296(1975).
- R. Owenius, M. Engström, M. Lindgren, and M. Huber, Influence of Solvent Polarity and Hydrogen Bonding on the EPR Parameters of a Nitroxide Spin Label Studied by 9-GHz and 95-GHz EPR Spectroscopy and DFT Calculations. *J. Phys. Chem. A* **105**, 10967-10977 (2001).
- T. K. Paine, T. Weyhermuller, L.D. Slep, F. Neese, E. Bill, E. Bothe, K. Wieghardt, and P. Chaudhuri, Nonoxovanadium(IV) and oxovanadium(V) complexes with mixed O, X, O-donor ligands (X = S, Se, P, or PO). *Inorg. Chem.*, **43**, 7324-7338 (2004).
- S. Patchkovskii and T. Ziegler, Prediction of EPR g Tensors in Simple d<sup>1</sup> Metal Porphyrins with Density Functional Theory. *J. Am. Chem. Soc.* **122**, 3506-3516 (2000).
- M. Pavone, C. Benzi, F. De Angelis, and V. Barone, Hyperfine coupling constants of dimethyl nitroxide in aqueous solution: Car-Parrinello molecular dynamics and discrete-continuum approaches. *Chem. Phys. Lett.* **395**, 120-126 (2004).
- T. T. Petrenko, T. L. Petrenko, and V. Ya. Bratus, The carbon <100> split interstitial in SiC. *J. Phys. Condens. Matter* **14**, 12433-12440 (2002).
- M. Plato, H.-J. Steinhoff, C. Wegener, J. T. Törring, A. Savitsky, and K. Möbius, Molecular orbital study of polarity and hydrogen bonding effects on the g and hyperfine tensors of site directed NO spin labeled bacteriorhodopsin. *Mol. Phys.* **100**, 3711-3721 (2002).
- K. Ray, T. Weyhermuller, F. Neese, and K. Weighardt, Electronic Structure of Square Planar Bis(benzene-1,2-dithiolato)metal Complexes [M(L)<sub>2</sub>]<sup>z</sup> (z = 2-, 1-, 0; M = Ni, Pd, Pt, Cu, Au): An Experimental, Density Functional, and Correlated ab initio Study. *Inorg. Chem.* **44**, 5345-5360 (2005).

- E. J. Reijerse and C. P. Keijzers, Model Calculations of Frequency-Domain ESEEM Spectra of Disordered Systems. *J. Magn. Reson.* **71**, 83-96 (1987).
- E. J. Reijerse, P. J. van Dam, A. A. K. Klaassen, W. R. Hagen, P. J. M. van Bentum, and G. M. Smith, Concepts in High-Frequency EPR – Applications to Bio-Inorganic Systems. *Appl. Magn. Reson.* **14**, 153-167 (1998).
- C. Remenyi and M. Kaupp, Where is the Spin? Understanding Electronic Structure and g-Tensors for Ruthenium Complexes with Redox-Active Quinonoid Ligands. *J. Am. Chem. Soc.* **127**, 11399-11413 (2005).
- Z. Rinkevicius, L. Telyatnyk, O. Vahtras, and K. Ruud, Electronic g-tensors of solvated molecules using the polarizable continuum model. *J. Chem. Phys.* **121**, 5051-5060 (2004).
- E. Ruiz, A. Rodriguez-Forteza, and S. Alvarez, Tailor-Made Strong Exchange Magnetic Coupling through Very Long Bridging Ligands: Theoretical Predictions. *Inorg. Chem.* **42**, 4881-4884 (2003).
- E. Ruiz, J. Cirera, and S. Alvarez, Spin density distribution in transition metal complexes. *Coord. Chem. Rev.* **249**, 2649-2660 (2005).
- A. C. Saladino and S. C. Larsen, Density Functional Theory Calculations of the Electron Paramagnetic Resonance Parameters for  $\text{VO}^{2+}$  Complexes. *J. Phys. Chem. A* **107**, 1872-1878 (2003).
- A. C. Saladino and S. C. Larsen, Relativistic DFT Calculations of Copper Hyperfine Coupling Constants: Effect of Spin-Orbit Coupling. *J. Phys. Chem. A* **107**, 5583-5587 (2003).
- A. C. Saladino and S. C. Larsen, DFT calculations of EPR parameters of transition metal complexes: Implications for catalysis. *Catalysis Today* **105**, 122-133 (2005).
- G. A. A. Saracino, A. Tedeschi, G. D'Errico, R. Improta, L. Franco, M. Ruzzi, C. Corvaia, and V. Barone, Solvent Polarity and pH Effects on the Magnetic Properties of Ionizable Nitroxide Radicals: A Combined Computational and Experimental Study of 2,2,5,5-Tetramethyl-3-carboxypyrrolidine and 2,2,6,6-Tetramethyl-4-carboxypiperidine Nitroxides. *J. Phys. Chem. A* **106**, 10700-10706 (2002).
- D. J. Schneider and J. H. Freed, Calculating Slow Motion Magnetic Resonance Spectra: A User's Guide. *Biol. Magn. Reson.* **8**, 1-76 (1989).
- J. Scott, S. Gambarotta, I. Korobkov, Q. Knijnenburg, B. de Bruin, and P. H. M. Budzelaar, Formation of a Paramagnetic Al Complex and Extrusion of Fe during the Reaction of (Diiminepyridine)Fe with  $\text{AlR}_3$  (R = Me, Et). *J. Am. Chem. Soc.* **127**, 17204-17206 (2005).

- J. J. Shane, L. P. Liesum, and A. Schweiger, Efficient Simulation of ESEEM Spectra Using Gamma. *J. Magn. Reson.* **134**, 72-75 (1998).
- S. Sinnecker, E. Reijerse, F. Neese, and W. Lubitz, Hydrogen Bond Geometries from Electron Paramagnetic Resonance and Electron-Nuclear Double Resonance Parameters: Density Functional Study of Quinone Radical Anion-Solvent Interactions. *J. Am. Chem. Soc.* **126**, 3280-3290 (2004).
- S. A. Smith, T. O. Levante, B. H. Meier, and R. R. Ernst, Computer Simulations in Magnetic Resonance. An Object-Oriented Programming Approach. *J. Magn. Reson. A* **106**, 75-105 (1994).
- Z. Sojka and P. Pietrzyk, Paramagnetic species on catalytic surfaces – DFT investigations into structure sensitivity of the hyperfine coupling constants. *Spectrochim. Acta Part A* **60**, 1257-1265 (2004).
- P. Stipa, Radical cations from dipyrindinium derivatives: A combined EPR and DFT study. *Spectrochim. Acta Part A* **64**, 653-659 (2006).
- S. Stoll and A. Schweiger, Rapid construction of solid-state magnetic resonance powder spectra from frequencies and amplitudes as applied to ESEEM. *J. Magn. Reson.* **163**, 248-256 (2003).
- S. Stoll and A. Schweiger, EasySpin, a comprehensive software package for spectral simulation and analysis in EPR. *J. Magn. Reson.* **178**, 42-55 (2006).
- Stefan Stoll, Spectral Simulations in Solid State EPR, ETH Zurich, <http://www.easyspin.ethz.ch/> (accessed 07/04/06)
- R. Szosenfogel and D. Goldfarb, Simulations of HYSORE spectra obtained with ideal and non-ideal pulses. *Mol. Phys.* **95**, 1295-1308 (1998).
- K. Tabaka and J. Jezierska, Molecular geometry and hyperfine interactions in iminoxy radicals with C=O or CH<sub>2</sub> group – DFT and EPR studies in liquid and rigid media. *Chem. Phys. Lett.* **394**, 298-306 (2004).
- R. Takeda, S. Mitsuo, S. Yamanaka, and K. Yamaguchi, Density functional study of zero-field splitting. *Polyhedron* **24**, 2238-2241 (2005).
- D. L. Turner, Recent Developments in Multiple Pulse NMR. *Annual Reports NMR Spectroscopy* **21**, 162-208 (1989)
- H. L. Van Camp and A. H. Heiss, Computer Applications in Electron Paramagnetic Resonance. *Magn. Reson. Rev.* **7**, 1-40 (1981).

J. A. Weil, J. R. Bolton, and J. E. Wertz, *Electron Paramagnetic Resonance. Elementary Theory and Practical Applications*. Wiley, New York, 1994.

F. Weinhold and C. Landis, *Valency and Bonding. A Natural Bond Orbital Donor-Acceptor Perspective*. Cambridge University Press, 2005.

T. Yagi, K. Morihashi,, and O. Kikuchi, MC/MO Study of the Solvent Effect on the Excitation Energies of the (CH<sub>3</sub>)<sub>2</sub>NO Radical in Hydrogen-Bonding and Non-Hydrogen-Bonding Solvents. *J. Phys. Chem. A* **105**, 8241-8247 (2001).

W.-C. Zheng and X.-X. Wu, Studies of the EPR g factors of the isoelectronic sd<sup>3</sup> series Cr<sup>3+</sup>, Mn<sup>4+</sup> and Fe<sup>5+</sup> in SrTiO<sub>3</sub> crystals. *J. Phys. Chem. Solids* **66**, 1701-1704 (2005).

C. Zhong, M. Zhao, T. Goslinski, C. Stern, A. G. M. Barrett, and B. M. Hoffman, Porphyrazines Peripherally Functionalized with Hybrid Ligands as Molecular Scaffolds for Bimetallic Metal-Ion Coordination. *Inorg. Chem.* **45**, 3983-39889 (2006).

### **Additional Bibliography**

#### ***Instructional***

R. Beck and J. W. Nibler, ESR Studies and HMO Calculations on Benzosemiquinone Radical Anions. *J. Chem. Ed.* **66**, 263-266 (1989).

#### ***Books***

Calculation of NMR and EPR Parameters. Theory and Applications. M. Kaupp, M. Bühl, and V. C. Malkin. Wiley-VCH Verlag, Weinheim, 2004.

EPR of Free Radicals in Solids. Trends in Methods and Applications. A. Lund and M. Shiotani, eds., Kluwer Academic Publishers, Dordrecht, 2003.

#### ***Reviews***

H. L. Vancamp and A. R. Heiss, Computer Applications in Electron Paramagnetic Resonance. *Magn. Reson. Rev.* **7**, 1-40 (1981).

B.Kirste, Computer Techniques, Chapter II in Handbook of Electron Spin Resonance, C, P, Poole, Jr., and H. A. Farach, eds., American Institute of Physics, AIP Press, New York, 1994.

J.R. Pilbrow, Principles of computer simulation of EPR Spectra. *Appl. Magn. Reson.* **10**, 45-53 (1996).

J. A. Weil, The simulation of EPR spectra: A mini-review. *Molecular Physics Reports* **26**, 11-24 (1999).

### **Analysis of overlapping or complicated spectra**

A. Keszler and N. Hogg, Post Processing Strategies in EPR Spin-Trapping Studies. *Biol. Magn. Reson.* 23, 111-123 (2005).

C. Chang, J. Ren, P. C. W. Fung, Y. S. Hung, J. G. Shen, F. H. Y. Chan, Novel sparse component analysis approach to free radical EPR spectra decomposition. *J. Magn. Reson.* 175, 242-255 (2005).

# **The Calculation of the g and Hyperfine Tensors of Paramagnetic Molecules and Organic Free Radicals**

Saba M. Mattar

*Department of Chemistry and Centre for Laser, Atomic and Molecular Sciences,  
University of New Brunswick, Fredericton, NB, Canada E3B 6E2*

## 1.1 The Eigenvalue Problem in Quantum Mechanics

The calculation of the g and A tensors involves solving the spin Hamilton Schrödinger equation (SE). The SE is a general wave equation of the form

$$\hat{O}\psi = \varepsilon\psi. \quad (0.1)$$

In this equation the operator,  $\hat{O}$ , is the mathematical form for any physically observable or measurable quantity. It could represent position, velocity, energy, momentum etc. The eigenvalue,  $\varepsilon$ , is the corresponding observed numerical value of this quantity. The eigenvector  $\psi$  is the wavefunction of the system. It contains all the information about the properties of that system. Equation (0.1) may be written in the equivalent “matrix form”

$$\begin{pmatrix} O_{11} & \cdots & O_{1n} \\ \vdots & \ddots & \vdots \\ O_{n1} & \cdots & O_{nn} \end{pmatrix} \begin{pmatrix} \psi_1 \\ \vdots \\ \psi_n \end{pmatrix} = \begin{pmatrix} \varepsilon_1 & 0 & 0 \\ 0 & \ddots & 0 \\ 0 & 0 & \varepsilon_n \end{pmatrix} \begin{pmatrix} \psi_1 \\ \vdots \\ \psi_n \end{pmatrix}. \quad (0.2)$$

Here, n is the number of degrees of freedom of the system.

The value of any observable is given as the statistical average of the numerical value (eigenvalue) of a single particle:

$$\langle O \rangle = \varepsilon = \int_{-\infty}^{\infty} \psi^*(\mathbf{r}, t) \hat{O} \psi(\mathbf{r}, t) d\mathbf{r} \quad (0.3)$$

The matrix form of Eq. (0.3) is:

$$\langle O \rangle = \varepsilon = (\psi_1 \quad \cdots \quad \psi_n) \begin{pmatrix} O_{11} & \cdots & O_{1n} \\ \vdots & \ddots & \vdots \\ O_{n1} & \cdots & O_{nn} \end{pmatrix} \begin{pmatrix} \psi_1 \\ \vdots \\ \psi_n \end{pmatrix}. \quad (0.4)$$

## 1.2 The Spin Hamiltonian for an Isolated “Spinless” Electron

For an isolated electron at a position,  $\mathbf{r}$ , in space the Schrödinger equation is:

$$\hat{H}\psi(\mathbf{r}, t) = E\psi(\mathbf{r}, t) \quad (0.5)$$

The operator,  $\hat{H}$ , represents the total energy of the system.

$$\begin{aligned} \hat{H} &= \text{Kinetic Energy} + \text{Potential Energy} \\ &= \frac{\hat{\mathbf{p}} \cdot \hat{\mathbf{p}}}{2m} + V(\mathbf{r}) \\ \hat{H} &= -\frac{\hbar^2}{2m} \nabla^2 + V(\mathbf{r}) \end{aligned} \quad (0.6)$$

### 1.3 The momentum operator and eigenvalue for a free particle

A free particle, traveling in the x direction, has no potential energy. Its wave function, in one dimension, may then be expressed as

$$\psi(x) = \exp(ip_x x) \quad (0.7)$$

A simple differentiation with respect to x yields

$$\begin{aligned} \frac{\partial \psi(x)}{\partial x} &= \frac{\partial}{\partial x} [\exp(ip_x x)] \\ &= \exp(ip_x x)(ip_x) \\ &= \psi(x)(ip_x) \end{aligned} \quad (0.8)$$

$$\frac{\partial}{\partial x} \psi(x) = (ip_x) \psi(x)$$

In other words the differentiation generated an “ $ip_x$ ”. Multiplying by “ $\hbar/i$ ” then the eigenvalue equation becomes

$$\underbrace{\frac{\hbar}{i} \frac{\partial}{\partial x}}_{\text{Operator}} \psi(x) = \underbrace{\hbar p_x}_{\text{Eigenvalue}} \psi(x). \quad (0.9)$$

The generated eigenvalue is the x-component of the linear momentum in  $\hbar$  units. Now, let us find the value of the linear momentum (in  $\hbar$  units). The wavefunction in three dimensional space is

$$\begin{aligned} \psi(\vec{r}) &= \exp(i\vec{p} \cdot \vec{r}) \\ &= \exp i(\hat{i}p_x x + \hat{j}p_y y + \hat{k}p_z z) \end{aligned} \quad (0.10)$$

Using (0.4)

$$\langle \hbar p \rangle = \varepsilon = \begin{pmatrix} \exp(-ip_x x) & \exp(-ip_y y) & \exp(-ip_z z) \end{pmatrix} \begin{pmatrix} \frac{\hbar}{i} \frac{\partial}{\partial x} & 0 & 0 \\ 0 & \frac{\hbar}{i} \frac{\partial}{\partial y} & 0 \\ 0 & 0 & \frac{\hbar}{i} \frac{\partial}{\partial z} \end{pmatrix} \begin{pmatrix} \exp(ip_x x) \\ \exp(ip_y y) \\ \exp(ip_z z) \end{pmatrix} \quad (0.11)$$

on expansion it results in

$$\langle \hbar p \rangle = \begin{pmatrix} \exp(-ip_x x) & \exp(-ip_y y) & \exp(-ip_z z) \end{pmatrix} \begin{pmatrix} \frac{\hbar}{i} \frac{\partial}{\partial x} [\exp(ip_x x)] + 0 + 0 \\ 0 + \frac{\hbar}{i} \frac{\partial}{\partial y} [\exp(ip_y y)] + 0 \\ 0 + 0 + \frac{\hbar}{i} \frac{\partial}{\partial z} [\exp(ip_z z)] \end{pmatrix} \quad (0.12)$$

Performing the differentiation gives

$$\begin{aligned} \langle \hbar p \rangle &= \begin{pmatrix} \exp(-ip_x x) & \exp(-ip_y y) & \exp(-ip_z z) \end{pmatrix} \begin{pmatrix} \frac{\hbar}{i} (ip_x) [\exp(ip_x x)] \\ \frac{\hbar}{i} (ip_y) [\exp(ip_y y)] \\ \frac{\hbar}{i} (ip_z) [\exp(ip_z z)] \end{pmatrix} \\ &= \hbar \begin{pmatrix} \exp(-ip_x x) & \exp(-ip_y y) & \exp(-ip_z z) \end{pmatrix} \begin{pmatrix} p_x [\exp(ip_x x)] \\ p_y [\exp(ip_y y)] \\ p_z [\exp(ip_z z)] \end{pmatrix}. \end{aligned} \quad (0.13)$$

Finally by multiplying the row and column vectors

$$\begin{aligned} \langle \hbar p \rangle &= \hbar \left\{ p_x \exp(-ip_x x) [\exp(ip_x x)] \right. \\ &\quad + p_y \exp(-ip_y y) [\exp(ip_y y)] \\ &\quad \left. + p_z \exp(-ip_z z) [\exp(ip_z z)] \right\} \\ \langle \hbar p \rangle &= \hbar p_x + \hbar p_y + \hbar p_z \end{aligned} \quad (0.14)$$

which is the required result.

## 1.4 The Electron Spin

Early experimental evidence seemed to indicate that an electron has an intrinsic magnetic moment. Consequently, Uhlenbeck and Goudsmit suggested that the electron had an intrinsic angular momentum called the “spin”. Pauli suggested that the spin could be incorporated in the wave equation if the original spatial wave function,  $\psi(\mathbf{r}, t)$ , is assumed to be a pair of degenerate wave functions

$$\psi(\mathbf{r}, t) = \begin{cases} \underbrace{\phi(\mathbf{r}, t)}_{space} \underbrace{\alpha}_{spin} \\ \underbrace{\phi(\mathbf{r}, t)}_{space} \underbrace{\beta}_{spin} \end{cases} \quad (0.15)$$

The spin “spin-up” and “spin-down” functions are the simple vectors in two dimensional space,

$$\alpha = \begin{bmatrix} 1 \\ 0 \end{bmatrix}, \quad \beta = \begin{bmatrix} 0 \\ 1 \end{bmatrix}, \quad (0.16)$$

respectively. The Cartesian components of the spin operator are

$$\hat{s}_x = \frac{1}{2} \begin{bmatrix} 0 & 1 \\ 1 & 0 \end{bmatrix}, \quad \hat{s}_y = \frac{1}{2} \begin{bmatrix} 0 & -i \\ i & 0 \end{bmatrix} \text{ and } \hat{s}_z = \frac{1}{2} \begin{bmatrix} 1 & 0 \\ 0 & -1 \end{bmatrix}. \quad (0.17)$$

Having defined the spin operators and wave functions we can calculate any spin eigen value. The wave equation for the pure spin functions is then easily written in matrix form as:

$$\langle O \rangle = \varepsilon = (\psi_1 \quad \dots \quad \psi_n) \begin{pmatrix} O_{11} & \dots & O_{1n} \\ \vdots & \ddots & \vdots \\ O_{n1} & \dots & O_{nn} \end{pmatrix} \begin{pmatrix} \psi_1 \\ \vdots \\ \psi_n \end{pmatrix} \quad (0.18)$$

To illustrate the use of this technique let us find the eigenvalue of  $s_z$  when the electron is in the  $\beta$  state. According to Eq. (0.18) we have,  $n=2$  and

$$\begin{aligned} \langle s_z \rangle &= (0 \quad 1) \cdot \frac{1}{2} \begin{pmatrix} 1 & 0 \\ 0 & -1 \end{pmatrix} \cdot \begin{pmatrix} 0 \\ 1 \end{pmatrix} \\ \langle s_z \rangle &= \frac{1}{2} (0 \quad 1) \cdot \begin{pmatrix} 1 & 0 \\ 0 & -1 \end{pmatrix} \cdot \begin{pmatrix} 0 \\ 1 \end{pmatrix} \\ \langle s_z \rangle &= \frac{1}{2} (0 \quad 1) \cdot \begin{pmatrix} (1 \times 0) + (0 \times 1) \\ (0 \times 0) + (1 \times -1) \end{pmatrix} \\ \langle s_z \rangle &= \frac{1}{2} (0 \quad 1) \cdot \begin{pmatrix} 0 \\ -1 \end{pmatrix} \\ \langle s_z \rangle &= -\frac{1}{2} \end{aligned} \quad (0.19)$$

which is equivalent to the well known result

$$s_z |\beta\rangle = -\frac{1}{2} |\beta\rangle \quad (0.20)$$

## 1.5 The Relativistic Dirac Equation of the Free Electron

In order to take into consideration the relativistic effects of the electron, time must also be considered. The time dependent form of the Schrödinger equation takes a slightly different form from Eq.(0.5)

$$-\frac{\hbar}{i} \frac{\partial \psi(\mathbf{r}, t)}{\partial t} = \hat{H} \psi(\mathbf{r}, t) \quad (0.21)$$

or

$$-\frac{\hbar}{i} \frac{\partial \psi(\mathbf{r}, t)}{\partial t} = -\frac{\hbar^2}{2m} \nabla^2 \psi(\mathbf{r}, t) + V(\mathbf{r}) \psi(\mathbf{r}, t). \quad (0.22)$$

If one includes the rest mass of the free electron, then square of its total energy,  $W$ , is

$$W^2 = [\mathbf{p} \cdot \mathbf{p} + m^2 c^2] c^2 \quad (0.23)$$

and Eq. (0.22) becomes

$$-\frac{\hbar}{i} \frac{\partial \psi(\mathbf{r}, t)}{\partial t} = \pm c \sqrt{-\hbar^2 \nabla^2 + m^2 c^2} \psi(\mathbf{r}, t). \quad (0.24)$$

This leads to a four component solution which is cumbersome and difficult to solve. Two approximations have been employed to convert the relativistic Dirac Equation to a form that retains the essential information of the original equation. The first is due to Foldy and Wouthsen (*Phys. Rev.* 78, (1950) 29.) and the second is due to Pauli (R. E. Moss, *Advanced Quantum Mechanics*, Chapman and Hall, London, 1973).

## 1.6 The Breit-Pauli Hamiltonian

The Hamiltonian for paramagnetic molecules and free radicals must include the interactions of the electron with the other electrons and nuclei. By employing the Pauli reductions Breit derived the following Hamiltonian for an N electron system (G. Breit, *Phys. Rev.* 34 (1929) 553, *Phys. Rev.* 36 (1930) 383, *Phys. Rev.* 39 (1932) 616):

$$\begin{aligned}
H = \sum_{i=1}^N & \left[ mc^2 + \frac{\boldsymbol{\pi}_i^2}{2m} - e\boldsymbol{\phi}_i + g_e\mu_B\mathbf{S}_i \cdot \mathbf{B} - \frac{g_e\mu_B\mathbf{S}_i}{4mc} \cdot [\boldsymbol{\pi}_i \times \mathbf{E}_i - \mathbf{E}_i \times \boldsymbol{\pi}_i] \right. \\
& + \frac{e\hbar^2}{8m^2c^2} \nabla \cdot \mathbf{E}_i - \frac{\boldsymbol{\pi}_i^4}{8m^3c^2} - \frac{g_e\mu_B\boldsymbol{\pi}_i^2}{2m^2c^2} \mathbf{S}_i \cdot \mathbf{B} \\
& + \sum_{i=1}^N \sum_{j \neq i}^N \left( \frac{e^2}{2r_{ij}} - \frac{e^2}{4m^2c^2} \left[ \boldsymbol{\pi}_i \cdot \frac{\boldsymbol{\pi}_j}{r_{ij}} + (\boldsymbol{\pi}_i \cdot \mathbf{r}_{ij}) \frac{\mathbf{r}_{ij} \cdot \boldsymbol{\pi}_j}{r_{ij}^3} \right] \right. \\
& - \frac{eg_e\mu_B}{4mc} \frac{1}{r_{ij}^3} \mathbf{S}_i \cdot (\mathbf{r}_{ij} \times \boldsymbol{\pi}_i) + \frac{eg_e\mu_B}{2mc} \frac{1}{r_{ij}^3} \mathbf{S}_i \cdot (\mathbf{r}_{ij} \times \boldsymbol{\pi}_j) \\
& \left. \left. + \frac{g_e^2\mu_B^2}{2} \left\{ \frac{\mathbf{S}_i \cdot \mathbf{S}_j}{r_{ij}^3} - 3(\mathbf{S}_i \cdot \mathbf{r}_{ij}) \frac{(\mathbf{r}_{ij} \cdot \mathbf{S}_j)}{r_{ij}^5} - \frac{8\pi}{3} \delta(\mathbf{r}_{ij})(\mathbf{S}_i \cdot \mathbf{S}_j) \right\} \right) \right] \\
& + \text{higher order terms}
\end{aligned} \tag{0.25}$$

The terms in this equation need further explanation; the ones that do not depend on the homogeneous external magnetic field are in blue. The one-electron terms follow:

The static potential and effective electric field felt by the  $i$ th electron are  $\boldsymbol{\phi}_i$  and  $\mathbf{E}_i$  respectively. The momentum of the  $i$ th electron in an external magnetic field,  $\mathbf{B}$ , is  $\boldsymbol{\pi}_i$ , it takes the explicit form

$$\boldsymbol{\pi}_i = -\frac{\hbar}{i} \nabla - \frac{e}{c} \mathbf{A}$$

where  $\mathbf{A}$  is the vector potential due to  $\mathbf{B}$ . As a result  $mc^2 + \frac{\boldsymbol{\pi}_i^2}{2m} - e\boldsymbol{\phi}_i$  is the energy of the  $i$ th electron rest mass, its kinetic energy and its interaction energy with the external electric field. The  $g_e\mu_B\mathbf{S}_i \cdot \mathbf{B}$  is the familiar electronic Zeeman interaction. The one-electron spin-orbit interaction is given by  $-\frac{g_e\mu_B\mathbf{S}_i}{4mc} \cdot [\boldsymbol{\pi}_i \times \mathbf{E}_i - \mathbf{E}_i \times \boldsymbol{\pi}_i]$  while  $\frac{e\hbar^2}{8m^2c^2} \nabla \cdot \mathbf{E}_i$  is the electric field interaction correction. The spin Zeeman interaction is responsible for the  $-\frac{g_e\mu_B\boldsymbol{\pi}_i^2}{2m^2c^2} \mathbf{S}_i \cdot \mathbf{B}$  term and the relativistic correction to the kinetic energy is  $-\frac{\boldsymbol{\pi}_i^4}{8m^3c^2}$ .

The two-electron interactions are, as expected, more complicated. The Columbic repulsion between the two electrons  $i$  and  $j$  is simply  $\frac{e^2}{2r_{ij}}$  while

$-\frac{e^2}{4m^2c^2} \left[ \boldsymbol{\pi}_i \cdot \frac{\boldsymbol{\pi}_j}{r_{ij}} + (\boldsymbol{\pi}_i \cdot \mathbf{r}_{ij}) \frac{\mathbf{r}_{ij} \cdot \boldsymbol{\pi}_j}{r_{ij}^3} \right]$  is the corresponding orbit-orbit interaction. The two-electron contributions to the spin-orbit interaction are given by the two terms

$$-\frac{eg_e\mu_B}{4mc} \frac{1}{r_{ij}^3} \mathbf{S}_i \cdot (\mathbf{r}_{ij} \times \boldsymbol{\pi}_i) + \frac{eg_e\mu_B}{2mc} \frac{1}{r_{ij}^3} \mathbf{S}_i \cdot (\mathbf{r}_{ij} \times \boldsymbol{\pi}_j).$$

The anisotropic components of the spin-spin interactions are

$$\frac{g_e^2\mu_B^2}{2} \left\{ \frac{\mathbf{S}_i \cdot \mathbf{S}_j}{r_{ij}^3} - 3(\mathbf{S}_i \cdot \frac{\mathbf{r}_{ij}}{r_{ij}^5}) \cdot \mathbf{S}_j \right\}$$

and the isotropic component is  $-\frac{8\pi}{3} \left( \frac{g_e^2\mu_B^2}{2} \right) \delta(\mathbf{r}_{ij}) \mathbf{S}_i \cdot \mathbf{S}_j$ .

The next step is to derive Hamiltonian components that linearly depend on the external homogenous magnetic field,  $\mathbf{B}$ . They are essential for EPR, ENDOR and g tensor calculations.

## 1.7 Derivation of the one electron spin-orbit interaction term

One starts with the one-electron spin-orbit coupling term in Eq. (0.25). It is:

$$-\frac{g_e\mu_B}{4mc} \sum_{i=1}^N \mathbf{S}_i \cdot [\boldsymbol{\pi}_i \times \mathbf{E}_i - \mathbf{E}_i \times \boldsymbol{\pi}_i] \quad (0.26)$$

By substituting the field dependent momentum as

$$\boldsymbol{\pi}_i = -\frac{\hbar}{i} \nabla - \frac{e}{c} \mathbf{A} \equiv \mathbf{p}_i - \frac{e}{c} \mathbf{A} \quad (0.27)$$

we obtain

$$-\frac{g_e\mu_B}{4mc} \sum_{i=1}^N \mathbf{S}_i \cdot \left[ \left( \mathbf{p}_i - \frac{e}{c} \mathbf{A}_i \right) \times \mathbf{E}_i - \mathbf{E}_i \times \left( \mathbf{p}_i - \frac{e}{c} \mathbf{A}_i \right) \right] \quad (0.28)$$

which upon expansion becomes

$$-\frac{g_e\mu_B}{4mc} \sum_{i=1}^N \mathbf{S}_i \cdot [\mathbf{p}_i \times \mathbf{E}_i - \mathbf{E}_i \times \mathbf{p}_i] + \frac{g_e\mu_B}{4mc} \frac{e}{c} \sum_{i=1}^N \mathbf{S}_i \cdot [\mathbf{A}_i \times \mathbf{E}_i - \mathbf{E}_i \times \mathbf{A}_i] \quad (0.29)$$

The electric field of an isolated molecule at the  $i$ th electron is

$$\mathbf{E}_i = \sum_{k=1}^{N_k} \frac{eZ_k}{r_{ik}^3} \mathbf{r}_{ik} \quad (0.30)$$

substituting this expression in the previous equation leads to

$$-\frac{g_e \mu_B}{4mc} \sum_{i=1}^N \sum_{k=1}^{N_k} \left( \frac{eZ_k}{r_{ik}^3} \right) \mathbf{S}_i \cdot [\mathbf{p}_i \times \mathbf{r}_{ik} - \mathbf{r}_{ik} \times \mathbf{p}_i] + \frac{g_e \mu_B e}{4mc c} \sum_{i=1}^N \sum_{k=1}^{N_k} \left( \frac{eZ_k}{r_{ik}^3} \right) \mathbf{S}_i \cdot [\mathbf{A}_i \times \mathbf{r}_{ik} - \mathbf{r}_{ik} \times \mathbf{A}_i] \quad (0.31)$$

The first term in this expansion is the one-electron spin-orbit coupling term because

$$\begin{aligned} & -\frac{g_e \mu_B}{4mc} \sum_{i=1}^N \sum_{k=1}^{N_k} \left( \frac{eZ_k}{r_{ik}^3} \right) \mathbf{S}_i \cdot [\mathbf{p}_i \times \mathbf{r}_{ik} - \mathbf{r}_{ik} \times \mathbf{p}_i] \\ &= -\frac{g_e \mu_B}{4mc} \sum_{i=1}^N \sum_{k=1}^{N_k} \left( \frac{eZ_k}{r_{ik}^3} \right) \mathbf{S}_i \cdot [-2\mathbf{r}_{ik} \times \mathbf{p}_i] \\ &= \frac{g_e \mu_B}{2mc} \sum_{i=1}^N \sum_{k=1}^{N_k} \left( \frac{eZ_k}{r_{ik}^3} \right) \mathbf{S}_i \cdot [\mathbf{r}_{ik} \times \mathbf{p}_i] \end{aligned} \quad (0.32)$$

since the orbital angular momentum is defined as  $\mathbf{l}_{ik} = \mathbf{r}_{ik} \times \mathbf{p}_i$  then

$$H^{SO}(1e) = \frac{g_e \mu_B}{2mc} \sum_{i=1}^N \sum_{k=1}^{N_k} \left( \frac{eZ_k}{r_{ik}^3} \right) \mathbf{S}_i \cdot \mathbf{l}_{ik}. \quad (0.33)$$

Note that the terms in (0.33) only deal with one electron at a time. The interactions are between the  $i$ th electron and the  $N$ th nucleus. Derivation of the two electron spin-orbit operator is similar to the one-electron case. We start with

$$\begin{aligned} H^{SO}(2e) &= -\frac{eg_e \mu_B}{4mc} \sum_{i=1}^N \sum_{j=1}^N \frac{1}{r_{ij}^3} \mathbf{S}_i \cdot (\mathbf{r}_{ij} \times \boldsymbol{\pi}_i) + \frac{eg_e \mu_B}{2mc} \sum_{i=1}^N \sum_{j=1}^N \frac{1}{r_{ij}^3} \mathbf{S}_i \cdot (\mathbf{r}_{ij} \times \boldsymbol{\pi}_j) \\ &= -\frac{eg_e \mu_B}{4mc} \sum_{i=1}^N \sum_{j=1}^N \frac{1}{r_{ij}^3} [\mathbf{S}_i \cdot (\mathbf{r}_{ij} \times \boldsymbol{\pi}_i) + 2\mathbf{S}_i \cdot (\mathbf{r}_{ij} \times \boldsymbol{\pi}_j)] \end{aligned} \quad (0.34)$$

and end with

$$H^{SO}(2e) = -\frac{g_e \mu_B}{2mc} \sum_{i=1}^N \sum_{j=1}^N \left( \frac{1}{r_{ij}^3} \right) (\mathbf{S}_i + 2\mathbf{S}_j) \cdot \mathbf{l}_{ij}. \quad (0.35)$$

## 1.8 Derivation of the one electron gauge correction term

By noting that the vector potential  $\mathbf{A}_i = \mathbf{B} \times \mathbf{r}_{ic} / 2$ , where  $\mathbf{r}_{ic}$  denotes the distance between the  $i$ th electron and an arbitrary defined origin (gauge)  $C$ . The second term in (0.31) becomes

$$\begin{aligned}
& \frac{g_e \mu_B e}{4mc^2} \sum_{i=1}^N \sum_{k=1}^{N_k} \left( \frac{eZ_{ik}}{r_{ik}^3} \right) \mathbf{S}_i \cdot \left[ \frac{1}{2} (\mathbf{B} \times \mathbf{r}_{iC}) \times \mathbf{r}_{ik} - \mathbf{r}_{ik} \times \frac{1}{2} (\mathbf{B} \times \mathbf{r}_{iC}) \right] \\
& = \frac{g_e \mu_B e^2}{8mc^2} \sum_{i=1}^N \sum_{k=1}^{N_k} \left( \frac{Z_{ik}}{r_{ik}^3} \right) \mathbf{S}_i \cdot [(\mathbf{B} \times \mathbf{r}_{iC}) \times \mathbf{r}_{ik} - \mathbf{r}_{ik} \times (\mathbf{B} \times \mathbf{r}_{iC})]
\end{aligned} \tag{0.36}$$

It is useful to use the identity for the triple vector product

$$\mathbf{O} \times \mathbf{P} \times \mathbf{Q} = \mathbf{P}(\mathbf{O} \cdot \mathbf{Q}) + \mathbf{Q}(\mathbf{O} \cdot \mathbf{P})$$

then

$$(\mathbf{B} \times \mathbf{r}_{iC}) \times \mathbf{r}_{ik} = \mathbf{r}_{iC}(\mathbf{B} \cdot \mathbf{r}_{ik}) + \mathbf{r}_{ik}(\mathbf{B} \cdot \mathbf{r}_{iC}) \tag{0.37}$$

and

$$\mathbf{r}_{ik} \times (\mathbf{B} \times \mathbf{r}_{iC}) = \mathbf{B}(\mathbf{r}_{ik} \cdot \mathbf{r}_{iC}) + \mathbf{r}_{iC}(\mathbf{r}_{ik} \cdot \mathbf{B}) \tag{0.38}$$

to give

$$H^{GC}(1e) = -\frac{g_e \mu_B e}{4mc^2} \sum_{i=1}^N \sum_{k=1}^{N_k} \left( \frac{eZ_{ik}}{r_{ik}^3} \right) [(\mathbf{S}_i \cdot \mathbf{B})(\mathbf{r}_{ik} \cdot \mathbf{r}_{iC}) - (\mathbf{S}_i \cdot \mathbf{r}_{ik}) \times (\mathbf{r}_{iC} \cdot \mathbf{B})] \tag{0.39}$$

The equivalent two electron term is:

$$H^{GC}(2e) = \frac{g_e \mu_B e^2}{4mc^2} \sum_{i=1}^N \sum_{j=1}^{N_j} \frac{1}{r_{ij}^3} \left( [(\mathbf{S}_i + 2\mathbf{S}_j) \cdot \mathbf{B}][\vec{\mathbf{r}}_{iK} \cdot \vec{\mathbf{r}}_{iC}] - [(\mathbf{S}_i + 2\mathbf{S}_j) \cdot \vec{\mathbf{r}}_{ij}][(\vec{\mathbf{r}}_{iC} \cdot \mathbf{B})] \right). \tag{0.40}$$

## 1.9 Derivation of the orbital-Zeeman term

Here we start from the kinetic energy term

$$\begin{aligned}
\sum_{i=1}^N \frac{\boldsymbol{\pi}_i^2}{2m} &= \frac{1}{2m} \sum_{i=1}^N \left( \mathbf{p}_i - \frac{e}{c} \mathbf{A}_i \right) \left( \mathbf{p}_i - \frac{e}{c} \mathbf{A}_i \right) \\
&= \frac{1}{2m} \sum_{i=1}^N \left[ \underbrace{\mathbf{p}_i \cdot \mathbf{p}_i}_{\text{neglect}} - \frac{e}{c} (\mathbf{p}_i \cdot \mathbf{A}_i + \mathbf{A}_i \cdot \mathbf{p}_i) + \underbrace{\left( \frac{e}{c} \right)^2 \mathbf{A}_i \cdot \mathbf{A}_i}_{\text{quadratic dismissed}} \right]
\end{aligned} \tag{0.41}$$

keeping only the linear terms in  $\mathbf{B}$ , this leaves

$$\begin{aligned}
\sum_{i=1}^N \frac{\pi_i^2}{2m} &= -\frac{1}{2m} \frac{e}{c} \sum_{i=1}^N (\mathbf{p}_i \cdot \mathbf{A}_i + \mathbf{A}_i \cdot \mathbf{p}_i) \\
&= -\frac{1}{m} \frac{e}{c} \sum_{i=1}^N \mathbf{A}_i \cdot \mathbf{p}_i
\end{aligned} \tag{0.42}$$

Again by making use of  $\mathbf{A}_i = \mathbf{B} \times \mathbf{r}_{iC} / 2$  then

$$\begin{aligned}
\sum_{i=1}^N \frac{\pi_i^2}{2m} &= -\frac{1}{2m} \frac{e}{c} \sum_{i=1}^N (\mathbf{B} \times \mathbf{r}_{iC}) \cdot \mathbf{p}_i \\
&= -\frac{1}{2m} \frac{e}{c} \sum_{i=1}^N \mathbf{B} \cdot (\mathbf{r}_{iC} \times \mathbf{p}_i) \\
H^{OZ} &= -\frac{1}{2m} \frac{e}{c} \sum_{i=1}^N \mathbf{B} \cdot \mathbf{l}_{iC}
\end{aligned} \tag{0.43}$$

## 1.10 Derivation of the relativistic mass correction

The final term that contributes to the Zeeman interaction in Eq. (0.25) is

$$-\frac{g_e \mu_B \pi_i^2}{2m^2 c^2} \mathbf{S}_i \cdot \mathbf{B} \tag{0.44}$$

It is treated in analogous way to the previous case. Mainly:

$$\begin{aligned}
H^{RMC} &= -\sum_{i=1}^N \left( \frac{g_e \mu_B}{2m^2 c^2} \right) \pi_i^2 \mathbf{S}_i \cdot \mathbf{B} \\
&= -\left( \frac{g_e \mu_B}{2m^2 c^2} \right) \sum_{i=1}^N \left( \mathbf{p}_i - \frac{e}{c} \mathbf{A}_i \right) \left( \mathbf{p}_i - \frac{e}{c} \mathbf{A}_i \right) \mathbf{S}_i \cdot \mathbf{B} \\
&= -\left( \frac{g_e \mu_B}{2m^2 c^2} \right) \sum_{i=1}^N \left[ \mathbf{p}_i \cdot \mathbf{p}_i - \underbrace{\frac{e}{c} (\mathbf{p}_i \cdot \mathbf{A}_i + \mathbf{A}_i \cdot \mathbf{p}_i)}_{\text{neglect}} + \underbrace{\left( \frac{e}{c} \right)^2 \mathbf{A}_i \cdot \mathbf{A}_i}_{\text{higher order dismissed}} \right] \mathbf{S}_i \cdot \mathbf{B}
\end{aligned} \tag{0.45}$$

By neglecting the term that are not linear in  $\mathbf{B}$ , this term reduces to

$$H^{RMC} = -\left( \frac{g_e \mu_B}{2m^2 c^2} \right) \sum_{i=1}^N p_i^2 \mathbf{S}_i \cdot \mathbf{B} \tag{0.46}$$

## 1.11 Summary

Thus in summary, the components of the Breit-Pauli Hamiltonian that are needed for the calculation of the  $\mathbf{g}$  tensor are found to be:

The spin Zeeman interaction

$$H^{SZ} = g_e \mu_B \sum_i \mathbf{S}_i \cdot \mathbf{B}. \quad (0.47)$$

The relativistic mass correction

$$H^{RMC} = \frac{g_e \mu_B}{2m^2 c^2} \sum_{i=1}^N p_i^2 \mathbf{S}_i \cdot \mathbf{B}. \quad (0.48)$$

The one and two electron-spin-Zeeman gauge corrections:

$$H^{GC} (1e) = \frac{g_e \mu_B e^2}{4mc^2} \sum_{i=1}^N \sum_{k=1}^{N_k} \frac{Z_k}{r_{ik}^3} p_i^2 \left[ (\mathbf{S}_i \cdot \mathbf{B})(\bar{\mathbf{r}}_{ik} \cdot \bar{\mathbf{r}}_{ic}) - (\mathbf{S}_i \cdot \bar{\mathbf{r}}_{ik})(\bar{\mathbf{r}}_{ic} \cdot \mathbf{B}) \right], \quad (0.49)$$

$$H^{GC} (2e) = \frac{g_e \mu_B e^2}{4mc^2} \sum_{i=1}^N \sum_{j=1}^N \frac{1}{r_{ij}^3} \left( \left[ (\mathbf{S}_i + 2\mathbf{S}_j) \cdot \mathbf{B} \right] [\bar{\mathbf{r}}_{ik} \cdot \bar{\mathbf{r}}_{ic}] - \left[ (\mathbf{S}_i + 2\mathbf{S}_j) \cdot \bar{\mathbf{r}}_{ij} \right] [(\bar{\mathbf{r}}_{ic} \cdot \mathbf{B})] \right). \quad (0.50)$$

There are three orbital terms:

$$H^{SO} (1e) = \frac{g_e \mu_B}{2mc} \sum_{i=1}^N \sum_{k=1}^{N_k} \left( \frac{eZ_k}{r_{ik}^3} \right) \mathbf{S}_i \cdot \mathbf{l}_{ik}, \quad (0.51)$$

$$H^{SO} (2e) = \frac{g_e \mu_B}{2mc} \sum_{i=1}^N \sum_{j=1}^N \left( \frac{1}{r_{ik}^3} \right) (\mathbf{S}_i + 2\mathbf{S}_j) \cdot \mathbf{l}_{ij} \quad (0.52)$$

and the orbital Zeeman operator

$$H^{OZ} = \frac{e}{2mc} \sum_{i=1}^N \mathbf{B} \cdot \mathbf{l}_{ic}. \quad (0.53)$$

## 1.12 Correlation between the experimental and computed $\mathbf{g}$ tensors

In the absence of any hyperfine interactions, the experimental  $\mathbf{g}$  tensor for a paramagnetic ion or radical with a doublet ground state is determined from

$$\Delta E = h\nu = \hat{\mathbf{S}} \cdot \tilde{\mathbf{g}} \cdot \mathbf{B} \quad (0.54)$$

and a particular calculated  $\mathbf{g}$  tensor component,  $g_{pq}$ , is obtained from

$$g_{\mu\nu} = \frac{\Delta E}{S_{\mu} B_{\nu}} \quad (0.55)$$

After some simple mathematical rearrangement of Eqs. (0.48) -(0.53), its components are found to be

$$g_{\mu\nu} = g_e \delta_{\mu\nu} + \Delta g^{RMC} \delta_{\mu\nu} + \Delta g_{\mu\nu}^{GC} + \Delta g_{\mu\nu}^{OZ/SOC}, \quad (0.56)$$

where

$$\Delta g^{RMC} = \left( \frac{\alpha^2}{S} \cdot \frac{g_e}{2} \right) \sum_{p,q} P_{p,q}^{\alpha-\beta} \left\langle \varphi_p \left| \sum_i \frac{-\nabla^2 s_{iz}}{2} \right| \varphi_q \right\rangle, \quad (0.57)$$

$$\Delta g_{\mu\nu}^{GC} = \frac{1}{2S} \sum_{p,q} P_{p,q}^{\alpha-\beta} \left\langle \varphi_p \left| \sum_A \xi(r_A) [\vec{r}_A \vec{r} - \vec{r}_{A,\mu} \vec{r}_\nu] s_{iz} \right| \varphi_q \right\rangle \quad (0.58)$$

and

$$\begin{aligned} \Delta g_{\mu\nu}^{OZ/SOC} = & -\frac{1}{2S} \sum_b \frac{1}{E_b - E_0} \times \\ & \left\{ \sum_{pq} P_{pq}^{(\alpha+\beta),0b} \left\langle \varphi_p \left| \ell_{\mu} \right| \varphi_q \right\rangle \sum_{pq} P_{pq}^{(\alpha-\beta),b0} \left\langle \varphi_p \left| \sum_A \xi(\vec{r}_A) \ell_{A,\nu} \right| \varphi_q \right\rangle \right. \\ & \left. + \sum_{pq} P_{pq}^{(\alpha-\beta),0b} \left\langle \varphi_p \left| \sum_A \xi(\vec{r}_A) \ell_{A,\mu} \right| \varphi_q \right\rangle \sum_{pq} P_{pq}^{(\alpha+\beta),b0} \left\langle \varphi_p \left| \ell_{\nu} \right| \varphi_q \right\rangle \right\}. \end{aligned} \quad (0.59)$$

The origin of the density matrices stems from the expansion of the wave function in orthonormal sets

$$\psi_i = \sum_p C_{pi} \varphi_p \quad (0.60)$$

Thus the expectation value, similar to Eq. (0.4), takes the form

$$\begin{aligned} \langle \psi | \hat{O} | \psi \rangle &= \left\langle \sum_p C_{pi} \varphi_p \left| \hat{O} \right| \sum_q C_{qi} \varphi_q \right\rangle \\ &= \sum_p C_{pi}^* \sum_q C_{qi} \langle \varphi_p | \hat{O} | \varphi_q \rangle \\ &= \sum_{pq} C_{pi}^* C_{qi} \langle \varphi_p | \hat{O} | \varphi_q \rangle = \sum_{pq} P_{pq} \langle \varphi_p | \hat{O} | \varphi_q \rangle. \end{aligned} \quad (0.61)$$

## 2.1 g Tensor calculation of the thiopheno-1,3,2-dithiazolyl $\pi$ -radical.

The thermally stable 1,3,2-dithiazolyl (DTA)  $\pi$ -radicals have non-zero magnetic moments and are essential building blocks for novel magnetic, conducting and spin-electronic (spintronic) materials. It is important to comprehend their structure-bonding relationships how they affect their electronic and magnetic properties. Thus, it is ideal to correlate experimental  $g$  and  $A$  tensor components for these radicals with their corresponding calculated values. A good correlation between theory and experiment gives a clear picture of the radical's electronic structure-bonding relationships, net spin density distribution and spin-orbit couplings.

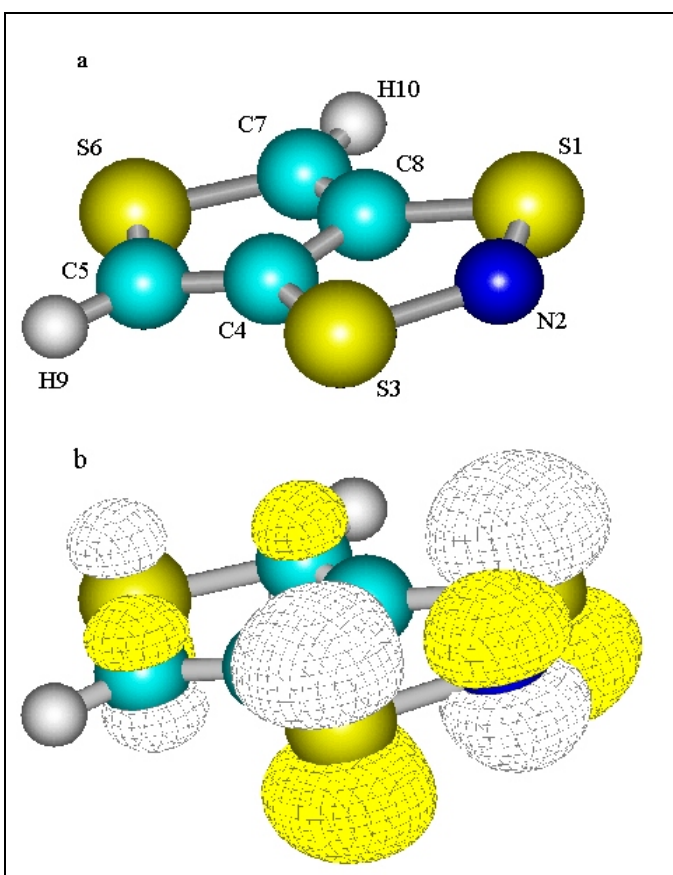


Figure 1.a) Orientation and atomic numbering of the thiopheno-1,3,2-dithiazolyl neutral radical. The molecule lies in the yz plane and the z axis is coincident with the vector connecting the S6 and N2 atoms.  
b) Three-dimensional isosurface contour plots of the singly occupied  $b_2$  molecular orbital (SOMO).

For radicals with ground states that are described by a predominant single determinant, hybrid density functional (HDF) techniques, in conjunction with moderate basis sets, have been very successful in calculating their electronic structure, optimal geometries and

**A** tensors. For DTA radicals, there are at least five accounts where HDF methods are used to calculate the **A** tensor components.

The computations of **g** tensors are less prevalent than those of **A** tensors. Neese's method utilizes the coupled-perturbed-Kohn-Sham formalism and has several advantages. For example, a variety of exchange, exchange-correlation and hybrid density functionals may be employed. Furthermore, the effects of the solvent may also be incorporated in the computations.

When judging the accuracy of a new computational technique, the accuracy of the experimental data itself is an important limiting consideration. In the case of DTA radicals, only the **BDTA•** and **TTTA•** have reliable *experimental g* tensor components. We have calculated their **g** tensor components and they were found to be within experimental accuracy (one part per thousand). The computed and experimental **g** tensor deviations from the value of the free electron,  $\Delta g_{ii}$  ( $i = x,y,z$ ), were found to be in the range of 140 – 750 ppm.

Recently Bond *et al.* have managed to accurately determine the experimental **g** and **A** components of a third radical, **TDTA•**. It is structurally related to **TTTA•** by replacement of two N atoms by their isoelectronic C-H counterparts. The tensor components were obtained by simulation of the EPR and ENDOR spectra at X and Q band frequencies. The simulations took into account the subtle low field undershoot effect common to this class of radicals. Bond *et al.* also factored in the fact that spatially equivalent atoms within the molecule are not magnetically equivalent. The existence of these reliable experimental values for this third radical presents a rare opportunity to further accurately compare the computed and experimental **g** and **A** tensor components of this class of radicals.

Here we show that the UB1LYP and UPBE0 HDF methods can also be used to compute the **g** and **A** tensors of **TDTA•** to within a 330-900 ppm of their experimental values. This good agreement continues the previous trend of understanding the EPR and ENDOR spectra of DTA radicals which, in turn, help us comprehend their structure-bonding relationships.

The **g** and **A** tensor components were calculated with the ORCA suite of programs using the UHF, UB1LYP and UPBE0 methods. The computations were carried out on a cluster of eight Linux computers using the message passing interface protocol, MPICH.

Two types of basis sets were used. The first is Barone's EPR-II basis sets, and the second is Dunning's larger, augmented correlation-consistent triple zeta polarization basis sets (aug-cc-pVTZ). Solvent effects were taken into account by surrounding the molecules with a solvent cavity of the appropriate dielectric constant,  $\epsilon$ , in accordance with the COSMO method.

## 2.2 Electronic ground states

The planar **TDTA•** radical has  $C_{2v}$  symmetry and a  ${}^2B_1$  ground state. The unpaired electron resides in a  $\pi$ -type one-electron singly occupied Kohn Sham orbital (SOMO), shown in Fig. 1. It is anti-bonding with respect to the N2, S1 and S3 atoms of the 1,3,2-dithiazolyl ring. The sulfur atoms are also anti-bonding with respect to the two thiopheno ring C atoms. On the other hand, the two C4 and C8 atoms are nonbonding and have very little net spin density.

In the liquid state, the radical's EPR spectrum displays three-lines of equal intensity due to the  $I({}^{14}N2) = 1$  of the 1,3,2-dithiazolyl group .

## 2.3 Numerical calculation of the g tensor components

The **TDTA•** experimental **g** tensor components were determined by simulation of the X-band EPR and ENDOR spectra at 100 K. These values were also confirmed by simulating the EPR taken at Q-band frequencies .

The calculated **g** tensor components using the UHF, UB1LYP and UPBE0 methods with EPR-II and aug-cc-pVTZ basis sets are listed in Table 1. Computations were carried out on the radical in the gas phase and with toluene or  $CD_2Cl_2$  as a solvent. At the bottom of Table 1 is a row labeled  $\Delta g(\text{ppm})$ . It represents the difference between the experimental and computed gas phase **g** tensor components, in parts per million, using the UB1LYP, UPBE0 and the EPR-II basis sets.

In the absence of solvent effects, the UHF/ EPR-II calculations show that, relative to the experimental **g** tensor, the  $g_{xx}$  and  $g_{zz}$  values are underestimated while the  $g_{yy}$  is overestimated. Table 1 also shows that the tetrahydrofuran or  $CD_2Cl_2$  solvents effects are found to be minimal and insignificant. In addition, increasing the basis set size from the EPR-II basis to the larger aug-cc-pVTZ set does not notably improve the situation.

When the UB1LYP or UPBE0 hybrid density functionals are used instead of the pure UHF exchange, a significant improvement is observed. For example, the agreement of the gas phase  $g_{yy}$  and  $g_{zz}$  computations with the experimental values improves by 1290 ppm and 2060 ppm respectively in going from UHF/EPR-II to UB1LYP/EPR-II.

**Table 1. Experimental and Computed Total g tensors.**

	$g_{xx}$	$g_{yy}$	$g_{zz}$	$\langle g \rangle$	$g_{xx}$	$g_{yy}$	$g_{zz}$	$\langle g \rangle$	
Experimental	2.00170	2.00510	2.01260	2.00650					a
<b>Gas Phase (Vacuum)</b>									
EPR-II	2.00161	2.00726	2.01021	2.00636					b
EPR-II	2.00207	2.00597	2.01227	2.00676	2.00209	2.00600	2.01225	2.00678	b
AUG-cc-pVTZ	2.00155	2.00657	2.01004	2.00605					b
AUG-cc-pVTZ	2.00204	2.00603	2.01236	2.00681	2.00210	2.00522	2.01145	2.00626	
<b>Tetrahydrofuran</b>									
EPR-II	2.00160	2.00727	2.01066	2.00651					b
EPR-II	2.00207	2.00609	2.01281	2.00699	2.00209	2.00613	2.01280	2.00700	b
<b>Methylene Chloride</b>									
EPR-II	2.00160	2.00728	2.01069	2.00652					b
EPR-II	2.00207	2.00609	2.01284	2.00700	2.00214	2.00510	2.01191	2.00638	b
$\Delta g(\text{ppm})$	-370	-870	-330	-260	-390	-900	-350	-280	b

a Bond et al.. Obtained by simulating the EPR spectra of the frozen radical in methylene chloride at 100K.

b This article. Due to the  $C_{2v}$  symmetry of the  $^2B_1$  radical, the total g tensor has no off-diagonal components.

Table 1 shows that the influence of the tetrahydrofuran or methylene chloride solvents on the neutral **TDTA•** **g** tensor components is very small. This was also found to be the case in our previous **g** tensor calculations for the **BDTA•** and **TTTA•** radicals.

When HDF methods are used, the **g** tensor components computed by the EPR-II basis sets are very similar to those obtained using the larger aug-cc-pVTZ sets. This indicates that the EPR-II, basis sets, like the aug-cc-pVTZ, have enough flexibility to properly describe the net electron spin density,  $\sum_{\mu,\nu} P_{\mu,\nu}^{\alpha-\beta}$ , required to compute the **g** tensor components. This is not surprising since the EPR-

II basis sets were originally designed for the difficult task of accurately computing the nuclear hyperfine **A** tensors. Therefore they properly express and balance the spin density in the core and valence regions of doublet state radicals. Calculations using the EPR-II basis sets were approximately 50 times faster than those employing the aug-cc-pVTZ sets. This offers a significant advantage, especially when computations of larger DTA radicals are to be attempted in the future. In the following discussions, the UB1LYP/EPR-II results will be used.

The accuracy of the experimental **g** tensor components is expected to be approximately 1 part per thousand (ppt) because they are indirectly determined by simulation of randomly oriented samples at low temperatures. The **TDTA•**  $\Delta g(\text{ppm})$  values, taken as the difference between the experimental **g** tensor components and those calculated using UB1LYP/EPR-II, range from 330 ppm to 870 ppm. Thus one may conclude that the calculated **g** tensor is within the limits of experimental accuracy.

When comparing the UB1LYP and UPBE0 methods, the maximum difference in  $\Delta g(\text{ppm})$  is small (30 ppm). It suggests that both HDF methods are quite accurate and yield similar results. This is because both the UB1LYP and UPBE0 functionals are very similar and mix 25% of the HF exchange with 75% of the density functional.

In conclusion, when compared to the UHF technique, the UB1LYP and UPBE0 HDF methods improve agreement of  $g_{yy}$  and  $g_{zz}$  with experiment. There is little difference whether the UB1LYP or UPBE0 methods are used or whether the basis set is enlarged from EPR-II to aug-cc-pVTZ.

## 2.4 Analysis of the **g** tensor components

The **g** tensor components may be broken down into four main components

$$g_{rs} = g_e \delta_{rs} + \Delta g^{RMC} \delta_{rs} + \Delta g_{rs}^{GC} + \Delta g_{rs}^{OZ/SOC} \quad (2.62)$$

Their UB1LYP/EPR-II numerical values are given in Table 2 and all their symbols in Eqs. 2.1-2.4, have been previously defined. The first term is the scalar value of the free electron,  $g_e = 2.002319$  and the  $\delta_{rs}$  Kronecker delta function restricts its contribution to the diagonal terms of the total **g** tensor. The relativistic mass correction to the kinetic energy is

$$\Delta g^{RMC} = \frac{\alpha^2}{S} \sum_{\mu,\nu} P_{\mu,\nu}^{\alpha-\beta} \left\langle \varphi_\mu \left| \frac{-\nabla^2}{2} \right| \varphi_\nu \right\rangle, \quad (2.63)$$

where the spin  $S = 1/2$  and  $\alpha$  is the fine structure constant. The  $\Delta g^{\text{RMC}}$  term decreases the diagonal  $\mathbf{g}$  tensor values by  $2.4750 \times 10^{-4}$  ppm.

Unlike the first two terms on the right hand side of Eq. 1, the diamagnetic correction term,  $\Delta g_{rs}^{\text{GC}}$ , is a second rank Cartesian tensor.

$$\Delta g_{rs}^{\text{GC}} = \frac{1}{2S} \sum_{\mu, \nu} P_{\mu, \nu}^{\alpha-\beta} \left\langle \varphi_{\mu} \left| \sum_A \left[ \frac{\alpha^2 Z_{\text{eff}}^4}{2 |\vec{r}_i - \vec{R}_A|^3} \right] (\vec{r}_A \vec{r}_O - \vec{r}_{A,r} \vec{r}_{O,s}) \right| \varphi_{\nu} \right\rangle. \quad (2.64)$$

Here the term in square brackets represents the effective spin orbit coupling interaction,  $\xi(A, i)$ , of the  $i$ th electron at the  $A$ th nucleus.  $Z_{\text{eff}}$  is its effective nuclear charge and . Table 2 indicates that the one- electron contributions to  $\Delta g_{xx}^{\text{GC}}$ ,  $\Delta g_{yy}^{\text{GC}}$  and  $\Delta g_{zz}^{\text{GC}}$  are positive while the corresponding two-electron terms are smaller and negative. The net results are positive values that counteract the corresponding  $\Delta g^{\text{RMC}}$  contributions.

The orbital-Zeeman spin-orbit term,  $\Delta g_{rs}^{\text{OZ/SOC}}$  is the largest contributing term to the deviation of the  $\mathbf{g}$  tensor from the free electron value. This second rank tensor, in the uncoupled representation, is defined as:

$$\Delta g_{\mu\nu}^{\text{OZ/SOC}} = -\frac{1}{2S} \sum_b \frac{1}{E_b - E_0} \times \left\{ \sum_{pq} P_{pq}^{(\alpha+\beta), 0b} \langle \varphi_p | \ell_{\mu} | \varphi_q \rangle \sum_{pq} P_{pq}^{(\alpha-\beta), b0} \left\langle \varphi_p \left| \sum_A \xi(\vec{r}_A) \ell_{A,\nu} \right| \varphi_q \right\rangle \right. \\ \left. + \sum_{pq} P_{pq}^{(\alpha-\beta), 0b} \left\langle \varphi_p \left| \sum_A \xi(\vec{r}_A) \ell_{A,\mu} \right| \varphi_q \right\rangle \sum_{pq} P_{pq}^{(\alpha+\beta), b0} \langle \varphi_p | \ell_{\nu} | \varphi_q \rangle \right\}. \quad (2.65)$$

Only the coupling of the  ${}^2B_1$  ground state with the excited  ${}^2A_2$  states contributes to the  $\Delta g_{xx}^{\text{OZ/SOC}}$  components. There are two doubly occupied  $a_2$  valence orbitals and seventeen empty ones that are sufficiently close in energy to significantly influence the  $\mathbf{g}_{xx}^{\text{OZ/SOC}}$  components. The  $1a_2$  is a core orbital while the  $2a_2$  orbital is out-of-plane  $\pi$  bonding that is delocalized over the S1, S3, C4, C5, C7 and C8 atoms. It has significant character from the thiophene ring. This, in conjunction with its large energy difference compared to the SOMO, render its contributions to  $\mathbf{g}_{xx}$  to be rather small. In spite of its being closer to the SOMO, the  $3a_2$  orbital is mainly carbon in character. Since the carbon spin-orbit coupling constant is smaller than that of sulfur and nitrogen it increases  $\mathbf{g}_{xx}^{\text{OZ/SOC}}$  by a relatively small amount. Since excitations from the SOMO to the seventeen  $a_2$  virtual orbitals counteract those from the filled  $2a_2$  and  $3a_2$  to the SOMO, the net result is a negative contribution to  $\mathbf{g}_{xx}$ . In addition, Table 2 indicates that the  $\Delta g^{\text{RMC}}$  and  $\Delta g_{xx}^{\text{GC}}$  are almost equal in magnitude but opposite in sign. Thus the negative  $\Delta g_{xx}^{\text{OZ/SOC}}$  is the deciding term and leads to a total  $\mathbf{g}_{xx}$  value that is less than  $\mathbf{g}_e$ .

**Table 2: Individual One and Two Electron Contributions to the Total g Tensor Diagonal Components<sup>a</sup>**

	UB1LYP			UPBE0		
$\Delta g_{rs}^{RMC} \delta_{rs}(\text{ppm})$	$g_{xx}$	$g_{yy}$	$g_{zz}$	$g_{xx}$	$g_{yy}$	$g_{zz}$
Total	$-2.4750 \times 10^{-4}$	$-2.4750 \times 10^{-4}$	$-2.4750 \times 10^{-4}$	$-2.4400 \times 10^{-4}$	$-2.4400 \times 10^{-4}$	$-2.4400 \times 10^{-4}$
$\Delta g_{rs}^{GC}(\text{ppm})$	$g_{xx}$	$g_{yy}$	$g_{zz}$	$g_{xx}$	$g_{yy}$	$g_{zz}$
One-electron	$3.2730 \times 10^{-4}$	$3.8670 \times 10^{-4}$	$3.0030 \times 10^{-4}$	$3.2500 \times 10^{-4}$	$3.8430 \times 10^{-4}$	$3.0010 \times 10^{-4}$
Two-electron	$-8.0100 \times 10^{-5}$	$-9.5100 \times 10^{-5}$	$-7.3400 \times 10^{-5}$	$-7.9600 \times 10^{-5}$	$-9.4500 \times 10^{-5}$	$-7.3200 \times 10^{-5}$
Total	$2.4720 \times 10^{-4}$	$2.9160 \times 10^{-4}$	$2.2690 \times 10^{-4}$	$2.4540 \times 10^{-4}$	$2.8980 \times 10^{-4}$	$2.2690 \times 10^{-4}$
$\Delta g_{rs}^{OZ/SOC}(\text{ppm})$	$g_{xx}$	$g_{yy}$	$g_{zz}$	$g_{xx}$	$g_{yy}$	$g_{zz}$
One-electron	$-6.4000 \times 10^{-4}$	$5.7160 \times 10^{-3}$	$1.2997 \times 10^{-2}$	$-6.2070 \times 10^{-4}$	$5.7300 \times 10^{-3}$	$1.2955 \times 10^{-2}$
Two-electron	$3.8580 \times 10^{-4}$	$-2.1121 \times 10^{-3}$	$-3.0242 \times 10^{-3}$	$3.8600 \times 10^{-4}$	$-2.0978 \times 10^{-3}$	$-3.0056 \times 10^{-3}$
Total	$-2.5430 \times 10^{-4}$	$3.60400 \times 10^{-3}$	$9.9726 \times 10^{-3}$	$-2.3470 \times 10^{-4}$	$3.6322 \times 10^{-3}$	$9.9490 \times 10^{-3}$
$g_{rs}^{\text{total}}$	$g_{xx}$	$g_{yy}$	$g_{zz}$	$g_{xx}$	$g_{yy}$	$g_{zz}$
	2.00207	2.00597	2.01227	2.00209	2.00600	2.01225

<sup>a</sup> Due to the  $C_{2v}$  symmetry of the molecule, all off diagonal g tensor terms,  $g_{ij}$ , are zero. Thus, only the diagonal elements are listed.

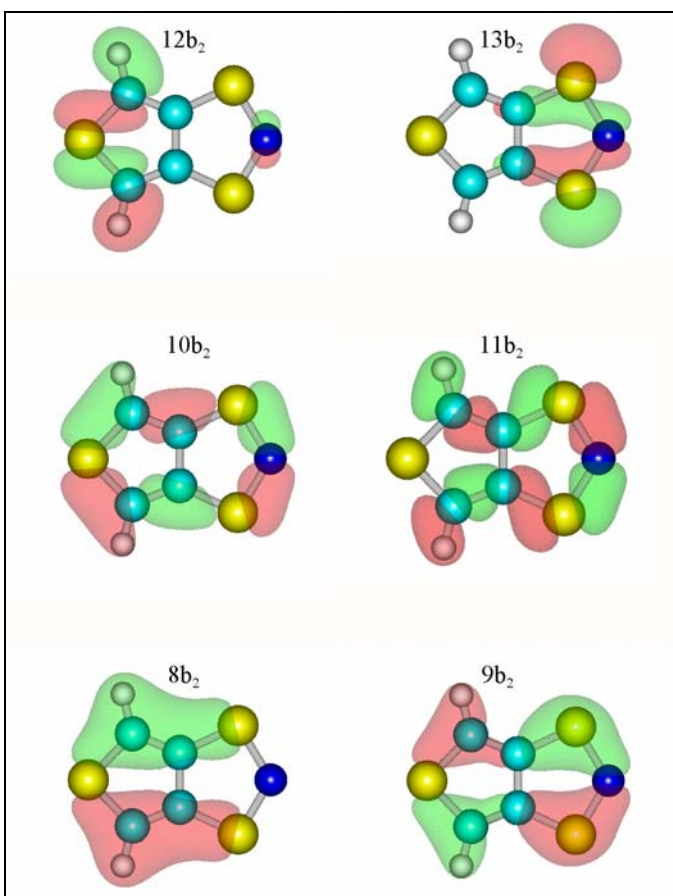


Figure 2. Isosurfaces of the six doubly occupied  $8b_2$  -  $13b_2$  one-electron Kohn-Sham molecular orbitals. The  $13b_2$  is the main contributor to the  $g_{zz}$  component via spin-orbit/orbital-Zeeman coupling. The isosurface contour cutoff is  $0.05 \text{ e/au}^3$ .

There are 58  $a_1$  orbitals that, upon excitation, will contribute to  $\Delta g_{yy}^{\text{OZ/SOC}}$ . Nineteen are doubly occupied and will increase  $\Delta g_{yy}^{\text{OZ/SOC}}$  when excited to the SOMO. In contrast, excitation of the unpaired electron from the SOMO to the 39 virtual  $a_1$  orbitals decreases  $\Delta g_{yy}^{\text{OZ/SOC}}$ . The sum of these numerous counteracting contributions leads to  $\Delta g_{yy}^{\text{OZ/SOC}} = 3.60400 \times 10^{-3}$ . Table 2 also shows that the one-electron contributions to  $g_{yy}^{\text{OZ/SOC}}$  are positive and offset the corresponding two-electron contributions which are negative. The net positive values of  $\Delta g_{yy}^{\text{OZ/SOC}}$  and  $\Delta g_{yy}^{\text{GC}}$ , overcome the negative value of  $\Delta g^{\text{RMC}}$  and lead to a  $g_{yy}$  component that is slightly larger than  $g_e$ .

The computed  $g_{zz}$  is 2.01227. By noting from Figure 1 that the SOMO is mainly  $S1(p_x)$ ,  $N2(p_x)$  and  $S3(p_x)$  in character then the largest contributions to  $g_{zz}$  are from the filled  $b_2$  orbitals with large  $S1(p_y)$ ,  $N2(p_y)$  and  $S3(p_y)$  components. In addition, the excited  $B_2$  states that are close to the  $B_1$  ground state will increase the  $g_{zz}$  more than those that are farther away. Figure 2 depicts the  $8b_2$  -  $13b_2$  one-electron Kohn-Sham orbitals. They are all in-plane bonding and possess a node along the N2-S6 direction. From these spin restricted one-electron orbitals one may *qualitatively* conclude that the  $8b_2$ ,  $9b_2$  and  $12b_2$

are less important than the  $10b_2$ ,  $11b_2$  and  $13b_2$  orbitals. The latter three orbitals are in-plane  $\pi$ -bonding with significant S1, N2 and S3 character. Inspection of Fig. 2 also shows that, in addition to being close to the SOMO, the  $13b_2$  orbital is predominantly S1 and S3 in character. The relatively large sulfur spin-orbit coupling of this orbital causes the largest positive increase to  $\Delta g_{zz}^{OZ/SOC}$ .

## 2.5 Summary and conclusions

Lately we have demonstrated that the UB1LYP and UPBE0 HDF methods can accurately reproduce the **A** tensor components of polycyclic DTA radicals. In contrast, only two **g** tensors have been accurately calculated for these types of radicals (**BDTA•** and **TTTA•**). Recently, a third radical, **TDTA•**, has been synthesized by Bond *et al.*. Its **g** and **A** tensors were accurately and reliably determined by simulation of its EPR and ENDOR spectra at X and Q band frequencies. The existence of these dependable experimental tensors for **TDTA•** present an excellent opportunity to accurately compare the computed and experimental **g** and **A** tensor components of yet a third DTA radical.

Here we show that the UB1LYP and UPBE0 functionals, in conjunction with Barone's EPR-II basis sets, can also be used to calculate the **g** tensors of **TDTA•** to within a 330-900 ppm of their experimental values. This very good agreement continues the previous trend and opens the field for further accurate and viable calculations of the spin Hamiltonian tensors. They in turn should lead correct interpretations of the EPR and ENDOR spectra of larger inorganic sulfur-nitrogen radicals.

The UB1LYP and UPBE0 HDFs, that include electron exchange and correlation, improve these calculations over those carried out at the UHF level. On the other hand, the solvent effects do not largely affect the calculated **g** tensor.

Finally, the isotropic hyperfine coupling constants and net spin densities at the **TDTA•**, determined by the present computations, are also in very good agreement with the experimental values and previous net spin density calculations.

## Reference List

1. Cordes, A. W.; Haddon, R. C.; Oakley, R. T. Molecular conductors from neutral heterocyclic p-radicals. *Advanced Materials (Weinheim, Germany)* **1994**, *6* (10), 798, 801-798, 802.
2. Rawson, J. M.; Palacio, F. Magnetic properties of thiazyl radicals. *Structure and Bonding (Berlin, Germany)* **2001**, *100* (p-Electron Magnetism), 93-128.
3. Barclay, T. M.; Cordes, A. W.; de Laat, R. H.; Goddard, J. D.; Haddon, R. C.; Jeter, D. Y.; Mawhinney, R. C.; Oakley, R. T.; Palstra, T. T. M.; Patenaude, G. W.; Reed, R. W.; Westwood, N. P. C. The Heterocyclic Diradical Benzo-1,2:4,5-bis(1,3,2-dithiazolyl). Electronic, Molecular and Solid State Structure. *J. Am. Chem. Soc.* **1997**, *119* (11), 2633-2641.
4. McManus, G. D.; Rawson, J. M.; Feeder, N.; van Duijn, J.; McInnes, E. J. L.; Novoa, J. J.; Burriel, R.; Palacio, F.; Oliete, P. Synthesis, crystal structures, electronic structure and magnetic behavior of the trithiatriazapentalenyl radical, C<sub>2</sub>S<sub>3</sub>N<sub>3</sub>. *Journal of Materials Chemistry* **2001**, *11* (8), 1992-2003.
5. Brusso, J. L.; Clements, O. P.; Haddon, R. C.; Itkis, M. E.; Leitch, A. A.; Oakley, R. T.; Reed, R. W.; Richardson, J. F. Bistability and the phase transition in 1,3,2-dithiazolo[4,5-b]pyrazin-2-yl. *Journal of the American Chemical Society* **2004**, *126* (45), 14692-14693.
6. Barclay, T. M.; Cordes, A. W.; George, N. A.; Haddon, R. C.; Oakley, R. T.; Palstra, T. T. M.; Patenaude, G. W.; Reed, R. W.; Richardson, J. F.; Zhang, H. Molecular materials from 1,3,2-dithiazolyls. Solid-state structures and magnetic properties of 2,3-naphthalene and quinoxaline derivatives. *Chemical Communications (Cambridge)* **1997**, (9), 873-874.
7. Mattar, S. M. g-Tensor calculations of bicyclic 1,3,2-dithiazolyl radicals using the coupled-perturbed Kohn-Sham UB1LYP and UPBE0 hybrid density functionals. *Chem. Phys. Lett.* **2005**, *405* (4-6), 382-388.
8. Improta, R.; Barone, V. Interplay of Electronic, Environmental, and Vibrational Effects in Determining the Hyperfine Coupling Constants of Organic Free Radicals. *Chemical Reviews (Washington, DC, United States)* **2004**, *104* (3), 1231-1253.
9. Di Matteo, A.; Adamo, C.; Cossi, M.; Barone, V.; Rey, P. Intrinsic and environmental effects in the physico-chemical properties of nitroxides. The case of 2-phenyl-4,4,5,5-tetramethyl-4,5-dihydro-1H-imidazol-1-oxyl 3-oxide. *Chemical Physics Letters* **1999**, *310* (1,2), 159-165.
10. Mattar, S. M. Calculation of the <sup>1</sup>H, <sup>13</sup>C, <sup>14</sup>N and <sup>33</sup>S hyperfine tensors of the 1,3,2-dithiazol-2-yl radical using hybrid density functionals. *Chemical Physics Letters* **1999**, *300* (5,6), 545-552.

11. Mattar, S. M.; Stephens, A. D. UB1LYP as an accurate and efficient method for computing the isotropic hyperfine tensor components of neutral bicyclic and tricyclic dithiazole radicals. *Chem. Phys. Lett.* **2000**, *327* (5,6), 409-419.
12. Mattar, S. M.; Stephens, A. D. Magnetic Inequivalency, Electron Paramagnetic Resonance, Electronic Structure, Optimal Geometry, and Electronic Spectra of the 4,5-Bis(trifluoromethyl)-1,3,2-dithiazol-2-yl Radical. *Journal of Physical Chemistry A* **2000**, *104* (16), 3718-3732.
13. Mattar, S. M. Role of the solvent in computing the 1,4-benzosemiquinone g-tensor by the coupled-perturbed Kohn-Sham hybrid density functional method. *Journal of Physical Chemistry B* **2004**, *108* (27), 9449-9455.
14. Neese, F. Prediction of electron paramagnetic resonance g values using coupled perturbed Hartree-Fock and Kohn-Sham theory. *Journal of Chemical Physics* **2001**, *115* (24), 11080-11096.
15. Alberola, A.; Farley, R. D.; Humphrey, S. M.; McManus, G. D.; Murphy, D. M.; Rawson, J. M. EPR studies on the thiophenodithiazolyl radical, C<sub>4</sub>H<sub>2</sub>S<sub>3</sub>N. *Dalton transactions (Cambridge, England : 2003)* **2005**, (24), 3838-3845.
16. Mattar, S. M. Minimum general requirements for equivalent atoms in a molecule. *Chem. Phys. Lett.* **1998**, *287* (5,6), 608-612.
17. Barone, V.; Fliszar, S. Applications of density functional theory approaching chemical accuracy to the study of typical carbon-carbon and carbon-hydrogen bonds. *THEOCHEM* **1996**, *369*, 29-37.
18. Improta, R.; Barone, V. Interplay of electronic, environmental, and vibrational effects in determining the hyperfine coupling constants of organic free radicals. *Chemical reviews* **2004**, *104* (3), 1231-1254.
19. Adamo, C.; Barone, V. Toward chemical accuracy in the computation of NMR shieldings: the PBE0 model. *Chemical Physics Letters* **1998**, *298* (1-3), 113-119.

### 3.1 Example: The Calculation of the DPPH g tensor

The 2,2'-diphenyl-1-picrylhydrazyl (**DPPH•**) neutral free radical, shown in Fig.1, is a stable radical, with an average **g** value of 2.0036. It has been commonly used as a standard marker in electron paramagnetic resonance (EPR) spectroscopy in the range of 1 - 465GHz. It is also an important radical scavenger that has been used as a spin trap in over 400 publications within the last three years.

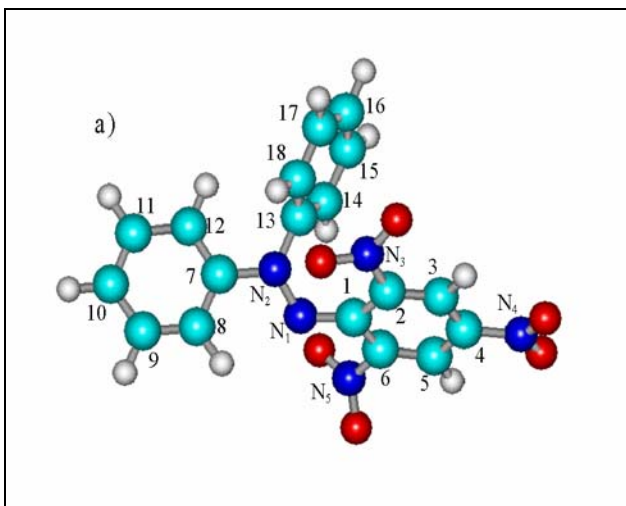


Fig. 1a Orientation and atomic numbering of **DPPH•**. For clarity, only the carbon skeletons and nitrogen atoms have been labelled.

It is important to understand the correlation between DPPH's reactivity, structure, bonding, spin Hamiltonian parameters and its environment. This may ideally be achieved by correlating the observed magnetic properties and spin Hamiltonian parameters with those calculated by a reliable computational method. A good agreement between theory and experiment enables one to relate the radical's electronic structure and geometry to its bonding, properties and reactivity.

In the absence of rotational or vibrational averaging, **DPPH•** has  $C_1$  symmetry and, as a result, all its nuclei are magnetically inequivalent. However, electron nuclear double resonance (ENDOR) studies by Dalal et al. indicate that although the pair of picryl protons are inequivalent, the phenyl protons appear to be magnetically equivalent. They suggested that the phenyl groups may rotate about their C-N<sub>2</sub> bonds and average out their proton inequivalency. From these experimental results, it is clear that dynamic

motions and rotational averaging must play an important role in influencing the magnetic properties of this molecule. Consequently, our primary aim is to find to what extent the EPR and ENDOR spectra of **DPPH•** are influenced by solvent interactions, fluctuations or restricted rotations. The main spin Hamiltonian parameters affecting the spectra are the **g** and hyperfine (**A**) tensors. As a first step, we investigate how these factors contribute to the magnitudes of the **g** tensor components. This is accomplished via hybrid density functional (HDF) calculations.

The UB1LYP and PBE0 HDFs, which have the advantage of containing no adjustable parameters, have been introduced. When used with moderate basis sets such as EPR-III, they yield slightly more accurate results when compared to the B3LYP functional.

During the last few years **g** tensor components have been computed using a variety of techniques. Using the UB1LYP HDF method and the EPR-II basis sets of Barone, we found that there is little loss of accuracy as the radicals increase in size from diatomics to aromatic ones such as 1,4-benzosemiquinone. This trend continues with inorganic radicals that include nitrogen, sulfur and fluorine. These past results have given us enough confidence to attempt the computation of the **DPPH• g** tensor. The calculations are quite demanding since **DPPH•** is a large molecule that has 41 atoms. In addition it is floppy and environmental effects, such as solvent-solute interactions, may influence its geometry and its **g** tensor components. Thus, thorough computations that reproduce the experimental spectra, must include phenyl ring rotations and solvent effects. These tensors, in conjunction with the total hyperfine **A** tensor components, allow us to assess the effects of magnetic inequivalent **DPPH•** atoms on its EPR and ENDOR spectra.

Since the geometry of **DPPH•** in the gas phase and in various solvents is not known, it had to be optimized in the gas phase. Once the optimized geometries were obtained the **g** tensor components were computed using the UB1LYP HDF method and Barone's double zeta EPR-II basis sets. The EPR-II bases properly express and balance the spin density in the core and valence regions of doublet state radicals.

The effects of solvents were investigated using Tomasi's polarized continuum (PCM) and COSMO methods, which place the radical in a solvent cavity. The cavity itself is constructed from a series of interlocking spheres.

### 3.2 Electronic Ground State and Relevant Bond Orders

The **DPPH•** radical (Fig. 1a) has one unpaired electron,  $C_1$  symmetry and a  $X^2A_1$  ground state. While the unpaired electron resides mainly on the  $N_1$ - $N_2$  moiety, it is nevertheless delocalized over the entire molecule. The Lowdin bond orders between the  $N_2$  and the phenyl rings are calculated to be 1.0934 and 1.0466, suggesting that they are single bonds. Thus, in the absence any other steric influence, the phenyl rings may rotate freely. In contrast,  $N_1$  - picryl ring bond has an order of  $\approx 1.5$ . It is a partial double bond rendering the picryl ring free rotation unlikely. The space filling model in Fig. 1(b) shows that although rotation of the phenyl rings is possible, there will be some steric hindrance. The effect of such restricted rotations will be discussed in section 3.4 below. The order of the  $N_1$ - $N_2$  bond is  $\approx 1.45$  indicating that there is a delocalization along the  $N_1$ - $N_2$ - $C_{13}$  bonds where the unpaired electron mainly resides.

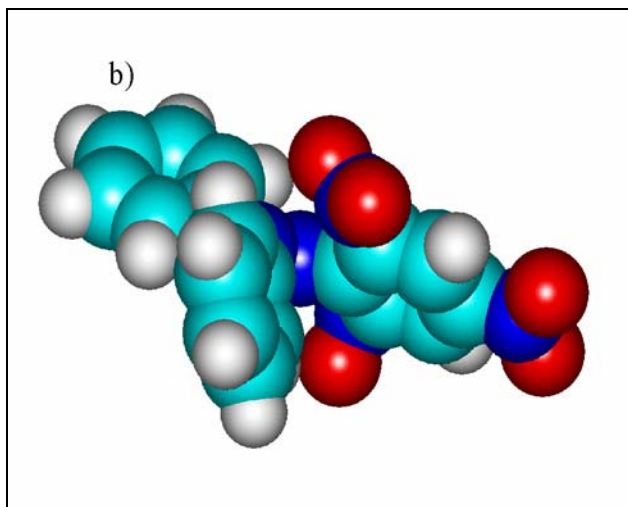


Fig. 1b Another view of **DPPH•**.using a space-filling model to illustrate the radical's non-planarity and steric crowding.

### 3.3 Numerical calculation of the **g** tensor components.

The experimental and calculated **g** tensor components using the UB1LYP and UPBE0 methods with the EPR-II basis set are listed in Table 1. Computations were carried out on the radical in the gas phase and with a variety of solvents. The geometry used in the calculations corresponds to the minimum energy configuration where the dihedral angle, formed between the N<sub>1</sub>, N<sub>2</sub>, C<sub>7</sub> and C<sub>8</sub> atoms, in Fig. 1a, is 35°. The row labeled  $\Delta g(\text{ppm})$ , at the bottom of Table 1, represents the difference between the latest experimental results and the computed gas phase **g** tensor components in parts per million using the UB1LYP hybrid density functional.

**Table 1. Experimental and Computed Total **g** tensors**

	$g_{11}$	$g_{22}$	$g_{33}$	$\langle g \rangle$	Ref.
Experimental	2.00390	2.00390	2.00280	2.00350	
	2.00400	2.00380	2.00310	2.00360	
	2.00390	2.00370	2.00320	2.00360	
	2.00392	2.00392	2.00295	2.00360	
	2.00435	2.00367	2.00245	2.00349	
Gas Phase UB1LYP	2.004601	2.003648	2.002331	2.003526	a
PCM CCl <sub>4</sub>	2.00445	2.00381	2.00244	2.00357	a
PCM Benzene	2.00445	2.00381	2.00244	2.00357	a
PCM Ethanol	2.00442	2.00380	2.00245	2.00356	a
PCM Methanol	2.00442	2.00380	2.00245	2.00356	a
PCM Acetonitrile	2.00442	2.00380	2.00245	2.00356	a
PCM DMSO	2.00442	2.00380	2.00245	2.00356	a
COSMO Mineral Oil UB1LYP	2.004567	2.003644	2.002326	2.003512	a
COSMO Mineral Oil UPBE0	2.004553	2.003633	2.002337	2.003507	a
$\Delta g(\text{ppm})$	251	22	119	36	

a This work

These particular experimental results were chosen as a benchmark because they are obtained from high frequency spectra (220 GHz) where the **g** tensor components suffer minimally from complicating factors such as spin exchange narrowing and dipolar broadening.

Table 1 shows that the influence of the solvents on the neutral **DPPH•** **g** tensor components is very small. Computations done using the PCM method show the effect due to ethanol, methanol, acetonitrile and DMSO are essentially the same. However, in the case of non-polar solvents such as CCl<sub>4</sub> and benzene, only a marginal increase in the g<sub>11</sub> component is observed. Table 1 also indicates that when the COSMO method was employed with mineral oil as a solvent, similar results were obtained.

The experimental **g** tensor components are usually determined from the broad EPR peaks of randomly oriented microcrystals, powdered or glassy samples. More accurate determination of these parameters is obtained from the simulation of the experimental EPR spectrum. Even with sophisticated simulation techniques, the accuracy of the experimental **g** tensor components is expected to be approximately 1 part per thousand (ppt). The difference between the latest experimental **g** tensor components and those calculated using gas phase UB1LYP/EPR-II [ $\Delta g$ (ppm), Table 1] range from 22 ppm to 251 ppm. These values allow us to safely conclude that the calculated **g** tensor is within the limits of experimental accuracy. The comparison of the UB1LYP and UPBE0 methods, given in the last two rows of Table 1, shows that the differences between the two techniques are only 14,11,11 and 5ppm for g<sub>11</sub>, g<sub>22</sub>, g<sub>33</sub> and <g>, respectively. The accuracy and similarity of the results from the UB1LYP and UPBE0 methods is understandable because the functionals are very similar and mix 25% of the HF exchange with 75% of the density functional.

### 3.4 Analysis of the DPPH **g** tensor components

From Section 2, the total **g** tensor may be expressed as the sum of four main components

$$g_{\mu\nu} = g_e \delta_{\mu\nu} + \Delta g^{RMC} \delta_{\mu\nu} + \Delta g_{\mu\nu}^{GC} + \Delta g_{\mu\nu}^{OZ/SOC}, \quad (3.66)$$

where all their symbols have been previously defined. The Kronecker delta function,  $\delta_{\mu\nu}$  constrains the contribution of the free electron value,  $g_e = 2.002319$ , to the diagonal components of the total  $\mathbf{g}$  tensor. The second term is the reduced mass correction to the kinetic energy

$$\Delta\mathbf{g}^{\text{RMC}} = \left( \frac{\alpha^2}{S} \cdot \frac{g_e}{2} \right) \sum_{p,q} P_{p,q}^{\alpha-\beta} \left\langle \psi_p \left| \sum_i \frac{-\nabla^2 s_{iz}}{2} \right| \psi_q \right\rangle, \quad (3.67)$$

where  $\alpha$  term in parenthesis is the fine structure constant,  $S$  is the total ground state spin. For the UB1LYP gas phase results, the  $\Delta\mathbf{g}^{\text{RMC}}$  term reduces the diagonal  $\mathbf{g}$  tensor values by  $2.363 \times 10^{-4}$  ppm.

In contrast to the previous term, the gauge correction term,  $\Delta\mathbf{g}_{\mu\nu}^{\text{GC}}$ , is a second rank Cartesian tensor

$$\Delta\mathbf{g}_{\mu\nu}^{\text{GC}} = \frac{1}{2S} \sum_{p,q} P_{p,q}^{\alpha-\beta} \left\langle \psi_p \left| \sum_A \xi(r_A) [\vec{r}_A \vec{r} - \vec{r}_{A,\mu} \vec{r}_\nu] s_{iz} \right| \psi_q \right\rangle \quad (3.68)$$

The term  $\xi(r_A)$  is the effective spin orbit coupling interaction of the  $i$ th electron at the  $A$ th nucleus. The  $\Delta\mathbf{g}_{11}^{\text{GC}}$ ,  $\Delta\mathbf{g}_{22}^{\text{GC}}$  and  $\Delta\mathbf{g}_{33}^{\text{GC}}$  terms, which are the diagonalized form of the  $\Delta\mathbf{g}_{\mu\nu}^{\text{GC}}$ , are listed in Table 2. Their one-electron contributions are positive while the corresponding two-electron terms are smaller and negative. The total results are positive values that counteract the corresponding  $\Delta\mathbf{g}^{\text{RMC}}$  contributions

The largest contributing term to the deviation of the  $\mathbf{g}$  tensor from the free electron value is the orbital-Zeeman spin-orbit term  $\Delta\mathbf{g}_{\mu\nu}^{\text{OZ/SOC}}$ . The uncoupled representation of this second rank tensor is:

$$\begin{aligned} \Delta\mathbf{g}_{\mu\nu}^{\text{OZ/SOC}} = & -\frac{1}{2S} \sum_b \frac{1}{E_b - E_0} \times \\ & \left\{ \sum_{pq} P_{pq}^{(\alpha+\beta),0b} \left\langle \psi_p \left| \ell_\mu \right| \psi_q \right\rangle \sum_{pq} P_{pq}^{(\alpha-\beta),b0} \left\langle \psi_p \left| \sum_A \xi(\vec{r}_A) \ell_{A,\nu} \right| \psi_q \right\rangle \right. \\ & \left. + \sum_{pq} P_{pq}^{(\alpha-\beta),0b} \left\langle \psi_p \left| \sum_A \xi(\vec{r}_A) \ell_{A,\mu} \right| \psi_q \right\rangle \sum_{pq} P_{pq}^{(\alpha+\beta),b0} \left\langle \psi_p \left| \ell_\nu \right| \psi_q \right\rangle \right\}. \end{aligned} \quad (3.69)$$

**Table 2: Individual One and Two Electron Contributions to the Diagonalized Total g Tensor Components**

	UB1LYP Gas Phase Minimum			UB1LYP Gas Phase Averaged		
$\Delta g^{\text{RMC}}$ (ppm)	$g_{11}$	$g_{22}$	$g_{33}$	$g_{11}$	$g_{22}$	$g_{33}$
Total	$-2.363 \times 10^{-4}$	$-2.363 \times 10^{-4}$	$-2.363 \times 10^{-4}$	$-2.367 \times 10^{-4}$	$-2.367 \times 10^{-4}$	$-2.367 \times 10^{-4}$
$\Delta g^{\text{GC}}$ (ppm)	$g_{11}$	$g_{22}$	$g_{33}$	$g_{11}$	$g_{22}$	$g_{33}$
One-electron	$2.612 \times 10^{-4}$	$2.601 \times 10^{-4}$	$2.260 \times 10^{-4}$	$2.604 \times 10^{-4}$	$2.594 \times 10^{-4}$	$2.244 \times 10^{-4}$
Two-electron	$-9.580 \times 10^{-5}$	$-9.380 \times 10^{-5}$	$-8.200 \times 10^{-5}$	$9.547 \times 10^{-5}$	$9.348 \times 10^{-5}$	$8.132 \times 10^{-5}$
Total	$1.654 \times 10^{-4}$	$1.664 \times 10^{-4}$	$1.440 \times 10^{-4}$	$1.649 \times 10^{-4}$	$1.660 \times 10^{-4}$	$1.143 \times 10^{-4}$
$\Delta g^{\text{OZ/SOC}}$ (ppm)	$g_{11}$	$g_{22}$	$g_{33}$	$g_{11}$	$g_{22}$	$g_{33}$
One-electron	$3.783 \times 10^{-3}$	$2.233 \times 10^{-3}$	$4.250 \times 10^{-5}$	$3.818 \times 10^{-3}$	$2.241 \times 10^{-3}$	$2.899 \times 10^{-5}$
Two-electron	$-1.431 \times 10^{-3}$	$-8.351 \times 10^{-4}$	$6.100 \times 10^{-5}$	$-1.446 \times 10^{-3}$	$-8.372 \times 10^{-4}$	$6.381 \times 10^{-5}$
Total	$2.352 \times 10^{-3}$	$1.398 \times 10^{-3}$	$1.035 \times 10^{-4}$	$2.372 \times 10^{-3}$	$1.404 \times 10^{-3}$	$9.280 \times 10^{-5}$
$g^{\text{total}}$	$g_{11}$	$g_{22}$	$g_{33}$	$g_{11}$	$g_{22}$	$g_{33}$
	2.00460	2.00365	2.00233	2.00462	2.00365	2.00232

The terms  $P_{pq}^{(\alpha+\beta),0b}$  and  $P_{pq}^{(\alpha-\beta),0b}$  are the total charge and net spin transition densities between the states 0 and b respectively. Equation 34 of reference is the fully coupled form of  $\Delta g_{rs}^{\text{OZ/SOC}}$  and was used to numerically calculate its tensor components. However, Eq.(3.69) is slightly simpler, yet also suitable to be used in the discussion below.

In molecules with high symmetry, only certain excitations that contribute to  $\Delta g_{rs}^{\text{OZ/SOC}}$  are allowed. The product of the irreducible representations appearing in the numerator of Eq.(3.69),  $\langle \psi_p | \ell_\mu | \psi_q \rangle$ , must be equal to the totally symmetric representation of the molecular point group. Alternatively,

$$\Gamma(\psi_p) \otimes \Gamma(\ell_\mu) \otimes \Gamma(\psi_q) = \Gamma_1. \quad (3.70)$$

This significantly reduces the number of allowed excitations and, in certain cases, full analysis of the contributions to  $\Delta g_{rs}^{\text{OZ/SOC}}$  is possible. However **DPPH•** has a  $C_1$  molecular point group,  $\Gamma(\psi_p) = \Gamma(\ell_\mu) = \Gamma(\psi_q) = \Gamma_1$ , and all transitions are allowed.

This results in a large number of excitations and it is impossible to practically analyze and comment on all their contributions to the nine tensor components. One is left with no alternative but to rely on the pure numerical results given in Table 2.

It is obvious from the excellent agreement between theory and experiment (within 251 ppm), in Tables 1 and 2, that the coupled perturbed Kohn Sham method, can reliably reproduce the **g** tensor components of large molecules such as **DPPH•**.

Examination of the data in Table 2 reveals that the  $\Delta g^{\text{RMC}}$  values are negative, while the  $\Delta g^{\text{GC}}$  and  $\Delta g^{\text{OZ/SOC}}$  values are positive. For the  $\Delta g_{11}$  and  $\Delta g_{22}$  components,  $\Delta g^{\text{GC}}$  and  $\Delta g^{\text{OZ/SOC}}$  are much larger than the  $\Delta g^{\text{RMC}}$  value, and increase the  $\Delta g_{11}^{\text{total}}$  and  $\Delta g_{22}^{\text{total}}$  values significantly. However, in the case of  $\Delta g_{33}$ ,  $\Delta g^{\text{RMC}} \approx \Delta g^{\text{GC}} + \Delta g^{\text{OZ/SOC}}$ , leading to  $\Delta g_{33}^{\text{total}}$  values that are very close to that of the free electron.

### 3.5 Effects of restricted rotations on the g tensor values

It is well known that the **g** tensor values are dependant on the geometry of the molecule. As discussed previously, the phenyl C and N<sub>2</sub> single bonds will allow their rings to rotate. However these phenyl ring rotations, as seen from Fig. 1(b), will be restricted due to steric hindrance. To assess the effect of these restricted rotations on the values of the **g** tensor, a series of computations were carried out. The dihedral angle formed between the N<sub>1</sub>, N<sub>2</sub>, C<sub>7</sub> and C<sub>8</sub> atoms ( $\varphi_{1278}$ ) was fixed at 0° and the remainder of the molecule was then allowed to geometry optimize to obtain the minimum energy conformation. This was followed by calculation of the **g** tensor components, and the total energy,  $E_{TOT}(\varphi_{1278})$  was noted. The dihedral angle,  $\varphi_{1278}$ , was then incremented by 5° and the entire process was repeated again. This continued for a total of 36 computations where  $\varphi_{1278}$  ranged between 0° and 175°. The probability that the molecule exists in a certain conformation with any specific dihedral angle,  $\varphi_{1278}$ , is, according to the Maxwell-Boltzman distribution, given by:

$$p(\varphi_{1278}) = \frac{\exp\left(-\frac{E_{TOT}(\varphi_{1278})}{kT}\right)}{\sum_{\varphi_{1278}=0}^{175} \exp\left(-\frac{E_{TOT}(\varphi_{1278})}{kT}\right)}. \quad (3.71)$$

From this probability, the averaged values of the diagonalized **g** tensor components,

$$\langle g_{ii} \rangle = \sum_{\varphi_{1278}=0}^{175} p(\varphi_{1278}) \cdot g_{ii}(\varphi_{1278}), \quad (3.72)$$

are then determined.

Figure 2 is a composite diagram depicting the **g** tensor and probabilities of occupation. The x-axis represents the dihedral angle,  $\varphi_{1278}$ . The left hand y-axis represents the principal **g** tensor values and the solid lines are the  $g_{11}$ ,  $g_{22}$ , and  $g_{33}$  as a function of angle. From this figure, it is seen that the  $g_{33}$  tensor component is the most sensitive to angle variations. Superimposed on the **g** tensor curves is the probability plot given by Eq. (3.71). It's values are given in the right hand side y-axis. The averaged values,

$\langle g_{11} \rangle$ ,  $\langle g_{22} \rangle$ ,  $\langle g_{33} \rangle$ , determined from Eq. (3.72), where  $T=303.18\text{K}$ , are represented by the three horizontal lines in the figure.

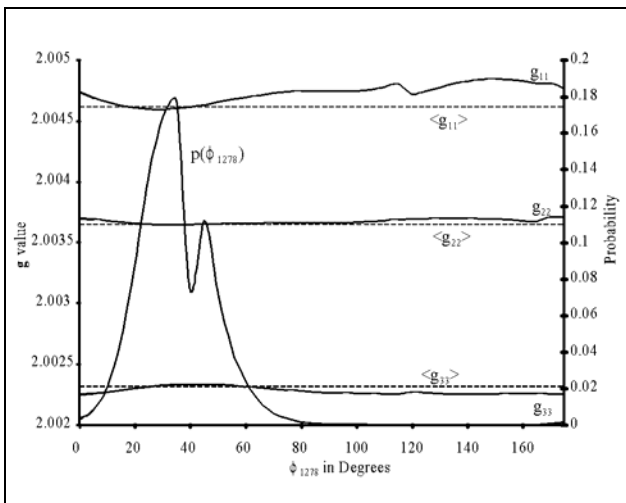


Fig. 2. Plot of the  $g$  tensor principal axes,  $g_{11}$ ,  $g_{22}$  and  $g_{33}$ , as a function of the phenyl ring rotation. Superimposed on the principal values is the probability that **DPPH**• exists in a given configuration. Finally the horizontal lines represent the averaged values, calculated from Eq. (3.72).

Table 3 compares the experimental, gas phase and averaged gas phase results. It also lists the  $\Delta g$  ppm values for the averaged and unaveraged calculations. It is quite clear that the effect of restricted rotational averaging is well within the experimental accuracy of 1ppt. In addition the largest difference between theory and experiment for the unaveraged values is 251 ppm for the  $g_{11}$  tensor component. Upon averaging, this already excellent agreement further improves to 185 ppm.

**Table 3. Effect of Weighted Averaging on the Computed Total  $g$  tensors**

	$g_{11}$	$g_{22}$	$g_{33}$	$\langle g \rangle$
Experimental	2.00435	2.00367	2.00245	2.00349
Gas Phase UB1LYP	2.004601	2.003648	2.002331	2.003526
$\Delta g(\text{ppm})$	251	22	119	36
Averaged Gas Phase UB1LYP	2.004620	2.003653	2.002318	2.003530
Averaged $\Delta g(\text{ppm})$	185	17	132	40

### 3.6 Summary

The **g** tensor components were computed, using UB1LYP and UPBE0 functionals, in the gas phase and in various solvents. Both functionals gave very similar results. All the calculated **g** tensors, whether in the gas phase, polar or nonpolar solvents, are in excellent agreement with experiment. This opens the field for further accurate and viable calculations of the spin Hamiltonian tensors for large organic radicals comparable to **DPPH•** (41 atoms). They, in turn, should help in the interpretation of the EPR and ENDOR spectra of this important class of molecules.

The **g** tensors were also investigated as the DPPH phenyl groups were rotated relative to the picryl ring. Their averaged principal values, according to the Maxwell-Boltzman distribution, at 303 K, marginally improve the already excellent agreement.

Solvent effects, whether polar or non-polar, are very well reproduced but quite small. On the other hand the nuclear hyperfine tensors are quite sensitive to the surrounding environment and internal rotations. Thus one may conclude that the EPR and ENDOR spectra will be predominantly influenced by the solvents and rotations via their nuclear **A** tensors. The results of such a study are a subject of a manuscript in preparation

## Reference List

1. Kolaczowski, S. V.; Cardin, J. T.; Budil, D. E. Some remarks on reported inconsistencies in the high-field EPR spectrum of DPPH. *Applied Magnetic Resonance* **1999**, *16* (2), 293-298.
2. Mattar, S. M. Minimum general requirements for equivalent atoms in a molecule. *Chemical Physics Letters* **1998**, *287* (5,6), 608-612.
3. Dalal, N. S.; Kennedy, D. E.; McDowell, C. A. ENDOR detection of conformational changes and internal rotations in organic stable free radicals in solution. *Chem. Phys. Lett.* **1975**, *30* (2), 186-189.
4. Mattar, S. M. Calculation of the <sup>1</sup>H, <sup>13</sup>C, <sup>14</sup>N and <sup>33</sup>S hyperfine tensors of the 1,3,2-dithiazol-2-yl radical using hybrid density functionals. *Chemical Physics Letters* **1999**, *300* (5,6), 545-552.
5. Improta, R.; Barone, V. Interplay of electronic, environmental, and vibrational effects in determining the hyperfine coupling constants of organic free radicals. *Chemical reviews* **2004**, *104* (3), 1231-1254.
6. Adamo, C.; Barone, V. Toward reliable adiabatic connection models free from adjustable parameters. *Chem. Phys. Lett.* **1997**, *274* (1,2,3), 242-250.
7. Patchkovskii, S.; Ziegler, T. Calculation of the EPR g-Tensors of High-Spin Radicals with Density Functional Theory. *J. Phys. Chem. A* **2001**, *105* (22), 5490-5497.
8. Neese, F. Prediction of electron paramagnetic resonance g values using coupled perturbed Hartree-Fock and Kohn-Sham theory. *Journal of Chemical Physics* **2001**, *115* (24), 11080-11096.
9. Engstrom, M.; Vahtras, O.; Agren, H. Hartree-Fock linear response calculations of g-tensors of substituted benzene radicals. *Chem. Phys.* **1999**, *243* (3), 263-271.
10. Ding, Z.; Gulla, A. F.; Budil, D. E. Ab initio calculations of electric field effects on the g-tensor of a nitroxide radical. *J. Chem. Phys.* **2001**, *115* (23), 10685-10693.
11. Bruna, P. J.; Grein, F. Comparing electron-spin g-tensor results of first-row radicals with those of higher rows. *Int. J. Quantum Chem.* **2000**, *77* (1), 324-335.
12. Malkina, O. L.; Vaara, J.; Schimmelpfennig, B.; Munzarova, M.; Malkin, V. G.; Kaupp, M. Density Functional Calculations of Electronic g-Tensors Using Spin-Orbit Pseudopotentials and Mean-Field All-Electron Spin-Orbit Operators  
*J. Am. Chem. Soc.* **2000**, *122* (38), 9206-9218.

13. Barone, V. Recent Advances in Density Functional Methods. **1995**.
14. Mattar, S. M. Role of the solvent in computing the 1,4-benzosemiquinone g-tensor by the coupled-perturbed Kohn-Sham hybrid density functional method. *Journal of Physical Chemistry B* **2004**, *108* (27), 9449-9455.
15. Mattar, S. M. g-Tensor calculations of bicyclic 1,3,2-dithiazolyl radicals using the coupled-perturbed Kohn-Sham UB1LYP and UPBE0 hybrid density functionals. *Chem. Phys. Lett.* **2005**, *405* (4-6), 382-388.
16. Mattar, S. M.; Sanford, J.; Goodfellow, A. D. g Tensor computation of the thiopheno-1,3,2-dithiazolyl radical by the coupled-perturbed Kohn-Sham hybrid density functional method. *Chem. Phys. Lett.* **2006**, *418* (1-3), 30-35.
17. Adamo, C.; Barone, V. Toward reliable density functional methods without adjustable parameters: the PBE0 model. *J. Chem. Phys.* **1999**, *110* (13), 6158-6170.
18. Cossi, M.; Scalmani, G.; Rega, N.; Barone, V. New developments in the polarizable continuum model for quantum mechanical and classical calculations on molecules in solution. *J. Chem. Phys.* **2002**, *117* (1), 43-54.
19. Barone, V.; Cossi, M.; Tomasi, J. A new definition of cavities for the computation of solvation free energies by the polarizable continuum model. *J. Chem. Phys.* **1997**, *107* (8), 3210-3221.
20. Klamt, A.; Jonas, V.; Burger, T.; Lohrenz, J. C. W. Refinement and Parametrization of COSMO-RS. *J. Phys. Chem. A* **1998**, *102* (26), 5074-5085.
21. Yodzis, P. P.; Koski, W. S. g-Tensor Anisotropy in Polycrystalline Diphenyl Picryl Hydrazyl. *The Journal of Chemical Physics* **1963**, *38* (9), 2313-2314.
22. Ryzhmanov, Y.; Yablokov, Y.; Kozyrev, B. M.; Matevosyan, R. O.; Stashkov, L. I. Electron paramagnetic resonance in meta-substituted a,a-diphenyl-b-picrylhydrazyls. *Doklady Akademii Nauk SSSR* **1964**, *156* (1), 106-109.
23. Chirkov, A. K.; Matevosyan, R. O. EPR determination of the principal values of the g-tensor of single crystals of a series of stable radicals. *Zh. Strukt. Khim.* **1970**, *11* (2), 258-263.
24. Gubanov, V. A.; Koryakov, V. I.; Chirkov, A. K. Anisotropic hyperfine interactions and the g-tensor in hydrazyl radicals. *Journal of Magnetic Resonance (1969-1992)* **1973**, *9* (2), 263-274.
25. Neese, F. Efficient and accurate approximations to the molecular spin-orbit coupling operator and their use in molecular g-tensor calculations. *Journal of Chemical Physics* **2005**, *122* (3), 34107.

## Appendix 1:

### ***A Concise Introduction to Hybrid Density Functional Theory***

#### **Historical Perspective of Quantum Mechanical Calculations.**

Quantum mechanical calculations, that predict total energies, electronic structure and molecular properties, may be classified into three categories. The first are *ab initio* calculations. They are "first principles" computations that are independent of any empirical parameters. The second are density functional theory (DFT) computations that are very similar in their methodology to *ab initio* techniques. However, DFT methods require a density functional that describes how the exchange and correlation energies of a molecule depend on the electron density. Furthermore, this density functional has additional parameters tailored to give optimal molecular energies. Depending on the choice of the density functional and its parameters it may yield results that are even better than high level *ab initio* computations. *Ab initio* and DFT methods give accurate electronic structures and molecular properties. However, they are expensive and limited to relatively small molecules.

Semi-empirical methods constitute the third class of computations. They make use of different parameters in their energy Hamiltonian for every atom with a particular atomic number. For example carbon and nitrogen have different parameters but sp<sup>2</sup> and sp<sup>3</sup> hybridized carbons would have the same parameters.

Although the approximations used in semi-empirical methods are more drastic than those made in *ab initio* and DFT techniques, this is offset by the accuracy of the experimental semi-empirical parameters used. In some cases, semi-empirical methods may be more accurate than low level *ab initio* calculations. In general, semi-empirical methods are more appropriate in dealing with large molecules where trends are important and numerical accuracy of the calculations is not paramount.

#### **The Restricted Form of the Hartree-Fock Equations**

The starting point of all quantum mechanical computations is to find the eigenvalues,  $E$ , and eigenfunctions,  $\Psi$ , of the wave equation

$$H(x, y, z, ict)\Psi_{rel}(x, y, z, ict) = E\Psi_{rel}(x, y, z, ict) \quad (\text{A.73})$$

Here the (x,y,z,ict) notation means that the relativistic Hamiltonian,  $H$ , is a function of the four component space-time coordinates x, y, z, and ict for every particle of the system. When dealing with molecules containing light atoms, this relativistic Dirac equation may be approximated by the conventional three component Schrodinger Equation

$$H(x, y, z)\Psi(x, y, z) = E\Psi(x, y, z) \quad (\text{A.74})$$

For convenience the functionality (x,y,z) is omitted and (A.74) is rewritten as

$$H\Psi = E\Psi \quad (\text{A.75})$$

In the above three equations, the H operator represents the different types of energy (kinetic, nuclear-nuclear, electron-nuclear, electron-electron.....etc) of all particles of the chemical system under consideration. The eigenfunctions,  $E_n$ , are the resulting total energy of the system in a particular quantum state, n. The eigenvectors,  $\Psi$ , are the multi-particle wave function of the system.

To define the H operator one needs to know the atomic numbers and spatial coordinates of all the nuclei and electrons. In addition, the total charge, total spin (S), spin multiplicity (2S+1), and spin state ( $M_S$ ) must also be defined.

The nuclear and electronic components of the Schrodinger equation, may be separated by invoking the Born-Oppenheimer approximation. The electronic component takes the form

$$H_{elec}\Psi_{elec} = E_{elec}\Psi_{elec} \quad (\text{A.76})$$

In this case,  $H_{elec}$  is the Hamiltonian of all electron interactions and  $\Psi_{elec}$  is the corresponding electronic "many body" wave function. To solve this equation one assumes that the all the electrons are independent of one another and consequently their energies are additive. Thus the  $H_{elec}$  becomes the sum of "one electron" effective Hamiltonians,  $H_i^{eff}$

$$H_{elec} = \sum_{i=1}^N H_i^{eff}, \quad (\text{A.77})$$

where N is the number of electrons. Since electrons are identical Fermions then

$$H_{elec} = NH_i^{eff}, \quad (\text{A.78})$$

and the Schrodinger equation in (A.76) is reduced to

$$H^{eff} \psi_{elec} = \varepsilon_{elec} \psi_{elec} \quad (A.79)$$

and can be solved numerically. The lower case "one electron" eigenfunctions,  $\psi_{elec}$ , are known as "one-electron" molecular orbitals and the resulting eigenvalues,  $\varepsilon_n$ , are called the orbital energies. The total probability of finding an electron in space is related to a specific quantized molecular orbital,  $\psi_i$ , via the relation

$$\iiint \psi_i^*(x, y, z) \psi_i(x, y, z) dx dy dz = \int |\psi_i(x, y, z)|^2 d\tau = 1 \quad (A.80)$$

The electrons of the system in its ground state populate the molecular orbitals of lowest energies first. A maximum of two electrons can occupy every orbital. When the number of electrons is even, in most cases, each molecular orbital contains either two electrons or is empty. This leads to a closed shell system. When the number of electrons is odd then at least one orbital must be singly occupied. The total electronic spin is  $S=1/2$  and the corresponding spin multiplicity is  $2S+1 = 2$  or a doublet state. This is the situation for the free radicals studied here.

The most convenient way to solve the eigenvalue problem of (A.79) is to represent  $\psi_{elec}$  as an expansion of known functions centered around the nuclei. These functions are known as atomic orbitals,  $\phi$ , and thus

$$\psi_i = \sum_{\nu} C_{\nu i} \phi_{\nu} \quad (A.81)$$

where the summation runs over the number of nuclei. Therefore (A.79) becomes

$$H^{eff} \sum_{\nu} C_{\nu i} \phi_{\nu} = \varepsilon_{elec} \sum_{\nu} C_{\nu i} \phi_{\nu} \quad (A.82)$$

and by multiplying from the left by  $\phi_{\mu}$  and rearranging one obtains

$$\sum_{\nu} C_{\nu i} \int \phi_{\mu} H^{eff} \phi_{\nu} d\tau = \varepsilon_{elec} \sum_{\nu} C_{\nu i} \int \phi_{\mu} \phi_{\nu} d\tau \quad (A.83)$$

This last equation takes the form

$$\sum_{\nu} C_{\nu i} H_{\mu\nu}^{eff} = \varepsilon_{elec} \sum_{\nu} C_{\nu i} S_{\mu\nu}. \quad (A.84)$$

or

$$H^{eff} C = \varepsilon_{elec} S C. \quad (A.85)$$

In (A.85) the overlap integral matrix elements,  $S_{\mu\nu}$ , are given by

$$S_{\mu\nu} = \int \varphi_{\mu} \varphi_{\nu} d\tau \quad (\text{A.86})$$

and are the overlap between atomic orbitals situated on the  $\mu$  and  $\nu$  nuclei. If there is no overlap between these nuclei then  $S_{\mu\nu} = 0$ . On the other hand, if the overlap is complete then  $S_{\mu\nu} = 1$ . Hence the S matrix is positive and definite. Similarly  $H_{\mu\nu}^{\text{eff}}$  is

$$H_{\mu\nu}^{\text{eff}} = \int \varphi_{\mu} H^{\text{eff}} \varphi_{\nu} d\tau. \quad (\text{A.87})$$

The matrix Schrodinger equation of (A.85) is a compound eigenvalue problem because it contains two matrix operators  $\mathbf{H}^{\text{eff}}$  and  $\mathbf{S}$ . Since  $\mathbf{S}$  is a positive definite symmetric matrix, it can first be diagonalized by a similarity transformation to yield the diagonal matrix  $\mathbf{s}$ . The  $\mathbf{s}^{-1/2}$  is then easily calculated taking the inverse square root of its diagonal elements  $s_{ii}$ . The non-diagonal form,  $\mathbf{S}^{-1/2}$ , is then obtained by the reverse similarity transformation and is used to diagonalize the Hamiltonian in Eq.(A.85). The end result, that yields the energy, is

$$\left(\frac{1}{\mathbf{S}^2\mathbf{C}}\right)^{\dagger} \left(\frac{1}{\mathbf{S}^2}\mathbf{H}\mathbf{S}^{\frac{1}{2}}\right) \left(\frac{1}{\mathbf{S}^2\mathbf{C}}\right) = \varepsilon \quad (\text{A.88})$$

Since electrons obey Fermi-Dirac statistics, their wave functions should be antisymmetric when a pair of electrons are exchanged in space. To fulfill this condition, Slater suggested that the multi-electron wave functions (spin orbitals), which written as a product of a spin part,  $\sigma = \alpha, \beta$ , and spatial component,  $\psi_i$ , must be expressed as determinants. For example the N electron wave function takes the normalized (spin restricted) form,

$$\chi(r_1, r_2, \dots, r_N) = \frac{1}{\sqrt{N!}} \begin{vmatrix} \psi_1(1)\alpha & \psi_1(2)\alpha & \psi_1(3)\alpha & \dots & \psi_1(N)\alpha \\ \psi_1(1)\beta & \psi_1(2)\beta & \psi_1(3)\beta & \dots & \psi_1(N)\beta \\ \psi_2(1)\alpha & \psi_2(2)\alpha & \psi_2(3)\alpha & \dots & \psi_2(N)\alpha \\ \psi_2(1)\beta & \psi_2(2)\beta & \psi_2(3)\beta & \dots & \psi_2(N)\beta \\ \dots & \dots & \dots & \dots & \dots \\ \psi_N(1)\beta & \psi_N(2)\beta & \psi_N(3)\beta & \dots & \psi_N(N)\beta \end{vmatrix} \quad (\text{A.89})$$

To properly apply the independent Hamiltonian approximation, all the Hamiltonian operators must be a function of a single electron or "one electron" operators. In general the electronic Hamiltonian operator for N electrons and M nuclei, in atomic units, is

$$\begin{aligned}
H_{elec} &= H_{kin} + H_{eN} + H_{ee} \\
&= \frac{-1}{2} \sum_{i=1}^N \nabla^2 - \sum_{i=1}^N \sum_{A=1}^M \frac{Z_A}{r_{iA}} + \sum_{i=1}^N \sum_{j>i}^N \frac{1}{r_{ij}}
\end{aligned} \tag{A.90}$$

The first term is the sum of the kinetic energies of the N electrons while the second term is the sum of the Coulomb attraction between all N electrons with M nuclei. They are the sum of a series of one electron operators. The last operator in Eq.(A.90) represents the electron-electron repulsions. Every one of its terms depends on the distance between the electrons i and j. It is a sum of "two electron" operators and causes the electrons to be dependent on one another. It impedes us from applying Eqs. (A.77)- (A.88) that solve the one-electron Schrodinger equation.

To overcome this problem, we make use of the Hartree-Fock approximation where  $H_{ee}$  is replaced by a sum of N operators. Each operator represents the energy of one-electron due to the average effects of the remaining N-1 electrons. This modified  $H_{elec}$  operator is now called the Fock operator,  $F$ . According to Roothan, we may now proceed to solve the Schrodinger equation starting from an equation equivalent to Eq. (A.85).

$$FC = \epsilon_{elec} SC. \tag{A.91}$$

Where the Fock matrix elements,  $F_{\mu\nu}$ , are equivalent to those of Eq.(A.87) and take the form

$$\begin{aligned}
F_{\mu\nu} &= \frac{-1}{2} \int \varphi_{\mu} \nabla^2 \varphi_{\nu} d\tau - \sum_{A=1}^M \int \varphi_{\mu} \frac{Z_A}{r_A} \varphi_{\nu} d\tau + \sum_{\lambda, \sigma=1}^N \sum_{i=1}^{occup} C_{\mu i} C_{\nu i} \\
&\times \left[ \int \varphi_{\mu}(r) \varphi_{\nu}(r) \frac{1}{r_{rs}} \varphi_{\lambda}(s) \varphi_{\sigma}(s) d\tau_r d\tau_s - \int \varphi_{\mu}(r) \varphi_{\lambda}(r) \frac{1}{r_{rs}} \varphi_{\nu}(s) \varphi_{\sigma}(s) d\tau_r d\tau_s \right]
\end{aligned} \tag{A.92}$$

When the two electron integrals, involving the electrons r and s, are abbreviated using the "chemist's notation" we obtain

$$F_{\mu\nu} = \frac{-1}{2} \int \varphi_{\mu} \nabla^2 \varphi_{\nu} d\tau - \sum_{A=1}^M \int \varphi_{\mu} \frac{Z_A}{r_A} \varphi_{\nu} d\tau + \sum_{\lambda, \sigma=1}^N \sum_{i=1}^{occup} C_{\mu i} C_{\nu i} \left[ (\mu\nu | \lambda\sigma) - \frac{1}{2} (\mu\lambda | \nu\sigma) \right] \tag{A.93}$$

The  $(\mu\nu|\lambda\sigma)$  two electron integrals in Eq. (A.93) are the Coulomb repulsion between the electron clouds of the two electrons. The exchange integrals  $(\mu\lambda|\nu\sigma)$  are a direct result of using the wave functions in the form of Slater determinants.

The  $F_{\mu\nu}$  matrix elements depend on the  $C_{\mu i}$  and  $C_{\nu i}$  coefficients. Thus to generate the eigenvalue problem in Eq. (A.91) an initial guess of the  $C_{\mu i}$  and  $C_{\nu i}$  coefficients (wave function) is done. Eq. (A.91) is then solved in a fashion identical to that going from Eq. (A.85) to (A.88). This yields a set of eigenvalues or molecular orbital energies,  $\varepsilon_n$ , and the corresponding molecular orbitals with new  $C_{\mu i}$  and  $C_{\nu i}$  coefficients. These coefficients are used once more to determine a new Fock matrix,  $F_{\mu\nu}$ , which is used to construct a new eigenvalue equation similar to that of (A.92). The process is repeated until the difference between the new total energy of the molecule and the one from the previous iteration is less than a certain defined value. This iterative process is known as the Self-Consistent-Field (SCF) procedure. Another convergence criterion for stopping the SCF procedure is that the electronic density,

$$P_{\mu\nu} = \sum_{i=1}^{occup} C_{\mu i} C_{\nu i} \quad (\text{A.94})$$

from one iteration to the next is less than a certain defined value.

## The Unrestricted Form of the Hartree-Fock Equations

The previous description has assumed that the spatial components of the  $i$ th electron,  $\psi_i$ , of the  $\psi_i\alpha$  and  $\psi_i\beta$  spin orbitals are the same. This is known as the spin restricted Hartree-Fock (RHF) formalism. However, to obtain the correct spin density at a given point in space or compute the isotropic hyperfine coupling constants, a spin unrestricted formalism (UHF) must be used. In a spin unrestricted wave function, the spatial components of  $\psi_i\alpha$  and  $\psi_i\beta$  are not necessarily the same. Thus one may express them as  $\psi_i^\alpha\alpha$  and  $\psi_i^\beta\beta$ .

Pople and Nesbet have derived the unrestricted Hartree-Fock equations. As a result, the wave functions come in pairs as:

$$\psi_i^\alpha = \sum_\nu C_{\nu i}^\alpha \phi_\nu \quad (\text{A.95})$$

for the  $\alpha$  spin and

$$\psi_i^\beta = \sum_\nu C_{\nu i}^\beta \phi_\nu \quad (\text{A.96})$$

for the  $\beta$  spin. The corresponding Fock matrices take the form

$$F_{\mu\nu}^\alpha = H_{\mu\nu}^\alpha + \sum_{\lambda,\sigma=1}^N \left[ P_{\lambda\sigma}^T (\mu\nu|\lambda\sigma) - \frac{1}{2} P_{\lambda\sigma}^\alpha (\mu\lambda|\nu\sigma) \right] \quad (\text{A.97})$$

and

$$F_{\mu\nu}^\beta = H_{\mu\nu}^\beta + \sum_{\lambda,\sigma=1}^N \left[ P_{\lambda\sigma}^T (\mu\nu|\lambda\sigma) - \frac{1}{2} P_{\lambda\sigma}^\beta (\mu\lambda|\nu\sigma) \right] \quad (\text{A.98})$$

Here  $H_{\mu\nu}^\alpha$  and  $H_{\mu\nu}^\beta$  are the one-electron operators for the  $\alpha$  and  $\beta$  spins respectively. The densities in the previous two equations are defined as

$$P_{\mu\nu}^T = P_{\mu\nu}^\alpha + P_{\mu\nu}^\beta = \sum_{i=1}^{occup} C_{\mu i}^\alpha C_{\nu i}^\alpha + \sum_{i=1}^{occup} C_{\mu i}^\beta C_{\nu i}^\beta \quad (\text{A.99})$$

At this stage it is worth noting that the difference between  $P_{\mu\nu}^\alpha$  and  $P_{\mu\nu}^\beta$  at a certain nucleus is proportional to the isotropic hyperfine coupling constant,  $a^{\text{iso}}$ , of that nucleus. It is very important to realize that  $F_{\mu\nu}^\alpha$  and  $F_{\mu\nu}^\beta$  are coupled to one another because they are functions of the total density,  $P_{\mu\nu}^T$ , in Eqs. (A.97) and (A.98).

This procedure ultimately leads to two coupled Hartree-Fock eigenvalue equations similar to Eq. (A.91). They are:

$$F^\alpha C^\alpha = \epsilon_{\text{elec}}^\alpha S C^\alpha \quad (\text{A.100})$$

and

$$F^\beta C^\beta = \epsilon_{\text{elec}}^\beta S C^\beta. \quad (\text{A.101})$$

Finally these two equations are solved by the above mentioned SCF procedure to yield the molecular orbitals and their energies. Once this is accomplished, the total energy and any other molecular property may then be computed.

## 2. The Basic Principles of Hybrid Density Functional Techniques

Hybrid density functional (HDF) computations have become extremely popular in the last few years. They are now the preferred form of routine quantum mechanical calculations in most laboratories. The methods are popular and yield results that are very accurate.

As presented in the previous section, during the procedure of an electronic structure quantum mechanical computation one attempts to find the eigenvalues,  $E_{elec}$ , and eigenvectors,  $\Psi_{elec}$ , of the non-relativistic Schrödinger equation

$$H_{elec} \Psi_{elec} = E_{elec} \Psi_{elec} \quad (\text{A.102})$$

The electron density at a particular point in space,  $r_1$ , therefore takes the form

$$\rho(r_1) = \int |\Psi_{elec}(r_1, r_2, r_3, \dots, r_N)|^2 dr_2 dr_3 \dots dr_N \quad (\text{A.103})$$

The integration over the variables  $dr_2, dr_3, \dots, dr_N$  in Eq. (A.103) simplifies the expression for the electron density since it becomes only a function of  $r_1$ . As a result, molecular quantum mechanical computations may be greatly simplified if  $\rho(r_1)$  can be used instead of  $\Psi_{elec}(r_1, r_2, r_3, \dots, r_N)$ . Hohenberg and Kohn proposed that the energy,  $E_{elec}$ , depends only on  $\rho(r_1)$  and E may be written as:

$$E = E[\rho]. \quad (\text{A.104})$$

However this dependency is a complicated unknown function of the electron density (called a functional).

Later Kohn and Sham formulated a procedure for solving the Schrödinger equation using Eq.(A.104). The resulting equations are very similar to those used in the Hartree-Fock procedure. The very close similarity between these equations made it possible to use the Hartree-Fock computer codes, developed over the years, to perform density functional calculations without too many changes.

Just as in the case of Hartree-Fock theory, there exists a corresponding "restricted" version of the Roothan equations leading to restricted density functional methods. Similarly there are "unrestricted" density functional techniques that solve

equations equivalent to the those of Pople and Nesbet. A discussion of the more general unrestricted form of density functional theory will be given below.

In a fashion similar to Hartree-Fock theory, basis functions are introduced and the corresponding wavefunctions, known as the Kohn-Sham orbitals, are [2]

$$\psi_i^\alpha = \sum_v C_{vi}^\alpha \varphi_i \quad (\text{A.105})$$

for the  $\alpha$  spin and

$$\psi_i^\beta = \sum_v C_{vi}^\beta \varphi_i \quad (\text{A.106})$$

for the  $\beta$  spin. From the coefficients of Eqs. (A.105) and (A.106) the corresponding spin density matrices may be obtained

$$P_{\mu\nu}^\alpha = \sum_{i=1}^{occup} C_{\mu i}^\alpha C_{\nu i}^\alpha \equiv \rho^\alpha \quad (\text{A.107})$$

and

$$P_{\mu\nu}^\beta = \sum_{i=1}^{occup} C_{\mu i}^\beta C_{\nu i}^\beta \equiv \rho^\beta. \quad (\text{A.108})$$

The total electron density is simply the sum of Eqs. (A.107) and (A.108).

$$P_{\mu\nu}^T = P_{\mu\nu}^\alpha + P_{\mu\nu}^\beta. \quad (\text{A.109})$$

The main difference between the Kohn Sham orbitals in Eqs. (A.105) and (A.106) and the Hartree-Fock orbitals is that they are solutions to the Kohn-Sham equations, which in principle, have an exact electron density leading to exact total energies [2].

From the Pople-Nesbet equations, of the previous section where the  $\mu\nu$ th Fock matrix elements of the  $\alpha$  and  $\beta$  spins are:

$$F_{\mu\nu}^\alpha = H_{\mu\nu}^\alpha + \sum_{\lambda\sigma} \left\{ P_{\lambda\sigma}^T (\mu\nu|\lambda\sigma) - P_{\lambda\sigma}^\alpha (\mu\lambda|\nu\sigma) \right\} \quad (\text{A.110})$$

and

$$F_{\mu\nu}^\beta = H_{\mu\nu}^\beta + \sum_{\lambda\sigma} \left\{ P_{\lambda\sigma}^T (\mu\nu|\lambda\sigma) - P_{\lambda\sigma}^\beta (\mu\lambda|\nu\sigma) \right\} \quad (\text{A.111})$$

The Kohn-Sham equations leave the Coulomb energy terms,  $P_{\lambda\sigma}^T (\mu\nu|\lambda\sigma)$ , unchanged but replace the exchange energy terms,  $P_{\lambda\sigma}^{\alpha,\beta} (\mu\lambda|\nu\sigma)$ , by the exchange correlations energy functionals,  $F^{XC}$ , to give [2]

$$F_{\mu\nu}^{\alpha} = H_{\mu\nu}^{\alpha} + \sum_{\lambda\sigma} P_{\lambda\sigma}^T (\mu\nu|\lambda\sigma) + F_{\mu\nu}^{XC\alpha} \quad (\text{A.112})$$

and

$$F_{\mu\nu}^{\beta} = H_{\mu\nu}^{\beta} + \sum_{\lambda\sigma} P_{\lambda\sigma}^T (\mu\nu|\lambda\sigma) + F_{\mu\nu}^{XC\beta} \quad (\text{A.113})$$

These equations are solved, by the self-consistent-field (SCF) procedure in exactly the same way as the Pople-Nesbet equations. The resulting energy, where  $E_{XC}$  is the exchange-correlation energy becomes:

$$E = \sum_{\mu\nu} P_{\mu\nu} H_{\mu\nu} + \frac{1}{2} \sum_{\mu\nu} \sum_{\lambda\sigma} P_{\mu\nu} P_{\lambda\sigma} (\mu\nu|\lambda\sigma) + E_{XC} \quad (\text{A.114})$$

The  $E_{XC}$  and  $F^{XC}$  are related to one another via the exchange-correlation energy density per unit volume,  $f$ . It is a function of both  $\alpha$  and  $\beta$  spin electron densities. In fact

$$E_{XC} = \int f(\rho^{\alpha}, \rho^{\beta}) d\tau, \quad (\text{A.115})$$

$$F_{\mu\nu}^{XC\alpha} = \int \left( \frac{\partial f(\rho^{\alpha}, \rho^{\beta})}{\partial \rho^{\alpha}} \right) \varphi_{\mu} \varphi_{\nu} d\tau \quad (\text{A.116})$$

and

$$F_{\mu\nu}^{XC\beta} = \int \left( \frac{\partial f(\rho^{\alpha}, \rho^{\beta})}{\partial \rho^{\beta}} \right) \varphi_{\mu} \varphi_{\nu} d\tau \quad (\text{A.117})$$

From the above treatment it is seen that the Kohn-Sham procedure avoids the complexity of post Hartree-Fock procedures such as configuration interaction. The correlation energy is obtained from an effective one-electron exchange-correlation term given in Eqs. (A.116) and (A.117).

Historically the first exchange energy functional was proposed by Slater at MIT and was based on the model of a uniform homogenous electron gas. It did not contain any electron-electron correlation energy terms [3]

$$f(\rho^{\alpha}, \rho^{\beta}) = -\frac{9}{4} \alpha \left( \frac{3}{4\pi} \right)^{1/3} \left[ (\rho^{\alpha})^{4/3} + (\rho^{\beta})^{4/3} \right]. \quad (\text{A.118})$$

leading to

$$F_{\mu\nu}^{XC\alpha} = -3\alpha \left( \frac{3}{4\pi} \right)^{1/3} \int (\rho^{\alpha})^{1/3} \varphi_{\mu} \varphi_{\nu} d\tau. \quad (\text{A.119})$$

and

$$F_{\mu\nu}^{XC\beta} = -3\alpha \left( \frac{3}{4\pi} \right)^{1/3} \int (\rho^\beta)^{1/3} \varphi_\mu \varphi_\nu d\tau. \quad (\text{A.120})$$

This is known as the local spin density (LSD) approximation.

While Eqs. (A.119) - (A.120) represent the exchange in a simple analytic form, there is no known simple form for the uniform electron gas correlation energy. LSD functionals that include electron-electron correlation terms are based on numerical Monte Carlo simulations of the homogeneous electron gas such as those obtained by Ceperly, Alder, Perdew and Zunger [4]. These numerical results are then fit to formulae which are, in turn, added as extra terms in Eqs.(A.119) - (A.120) as has been done by Vosko, Wilk and Nussair [5].

In reality molecular electron densities are higher near a nucleus and lower in the interatomic regions. They asymptotically go to zero at infinite distances. This density change implies that it has a gradient. Improved functionals that take this fact into account are called *generalized gradient functionals* [6].

$$F_{\mu\nu}^{XC\alpha} = \int \left\{ \frac{\partial f(\rho^\alpha, \rho^\beta)}{\partial \rho^\alpha} \varphi_\mu \varphi_\nu + \left[ 2 \frac{\partial f(\rho^\alpha, \rho^\beta)}{\partial \gamma_{\alpha\alpha}} \nabla \rho^\alpha + \frac{\partial f(\rho^\alpha, \rho^\beta)}{\partial \gamma_{\alpha\beta}} \nabla \rho^\beta \right] \cdot \nabla (\varphi_\mu \varphi_\nu) \right\} d\tau. \quad (\text{A.121})$$

In the last equation  $\nabla$  is the gradient operator and  $\gamma_{ij} = \nabla \rho^i \cdot \nabla \rho^j$ . As similar equation exists for the  $\beta$  spin.

## **Hybrid Density Functionals**

If a percentage of the original Hartree-Fock exchange term is included in Eq. (A.121) better agreement between theory and experiment is obtained. This modified functional is known as a hybrid density functional (HDF). The most popular HDF is the B3LYP functional. This functional's exchange component consists of a 20% Hartree-Fock exchange term, an 8% Slater exchange term [3], given by Eqs. (A.119) - (A.120) and a 72% Becke-88 gradient exchange term [7] that takes the form

$$E_{xc} = -\frac{9}{4} \alpha \left( \frac{3}{4\pi} \right)^{1/3} \int \left[ (\rho^\alpha)^{1/3} + (\rho^\beta)^{1/3} \right] g(x) d\tau. \quad (\text{A.122})$$

with

$$g(x) = 1 + \frac{2}{3} \left( \frac{4\pi}{3} \right)^{1/3} \frac{bx^2}{\left[ 1 + 6bx \frac{3}{2} \left( \frac{3}{4\pi} \right)^{1/3} \sinh(x) \right]}, \quad (\text{A.123})$$

and  $b = 0.0042$ . The correlation component consists of 19% Vosko-Wilk-Nussair functional [61] and the rest is the Lee-Yang-Parr functional [8].

The percentages in the B3LYP functional were determined empirically by comparing the 42 ionization potentials, 56 atomization energies, 10 atomic energies and 8 proton affinities of a standard set of molecules known as the G1 set. HDF codes are now available commercially such as Gaussian 03. In summary the B3LYP functional may be written in the condensed form as:

$$E_{XC}^{\text{B3LYP}} = 0.08E_X^{\text{LSD}} + 0.2E_X^{\text{HF}} + 0.72E_X^{\text{Becke}} + 0.19E_C^{\text{VWN}} + 0.81E_C^{\text{LYP}}.$$

Purdue, Ernzerhof and Burke [9], using Gorling-Levy perturbation theory [10] suggested that the empirical exchange coefficients be replaced by a ratio of 1/4. Adamo and Barone [11] have implemented this non-empirical functional which takes the form

$$E_{XC}^{\text{B1LYP}} = 0.75(E_X^{\text{LSD}} + E_X^{\text{Becke}}) + 0.25E_X^{\text{HF}} + E_C^{\text{LYP}}.$$

It is found to give superior results when compared to the B3LYP functional and has been used in our laboratories to compute the electronic structure, optimal geometries and hyperfine coupling constants of a variety of open shell free radicals.

## References

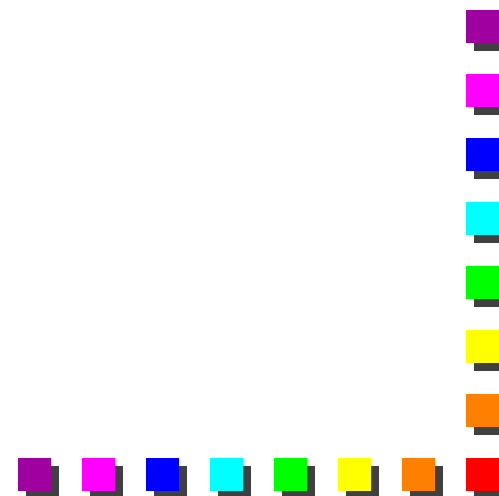
- [1] P. Hohenberg and W. Kohn, *Physical Review B*, 136, (1964) B864.
- [2] W. Kohn and L. J. Sham, *Physical Review*, 140, (1965) A1133.
- [3] J. C. Slater, *Quantum Theory of Molecules and Solids, Vol 4: The Self Consistent Field Theory for Moles and Solids* (McGraw Hill, New York, 1974).
- [4] J. P. Perdew and A. Zunger, *Phys. Rev. B*, 23, (1981) 5048.
- [5] S. H. Vosko, L. Wilk and M. Nussair, *Can. J. Phys.* 58, (1980) 1200.
- [6,7] A. D. Becke, *Phys. Rev. A*, 38, (1988) 3098.
- [8] C. Lee, W. Yang and R. G. Parr, *Phys. Rev. B*, 37, (1988) 785.
- [9] J. P. Perdew, M. Ernzerhof and K. Burke, *J. Chem. Phys.*, 105, (1996) 9982.
- [10] A. Gorling and M. Levy, *Phys. Rev. B*, 47, (1993) 13105.
- [11] C. Adamo, V. Barone, *Chem. Phys. Lett.* 274 (1997) 242.

# Introduction to Calculations of $g$ and $A$ Values for Transition Metal Complexes

*48th Rocky Mountain Conference on Analytical Chemistry*

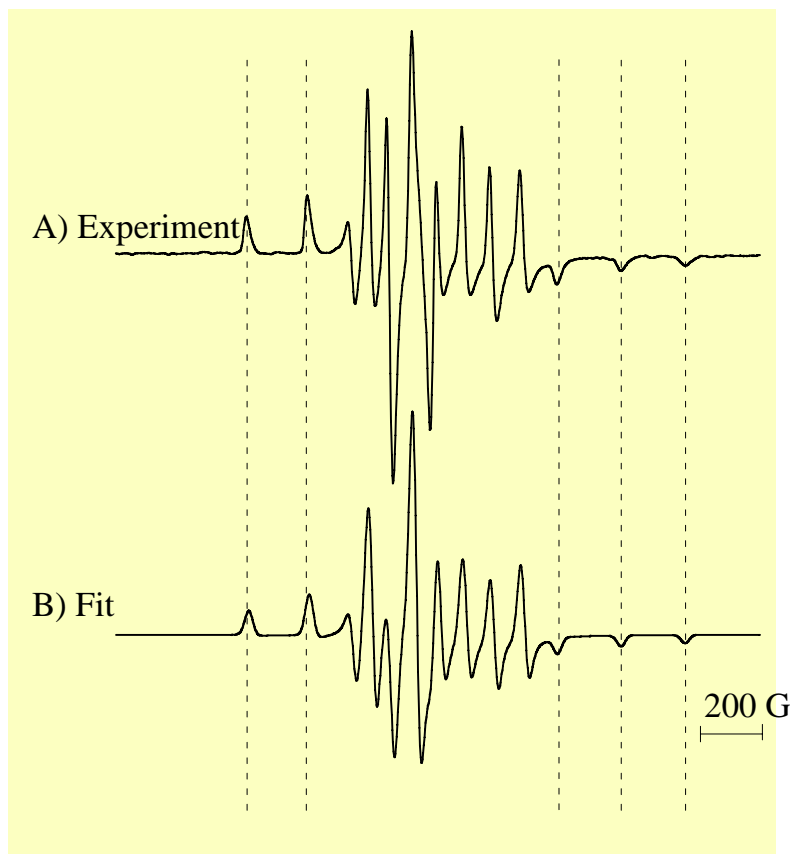
*EPR Workshop: Computation of EPR Parameters and Spectra*  
*July 23, 2006*

**Sarah C. Larsen**  
**Department of Chemistry**  
**University of Iowa**



# Motivation for Quantum Chemical Calculations from an Experimentalist's Perspective

EPR Spectrum of Hydrated  $\text{VO}^{2+}$ - ZSM-5



$\text{V}^{4+}$ ,  $d^1$ ;  $S=1/2$ ,  $I=7/2$

To obtain the EPR parameters, the experimental EPR spectra are fitted using a least squares fitting routine. The fits are quite good as can be seen from this example of hydrated  $\text{VO}^{2+}$ - ZSM-5.<sup>1</sup>

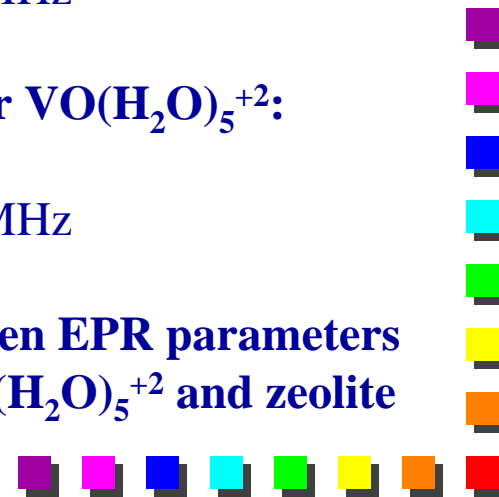
**Experimental values from fitted spectrum<sup>1</sup>:**

$$g_{\parallel}=1.933, g_{\perp}=1.997$$
$$A_{\parallel}=549 \text{ MHz} \quad A_{\perp}=218 \text{ MHz}$$

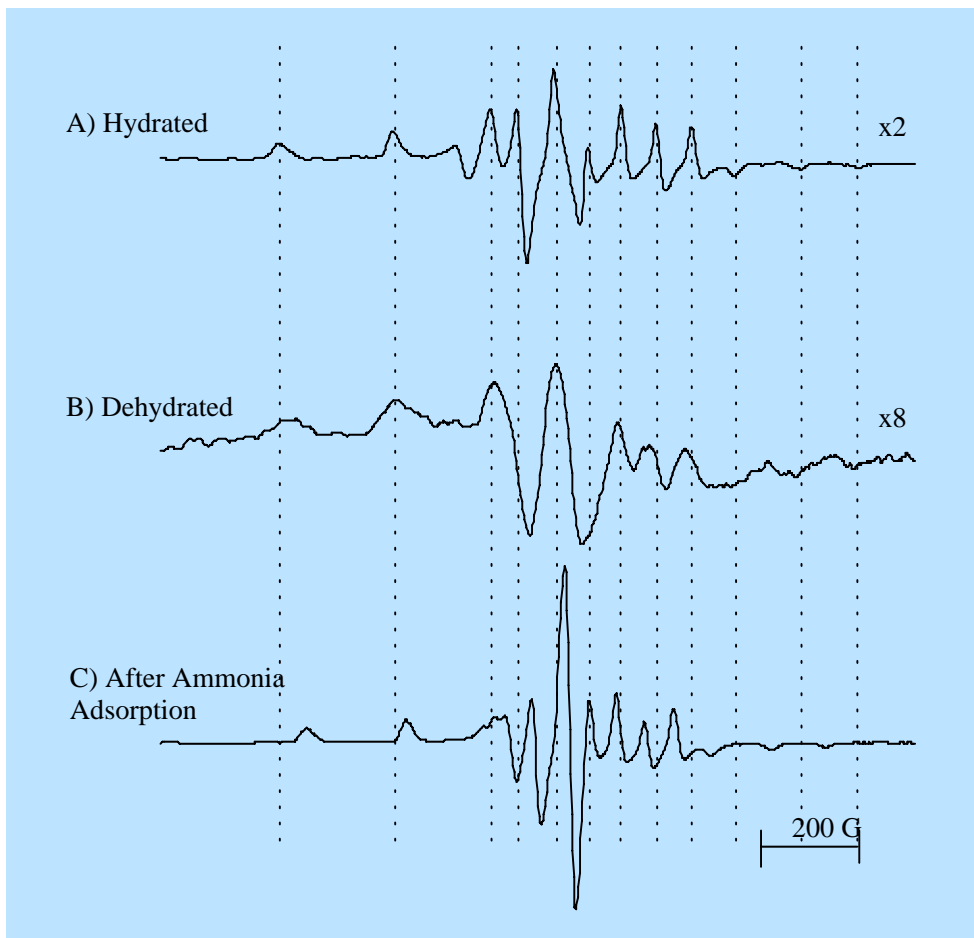
**From the literature<sup>2</sup> for  $\text{VO}(\text{H}_2\text{O})_5^{+2}$ :**

$$g_{\parallel}=1.933, g_{\perp}=1.978$$
$$A_{\parallel}=547 \text{ MHz} \quad A_{\perp}=212 \text{ MHz}$$

**Good agreement between EPR parameters for model complex  $\text{VO}(\text{H}_2\text{O})_5^{+2}$  and zeolite complex.**



# Obtaining Structural Interpretations of Spectral Changes



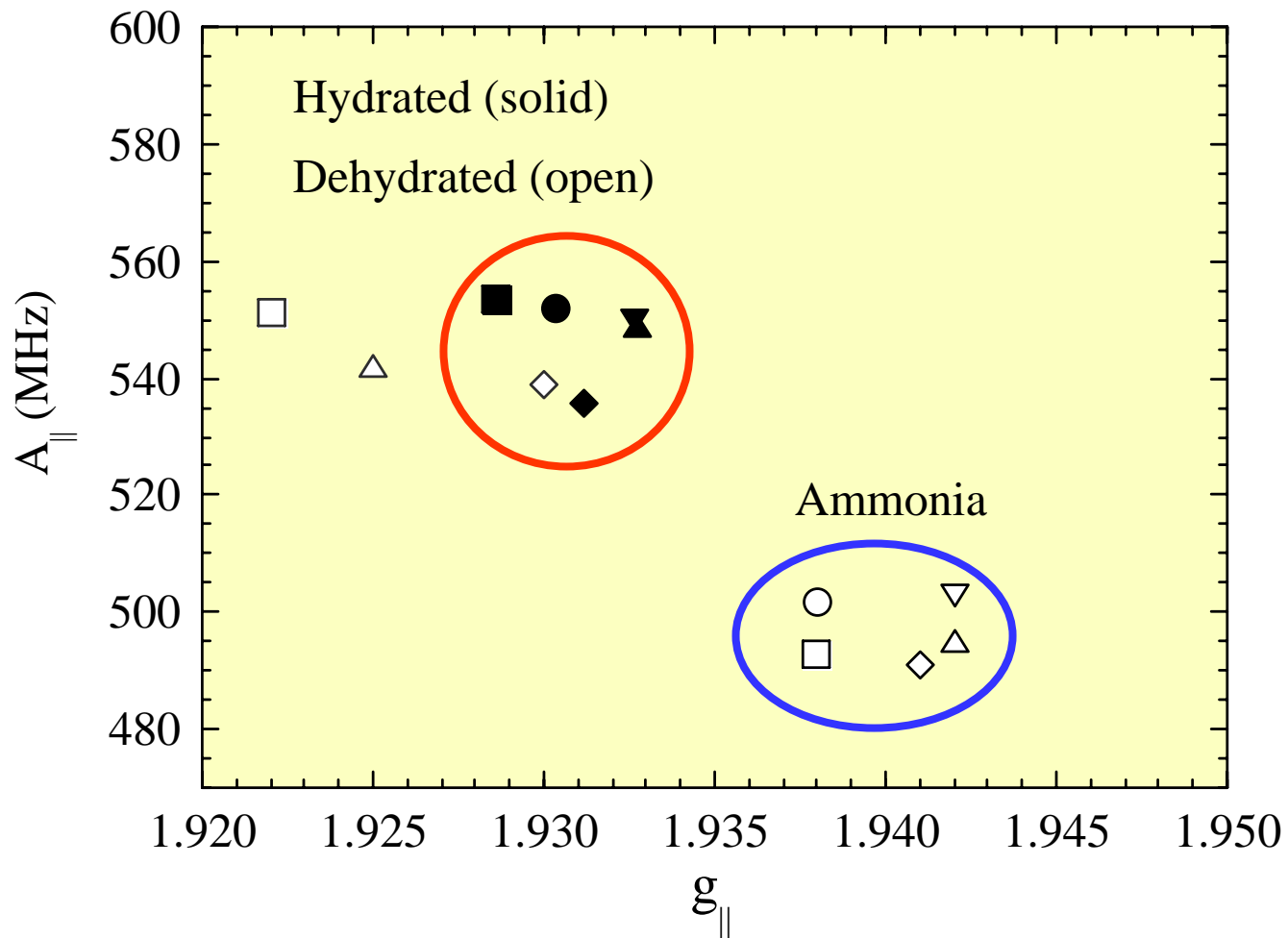
Changes are observed in the EPR spectra of the zeolite complexes when the sample is dehydrated or ammonia is adsorbed.

**How can we interpret these EPR spectral changes (in  $g$  and  $A$  values) in terms of structural changes in the vanadium complexes in the zeolites?**

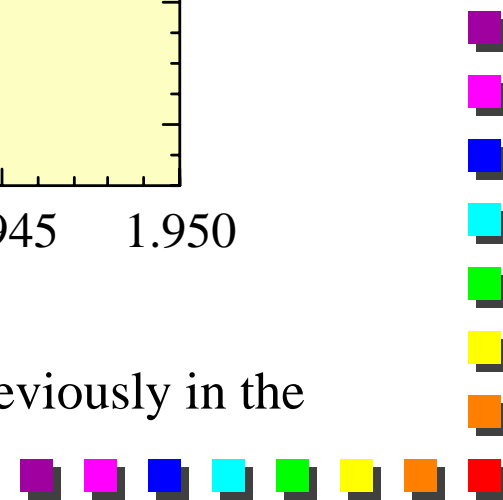
**For a protein complex, how can we use EPR experimental data to determine the structure at the active site?**



# Correlation Plot of Experimental Values



These systematic trends in  $g_{\parallel}$  and  $A_{\parallel}$  have been defined previously in the literature through model complex studies.<sup>1,2</sup>



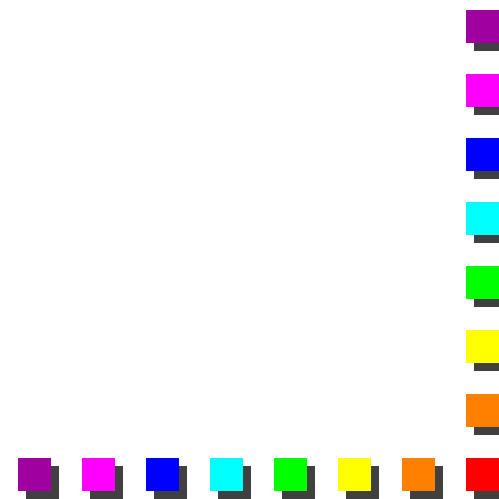
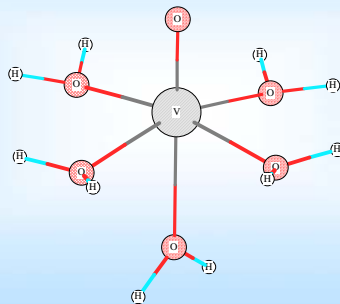
# Experimental EPR Spectrum



Spectral Simulations  
 $g, A$

Quantum Calculations  
 $g, A$

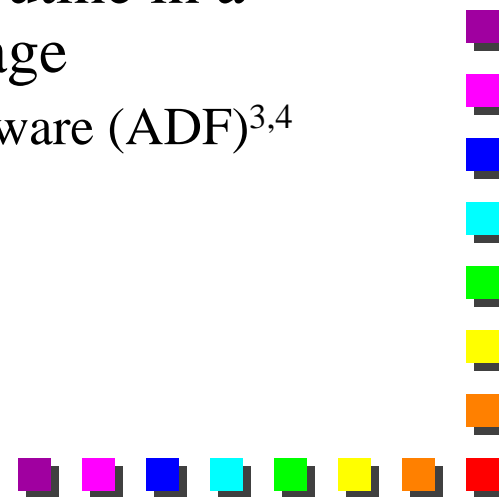
# Electronic and Geometric Structure



# DFT Calculations of Transition Metal $g$ and $A$ Values

## Getting Started.....

- ✓ Structure of transition metal complex
  - ✓ Input coordinates from single crystal structure
  - ✓ Geometry optimization of transition metal complex of interest
  - ✓ **Calculations of EPR parameters are only as good as the input structure of the complex.**
- ✓ Calculation of  $g$  and  $A$  using EPR subroutine in a commercial or academic software package
  - ✓ Amsterdam Density Functional Theory software (ADF)<sup>3,4</sup>
  - ✓ Gaussian<sup>5</sup>
  - ✓ ORCA (Neese)<sup>6</sup>
  - ✓ MagRespect (Kaupp)<sup>7</sup>



# Comparison of Software Packages

## v **ADF (commercial)**<sup>3,4</sup>

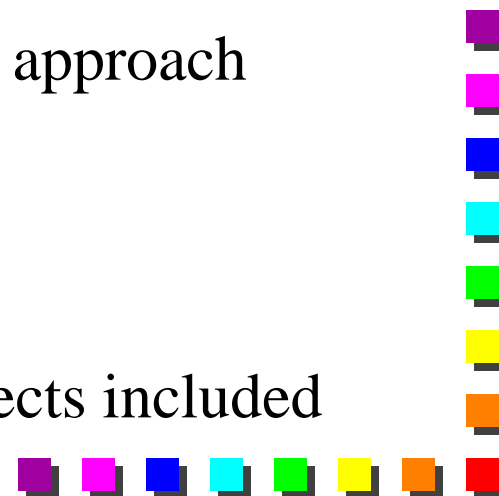
- v Slater type orbitals (STO's)
- v Unrestricted calculations, relativistic effects included
- v Hybrid functionals not available for EPR calculations

## v **Gaussian (commercial)**<sup>5</sup>

- v Gaussian type orbitals (GTO's)
- v Unrestricted calculations, nonrelativistic approach
  - v Only a-value calculations
- v Many hybrid functionals available

## v **ORCA<sup>6</sup>, MagRespect<sup>7</sup> (academic)**

- v Unrestricted calculations, relativistic effects included



# DFT Calculations of EPR Parameters for Transition Metals

## Structure for input to DFT calculation:

- Geometry Optimization
- Input Crystal Structure

*Is this structure an accurate representation of the transition metal complex?*

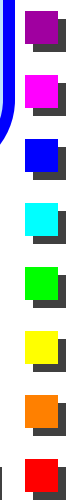
## Transition metal g-value calculation

- Need relativistic method (ADF, ORCA, MagRespect)
- Choice of functional, basis set

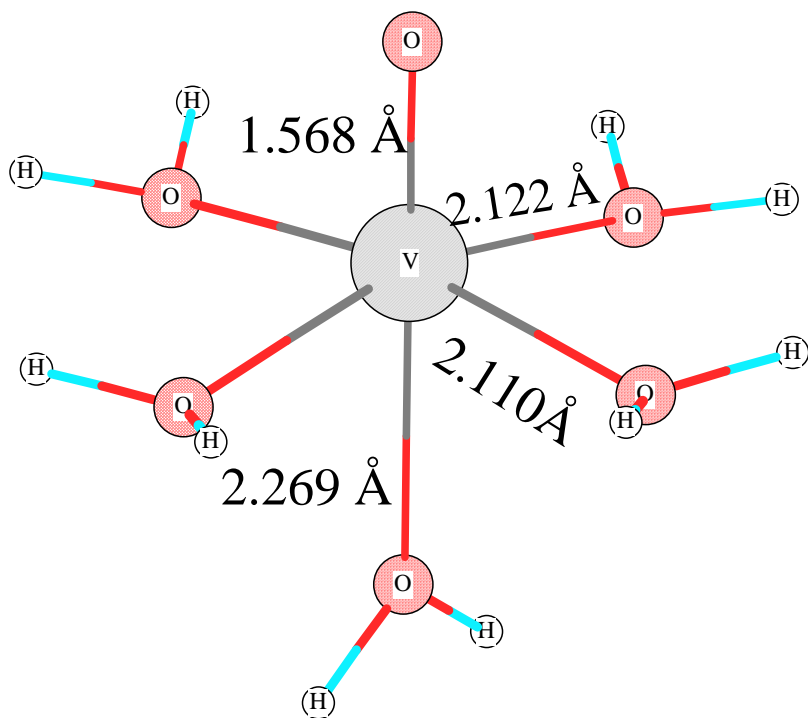
## Transition Metal A-value calculation

- Relativistic method (ADF, ORCA, MagRespect)-fewer functionals
- Non-relativistic method, wide range of hybrid functionals (Gaussian)
- Choice of basis set critical

- Are the calculated results basis set or functional dependent?*
- Do the calculated results deviate systematically from experiment?*



# Example: $\text{VO}(\text{H}_2\text{O})_5^{2+}$ Geometry Optimization



Experimental Distances<sup>8</sup> for  $\text{VOSO}_4 \cdot 5\text{H}_2\text{O}$ :

$R_{\text{V}=\text{O}}$ : 1.591 Å

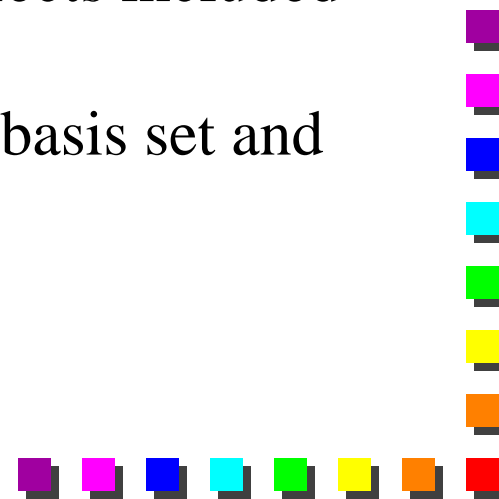
$R_{\text{V}-\text{L}(\text{eq})}$ : 2.035, 2.038, 2.048, 1.983

$R_{\text{V}-\text{L}(\text{ax})}$ : 2.223

**Symmetry restrictions included-** structure may not represent energy minimum

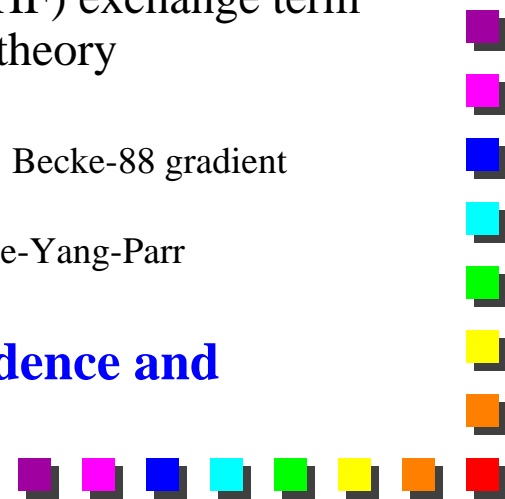
**Gas phase structure-** no solvent effects included

Choice of basis set and functional



# Choice of Basis Sets and Density Functionals

- ✓ Basis sets:
  - ✓ Dependent on software package
  - ✓ Specialized basis sets may be required for hyperfine calculations - need flexibility in core region beyond that required for geometry optimization
- ✓ Functionals (see Appendix I for more detail):
  - ✓ Generalized gradient functionals
    - ✓ For example, BP86
  - ✓ Hybrid Density Functionals include a Hartree Fock (HF) exchange term leading to better agreement between experiment and theory
    - ✓ Most popular, B3LYP
      - ✓ Exchange: 20% HF exchange, 8% Slater exchange, 72% Becke-88 gradient exchange term
      - ✓ Correlation: 19% Vosko-Wilk-Nussair (VSN), rest is Lee-Yang-Parr
- ✓ **Always good practice to examine basis set dependence and functional dependence for calculations**



# DFT Calculations of Vanadium g and A-values

- ✓ Different computational methods have been implemented
  - ✓ **g-values**
    - ✓ ADF
      - ✓ SO+SR UKS (spin orbit coupling and scalar relativistic spin unrestricted open shell Kohn Sham)
    - ✓ Gaussian- none
    - ✓ ORCA- coupled perturbed SCF calculations
  - ✓ **A-values**
    - ✓ ADF-
      - ✓ SO+SR UKS (new addition to ADF- preferred method)
        - ✓ Spin orbit with collinear approximation
        - ✓ Spin unrestricted open shell Kohn Sham (UKS)
      - ✓ SR UKS (scalar relativistic spin unrestricted open shell Kohn Sham)
        - ✓ Can be used if spin orbit effects are negligible
    - ✓ Gaussian
      - ✓ No relativistic effects, many functionals available
    - ✓ ORCA, MagREspect
      - ✓ Relativistic, unrestricted



## Comparison of Results:

### Table 1: g-value DFT calculations for $\text{VO}(\text{H}_2\text{O})_5^{2+}$

	$g_{xx}$	$g_{yy}$	$g_{zz}$	Program	Method	Ref
Exp.	1.978	1.978	1.933	-	-	2
DFT	1.9852	1.9852	1.9495	ORCA	B3LYP, coupled perturbed SCF equations (Neese, 2001)	9
DFT	1.986	1.986	1.930	ADF	BP86, SO+SR ROKS	1

DFT methods have been utilized to calculate the g-tensor for  $[\text{VO}(\text{H}_2\text{O})_5]^{2+}$ . DFT results for g-value calculations for  $[\text{VO}(\text{H}_2\text{O})_5]^{2+}$  are included in the table, along with experimental g-values from the literature for comparison. Reasonably good agreement between the experimental and DFT calculated g-values is observed.



# Definitions

- Two interactions contribute to the vanadium hyperfine coupling tensor: an isotropic or Fermi contact interaction,  $A_{\text{iso}}$ , and an anisotropic or dipolar hyperfine interaction,  $A_{\text{D}}$ .
- $A_{\text{iso}}$  and  $A_{\text{D}}$  can be calculated from the principal values of the  $A$ -tensor using the following equations:

$$A_{\text{iso}} = (A_{11} + A_{22} + A_{33})/3$$

$$A_{\text{D},x} = A_{11} - A_{\text{iso}}$$

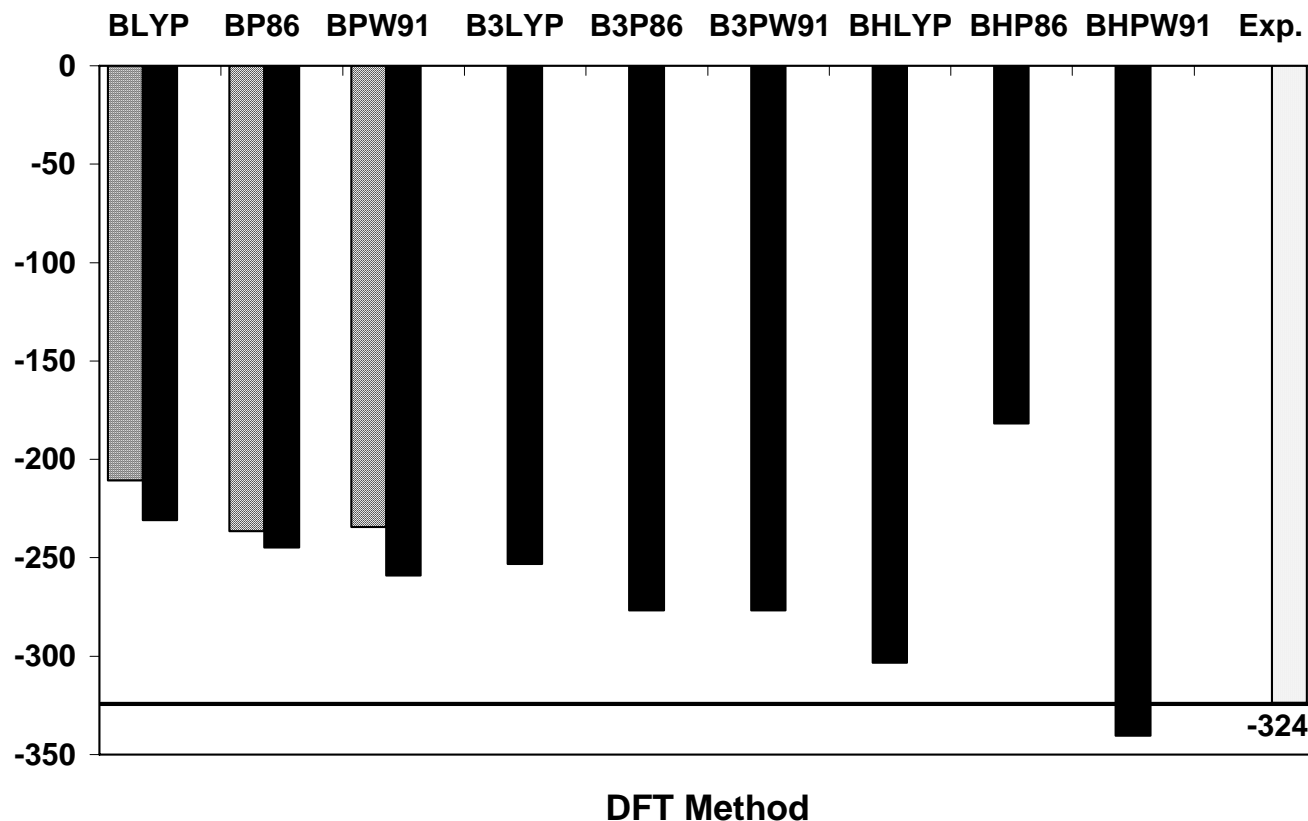
$$A_{\text{D},y} = A_{22} - A_{\text{iso}}$$

$$A_{\text{D},z} = A_{33} - A_{\text{iso}}$$

- The isotropic hyperfine interaction,  $A_{\text{iso}}$ , is related to the spin density at the magnetic nucleus, and therefore inclusion of spin polarization effects is particularly important for accurate calculations of  $A_{\text{iso}}$ .



# DFT Calculations of $A_{iso}$ for $[VO(H_2O)_5]^{2+}$

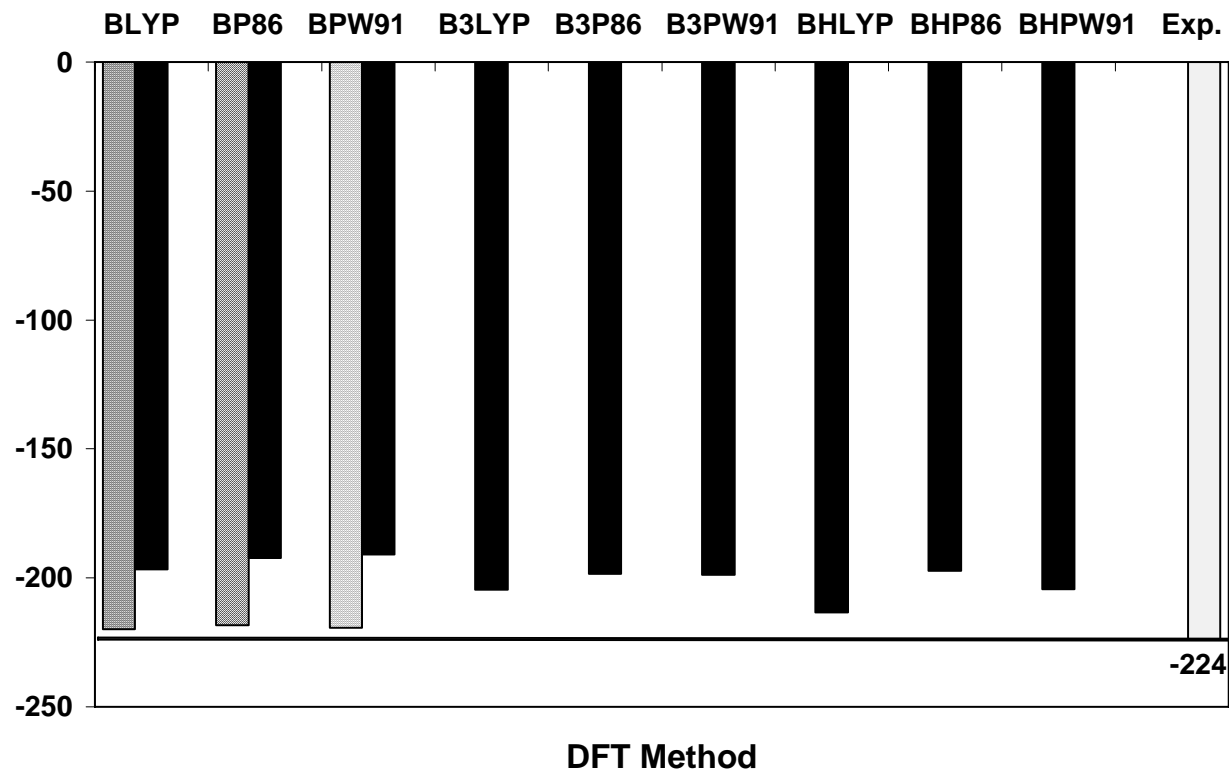


Comparison of ADF (hatched) and G98 (solid) calculations<sup>11</sup>:

- Same functional- similar results
- Overall, hybrid functionals perform best

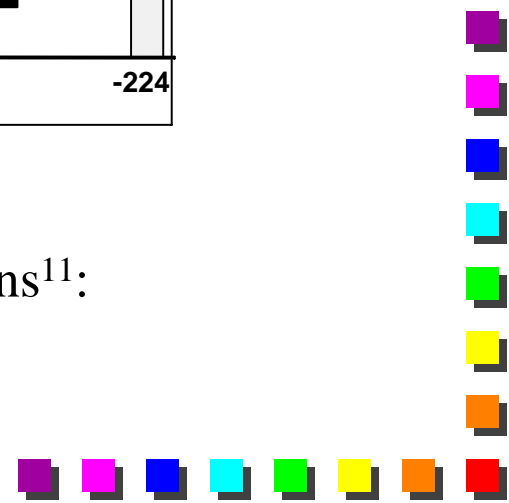


# DFT Calculations of $A_D$ for $[VO(H_2O)_5]^{2+}$



Comparison of ADF (hatched) and G98 (solid) calculations<sup>11</sup>:

- Same functional- similar results
- Less dependent on method than  $A_{iso}$  calculations

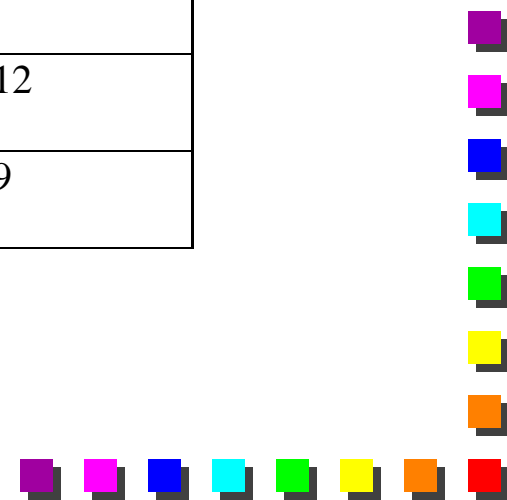


## Comparison of Results:

### Table 2: A-value<sup>a</sup> calculations for VO(H<sub>2</sub>O)<sub>5</sub><sup>2+</sup>

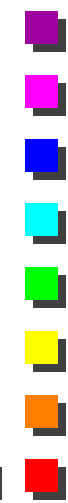
	<b>A<sub>iso</sub></b>	<b>A<sub>D,x</sub></b>	<b>A<sub>D,y</sub></b>	<b>A<sub>D,z</sub></b>	<b>Method</b>	<b>Ref</b>
Exp.	-324	112	112	-224	-	10
DFT	-246	95	96	-192	Gaussian, BP86	11
DFT	-236	89	90	-180	ADF, BP86, SRUKS	11
DFT	-304	97	98	-198	Gaussian, B3PW91	11
DFT	-268	96	105	-201	ORCA, B3LYP	12
DFT	-249	91	101	-193	ORCA, BP86	12
DFT	-293	103	103	-207	ORCA B3LYP	9

<sup>a</sup>All A-values are given in MHz



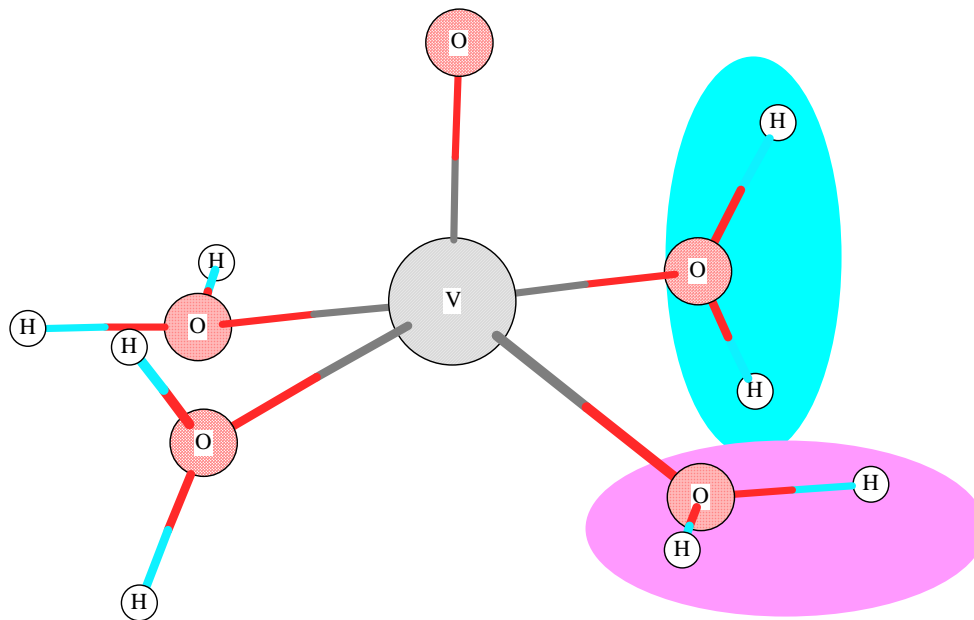
# Summary of DFT A-Value Calculations for $\text{VO}(\text{H}_2\text{O})_5^{2+}$

- ✓ The vanadium isotropic hyperfine coupling constant calculated with ADF or Gaussian and the BP86 functional systematically underestimates the experimental value by approximately 80 MHz.
- ✓ The hybrid functionals, such as BHPW91 and B3PW91, incorporate Hartree-Fock exchange, and provide more accurate vanadium hyperfine coupling tensors relative to the GGA functionals.
  - ✓ As shown in Table 2, the vanadium isotropic hyperfine coupling constant calculated with the hybrid functional B3PW91 is -304 MHz, which only deviates by 20 MHz from the experimental value.
- ✓ DFT calculated vanadium isotropic coupling constants from other research groups are also presented in the table for comparison, with the realization that some of the variability of results is due to the fact that all groups did not use the same structural coordinates for  $[\text{VO}(\text{H}_2\text{O})_5]^{2+}$ .
- ✓ For  $\text{VO}^{2+}$  systems, with small spin orbit coupling contributions, the nonrelativistic DFT calculations provide very good accuracy for isotropic hyperfine coupling constants with hybrid functionals. Currently, hybrid functionals cannot be used in relativistic calculations with ADF, thus limiting the accuracy of these calculations. The implications for transition metals with significant spin orbit coupling such as  $\text{Cu}^{2+}$  are much greater.



# Ligand Hyperfine Coupling Constants:

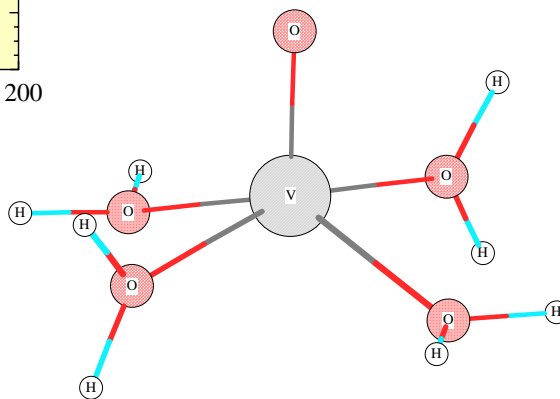
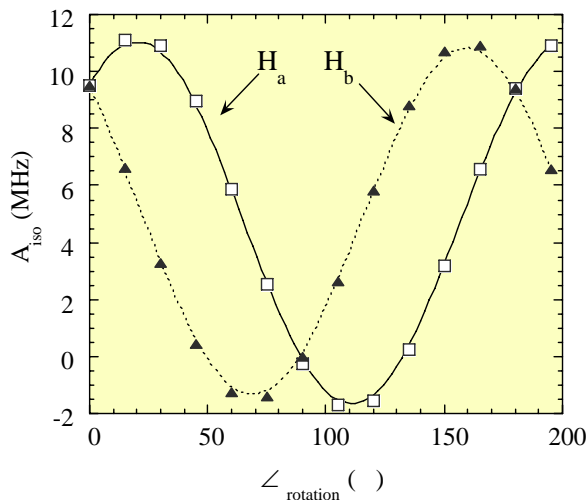
## Calculated Proton Hyperfine Coupling Constants<sup>13</sup> in $\text{VO}(\text{H}_2\text{O})_4^{2+}$



Proton hyperfine coupling constants vary depending on orientation of the water molecule.



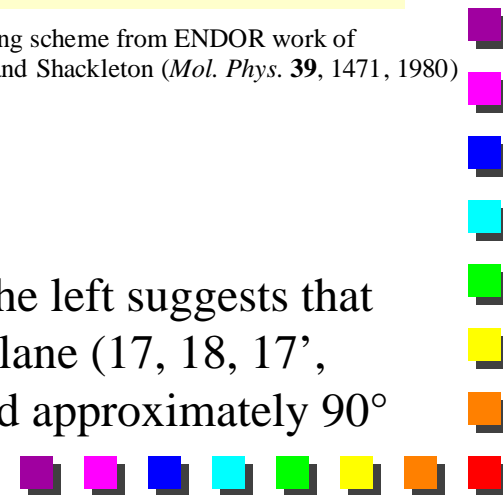
# Comparison of Calculated Proton Hyperfine Coupling Constants<sup>9</sup> with Single Crystal ENDOR Data<sup>10</sup>



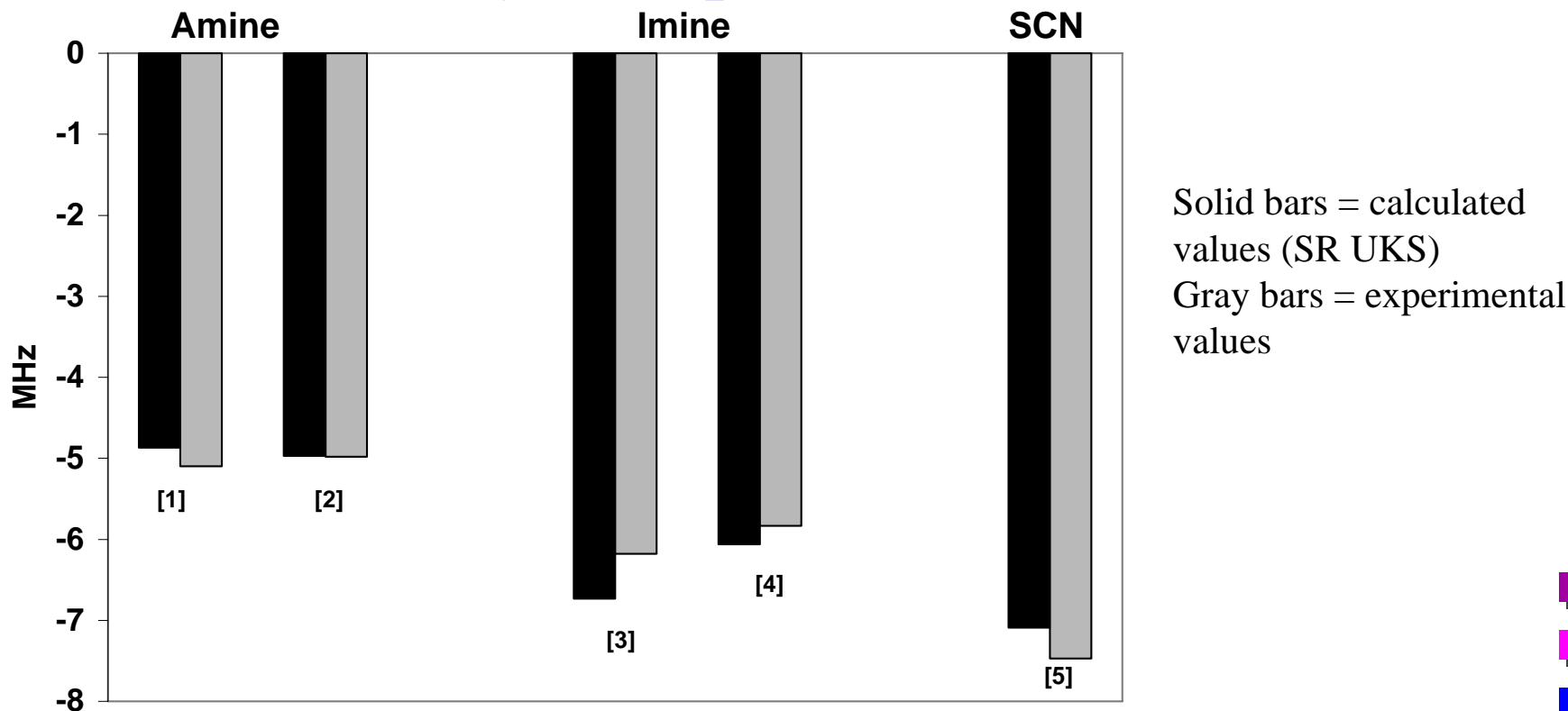
Proton Number <sup>a</sup>	$A_{iso}$ / MHz
17	-0.39
18	4.08
17'	-0.05
18'	4.57
19	8.67
20	7.14
19'	7.73
20'	6.96

<sup>a</sup> Numbering scheme from ENDOR work of Atherton and Shackleton (*Mol. Phys.* **39**, 1471, 1980)

Proton ENDOR data (table above)<sup>14</sup> interpreted using the graph at the left suggests that two water molecules are oriented approximately in the equatorial plane (17, 18, 17', 18') and the other two water molecules (19, 20, 19', 20') are rotated approximately 90° relative to the equatorial plane.



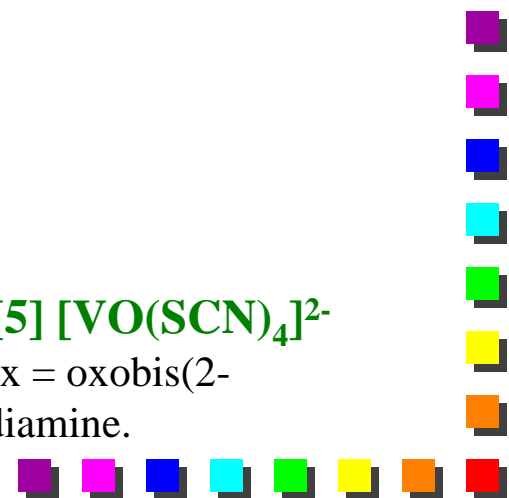
# Calculated Nitrogen $A_{iso}$ Values for Selected Vanadyl Complexes<sup>15</sup> (ADF, BP86)



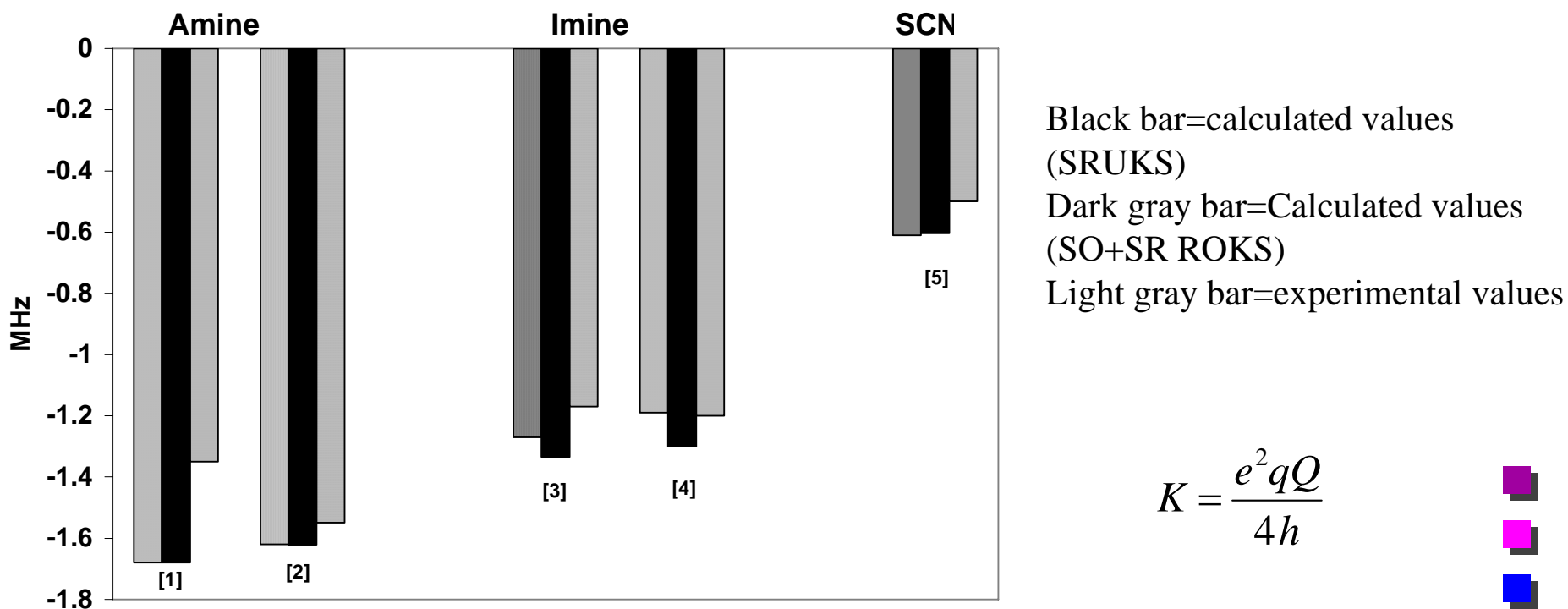
Complexes investigated include:

[1]VO(gly)<sub>2</sub>, [2]VO(edda), [3]VO(meox)<sub>2</sub>, [4]VO(salen), and [5] [VO(SCN)<sub>4</sub>]<sup>2-</sup>

where gly-glycinate, H<sub>2</sub>edda = ethylenediamine-N,N'-diacetic acid, meox = oxobis(2-methylquinolim-8-olato), and H<sub>2</sub>salen = N,N'-bis(salicylidene)ethylenediamine.



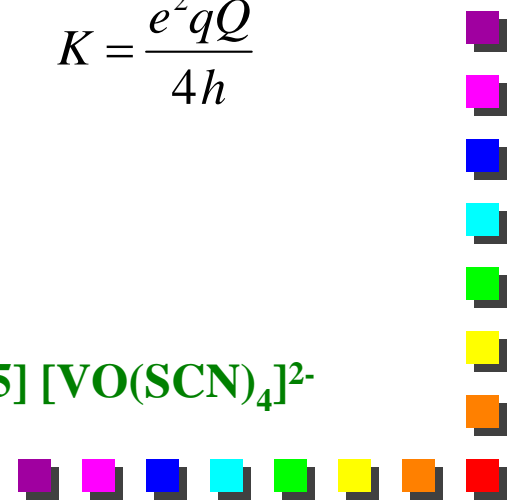
# Calculated Nitrogen $Q_{11}$ (or 3K) Values for Selected Vanadyl Complexes<sup>15</sup> (ADF, BP86)



$$K = \frac{e^2 q Q}{4h}$$

Complexes investigated include:

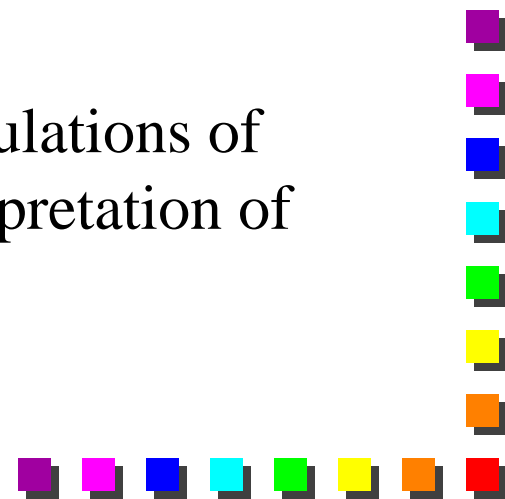
[1]VO(gly)<sub>2</sub>, [2]VO(edda), [3]VO(meox)<sub>2</sub>, [4]VO(salen), and [5] [VO(SCN)<sub>4</sub>]<sup>2-</sup>



## Summary of Results:

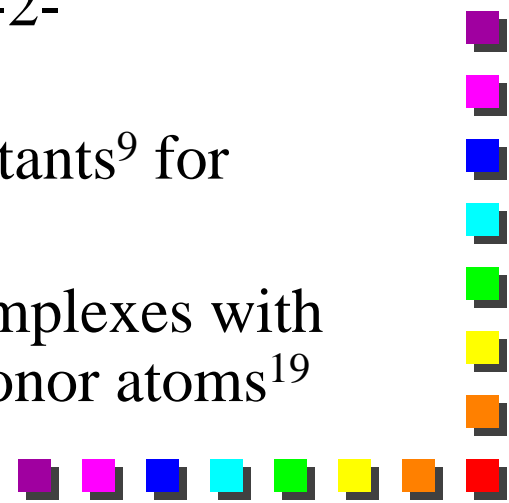
### Ligand Coupling Constants (HCC, QCC)

- ✓ Better quantitative agreement can be obtained for DFT calculations of ligand A-values in vanadyl complexes relative to the transition metal hyperfine coupling constants.
- ✓ Less sensitive to choice of functional
- ✓ Good agreement also observed for calculated ligand quadrupole coupling constants
- ✓ Many promising applications for DFT calculations of ligand coupling constants to assist the interpretation of pulsed EPR and ENDOR experiments.



## Other Selected DFT Studies of Vanadyl Complexes in the Literature:

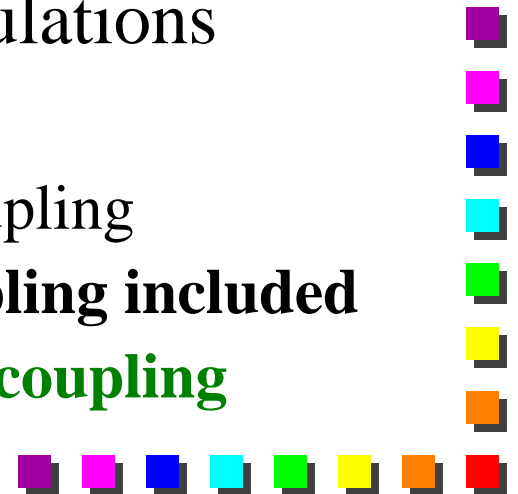
- ✓ Calculated hyperfine coupling constants of vanadyl complexes with Schiff bases<sup>16</sup>
- ✓ Calculations of the effect of the orientation of an imidazole ligand in a vanadyl complex on the vanadium hyperfine coupling constant.<sup>17</sup>
- ✓ Vanadyl complexes of Hcapca ((N-{2-(2-pyridylmethylene(amino)phenyl]pyridine}-2-carboxamide))<sup>18</sup>
- ✓ Calculation of <sup>17</sup>O hyperfine coupling constants<sup>9</sup> for V(H<sub>2</sub>O)<sub>5</sub><sup>2+</sup>
- ✓ Calculation of <sup>31</sup>P HCC's for vanadium complexes with tridentate bisphenol ligands with various donor atoms<sup>19</sup>



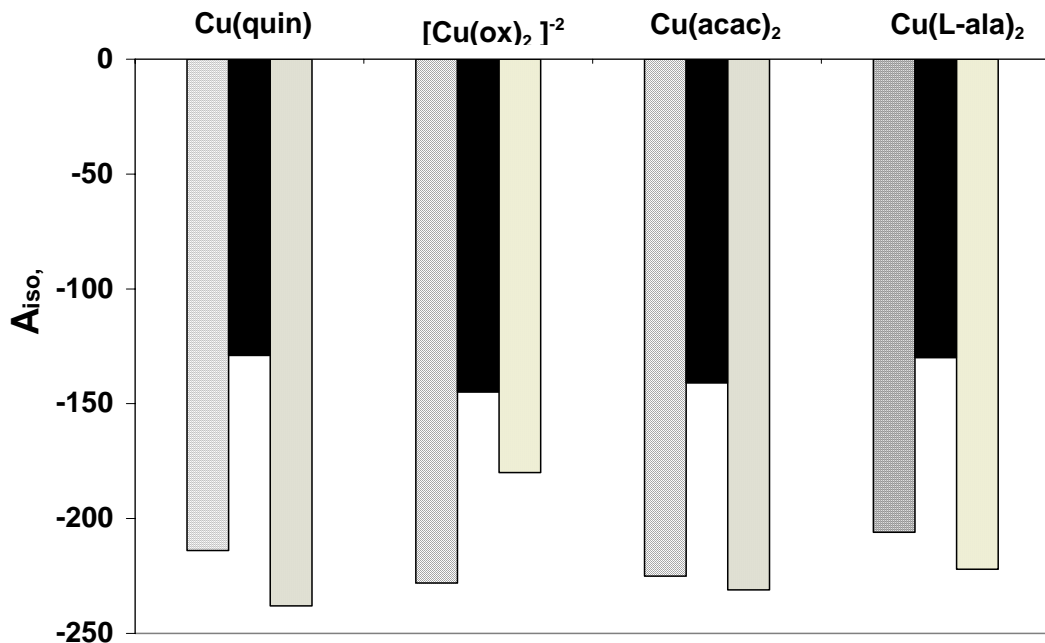
# Other Transition Metals:

## DFT Calculations of g and A-values for Copper Complexes

- ✓ Cu(II)-  $d^9$  electronic configuration,  $I=3/2$
- ✓ Calculations of A-values and g-values
- ✓ Spin-orbit coupling much larger for copper relative to vanadium
- ✓ Gaussian calculations- no relativistic effects-not a good choice for copper A-value calculations
- ✓ ADF-
  - ✓ SR UKS- unrestricted, no spin orbit coupling
  - ✓ **SO ROKS- restricted, spin orbit coupling included**
  - ✓ **SO SR UKS- unrestricted, spin orbit coupling included**



# DFT Calculation of Copper $A_{iso}^{20}$ for Selected Copper Complexes



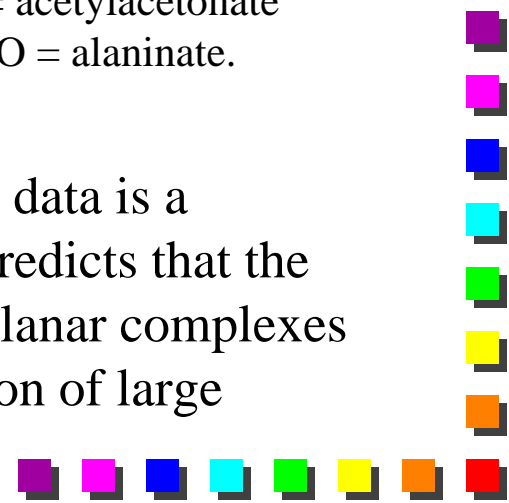
Gray bars (left) = SR UKS (BP86)  
 Black bars (middle) = SO+SR UKS (BP 86)  
 Tan bars (right)=experimental results

**Cu(Quin)<sub>2</sub>, [Cu(ox)<sub>2</sub>]<sup>2-</sup>, Cu(acac)<sub>2</sub>,  
 and Cu(L-ala)<sub>2</sub>,**

Where,

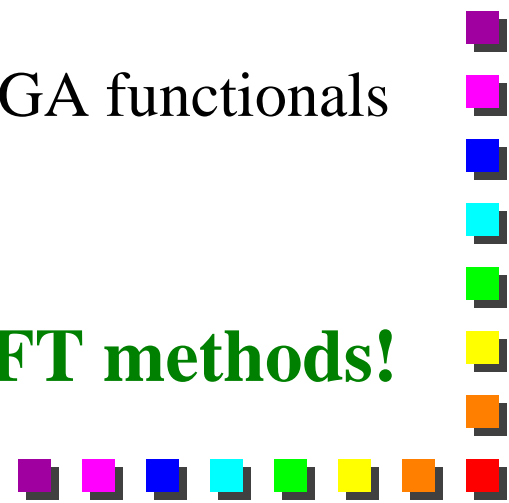
quin = 8-quinolinolato,  
 ox = oxalate,  
 acac = acetylacetonate  
 L-alaO = alaninate.

Good agreement of SR UKS calculations with experimental data is a consequence of cancellation of errors. Ligand field theory predicts that the Fermi contact and dipolar terms are **negative** for  $d^9$ , square planar complexes and 2<sup>nd</sup> order SO effects are **positive** resulting in a cancellation of large errors.<sup>21</sup>

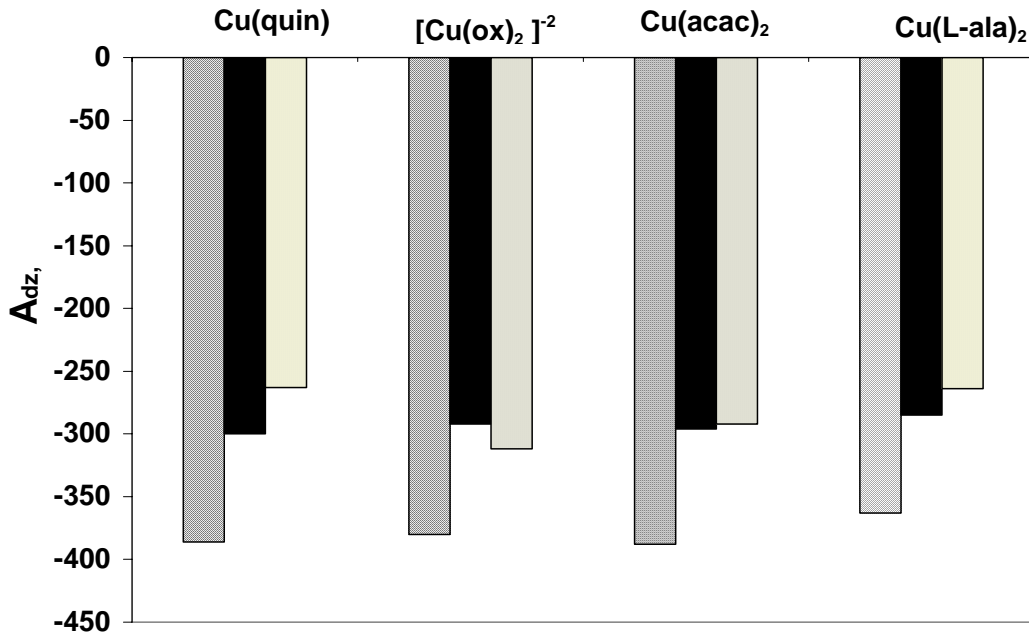


## Good Agreement??

- ✓ Cancellation of errors:<sup>20, 21</sup>
- ✓ Example:  $\text{Cu}(\text{acac})_2$  with BP86 functional:
  - ✓  $A_{\text{iso}}(\text{SR UKS}) = -225 \text{ MHz}$
  - ✓  $A_{\text{iso}}(\text{SO SR UKS}) = -141 \text{ MHz}$
  - ✓ Difference = spin orbit coupling = 84 MHz
  - ✓  $A_{\text{iso}}(\text{exp}) = -231 \text{ MHz}$
- ✓ Cancellation of errors causes best quantitative agreement for SR UKS method
  - ✓ underestimation of spin polarization by GGA functionals
  - ✓ exclusion of spin orbit coupling
- ✓ **Must exercise caution when using DFT methods!**



# DFT Calculation of Copper $A_{D,z}^{20}$ for Selected Copper Complexes



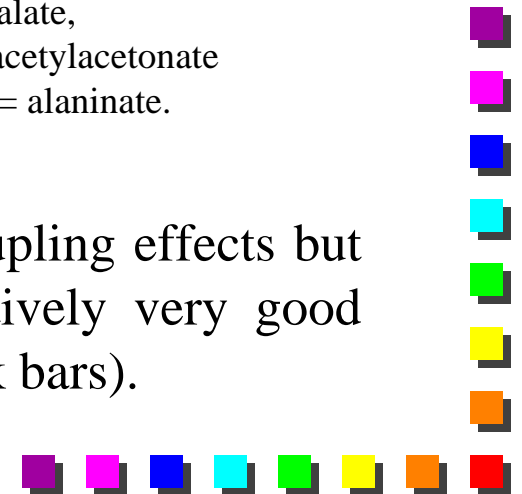
Gray bars (left) = SR UKS (BP86)  
 Black bars (middle) = SO+SR UKS (BP 86)  
 Tan bars (right)=experimental results

**Cu(Quin)<sub>2</sub>, [Cu(ox)<sub>2</sub>]<sup>2-</sup>, Cu(acac)<sub>2</sub>, and Cu(L-ala)<sub>2</sub>,**

Where,

quin = 8-quinolinolato,  
 ox = oxalate,  
 acac = acetylacetonate  
 L-alaO = alaninate.

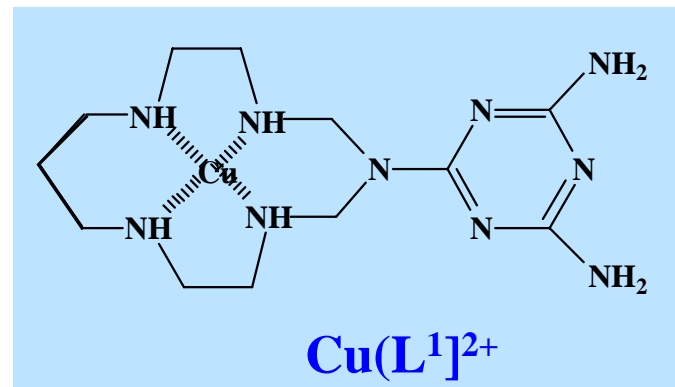
The DFT calculations of  $A_d$  are sensitive to spin orbit coupling effects but not very sensitive to spin polarization effects. Quantitatively very good results were obtained using the SO+SR UKS method (black bars).



# Calculated Cu(II) g-values <sup>22</sup>



- ✓  $g_{\perp} = 2.041$  (exp)
- ✓  $g_{\perp} = 2.043$  (B3LYP, ORCA)
- ✓  $g_{\parallel} = 2.191$  (exp)
- ✓  $g_{\parallel} = 2.137$  (B3LYP, ORCA)

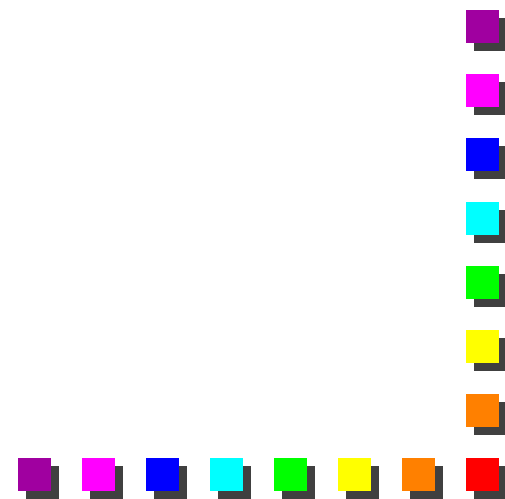


- ✓ Good agreement for  $g_{\perp}$  and not as good for  $g_{\parallel}$ .
- ✓ Believed to be a result of an overestimation of covalency in Cu(II) complexes by DFT functionals.<sup>22</sup>
  - ✓ Generally  $\Delta g_{\parallel}$  (exp. vs. DFT) is approximately 0.05 for Cu(II) complexes.



## Other Selected DFT Studies of Copper Complexes in the Literature:

- v Calculated g and A-values for di and tri-nuclear Cu(II) complexes with melamine-based oligomacrocyclic ligands<sup>22</sup>
- v DFT calculations of ligand superhyperfine structure of Cu(II) complexes<sup>23</sup>
- v CuNO complexes on a catalyst surface<sup>24</sup>



# Conclusions

- ✓ DFT calculations of EPR parameters can be used to predict trends in transition metal hyperfine coupling constants for transition metals.
  - ✓ Quantitative agreement with experiment still difficult to achieve with currently available methods.
    - ✓ Accurate calculation of spin polarization is the major barrier to quantitative agreement
      - ✓ Improved density functionals necessary
  - ✓ Deviations are systematic for similar complexes so trends in EPR experimental parameters can be predicted.
  - ✓ Solvent effects generally not considered since methods are generally not yet accurate enough to warrant their inclusion.
- ✓ DFT calculations of **ligand hyperfine coupling constants** generally show better quantitative agreement with experiment than transition metals.



# References

1. Carl, P.J., S.L. Isley, and S.C. Larsen, *Combining Theory and Experiment to Interpret the EPR Spectra of VO<sup>2+</sup> -Exchanged Zeolites*. J. Phys. Chem. B, 2001. **105**: p. 4563-4573.
2. Chasteen, N.D., *Vanadyl(IV) EPR Spin Probes: Inorganic and Biochemical Aspects*, in *Biological Magnetic Resonance*, L.J. Berliner and J. Reuben, Editors. 1981, Plenum: New York. p. 53.
3. *ADF2005.01*. 2005, Theoretical Chemistry, Vrije Universiteit: Amsterdam, The Netherlands.
4. Te Velde, G., F.M. Bickelhaupt, S.J.A. van Gisbergen, C. Fonseca Guerra, E.J. Baerends, J.G. Snijders, and T. Ziegler, *Chemistry with ADF*. J. Comput. Chem., 2001. **22**(22): p. 931-967.
5. Frisch, M. J.; Trucks, G. W.; Schlegel, H. B.; Scuseria, G. E.; Robb, M. A.; Cheeseman, J. R.; Montgomery, Jr., J. A.; Vreven, T.; Kudin, K. N.; Burant, J. C.; Millam, J. M.; Iyengar, S. S.; Tomasi, J.; Barone, V.; Mennucci, B.; Cossi, M.; Scalmani, G. ; Rega, N.; Petersson, G. A.; Nakatsuji, H.; Hada, M.; Ehara, M.; Toyota, K.; Fukuda, R.; Hasegawa, J.; Ishida, M.; Nakajima, T.; Honda, Y.; Kitao, O.; Nakai, H.; Klene, M.; Li, X.; Knox, J. E.; Hratchian, H. P.; Cross, J. B.; Bakken, V.; Adamo, C.; Jar amillo, J.; Gomperts, R.; Stratmann, R. E.; Yazyev, O.; Austin, A. J.; Cammi, R.; Pomelli, C.; Ochterski, J. W.; Ayala, P. Y.; Morokuma, K.; Voth, G. A.; Salvador, P.; Dannenberg, J. J.; Zakrzewski, V. G.; Dapprich, S.; Daniels, A. D.; Strain, M. C.; Far kas, O.; Malick, D. K.; Rabuck, A. D.; Raghavachari, K.; Foresman, J. B.; Ortiz, J. V.; Cui, Q.; Baboul, A. G.; Clifford, S.; Cioslowski, J.; Stefanov, B. B.; Liu, G.; Liashenko, A.; Piskorz, P.; Komaromi, I.; Martin, R. L.; Fox, D. J.; Keith, T.; Al-Lah am, M. A.; Peng, C. Y.; Nanayakkara, A.; Challacombe, M.; Gill, P. M. W.; Johnson, B.; Chen, W.; Wong, M. W.; Gonzalez, C.; and Pople, J. A.; Gaussian, Inc., Gaussian 03, Revision C.02, Wallingford CT, 2004.
6. Neese, F., *ORCA-an ab initio Density Functional and semi-empirical program package, version 2.4- Revision 13*; Max Planck Institute for Bioinorganic Chemistry. August, 2004.
7. Malkin, V.G., O.L. Malkina, R. Reviakine, A. Arbuznikov, M. Kaupp, B. Schimmelpfennig, I. Malkin, T. Helgaker, and K. Ruud, *MAG-ReSpect program package, version 1.1*. 2003.
8. Balhausen, C.J. and H.B. Gray, *The Electronic Structure of the Vanadyl Ion*. Inorg. Chem., 1962. **1**: p. 111-122.
9. Baute, D. and D. Goldfarb, *The <sup>17</sup>O hyperfine interaction in (VO)-O-17((H<sub>2</sub>O)-O-17)<sub>(5)</sub>(<sup>2+</sup>) and Mn ((H<sub>2</sub>O)-O-17)<sub>(6)</sub>(<sup>2+</sup>) determined by high field ENDOR aided by DFT calculations*. Journal Of Physical Chemistry A, 2005. **109**(35): p. 7865-7871.
10. Albanese, N.F. and N.D. Chasteen, *Origin of Electron Paramagnetic Resonance Linewidths in Frozen Solutions of the Oxovanadium(IV) Ion*. J. Phys. Chem., 1978. **82**: p. 910-914.
11. Saladino, A.C. and S.C. Larsen, *Density Functional Theory Calculations of the EPR Parameters for VO<sup>2+</sup> Complexes*. J. Phys. Chem. A, 2003. **107**: p. 1872-1878.



## References (Continued)

12. Neese, F., *Metal and ligand hyperfine couplings in transition metal complexes: The effect of spin-orbit coupling as studied by coupled perturbed Kohn-Sham theory*. J. Chem. Phys., 2003. **118**: p. 3939-3948.
13. Larsen, S.C., *DFT Calculations of Proton Hyperfine Coupling Constants for  $[VO(H_2O)_5]^{2+}$ : Comparison with Proton ENDOR Data*. J. Phys. Chem. A, 2001. **105**: p. 4563-4573.
14. Atherton, N.M. and J.F. Shackleton, *Proton ENDOR of  $VO(H_2O)_5^{2+}$  in  $Mg(NH_4)_2(SO_4)_2 \cdot 6H_2O$* . Mol. Phys., 1980. **39**: p. 1471-1485.
15. Saladino, A.C. and S.C. Larsen, *Density Functional Theory Calculations of Nitrogen Hyperfine and Quadrupole Coupling Constants in Oxovanadium(IV) Complexes*. J. Phys. Chem. A, 2003. **107**: p. 4735-4740.
16. Munzarova, M.L. and M. Kaupp, *A Density Functional Study of EPR Parameters for Vanadyl Complexes Containing Schiff Base Ligands*. J. Phys. Chem. B., 2001. **105**: p. 12644-12652.
17. Saladino, A.C. and S.C. Larsen, *Computational Study of the Effect of the Imidazole Ring Orientation on the EPR Parameters for Vanadyl-Imidazole Complexes*. J. Phys. Chem. A, 2002. **106**: p. 10444.
18. Aznar, C.P., Y. Deligiannakis, E.J. Tolis, T. Kabanos, M. Brynda, and D. Britt, *ESE-ENDOR study and DFT calculations on oxovanadium compounds: Effect of axial anionic ligands on the V-51 nuclear quadrupolar coupling constant*. Journal Of Physical Chemistry A, 2004. **108**(19): p. 4310-4321.
19. Paine, T.K., T. Weyhermuller, L.D. Slep, F. Neese, E. Bill, E. Bothe, K. Wieghardt, and P. Chaudhuri, *Nonoxovanadium(IV) and oxovanadium(V) complexes with mixed O, X, O-donor ligands (X = S, Se, P, or PO)*. Inorganic Chemistry, 2004. **43**(23): p. 7324-7338.
20. Saladino, A.C. and S.C. Larsen, *Relativistic DFT Calculations of Copper Hyperfine Coupling Constants: Effect of Spin-Orbit Coupling*. J. Phys. Chem. A, 2003. **107**: p. 5583-5587.
21. Neese, F., *Metal and ligand hyperfine couplings in transition metal complexes: The effect of spin-orbit coupling as studied by coupled perturbed Kohn-Sham theory*. J. Chem. Phys., 2003. **118**: p. 3939-3948.
22. Comba, P., Lampeka, Y., Prikhod'ko, A.I., Rajaraman, G. *Determination of the solution structures of melamine-based bis- and tris-macrocyclic ligand copper(II) complexes*. Inorganic Chemistry, 2006. **45**(9): p. 3632-3638.
23. Neese, F., *Theoretical Study of Ligand Superhyperfine Structure. Application to Cu(II) Complexes*. J. Phys. Chem. A., 2001. **105**: p. 4290-4299.
24. Sojka, Z. and P. Pietrzyk, *Paramagnetic species on catalytic surfaces - DFT investigations into structure sensitivity of the hyperfine coupling constants*. Spectrochimica Acta Part a-Molecular and Biomolecular Spectroscopy, 2004. **60**(6): p. 1257-1265.



# Acknowledgements

## v Graduate Students

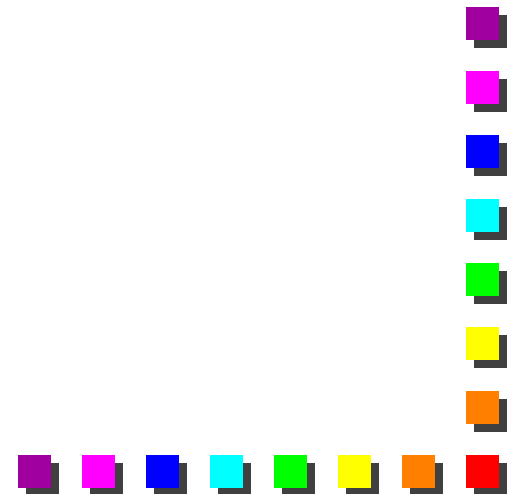
- v *Dr. Patrick Carl - Bruker*
- v *Dr. Alexander Saladino-  
University of Pittsburgh*

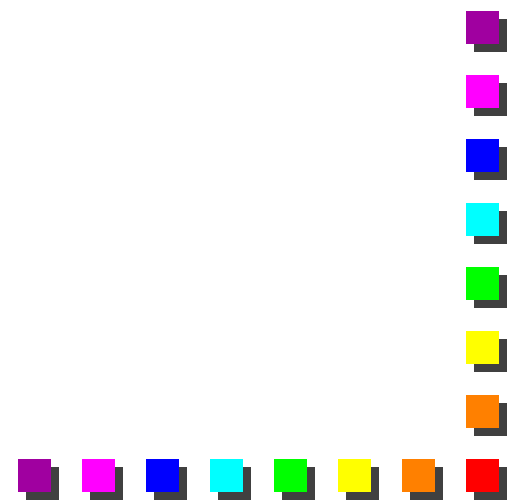
## v \$\$\$ Funding \$\$\$:

- v *NSF (CHE-0204847)*
- v *University of Iowa*
  - v *Carver Research  
Initiative*

## v Computational Resources:

- v *Origin 2000, NCSA (CHE010042)*
- v *SGI Octane Workstation*
- v *PQS 4 node cluster*





# Introduction to CW EPR Simulation

Ralph T. Weber  
*EPR Division Bruker BioSpin Corporation*  
*44 Manning Drive*  
*Billerica, MA 01821 USA*

## Introduction

As we have seen from the previous two sections, the hamiltonians for molecules can be very complicated, but this complexity yields the important details of the molecule's reactivity and structure. This section deals with extracting the important parameters from the EPR experimental data in order to test the theoretical results obtained from the calculations. Successful simulation of the experimental EPR spectra yields the spin hamiltonian parameters that summarize the EPR results and can be used to test the theoretical calculations. This section is not meant to be exhaustive treatise on EPR simulation, but to introduce the essential concepts and nomenclature. The reader is encouraged to investigate the EPR references at the end of this section. [1-3]

## The Spin-hamiltonian

Many people use the spin-hamiltonian, but are not aware of its history and why it was developed. In the early days of EPR, much of the research involved signal crystals containing transition metal ions. The actual hamiltonians of these systems are described by a bewildering collection of crystal field, spin-orbit coupling, spin-spin interaction and nuclear hyperfine effects. These hamiltonians contain many of the terms used in the theoretical calculations.

One major drawback in using this general hamiltonian is that in order to faithfully report your experimental results, you would have to list all the fields for resonance as a function of magnetic field orientation and microwave frequency. Also, many of the effects of the many interactions influence the EPR spectra in subtle ways. It is these subtle effects in the EPR spectra that offer the insight into the general picture of the electronic structure of the complex.

In 1951, Abragam and Pryce [4] resolved these two issues in their seminal paper deriving the spin-hamiltonian. First, it derives a formalism with a minimum number of parameters to describe the EPR data. Now, a few important parameters such as g values and hyperfine coupling constants can be used to succinctly quantify many pages of experimental results. Second, it concentrates on the effects, almost as if with a magnifying glass, that the big picture and all the interactions have on the EPR data. The spin-hamiltonian parameters thus afford a means of obtaining insights into the electronic structure of the complex.

The result of the paper is the familiar spin-hamiltonian that we commonly see in EPR papers:

$$\mathcal{H} = \beta_e \underline{\underline{B}}_0^T \cdot \underline{\underline{g}} \cdot \underline{\underline{S}} + \underline{\underline{S}}^T \cdot \underline{\underline{D}} \cdot \underline{\underline{S}} + \underline{\underline{S}} \cdot \underline{\underline{A}} \cdot \underline{\underline{I}} + \underline{\underline{I}}^T \cdot \underline{\underline{Q}} \cdot \underline{\underline{I}} - \gamma_N \beta_N \underline{\underline{B}}_0^T \cdot \underline{\underline{I}}$$

where:

$\beta_e$	Bohr magneton
$\underline{\underline{B}}_0$	Externally applied magnetic field
T	Signifies the transpose of a vector
$\underline{\underline{g}}$	g-matrix
$\underline{\underline{S}}$	Electron spin operator
$\underline{\underline{D}}$	Zero field splitting tensor
$\underline{\underline{A}}$	Nuclear hyperfine coupling matrix
$\underline{\underline{I}}$	Nuclear spin operator
$\underline{\underline{Q}}$	Nuclear quadrupolar interaction matrix
$\gamma_N$	Nuclear gyromagnetic ratio
$\beta_N$	Nuclear magneton

The first term,  $\beta_e \underline{\underline{B}}_0^T \cdot \underline{\underline{g}} \cdot \underline{\underline{S}}$ , is interpreted as the electronic Zeeman interaction. The g-matrix reflects the interaction of the electron spin and orbital angular momentum with the external applied magnetic field. The g-value can help identify a paramagnetic species as well as tell us about the electronic state, spin-orbit coupling and symmetry of the paramagnetic site.

The second term,  $\underline{\underline{S}}^T \cdot \underline{\underline{D}} \cdot \underline{\underline{S}}$ , is the zero-field splitting (ZFS). It represents spin-spin interactions, spin-orbit coupling, and exchange terms. The ZFS terms inform us about the spin and valence state as well as symmetry of paramagnetic centers. This term arises only for systems with  $S > 1/2$ .

The third term,  $\underline{\underline{S}} \cdot \underline{\underline{A}} \cdot \underline{\underline{I}}$ , reflects the hyperfine interaction between the electrons and the nuclei. The nuclear hyperfine interactions supply us with identity, number, and distances of surrounding nuclei. It is also a good reporter of electron spin density at specific places in a complex or radical. This interaction only occurs for nuclei with  $I > 0$ .

The  $\underline{\underline{I}}^T \cdot \underline{\underline{Q}} \cdot \underline{\underline{I}}$  term represents the quadrupolar interaction of the nuclei with the local electric field gradients. This gives us information about local symmetry and charge density near the nucleus. This term only arises for nuclei with  $I > 1/2$ .

The last term,  $-\gamma_N \beta_N \underline{\underline{B}}_0^T \cdot \underline{\underline{I}}$ , is the nuclear Zeeman interaction. This interaction only occurs for nuclei with  $I > 0$ .

At times, there may be other terms that are needed to describe the data. In high spin systems such as iron, many other terms are included.

This spin-hamiltonian is a second-order perturbation treatment of the actual hamiltonian. As with any approximation, there are always a few caveats. First, depending on the interactions in your system, it may not parameterize your EPR data. Second, though the spin-hamiltonian may successfully parameterize your EPR data, there may be some circumstances in which the assumptions regarding the spin-hamiltonian derivation do not hold or additional interactions have been neglected. This rarely occurs, however, you should be aware that this happens from time to time.

## Calculating Field Positions from Spin-hamiltonian Parameters

In order to extract the spin-hamiltonian parameters from the EPR data, we must be able to simulate the EPR spectrum given a specific set of spin-hamiltonian parameters in order that experimental data can be compared with the theoretical spectrum. If we were able to sweep our microwave frequency instead of the magnetic field, life would be easy. If you construct the hamiltonian matrix, you could simply find the eigenvalues for the given magnetic field and you have the EPR spectrum.

EPR spectra are usually acquired with constant microwave frequency and the magnetic field is scanned. Calculation of the field positions is not as simple a task as the solution of a single eigenvalue. Several approximations and approaches have been developed to deal with this difficult. The following sections describe some of these solutions in order of increasing precision.

### *First Order Perturbation Theory*

Perturbation theory allows you to calculate the approximate eigenvalues of the spin-hamiltonian. The approximate solution can then be solved to yield an analytical expression for the magnetic field. For the electron Zeeman and nuclear hyperfine interaction, you obtain the following simple expression for the fields for resonance in the EPR spectrum.

$$\frac{h\nu - Am_I}{g\beta_e} = B_0$$

where  $m_I$  is the nuclear spin quantum number. The spectrum center is determined by the electronic g-value and the line is split into several lines at regular intervals determined by the hyperfine coupling constant.

Perturbation theory uses the approximation that one interaction is far stronger than the other interactions. In EPR, the electron Zeeman term is usually the dominant term and the nuclear hyperfine interaction is smaller. This approach works very well for small hyperfine coupling constants (for X-band, splittings less than 10 G and you do not want very precise field positions) and even for considerably larger splittings, it gives you an estimate of the hyperfine coupling constants.

### ***Higher Order Perturbation Theory***

Sometimes the approximations for first-order perturbation theory are no longer valid. There are higher order approximations that correct the results of less higher order solutions to yield more precise field positions. Historically, second order perturbation theory has been used; Weil [5] derived all the terms to second order. What you will notice is that compared to first order perturbation theory, the center of the spectrum is no longer completely determined by the g-value and the splittings are no longer equal. Higher order perturbation theory works well for nuclear hyperfine splittings less than 100 G at X-band. It should be noted that many of the other interactions in the spin-hamiltonian such as the ZFS and quadrupolar interaction do not show any effects in the calculation of an EPR spectrum until these higher order effects are included.

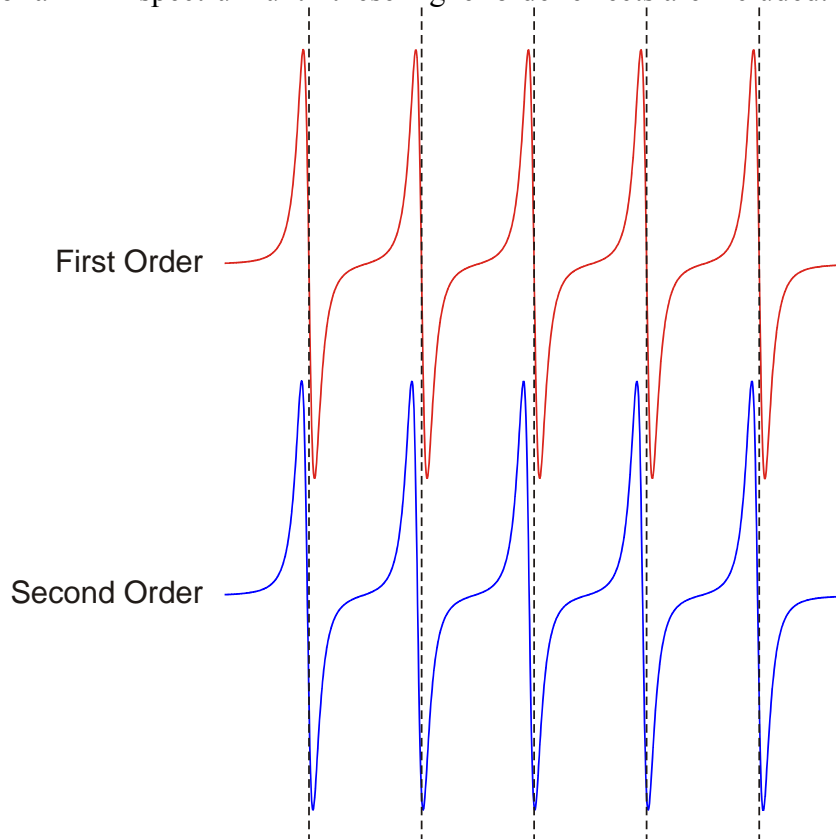


Figure 1. The higher order terms result in a shift of the center line and the lines no longer have a regular spacing when compared to the first-order spectrum.

## ***Exact Diagonalizations***

Exact diagonalization simulations of EPR spectra involve exact solutions of the spin-hamiltonian matrix at many different field values. This is a computationally intensive process, but does not suffer from the approximations of the perturbation technique. For high spin systems and systems with large forbidden transitions, this is the preferred method.

Traditionally EPR has benefited from technology that has been developed for other purposes. The development of RADAR during World War II is an example where EPR benefit from the new microwave technology. Today, the hardware power that sits on our desk that allows us to listen to music and watch movies also allows us to simulate EPR spectra with more computationally intensive but also more precise simulations.

One of the earlier solutions was the use of eigenfields. [6] Later on, computationally more efficient algorithms were developed [7] that are used in XSophe.

## **Lineshapes**

Typically the field for resonance for each EPR transition is calculated. If this is all we did, we would get a collection of stick spectra. In order to correctly simulate the spectra, we need to assume a line shape model for each of the calculated resonances.

### ***Homogeneously vs. inhomogeneously broadened lines***

For homogeneous broadening, the lineshape is determined by the relaxation times. In cases of resolved spin-packets or relaxation so fast that overlap or spin-spin splitting is a minor perturbation, we obtain relaxation determined lorentzian lineshapes. The EPR spectrum is the sum of a large number of lines each having the same Larmor frequency and linewidth.

For inhomogeneous broadening, the lineshape is determined by unresolved couplings because the EPR spectrum is the sum of a large number of narrower individual homogeneously broadened lines that are each shifted in frequency with respect to each other. Gaussian lineshapes are a common result.

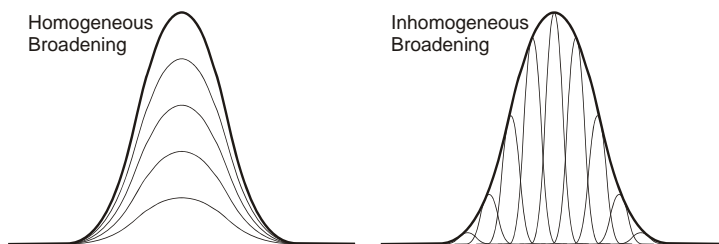


Figure 7. Homogeneous and inhomogeneous broadening.

### ***Kivelson Model for Intermediate Regime Motion***

For intermediate regime motion in which the anisotropic interactions are not averaged out, the linewidths can be often parameterized by a polynomial as a function of  $m_I$ , the nuclear spin quantum number [8]. The coefficients  $a$ ,  $b$ ,  $c$ , and  $d$  can be related to the solvent viscosity, correlation time, molecular hydrodynamics radius and the anisotropy of the spin system.

$$\sigma_v = a + b m_I + c m_I^2 + d m_I^3$$

### ***Angular Variation of Linewidths***

In solids, the linewidth may vary with the orientation of the applied magnetic field with respect to principal axes of the g-matrix [2]:

$$\sigma_v^2 = (\sigma_x^2 g_x^2 l_x^2 + \sigma_y^2 g_y^2 l_y^2 + \sigma_z^2 g_z^2 l_z^2) / g^2$$

where  $\sigma_i$  (i=x,y,z) are the input linewidth parameters,  $g_i$  (i=x,y,z) are the principal values of the g matrix,  $l_i$  (i=x,y,z) are the direction cosines of the magnetic field with respect to the principal axes of the g matrix, and  $g^2 = g_x^2 l_x^2 + g_y^2 l_y^2 + g_z^2 l_z^2$ .

### ***Strain Models***

Many times, the spin-hamiltonian parameters may not have a single value. Species within a sample may vary in structure owing to a number of factors such as slight changes in local structure. A protein may assume several different conformations when it freezes. These situations may often be simulated by assuming a correlated g-A strain model in which both the g and A values are assumed to be described by a Gaussian distribution [9]. Similar models have been developed for D and E strain for high spin systems [10].

### ***Types of Samples***

The type of sample has a great influence on the strategies and techniques used for simulating EPR spectra.

### ***Liquids***

The spin-hamiltonian is typically anisotropic, i.e. the EPR spectrum is dependent on the direction of the magnetic field with respect to the molecular axes. In many liquids, the paramagnetic species are tumbling so fast that the anisotropic components are averaged out and only the isotropic parts remain. These systems are often the fastest to simulate because only one orientation of the externally applied magnetic field needs to be simulated.

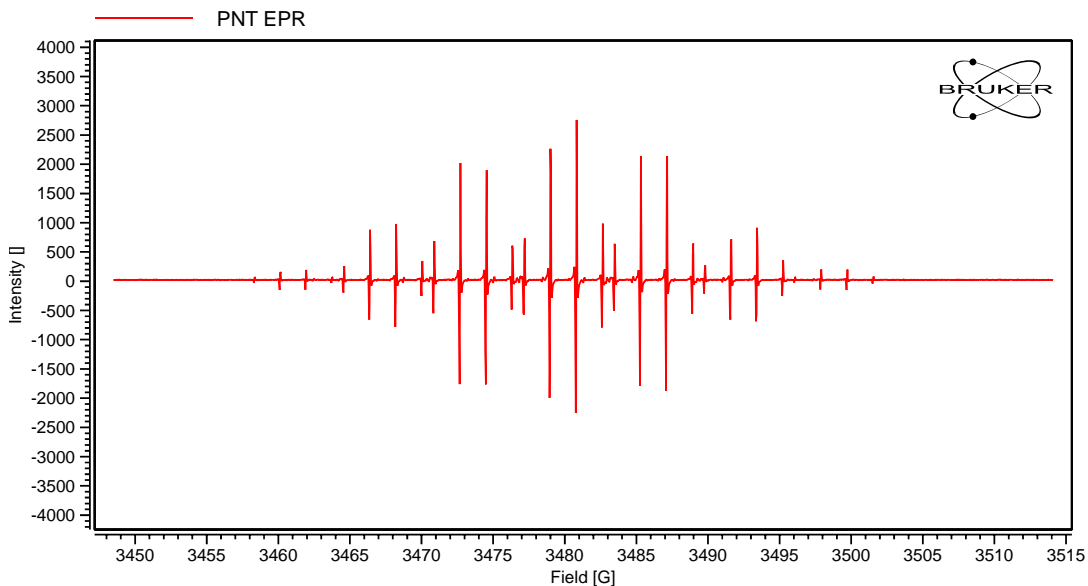


Figure 2. EPR spectrum of PNT (perynaphthalene) in oil.

### Single Crystals

For single crystal experiments, the sample orientation is varied with respect to the externally applied magnetic field. When you rotate the crystal in a specific plane and acquire the EPR spectra at regularly spaced angles, a “roadmap” is produced. A simulation for each angle is then required in order to simulate the roadmap.

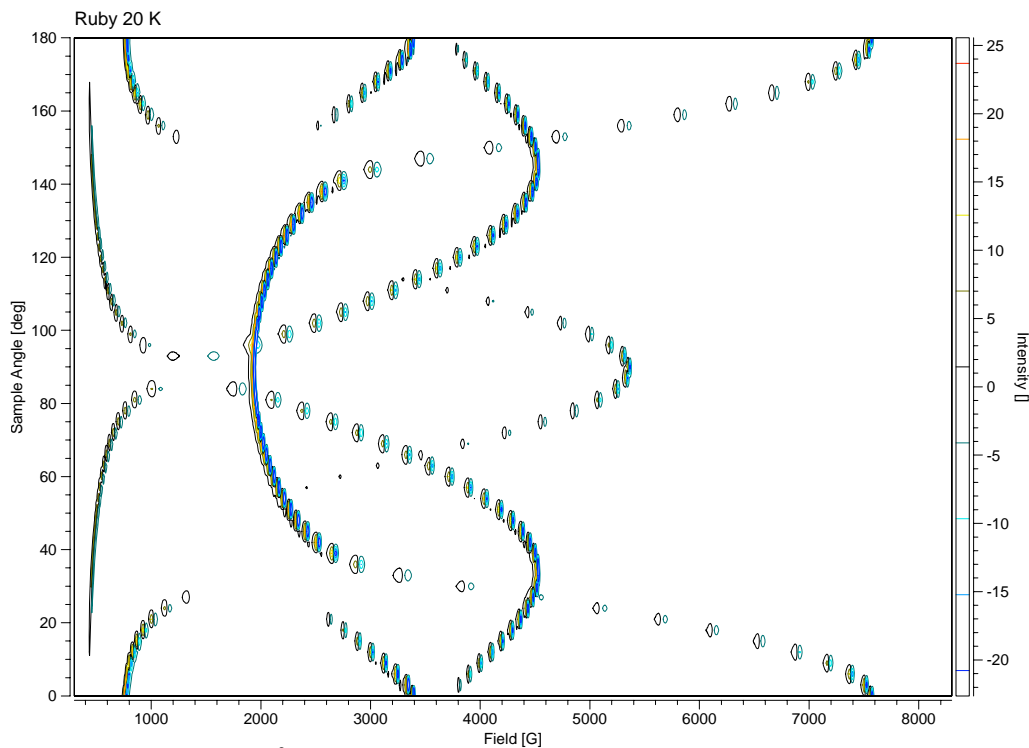


Figure 3. Roadmap of  $\text{Cr}^{+3}$  in a ruby single crystal.

## Powders and Frozen Solutions

Powders are essentially ground up crystals. In order to simulate spectra for such samples, we need to add up all the contributions from all of the magnetic field orientations. Typically this is done by creating a grid of orientations. There are several grids that can be used and many are optimized for the minimum number of orientations required to faithfully characterize the EPR spectrum with maximum computational efficiency.

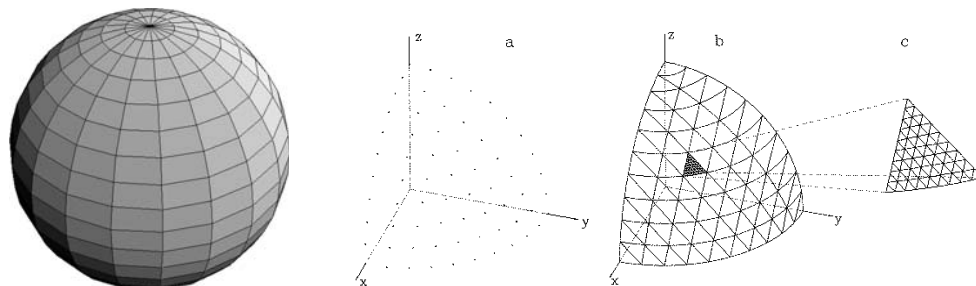


Figure 4. A simple grid for simulating powder spectra and the more efficient SOPHE grid [11].

We are sampling a finite number of orientations to create simulations for this class of samples. If we do not sample sufficient orientations, you may notice a somewhat spiky simulation (the “grass” effect). (This is similar to what happens if you do not grind your powder sample finely enough.) If you see this type of feature, increasing the number of orientations usually remedies the problem.

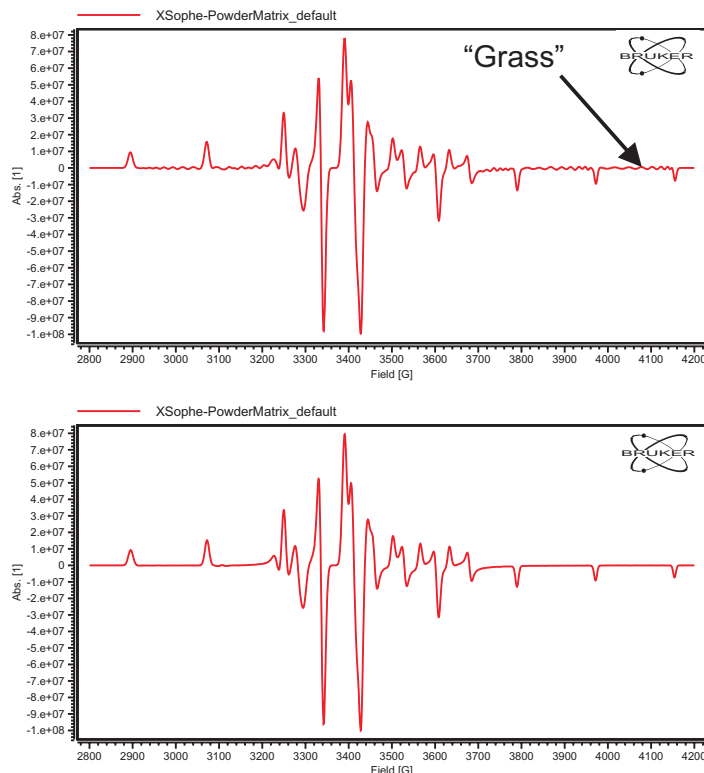


Figure 5. Upper spectrum shows “grass” from insufficient orientations. Lower spectrum was simulated with more orientations, showing much less “grass”.

## Intermediate Motional Regime

Liquid samples are an example of the fast limit motional regime in which the reciprocal of the rotational correlation times are much faster than the anisotropic interactions and the anisotropy is averaged out. The other types of samples are examples of the slow limit motional regime in which the reciprocal of the rotational correlation times are much slower than the anisotropic interactions and the anisotropy is clearly present in the EPR spectrum. For the intermediate regime in which the reciprocal of the rotational correlation times are of the same order of magnitude as the frequencies of the anisotropic interactions, the EPR spectra can exhibit unusual lineshapes owing to incomplete averaging of the anisotropic interactions. Examples are slow tumbling of radicals in a viscous solution, slow local motions, or large anisotropy.

Calculation of such spectra for this class of samples a priori is much more complicated than for the previously mentioned types of samples. Jack Freed [12] has advanced the topic with theory development and software. In some cases, the linewidths can be characterized with polynomials in  $m_l$  [8].

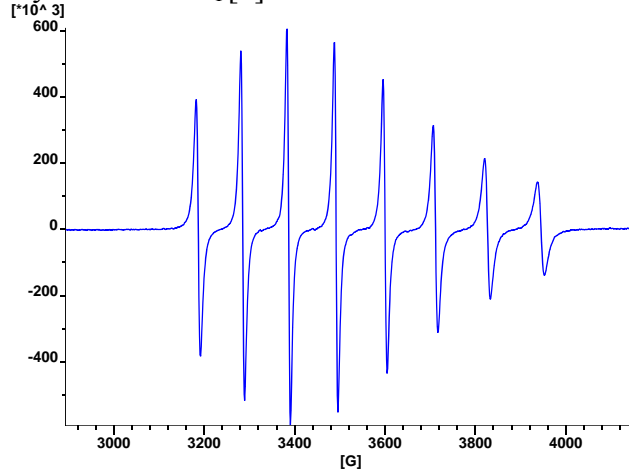


Figure 6. Vanadyl-acac showing varying linewidths due to incomplete averaging of anisotropy.

## Optimization

The purpose of simulation is to obtain the spin-hamiltonian parameters from the experimental spectra. So far, we have only discussed simulating spectra with known spin-hamiltonian parameters. In the past, you would simulate the spectrum, compare it to the experimental spectrum, modify the spin-hamiltonian parameters and hope at some point the simulation matches the experimental spectrum.

Because of efficient simulation algorithms and the powerful computing hardware available today, there are a number of computer optimization methods that can extract the parameters. If we have some good initial estimates (or guesses) for a starting point, these methods will seek the parameters by optimizing (or minimizing) GF (Goodness of Fit):

$$GF = \left( \sum_{i=1}^N (Y_{\text{exp}} - S(B, \nu_c) * \alpha)^2 \right)^{1/2} / (N * \sigma)$$

where the experimental spectrum ( $Y_{\text{exp}}$ ) has been baseline corrected assuming a linear baseline and the simulated spectrum has been scaled ( $\alpha$ ) to  $Y_{\text{exp}}$ .  $N$  is the number of points in common between the experimental and simulated spectra and  $\sigma$  is the magnitude of noise in the spectrum.

There are a number of optimization methods available such as Hookes and Jeeves [13], Simplex [14], quadratic, and simulated annealing [7]. It is difficult to judge which one will work the best (with regards to computation time or quality of the fitted parameters) for your particular optimization. It is probably best to try several methods and compare the final results.

Before optimization, it is important to baseline correct the EPR data first. Another important issue when fitting is the scaling between the experimental and simulated data. This scaling can be performed with respect to the peak to peak amplitudes or the integrated intensities. The integrated intensity normalization has advantages when the spectrum is noisy owing to the noise suppression of the integration.

There may be cases in which comparison of the FFT (Fast Fourier Transform) of the experimental and simulated spectra may be better than a direct comparison. The FFT method provides increased resolution through separating the high and low frequency components [15].

Background signals or impurities can skew the spin-hamiltonian parameters. Also overlapping spectra of different species can cause problems. In such cases it may be advantageous to not simulate the whole spectrum but only the portion relevant to the species of interest.

There are a few issues that are important when using optimization methods. First, it is important to have good initial guesses for the parameters. If not, the optimization method may not converge to a good solution and may do so only after a very lengthy calculation. Second, it is important to recognize that there may cases in which your experimental spectrum may not yield meaningful parameters. The optimization method will spit out an answer, but is the answer unique or meaningful? Inhomogeneous broadening may mask the information you are seeking. If some of the interactions are close in magnitude, the answer may not be unique. The optimization method may have found a false minimum got GF. Always scrutinize the answer you have obtained with a critical eye. Even better, if there are any doubts, you may want to consider data from other microwave frequencies.

## **Importance of Multi-frequency Measurements**

There are magnetic field dependent (electron and nuclear Zeeman interactions) terms and field independent (most of the other interactions) terms. By acquiring EPR spectra at low frequency, you accentuate the effects of the field independent part on the EPR spectrum such as the hyperfine interactions. By acquiring EPR spectra at high frequency, you accentuate the effects of the field dependent part on the EPR spectrum such as the  $g$ -values. Much of this topic was covered in the 2001 Workshop on Multi-Frequency EPR.

Here is an example in which performing experiments at three frequencies (S, X, and Q-band) yields important information regarding a low symmetry Molybdenum complex.

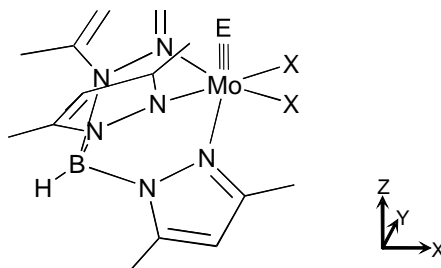


Figure 8. The low symmetry Mo site of  $\text{Tp}^*\text{Mo}^{\text{V}}\text{SX}_2$  [ $\text{Tp}^*$  = hydrotris(3,5—dimethylpyrazol-1-yl)borate; X = benzene-1,2-diolate (cat)][16].

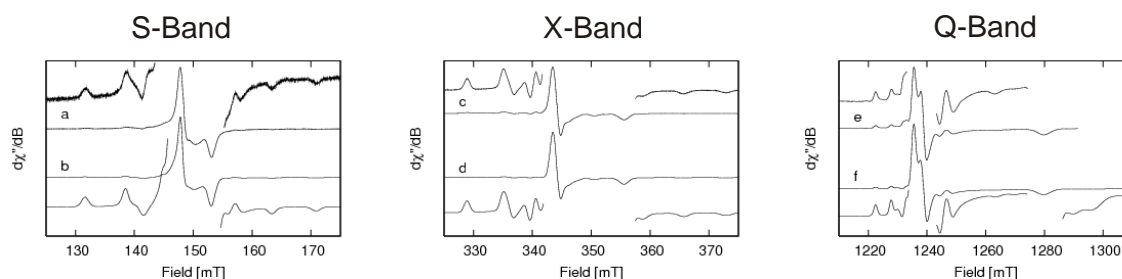


Figure 9. Multifrequency EPR of a low symmetry Mo(V) site [16].

The Q-band spectrum yields precise  $g$ -values because the field dependent interactions (electron Zeeman interaction) are emphasized at higher magnetic fields and frequency. The S-band spectrum yields the Euler angles between the principal axes of the  $g$  and  $A$  matrices. One set of parameters is able to simulate the spectra at all three frequencies. The DFT calculations are in agreement with the spin-hamiltonian parameters and yield information regarding the electronic structure of the complex.

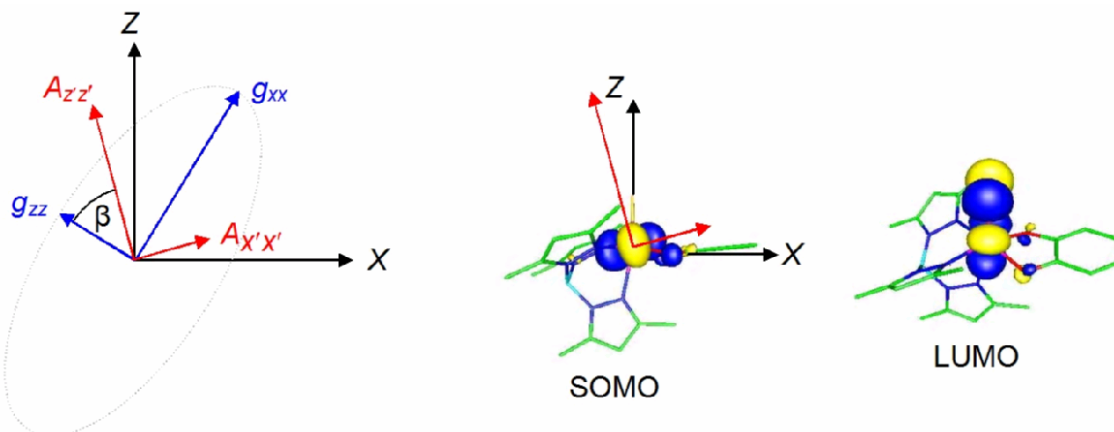


Figure 10. Interpretation of the spin-hamiltonian parameters via DFT calculations [16].

## References

1. Weil, J.A.; Bolton, J.R.; Wertz, J.E. *Electron Paramagnetic Resonance Elementary Theory and Practical Applications* 1994 (Wiley, New York).
2. Pilbrow, J.R. *Transition Ion Electron Paramagnetic Resonance* **1990** (Clarendon Press, Oxford).
3. Atherton, N.M. *Principles of Electron Spin Resonance* 1993 (Horwood, Chichester).
4. Abragam, A.; Pryce, M.H.L. Theory of the Nuclear Hyperfine Structure of Paramagnetic Resonance Spectra in Crystals. *Proceedings of the Royal Society of London Series A* **1951**, 205(1080), 135-153.
5. Weil, J. Comments on Second-Order Spin-Hamiltonian Energies. *Journal of Magnetic Resonance* **1975**, 18, 113-116.
6. Belford, G. G.; Belford, R.L.; Burkhalter, J.F. Eigenfields: A Practical Direct Calculation of Resonance Fields and Intensities for Field Swept Fixed Frequency Spectrometers. *Journal of Magnetic Resonance* **1973**, 11, 251-265.
7. Griffin, M.; Muys, A.; Noble, C.; Wang, D.; Eldershaw, C.; Gates, K.E.; Burrage, K.; Hanson, G.R. XSophe, A computer Simulation Software Suite for the Analysis of Electron Paramagnetic Spectra. *Molecular Physics Reports* **1999**, 26, 60-84.
8. D. Kivelson Theory of ESR Linewidths of Free Radicals. *Journal of Chemical Physics* **1960**, 33,1094.
9. (a) Froncisz, W; Hyde, J.S. Broadening by Strains of Lines in the g Parallel Region of Cu<sup>2+</sup> Spectra. *Journal Chemical Physics* **1980** 73, 3123.  
(b) Hyde, J.S.; Froncisz, W. The Role of Microwave Frequency in EPR Spectroscopy of Copper Complexes. *Annual Review of Biophysics & Bioengineering* **1982** 11, 391.
10. Wenzel, R.F.; Kim, Y.W. Linewidth of the Electron Paramagnetic Resonance of (Al<sub>2</sub>O<sub>3</sub>)<sub>1-x</sub>(Cr<sub>2</sub>O<sub>3</sub>)<sub>x</sub>. *Physical Review* **1965** 140, 1592.
11. Wang, D.M.; Hanson, G.R. A New Method for Simulating Randomly Oriented Powder Spectra in Magnetic Resonance: The Sydney Opera House (SOPHE) Method. *Journal of Magnetic Resonance A* **1995**, 117, 1-8.
12. Schneider, D.J.; Freed J.H. Calculating Slow Motional Magnetic Resonance Spectra: A User's Guide. *Spin Labeling: Theory and Applications, Vol. III, Biological Magnetic Resonance* **1989** 8, 1-76 (Plenum, NY).
13. Hooke, R.; Jeeves, T.A. Direct Search Solution of Numerical and Statistical Problems. *Journal of the Association of Computing Machinery* **1961**, 8, 212.
14. Spendley, W.; Hext, G.R.; Himsforth, F.R. Sequential Application of Simplex Design in Optimisation and Evolutionary Operation. *Technometrics*, **1962**, 4, 441.
15. Basosi, R.; Della Lunga, G.; Pogni, R. Resolution Enhancement of Nitrogen Hyperfine Patterns in the EPR Spectra of Cu(II) Complexes: FT Analysis of Cu(II) (His-Gly)<sub>2</sub> *Applied Magnetic Resonance* **1996**, 11, 437.
16. Drew, S.C.; Hill, J.P.; Lane, I.; Hansen, G.R.; Gable, R.W.; Young, C.G. Synthesis, Structural Characterization and Multifrequency Electron Paramagnetic Resonance Studies of Mononuclear Thiomolybdenyl Complexes. *Inorganic Chemistry* **2006** (submitted).

# **Introduction to Molecular Sophe**

## **The Next Generation of Computer Simulation Software**



**Graeme R. Hanson, Christopher J. Noble, Simon Benson**

**Centre for Magnetic Resonance**

**The University of Queensland**

**St. Lucia, Queensland, Australia**

**[graeme.hanson@cmr.uq.edu.au](mailto:graeme.hanson@cmr.uq.edu.au), [mosophe@cmr.uq.edu.au](mailto:mosophe@cmr.uq.edu.au)**

## 1. Introduction

Multifrequency continuous wave electron paramagnetic resonance (CW EPR) and pulsed EPR spectroscopy [1-8] are powerful tools for characterising metal centres in transition metal ion complexes, metalloproteins and other paramagnetic, ferromagnetic and antiferromagnetic materials, such as free radicals molecular magnets, nanomaterials, surface coatings, solid state materials and metallodrugs. Metalloenzymes comprise approximately 50% of all known proteins and are involved in a variety of biologically important processes, including oxygen transport, bio-synthesis, bio-degradation, drug metabolism, proteolysis and hydrolysis of amides and esters, environmental sulfur and nitrogen cycles and disease mechanisms.[9-11] The diversity of reactions catalysed by these metalloenzymes is reflected in the large number of different redox cofactors incorporated into and stabilised by the secondary and tertiary protein structure. Examples of some these cofactors are shown in Figure 1.

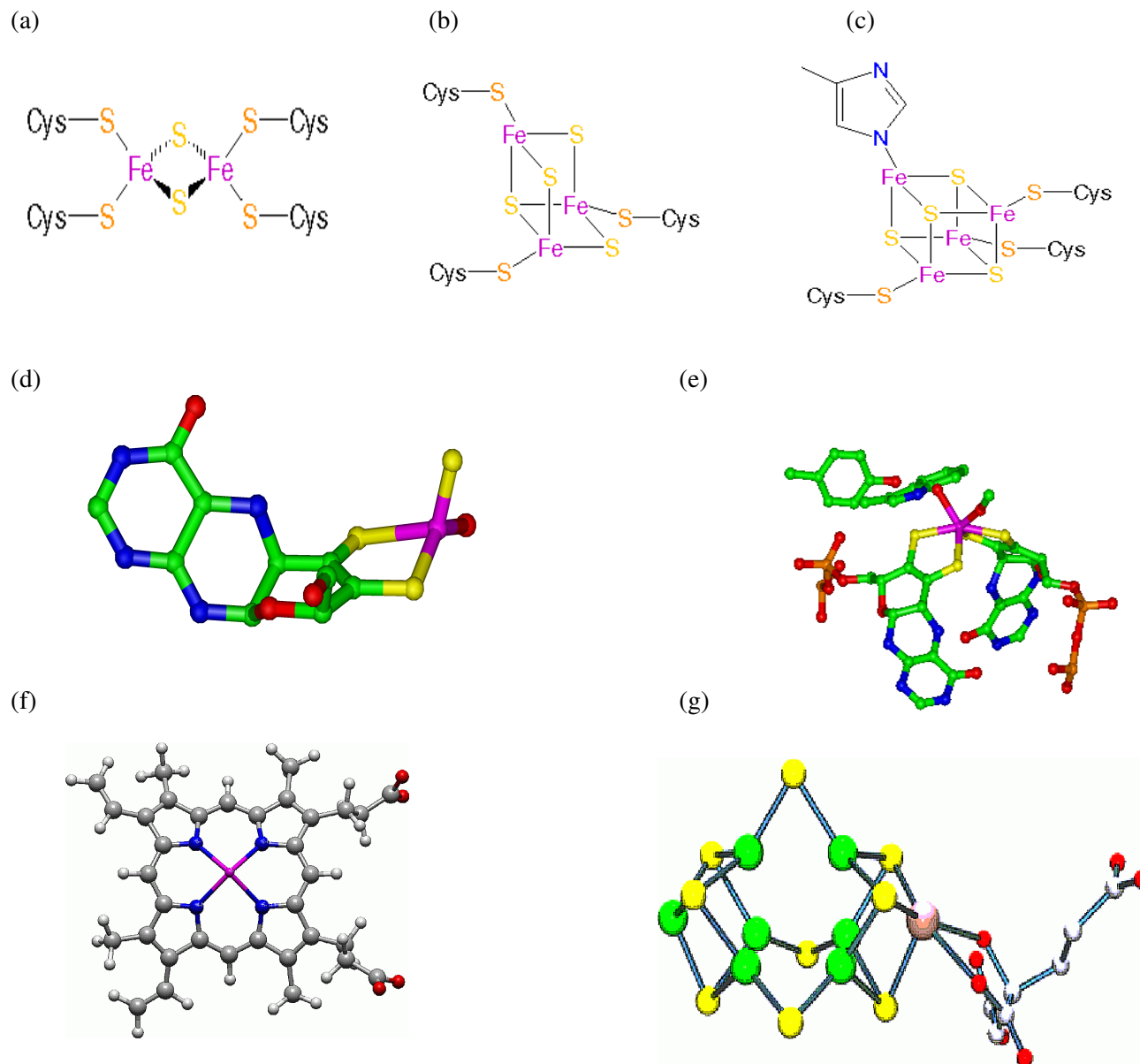


**Figure 1:** Examples of redox cofactors found in metalloproteins. (a) A  $[\text{Fe}_2\text{-S}_2]^{2+;1+}$  cluster, (b) A  $[\text{Fe}_3\text{-S}_4]^{1+;0}$  cluster, (c) A  $[\text{Fe}_4\text{-S}_4]^{3+;2+/2+;1+}$  cluster, (d) The molybdenum cofactor in xanthine oxidase, (e) The molybdenum cofactor in dimethylsulfoxide reductase, (f) A heme prosthetic group and (g) The iron molybdenum cofactor in nitrogenase.

Computer simulation of the experimental randomly oriented or single crystal EPR spectra from isolated or coupled paramagnetic centres is often the only means available for accurately extracting the spin Hamiltonian parameters required for the determination of structural information [1,2,12-28]. EPR spectra are often complex and arise through a range of interactions involving one or more unpaired electrons, the external magnetic field and one or more nuclei. Pictorially, these interactions are shown in Figure 2 and in summary:

- the electron Zeeman interaction involves the interaction of the magnetic dipole moment associated with the spin and orbital angular momentum of the unpaired electron with an externally applied magnetic field. The magnitude of this interaction is described the 3x3 matrix.  $(\mathbf{B}, \mathbf{g}, \mathbf{S})$ ;
- the fine structure interaction involves the interaction between the magnetic dipole moments of electrons on an atom containing more than one unpaired electron. The magnitude of this interaction is described by the second rank D tensor. Second order terms, D and E/D correspond to the axial zero field splitting (D) and the asymmetry parameter E/D which varies from 0 (axial symmetry) to 1/3 (rhombic symmetry) (S.D.S),

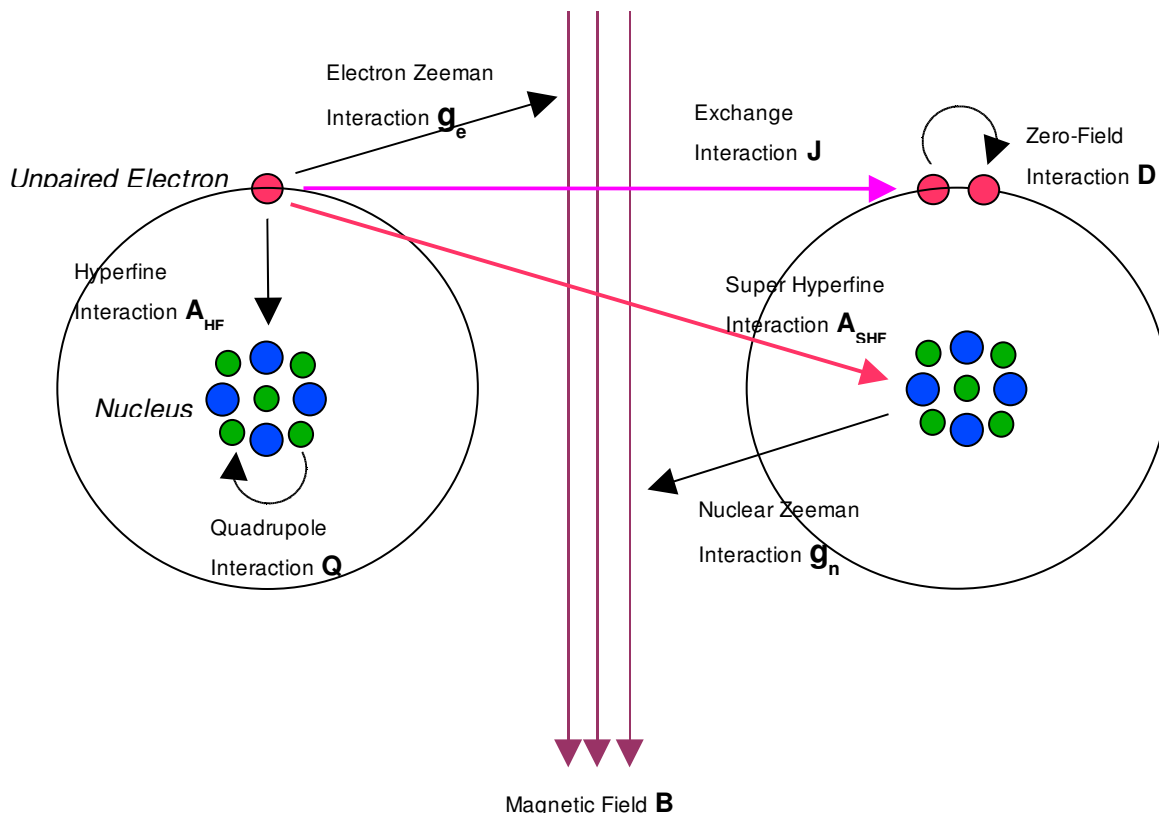


**Figure 2:** Spin Hamiltonian Interactions

- the hyperfine interaction involves the interaction between the magnetic dipole moments of the unpaired electron(s) and the nucleus of the same atom. The magnitude of this interaction is described by the hyperfine (A) 3x3 matrix. (S.A.I);
- the superhyperfine interaction involves the interaction between the magnetic dipole moments of the unpaired electron and nucleus of different atoms. The magnitude of this interaction is described by the hyperfine (A) 3x3 matrix. (S.A.I);
- the quadrupole interaction requires the existence of a quadrupole moment which arises from an inhomogeneous electric field gradient at the nucleus. By necessity, the nuclear spin must be greater than  $\frac{1}{2}$  and the nucleus must experience a symmetry lower than cubic. The magnitude of this interaction is

described by a second rank tensor  $Q$  or  $P$ , both of which are used interchangeably in the literature and throughout this document ( $\mathbf{I.Q.I}$ ) or ( $\mathbf{I.P.I}$ );

- the nuclear Zeeman interaction involves the interaction of the magnetic dipole moment arising from the nuclear spin with an externally applied magnetic field ( $\gamma \mathbf{B.I}$ ) and
- the exchange interaction involves the interaction of magnetic dipole moments of unpaired electrons on different atoms. This interaction can occur through molecular orbitals ( $\mathbf{J S.S, G SxS}$ ) or space ( $\mathbf{S.J.S}$ ).

Mathematically these interactions can be written using a spin Hamiltonian formalism. For an isolated paramagnetic centre (A) a general spin Hamiltonian [1,2,12] is:

$$H_A = \mathbf{S} \cdot \mathbf{D} \cdot \mathbf{S} + \beta \mathbf{B} \cdot \mathbf{g} \cdot \mathbf{S} + \mathbf{S} \cdot \mathbf{A} \cdot \mathbf{I} + \mathbf{I} \cdot \mathbf{Q} \cdot \mathbf{I} - \gamma (1 - \sigma) \mathbf{B} \cdot \mathbf{I} \quad (1)$$

where  $\mathbf{S}$  and  $\mathbf{I}$  are the electron and nuclear spin operators respectively,  $\mathbf{D}$  the zero field splitting tensor,  $\mathbf{g}$  and  $\mathbf{A}$  are the electron Zeeman and hyperfine coupling matrices respectively,  $\mathbf{Q}$  the quadrupole tensor,  $\gamma$  the nuclear gyromagnetic ratio,  $\sigma$  the chemical shift tensor,  $\beta$  the Bohr magneton and  $\mathbf{B}$  the applied magnetic field. Additional hyperfine, quadrupole and nuclear Zeeman interactions will be required when superhyperfine splitting is resolved in the experimental EPR spectrum. When two or more paramagnetic centres ( $A_{ij}$ ,  $i, j = 1, \dots, N$ ) interact, the EPR spectrum is described by a total spin Hamiltonian ( $H_{Total}$ ) which is the sum of the individual spin Hamiltonians ( $H_{Ai}$ , Eq. (1)) for the isolated centres ( $A_i$ ) and the interaction Hamiltonian ( $H_{Aij}$ ) which accounts for the isotropic exchange, antisymmetric exchange and the anisotropic spin-spin (dipole-dipole coupling) interactions between a pair of paramagnetic centres [1,13,14].

$$H_{Total} = \sum_{i=1}^N H_{A_i} + \sum_{i, j=1, i \neq j}^N H_{A_{ij}} \quad (2)$$

$$H_{A_{ij}} = J_{A_{ij}} \mathbf{S}_{A_i} \cdot \mathbf{S}_{A_j} + G_{A_{ij}} \mathbf{S}_{A_i} \times \mathbf{S}_{A_j} + \mathbf{S}_{A_i} \cdot \mathbf{D}_{A_{ij}} \cdot \mathbf{S}_{A_j}$$

Computer simulation of randomly oriented or single crystal EPR spectra from isolated or coupled paramagnetic centres is required to accurately determine the spin Hamiltonian parameters (Eqs. 1 and 2) and the electronic and geometric structure of the paramagnetic centre. The simulation of randomly oriented EPR spectra is performed in frequency space through the following integration [1,26]:

$$S(\mathbf{B}, \nu_c) = C \int_{\theta=0}^{\pi} \int_{\phi=0}^{\pi} \sum_{i=0}^N \sum_{j=i+1}^N |\mu_{ij}|^2 f[\nu_c - \nu_0(\mathbf{B}), \sigma_\nu] d\cos\theta d\phi \quad (3)$$

where  $S(\mathbf{B}, \nu_c)$  denotes the spectral intensity,  $|\mu_{ij}|^2$  is the transition probability,  $\nu_c$  the microwave frequency,  $\nu_0(\mathbf{B})$  the resonant frequency,  $\sigma_\nu$  the spectral line width,  $f[\nu_c - \nu_0(\mathbf{B}), \sigma_\nu]$  a spectral lineshape function which normally takes the form of either Gaussian or Lorentzian, and  $C$  a constant which incorporates various experimental parameters. The summation is performed over all the transitions ( $i, j$ ) contributing to the spectrum and the integrations, performed numerically, are performed over half of the unit sphere (for ions possessing triclinic symmetry), a consequence of time reversal symmetry [1,12]. For paramagnetic centres exhibiting orthorhombic or monoclinic symmetry, the integrations in Eq. (3) need only be performed over one or two octants respectively. Whilst paramagnetic centres with an axially symmetric spin Hamiltonian only require integration over  $\theta$  between

0 and  $\pi/2$ , those possessing a spin Hamiltonian with cubic symmetry require only a single orientation. Whilst perturbation theory involves an analytical expression for the calculation of resonant field positions and is therefore inherently computationally very fast, it breaks down when state mixing occurs. Consequently, the better and more general approach is to employ numerical matrix diagonalization which does not suffer from this problem, though for large spin Hamiltonian matrices this can be computationally expensive.

Experimentally the CW EPR experiment is a field swept experiment in which the microwave frequency ( $\nu$ ) is held constant and the magnetic field varied. Computer simulations performed in field space assume a symmetric lineshape function,  $f$  in Eq. (3) ( $f(\mathbf{B}-\mathbf{B}_{\text{res}}), \sigma_{\text{B}}$ ), which must be multiplied by  $d\nu/dB$  and assume a constant transition probability across a given resonance [1,29]. Sinclair and Pilbrow [30,31] have described the limitations of this approach in relation to asymmetric lineshapes observed in high spin Cr(III) spectra and the presence of a distribution of  $g$ -values (or  $g$ -strain broadening). The following approach has been employed by Pilbrow *et al.* in implementing Eq. (3) (frequency swept) into computer simulation programmes based on perturbation theory [1,29]. Firstly, at a given orientation of  $(\theta, \phi)$ , the resonant field positions ( $\mathbf{B}_{\text{res}}$ ) are calculated with perturbation theory and then transformed into frequency space ( $\nu_0(\mathbf{B})$ ). Secondly, the lineshape [ $f(\nu_c-\nu_0(\mathbf{B}), \sigma_0)$ ] and transition probability are calculated in frequency space across a given resonance and the intensity at each frequency stored. Finally, the frequency swept spectrum is transformed back into field space. Performing computer simulations in frequency space produces asymmetric lineshapes (without having to artificially use an asymmetric lineshape function) and secondly, in the presence of a large distribution of  $g$ -values will correctly reproduce the down field shifts of resonant field positions [29]. Unfortunately, this approach cannot be used in conjunction with matrix diagonalization as a very large number of matrix diagonalizations would be required to calculate  $f$  and the transition probability across a particular resonance resulting in unacceptably large computational times. In Sophe (field space version), we assume a symmetric lineshape function, multiplied by  $d\nu/dB$  and a constant transition probability across a given resonance.

Previously we developed the XSophe-Sophe-XeprView<sup>®</sup> computer simulation software suite [19-24,31] (Figure 3) for the analysis of isotropic, randomly oriented and single crystal CW EPR spectra. The software suite consists of: XSophe, an X-windows interface; the Sophe authentication and Common Object Request Broker Architecture (CORBA) daemons; Sophe, a state-of-the-art computational programme for simulating CW EPR spectra and XeprView<sup>®</sup>, Bruker Biospin's programme for visualising and comparing experimental and simulated spectra. The functionality of the XSophe software suite is shown below [23-24]:

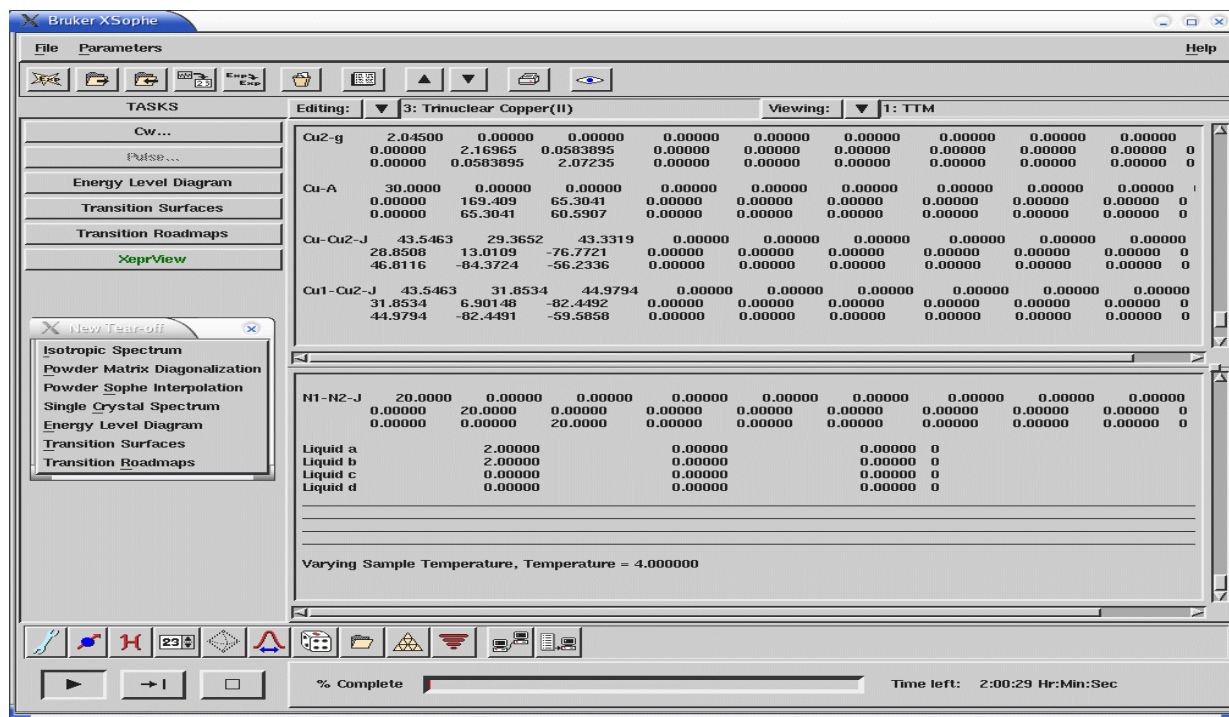


**Figure 3:** The XSophe (v 1.1.4) main Window. The interface allows the creation and execution of multiple input files on local or remote hosts. There are macro task buttons to guide the novice through the various menus and two button bars to allow easy access to the menus. For example the bottom bar (left to right), Experimental Parameters, Spin System, Spin Hamiltonian, Instrumental Parameters, Single Crystal Settings, Lineshape Parameters, Transition Labels/Probabilities, File Parameters, Sophe Grid Parameters, Optimisation Parameters, Execution Parameters and Batch Parameters.

### Experiments

Continuous Wave EPR Spectra displayed in XeprView<sup>®</sup>.

Energy level diagrams, transition surfaces and transition roadmaps displayed in a Web Browser (Mozilla).

### Spin Systems

Isolated and magnetically coupled spin systems.

An unlimited number of electron and nuclear spins is supported with nuclei having multiple isotopes.

### Spin Hamiltonian Interactions

2<sup>nd</sup> order Fine Structure Interaction, 4<sup>th</sup> and 6<sup>th</sup> order corrections (S.D.S, B4, B6) [12].

Isotropic and Anisotropic Electron Zeeman ( $g\beta\mathbf{B}\cdot\mathbf{S}$ ,  $\beta\mathbf{B}\cdot\mathbf{g}\cdot\mathbf{S}$ ).

Isotropic and Anisotropic Hyperfine ( $a\mathbf{S}\cdot\mathbf{I}$ ,  $\mathbf{S}\cdot\mathbf{A}\cdot\mathbf{I}$ ).

Nuclear Zeeman Interaction for nuclei ( $g_N\beta_N\mathbf{B}\cdot\mathbf{I}$ ).

Quadrupole ( $\mathbf{I}\cdot\mathbf{P}\cdot\mathbf{I}$ ).

Isotropic Exchange ( $J_{\text{iso}} \mathbf{S}_i \cdot \mathbf{S}_j$ ).

Anisotropic Exchange (dipole dipole coupling) ( $\mathbf{S}_i \cdot \mathbf{J} \cdot \mathbf{S}_j$ ).

### *Continuous Wave EPR Spectra*

Spectra types:

Solution, randomly oriented and single crystal.

Symmetries:

Isotropic, axial, orthorhombic, monoclinic and triclinic.

Multidimensional spectra:

Variable temperature, multifrequency and the simulation of single crystal spectra in a plane.

### *Methods*

Matrix diagonalization - mosaic misorientation linewidth model.

Sophe Interpolation.

A choice of perturbation theory or matrix diagonalization for superhyperfine interactions.

### *Optimisation (Direct Methods)*

Methods:

Hooke and Jeeves.

Quadratic variation of Hooke and Jeeves.

Simplex.

Two Simulated Annealing methods.

Spectral Comparison:

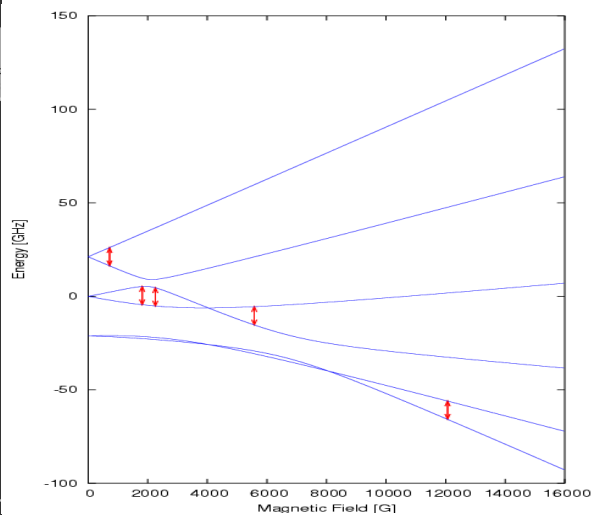
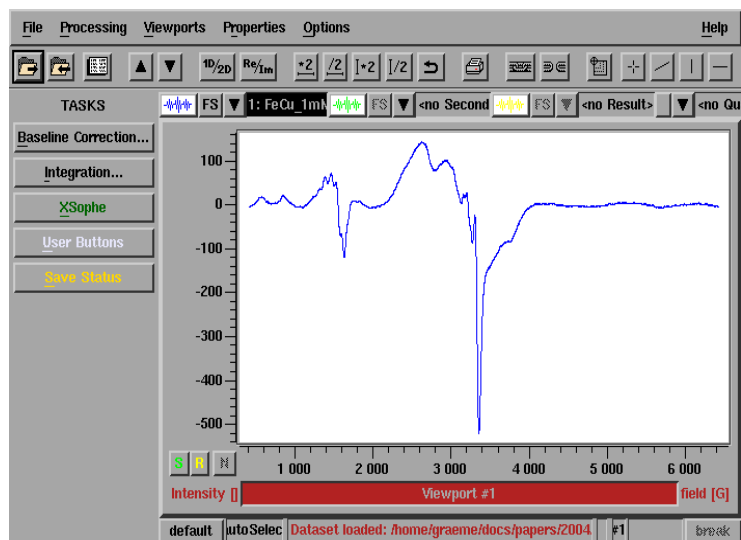
Raw data and Fourier transform.

XSophe allows transparent transfer of EPR spectra and spectral parameters between XSophe, Sophe and XeprView<sup>®</sup>, using state-of-the-art platform-independent CORBA libraries. This interactivity allows the execution and interaction of the XSophe interface with Sophe on the same computer or a remote host through a simple change of the hostname. XSophe contacts the Sophe CORBA daemon, which then interacts with the Sophe authentication daemon *via* a Unix socket to validate the username and password which was encrypted with 128 bit encryption and embedded in a CORBA string. Once validated the Sophe authentication daemon forks a Sophe which then performs the simulation.

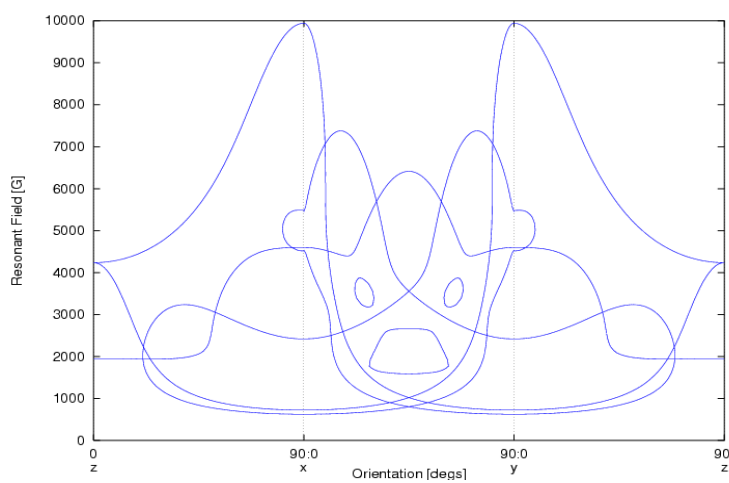
The output of CW EPR spectra (1D and 2D) from the Sophe program can be visualised in conjunction with the experimental spectrum in XeprView<sup>®</sup> or Xepr<sup>®</sup>. Computer simulation of single crystal spectra measured in a plane perpendicular to a rotation axis can be performed by defining the rotation axis and the initial and final angles of the magnetic field in the plane perpendicular to this axis. Energy level diagrams, transition roadmaps and transition surfaces aid the interpretation of complicated randomly oriented EPR spectra and can be viewed with a web browser (mozilla) and an OpenInventor scene graph viewer (ivview) (Figure 4).

(a)

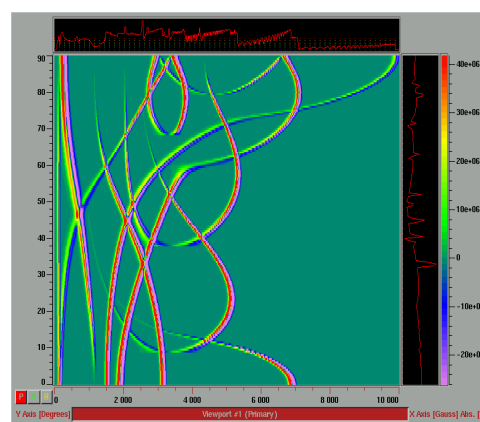
(b)



(c)



(d)



(e)

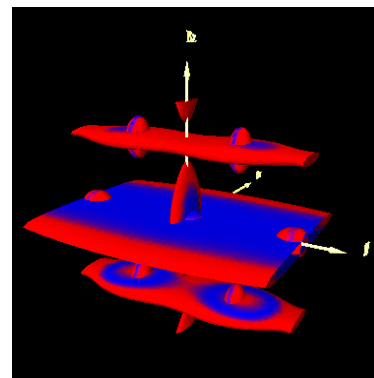


**Figure 4:** Output from XSophe (a) CW EPR Spectrum, (b) Energy level diagram, (c) Transition Roadmap, (d) Single crystal EPR spectrum and (e) Transition surface with a transition probability colour map.

Elucidation of the three dimensional crystallographic information (distance and orientation of nuclei with respect to the atom containing the unpaired electron) of redox active cofactors within a metalloenzyme relies on the observation of hyperfine coupling between nuclei and the electron spin which is often unresolved in randomly orientated CW-EPR spectra. The advent of multidimensional pulsed EPR and electron nuclear double (triple) resonance (END(T)OR) spectroscopy in conjunction with orientation selective experiments and computer simulation overcome this problem and allows three dimensional structures (electronic and geometric) of paramagnetic centres to be determined. While electron spin echo envelope modulation (ESEEM) experiments are particularly sensitive for extremely weak couplings from 4-6 Å away from the paramagnetic centre, the ENDOR experiment is far more sensitive to strongly coupled nuclei 2-4 Å away from the paramagnetic centre. Two dimensional correlation experiments can be applied to ESEEM or ENDOR pulse sequences, yielding detailed structural information on the number and type of nuclei present and their distance and relative orientation from the paramagnetic centre. For example, the complete structural characterisation of the spin density distribution and consequently the structure of the photosynthetic reaction centre (PS I) has been ascertained through careful two dimensional ESEEM and END(T)OR spectroscopy by Lubitz *et al.* [32] Pulse sequences based on pulsed ENTOR have been developed for directly determining crystallographic information (internuclear separations between nuclei and the paramagnetic centre and their relative orientation with respect to the paramagnetic centre) directly through the dipole-dipole interaction. [33]

Elucidation of three dimensional crystallographic information (distance and orientation) of multiple paramagnetic centres within a metalloenzyme relies on the observation of anisotropic exchange (dipole-dipole) coupling between the multiple electron spins. Whilst CW-EPR can be used to measure the distance and orientation of redox active centres up to about 8 Å apart and power saturation studies can be used to infer slightly larger distances, pulsed ELDOR allows distances up to 80 Å to be measured directly from a Pake doublet. [34]

Traditionally, interpretation of EPR spectra has relied on computer simulation to determine the EPR parameters which have either then been compared to parameters from well characterised materials to determine molecular structure or quantum chemistry has been employed to reproduce the EPR parameters (Figure 5).

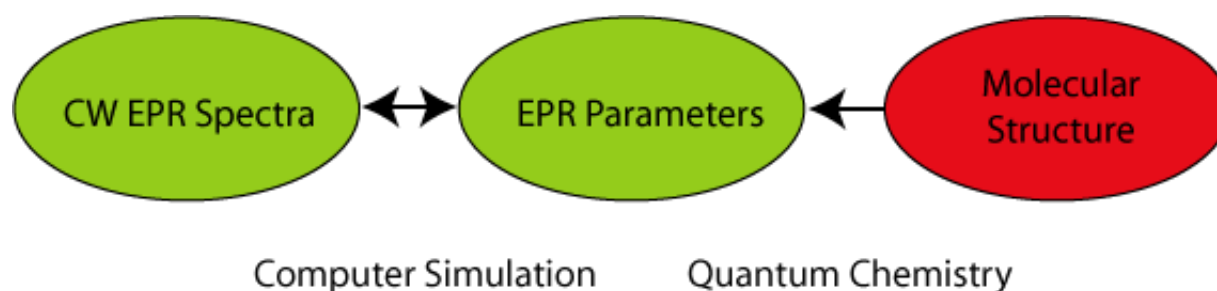


**Figure 5:** Traditional Approach to determining molecular structure of molecules from EPR spectra.

Herein we describe an integrated approach '*Molecular Sophie*' for the computer simulation of continuous wave and pulsed EPR and electron nuclear double resonance (ENDOR) spectra, energy level diagrams, transition roadmaps and transition surfaces. This approach, based on molecular structure, will revolutionise the 3-dimensional molecular characterization of paramagnetic materials using high resolution EPR spectroscopy. Until now the analysis of complex CW and pulsed EPR spectra has been based on a spin system rather than molecular structure and the analysis of pulsed EPR spectra has mainly relied upon analytical expressions involving perturbation theory.

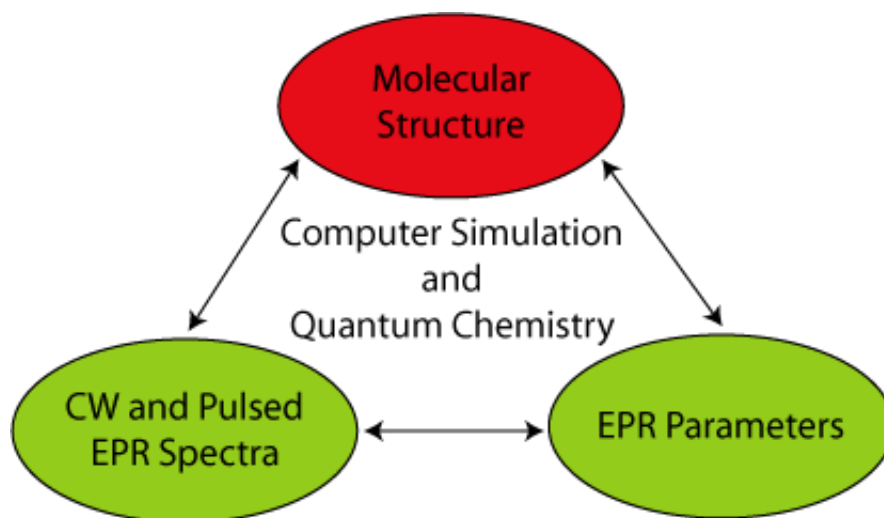
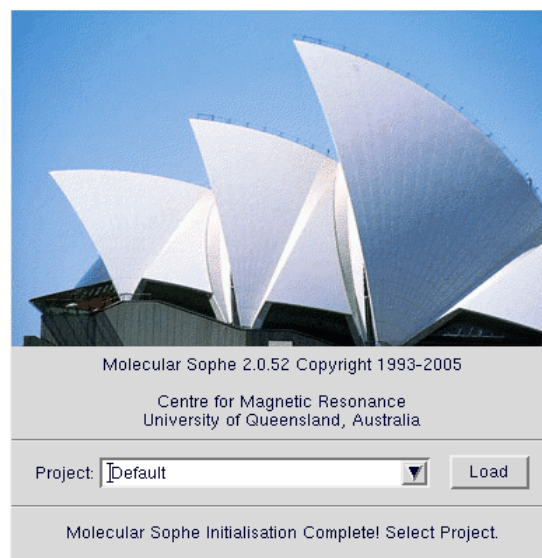


**Figure 6:** New Approach to determining molecular structure of molecules from EPR spectra.

## 2. *Molecular Sophe Computational Software Suite*

The Molecular Sophe software suite consists of a graphical user interface, the computational programme Sophe and a variety of software tools (XepView®, Gnuplot, ivview and Ghostview) for visualising and comparing simulations and experimental EPR spectra. This provides scientists with a powerful research tool for determining the geometric and electronic structure of magnetically isolated and coupled paramagnetic centres within metalloproteins and other paramagnetic centres. Molecular Sophe is Project oriented. Each project can contain a number of simulations, each of which contains a sample with one or molecules and then the scientist can choose a range of experiments to be applied to that sample to elucidate the geometric and electronic structure of the molecule(s). Upon starting Molecular Sophe (**mosophe**) a splash screen, similar to that shown in Figure 7 is displayed showing the progress of loading the software and finally allows the user to choose a project from the Project list to load into Molecular Sophe. This list of projects is stored in the user's home directory (/home/user/.mosophe/projects).

**Figure 7:** Splash Screen for Molecular Sophe allowing the user to choose a project from the user's list of Projects.



Pressing the Load button displays the graphical user interface for Molecular Sophe (Figure 8). Molecular Sophe's graphical user interface incorporates a Menu, Tool bar, Explorer Tree, Forms, Control bar and Message

bar (Figure 8). The main menu provides access to all functions whilst the toolbar contains some of the commonly used functions in creating a sample, adding experiments and running external programmes (XeprView®, printing and the units calculator). The choice of external programmes and CORBA settings should be set through the Preferences window accessed from the menu (Edit, Edit Preferences) and saved to disk so that in future runs of Molecular Sophe, the settings are loaded upon startup. All of the Buttons, Fields, Tree Nodes have context sensitive help which can be accessed by moving the mouse onto the desired widget.

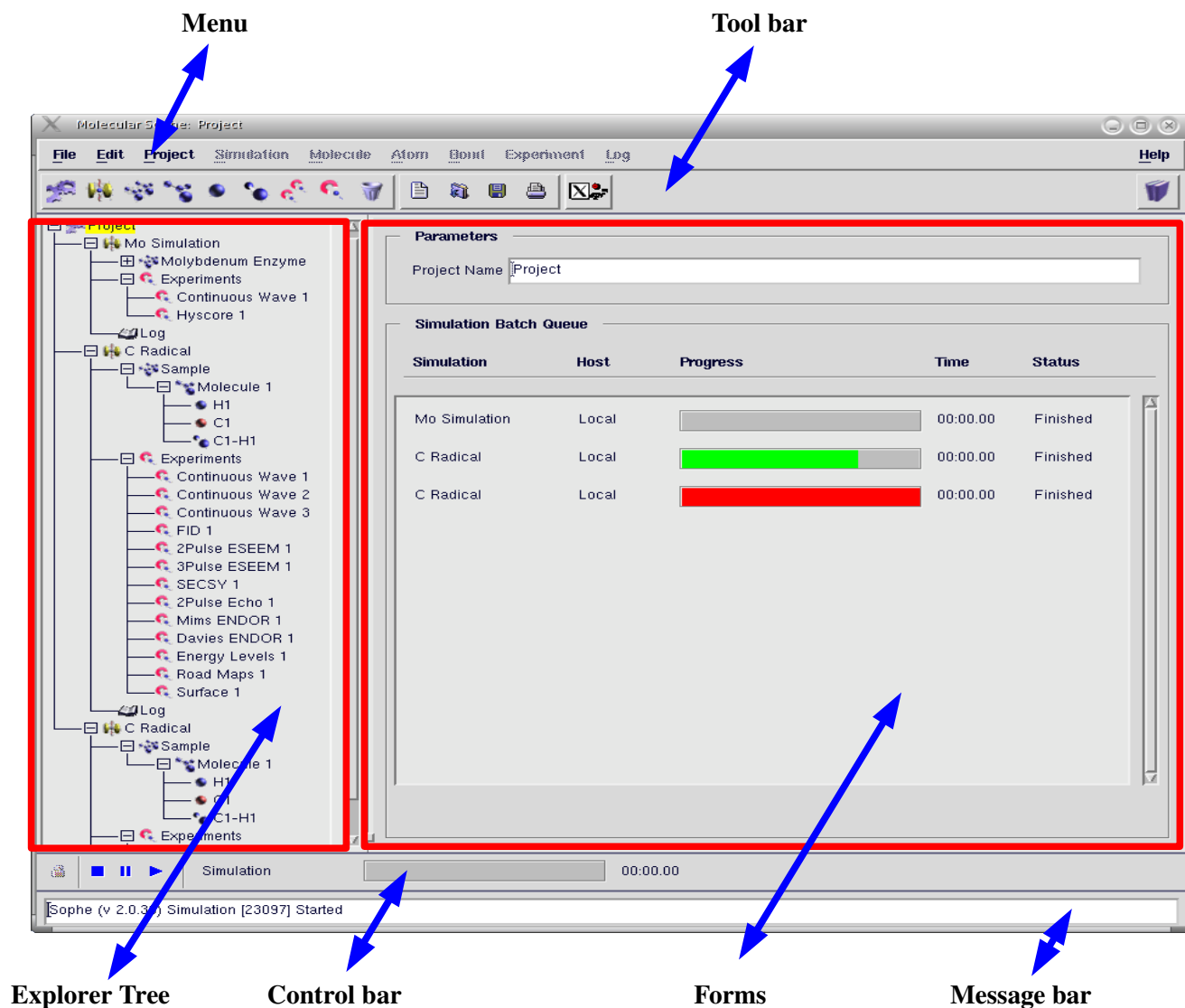


**Figure 8:** Molecular Sophe Graphical User Interface showing the Explorer Tree and the Project Form.

## 2.1 Project Form

The Project Form (Figure 8) displays the status of the multiple simulations through timing bars for each simulation. The timing bars are colour coded: grey – simulation has not been started; green – simulation running; and red – simulation finished. A right mouse click on the Project Node displays a menu enabling the user to add and load a simulation, create a new, load, save and delete a project.

## 2.2 Simulation Form

The Simulation Form (Figure 9) displayed by a left mouse click on the Simulation Node (entitled 'Mo Simulation' or 'C Radical' in Figure 8) in the Explorer Tree allows the choice of Host on which to execute the computational programme Sophe (currently only localhost), the process priority, whether to run it interactively or in a batch queue (currently only interactively) and the XeprView<sup>®</sup> programme in which to display the resultant spectra. The name of the simulation can also be modified through the Simulation Form. A right mouse click on the Simulation Node displays a menu enabling the user to save, delete, copy, print and run a simulation.

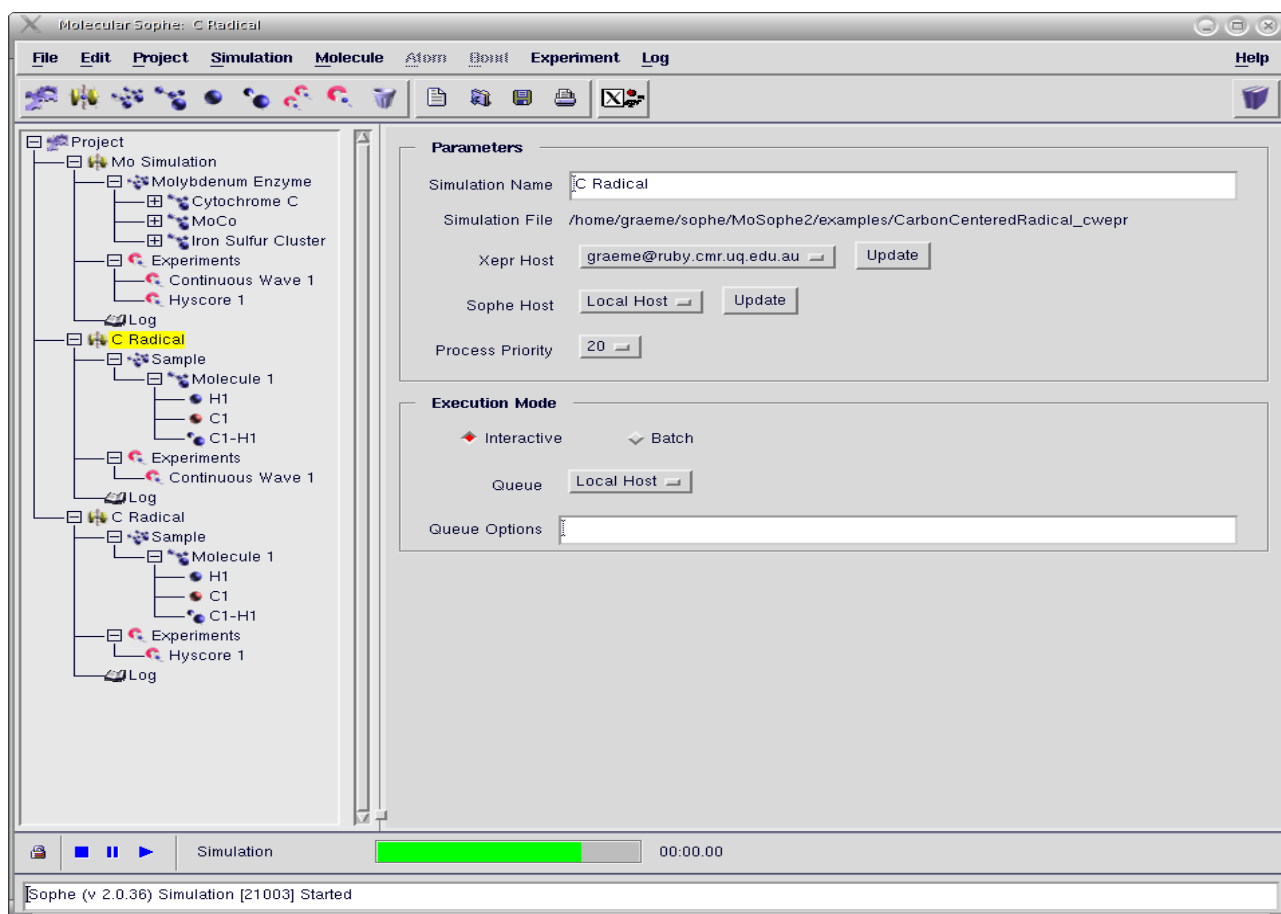


**Figure 9:** Molecular Sophe Graphical User Interface showing the Explorer Tree and the Simulation Form.<sup>§</sup>

## 2.3 Sample Form

The Sample Node (entitled 'Sample' or 'Molybdenum Enzyme' in Figure 8) is the next level of the Explorer Tree and a left click displays the Form shown in Figure 10. The sample can consist of multiple molecules (added through the Molecule menu (top toolbar or right mouse click) in different proportions which itself will be able to be optimised.<sup>§</sup> This is important for many paramagnetic samples, for example metalloproteins often have more than a single prosthetic group which is paramagnetic and consequently gives rise to multicomponent EPR spectra. Inclusion or exclusion of a particular molecule / molecular fragment can be toggled with the radio

<sup>§</sup>Note: currently, the computational code does not contain optimisation algorithms.

button adjacent to the Molecule name in the Molecule Form.

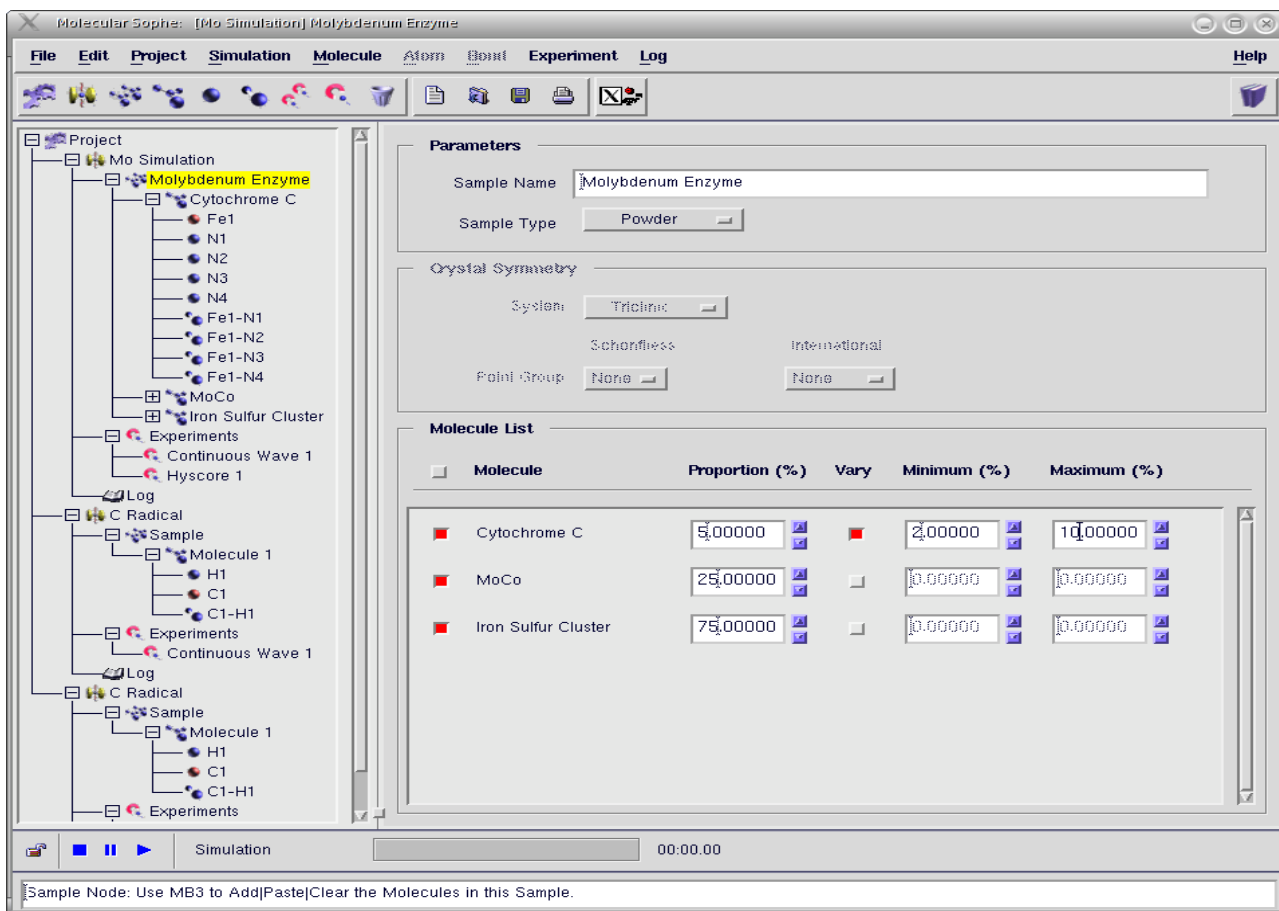


**Figure 10:** Molecular Sophe Graphical User Interface showing the Explorer Tree and the Sample Form.

The state of the sample (Crystal, Powder, Frozen Solution, Liquid, Gas or Glass) may also be chosen which will govern various aspects of the computational programme, Sophe. If the Crystal state is chosen, the user can then select the Point Group for the host crystal.

## 2.4 Molecule Form

The name of the molecule (Cytochrome C, in Figure 11) can be changed in the Molecule Form and a comment added if desired. The units for the atom's positional coordinates within the molecule and the lineshape function for all of the experiments (simulations) can be defined in the Molecule Form (Figure 11).

## 2.5 Adding Atoms

Once a molecule (Figure 11) has been added at the sample Node, the user can add atoms and subsequently bonds (really interactions, see Section 2.14) through the Molecule menu or by a right mouse click on the Molecule Node. In this context, the term bond is loosely defined to include not only bonds but also interactions between electron spins and either nuclear spins (superhyperfine interaction) or other electron spins (exchange interaction). Adding an atom displays a Periodic Table (Figure 12) from which the user can select an atom by clicking (left mouse button) on the appropriate element. The atom is then added to the Molecule in the Explorer.

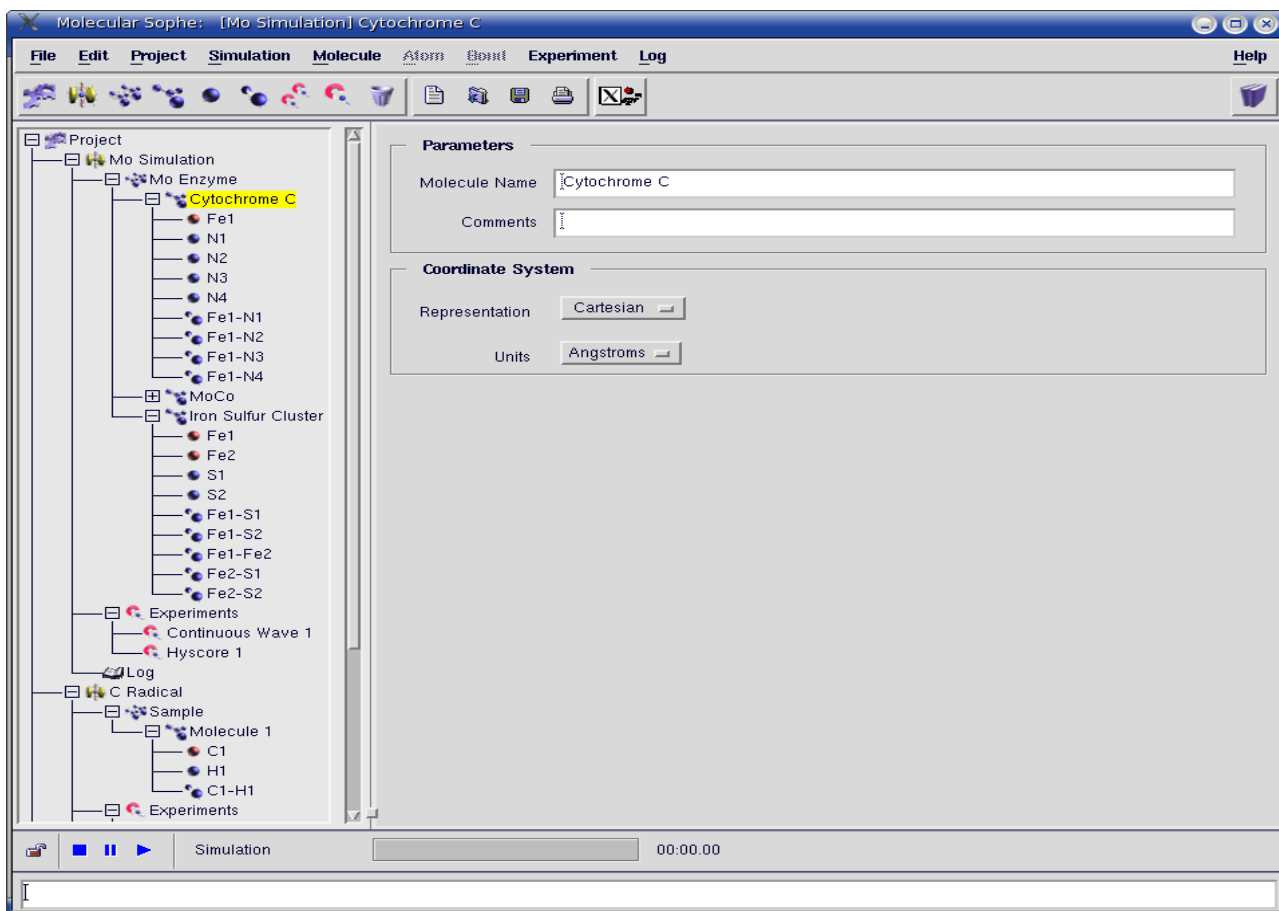


Figure 11: Molecular Sophe Graphical User Interface showing the Molecule Form.

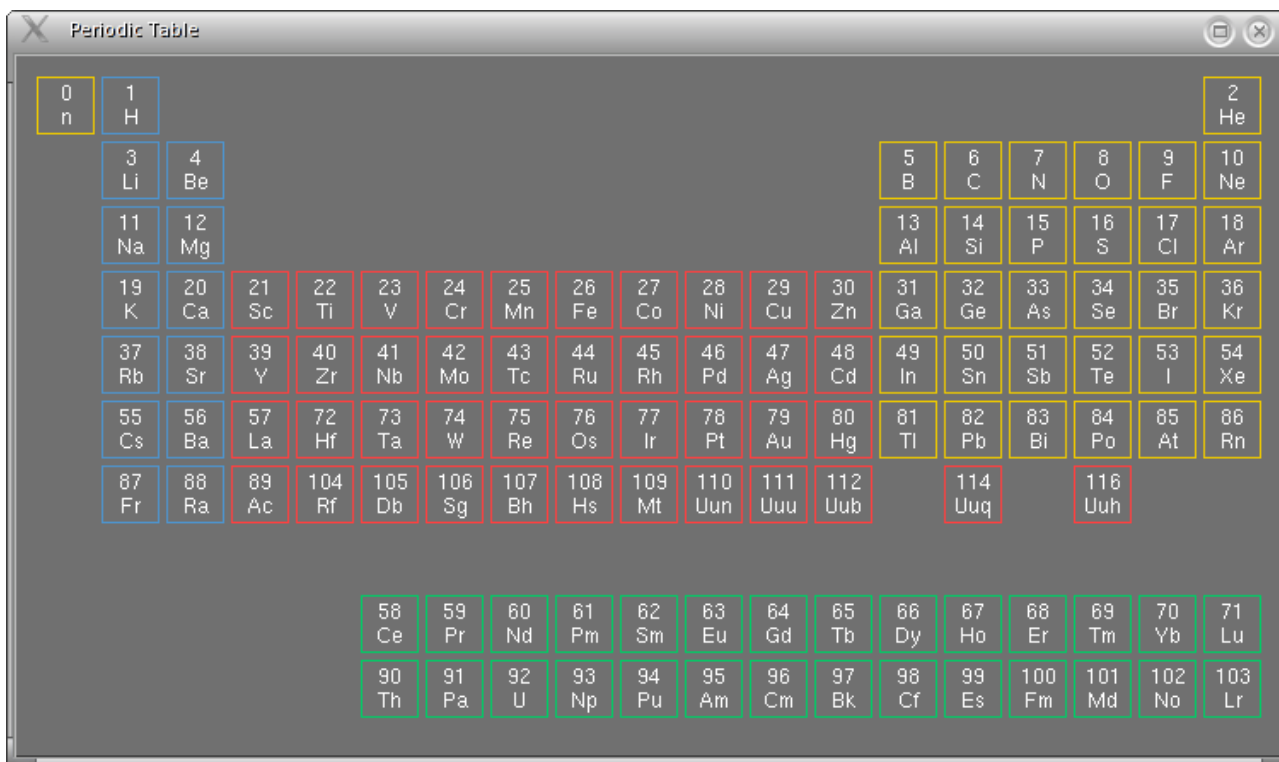


Figure 12: Molecular Sophe Graphical User Interface showing the Periodic Table.

## 2.6 Atom Form

A left mouse click on the atom (Explorer Tree) displays the atom forms: Electron Zeeman (Figures 13); Hyperfine (Figure 15); Fine Structure (Figure 16,17); Quadrupole (Figure 18); Linewidth (Figure 19); Isotopes (Figure 20) and Position (Figure 21). Each Tab also has a three state button (colour coded tick) associated with it which may be changed by a middle mouse click. The three states are: Red Tick – **Active and Valid**; Blue Tick – **Inactive and Valid** and No Tick – **Inactive and Invalid**. A right mouse click on the value, minimum, maximum fields enables the user to set the range of the parameter to be varied using the toggle up and down arrows to the right of the parameter field. Currently the Sophe computational code does not have any optimisation algorithms present as a new method is being developed for the global optimisation of all spin Hamiltonian parameters from multiple experiments.

## 2.7 Electron Zeeman Interaction ( $\beta$ B.g.S) (Figure 2)

The value of the electron spin can be selected and if greater than zero, the atom in the Explorer Tree is coloured orange (Figure 13) and the Electron Zeeman Tab now has a Red Tick. The symmetry of the Electron Zeeman Interaction can be chosen by selecting the appropriate Representation (Orthorhombic, Axial and Isotropic). The Orthorhombic Representation is shown in Figure 13. Note the g matrix is dimensionless and therefore has no units.

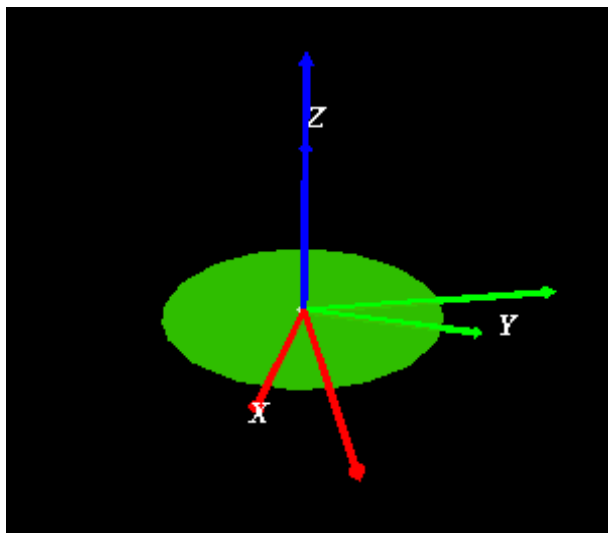
The screenshot displays the Molecular Sophe software interface. On the left is the Explorer Tree showing a project structure with a Molybdenum Enzyme simulation. The central panel shows the selected atom, Mo1 (Molybdenum), with its atomic number (42), mass (95.94), and isotopes (23). The Electron Spin is set to 1/2. The Spin Hamiltonian is set to View Matrix. The Electron Zeeman tab is active, indicated by a red tick. The Representation is set to Orthorhombic and Units to None. The Orthorhombic interaction parameters are shown in a table below.

Parameter	Value	Vary	Minimum	Maximum
$g_x$	1.97050	<input type="checkbox"/>	0.00000	2.00010
$g_y$	1.96780	<input type="checkbox"/>	0.00000	2.00010
$g_z$	1.95600	<input type="checkbox"/>	0.00000	2.00010
$\alpha$	0.00000	<input type="checkbox"/>	0.00001	0.00010
$\beta$	0.00000	<input type="checkbox"/>	0.00001	0.00010

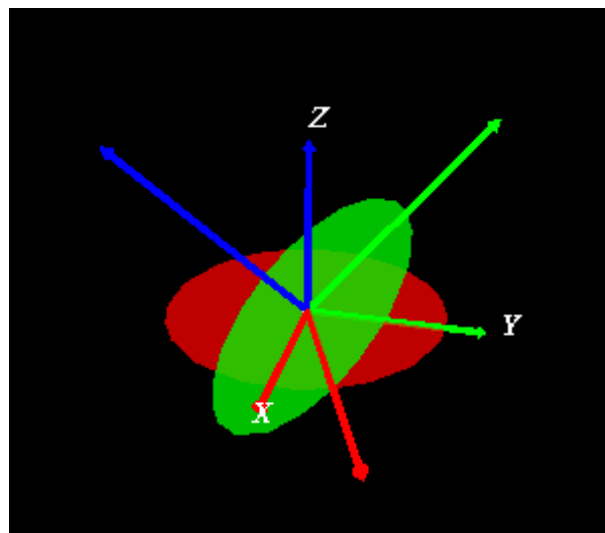
**Figure 13:** Molecular Sophe Graphical User Interface showing the Explorer Tree and the Orthorhombic Electron Zeeman Interaction Form.

For site symmetries lower than orthorhombic, one or more of the three Euler angles  $\alpha$ ,  $\beta$  and  $\gamma$  will be greater than zero. Rotation of the principal  $g$  components ( $g_x$ ,  $g_y$  and  $g_z$ ) away from the the internal (crystal)axes is shown in Figure 14.  $\alpha$  ( $\beta = \gamma = 0$ ) greater than zero rotates (about the Z axis)  $g_x$ ,  $g_y$  away from the X and Y axes (Figure 14a), corresponding to  $C_{2h}$  monoclinic sites. A rotation of  $\beta$  ( $\alpha = \gamma = 0$ ) rotates (about X) the  $g_y$  and  $g_z$  axes away from the Y and Z axes corresponds to  $C_s$  symmetric sites. In randomly oriented samples containing a single unpaired electron the  $g$  matrix is assumed to be coincident with the internal coordinate system and the hyperfine matrix is rotated from away from the  $g$  matrix.

(a)



(b)



(c)

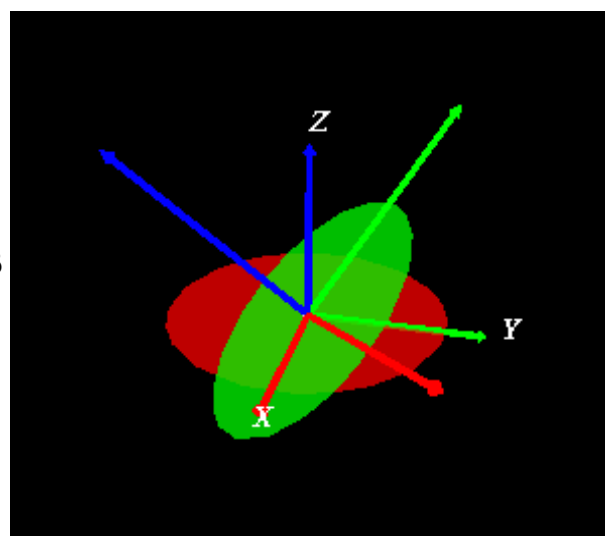


**Figure 14:** Euler Angle Rotations. (a)  $\alpha$  about Z, (b)  $\beta$  about  $g_x$  (red, unlabeled), (c)  $\gamma$  about  $g_z$  (blue, unlabeled).

The symmetry can be further lowered to triclinic symmetry ( $C_1$ ) by making  $\alpha$ ,  $\beta$  and  $\gamma$  greater than zero. The angle  $\alpha$  rotates  $g_x$  and  $g_y$  about Z, (Figure 14a),  $\beta$  rotates  $g_y$  and  $g_z$  about  $g_x$  (Figure 14b) and  $\gamma$  rotates  $g_x$  and  $g_y$  about the new  $g_z$  (Figure 14c). There are two Euler angles available for an axially symmetric site and none for an isotropic site.

## 2.8 Hyperfine Interaction (S.A.I) (Figure 2)

The Hyperfine Tab (Figure 15) is only valid if the atom containing one or more unpaired electrons (the electron spin is greater than zero) has isotopes with a non zero nuclear spin. The interaction can be turned off/on with a middle mouse click on the 'red/blue' tick on the hyperfine tab. Identical representations (isotropic, axial and orthorhombic) to those for the electron Zeeman interaction are available for the hyperfine interaction. The hyperfine coupling constants correspond to the isotope of the particular atom which has the largest isotopic abundance. For randomly orientated solutions, containing a single unpaired electron with monoclinic or triclinic symmetries, the Euler angles,  $\alpha$ ,  $\beta$  and  $\gamma$  will be non zero.  $\alpha$  corresponds to a rotation about the 'z' ( $g_z$ ) axis,  $\beta$  a rotation about the new  $A_x$  axis and  $\gamma$  a rotation about the new  $A_z$  axis.

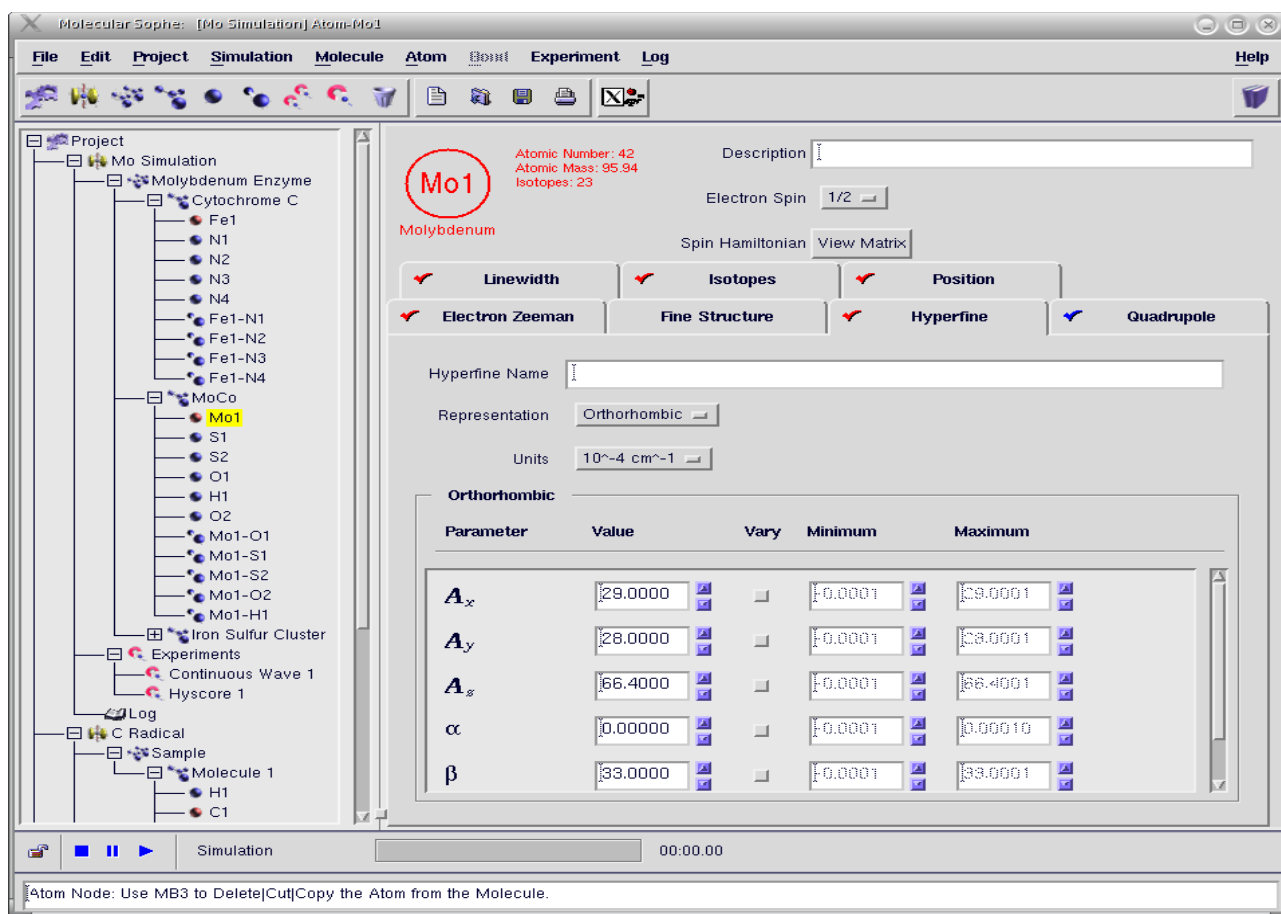


**Figure 15:** Molecular Sophe Graphical User Interface showing the Explorer Tree and the Hyperfine Interaction Form.

All interactions apart from from the electron Zeeman interaction have their own units. For the hyperfine interaction these are: MHz and  $10^{-4} \text{ cm}^{-1}$  and can be selected from the Units drop down list. Since the hyperfine couplings ( $A/g\beta$ ) measured directly from the field swept continuous wave EPR spectrum are dependent upon the g-value, it is far easier to determine A-values if the simulation employs frequency units as the g- and A-values are then independent. Consequently, we have provided a units calculator, accessible from the main Tool bar to convert Gauss and mT into units of frequency.

## 2.9 Fine Structure Interaction (S.D.S) (Figure 2)

The fine structure interaction (Figure 16) is only valid when the electron spin is greater than  $\frac{1}{2}$  and only has Axial and Orthorhombic representations as it is a traceless tensor. D is the axial zero field splitting and E/D, the rhombicity parameter can vary between 0 (axial symmetry) and 1/3 (rhombic symmetry).

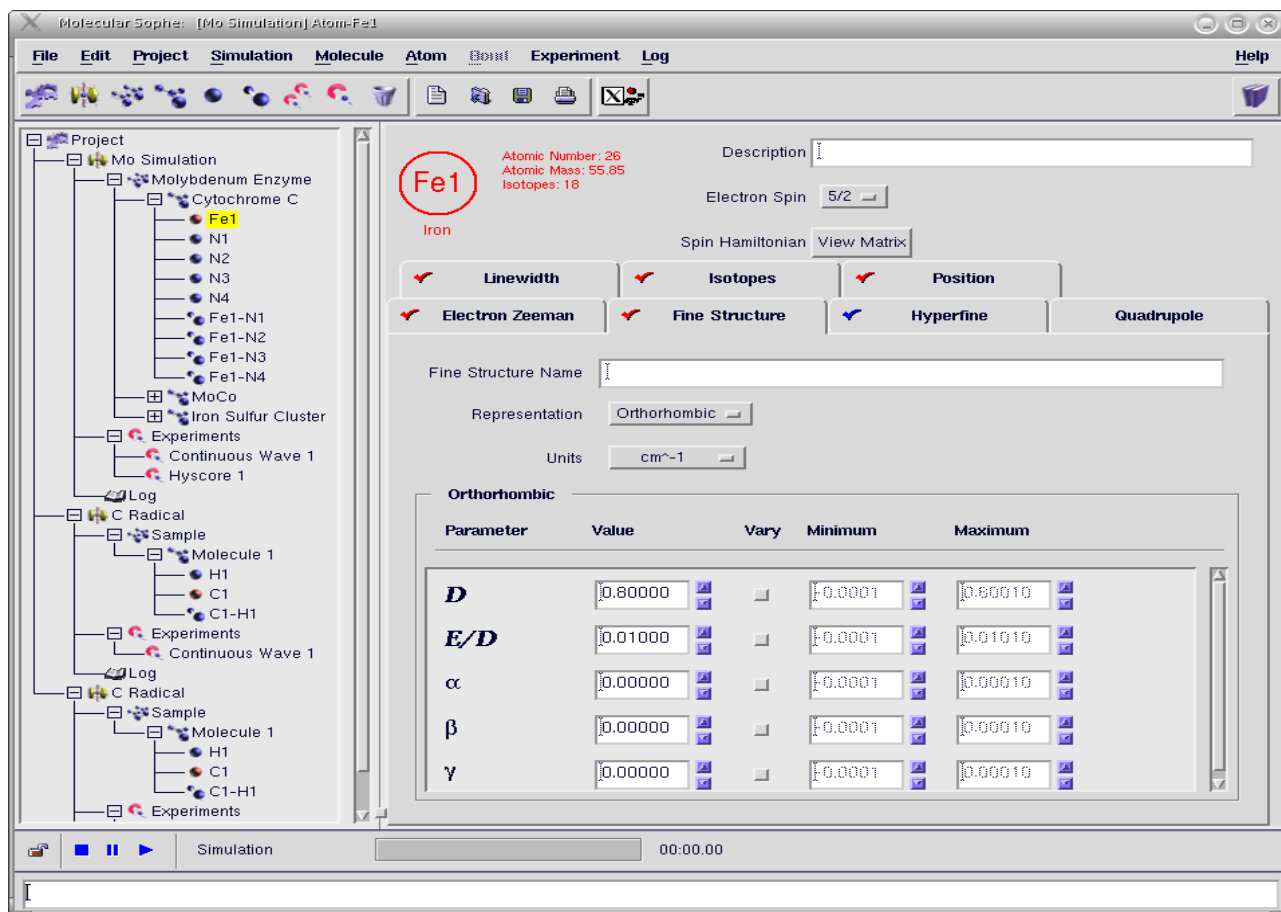


**Figure 16:** Molecular Sophie Graphical User Interface showing the Explorer Tree and the Second Order Fine Structure Interaction Form.

In addition to axial and orthorhombic representations, the Fine Structure also has B4 (fourth order corrections) and B6 (sixth order corrections). [12] If the B4 representation is chosen (Figure 17), then the terms  $b_2^0$  and  $b_2^2$  correspond to D and E, respectively. The units for the Fine Structure Interaction include MHz, GHz,  $10^{-4}\text{cm}^{-1}$  and  $\text{cm}^{-1}$ .

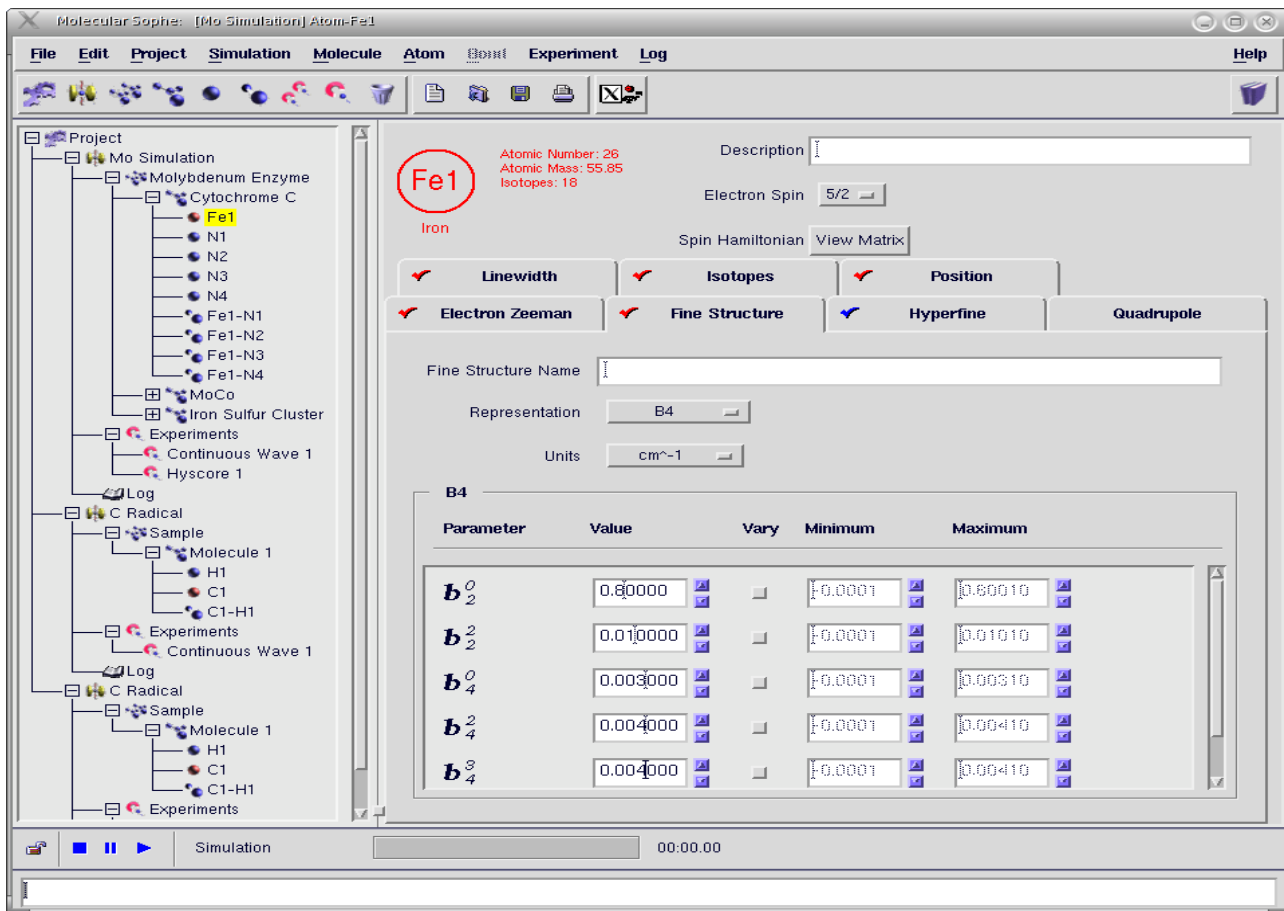


**Figure 17:** Molecular Sophe Graphical User Interface showing the Explorer Tree and the Fourth Order Fine Structure Interaction Form.

## 2.10 Quadrupole Interaction (I.P.I) (Figure 2)

The quadrupole interaction (Figure 18), a traceless tensor, is only valid when an isotope of an atom contains a nuclear spin greater than  $\frac{1}{2}$ . This interaction only has Axial and Orthorhombic representations. The quadrupole interaction is included in the calculation if it is active and valid (red tick on the interaction tab) and may be toggled off/on through a middle mouse click on the tick. When it is inactive and valid (blue tick), the parameters are written to the simulation file, but are not used in the calculation. If there is no tick on the tab, then the interaction is invalid, as there are no isotopes which have a nuclear spin greater than  $\frac{1}{2}$ .

The principal components of the quadrupole tensor (P or Q) are given by

$$\begin{aligned}
 P_x &= -P - \eta \\
 P_y &= -P + \eta \\
 P_z &= 2P
 \end{aligned}
 \tag{4}$$

From Schweiger and Jeschke [8]:

$$\begin{aligned}
 a &= e^2 q Q / ( 4 I ( 2 I - 1 ) h / 2 \pi ) \\
 P_x &= a ( - 1 + \eta ) \\
 P_y &= a ( - 1 - \eta ) \\
 P_z &= 2 a \\
 \eta &= ( P_x - P_y ) / P_z
 \end{aligned}
 \tag{5}$$

hence

$$\begin{aligned}
 P(\text{MoSophe}) &= a = e^2 q Q / ( 4 I ( 2 I - 1 ) h / 2 \pi ) \\
 \eta(\text{MoSophe}) &= - a \eta = - \eta e^2 q Q / ( 4 I ( 2 I - 1 ) h / 2 \pi )
 \end{aligned}
 \tag{6}$$

and the units for the quadrupole interaction include MHz and  $10^4 \text{cm}^{-1}$ .

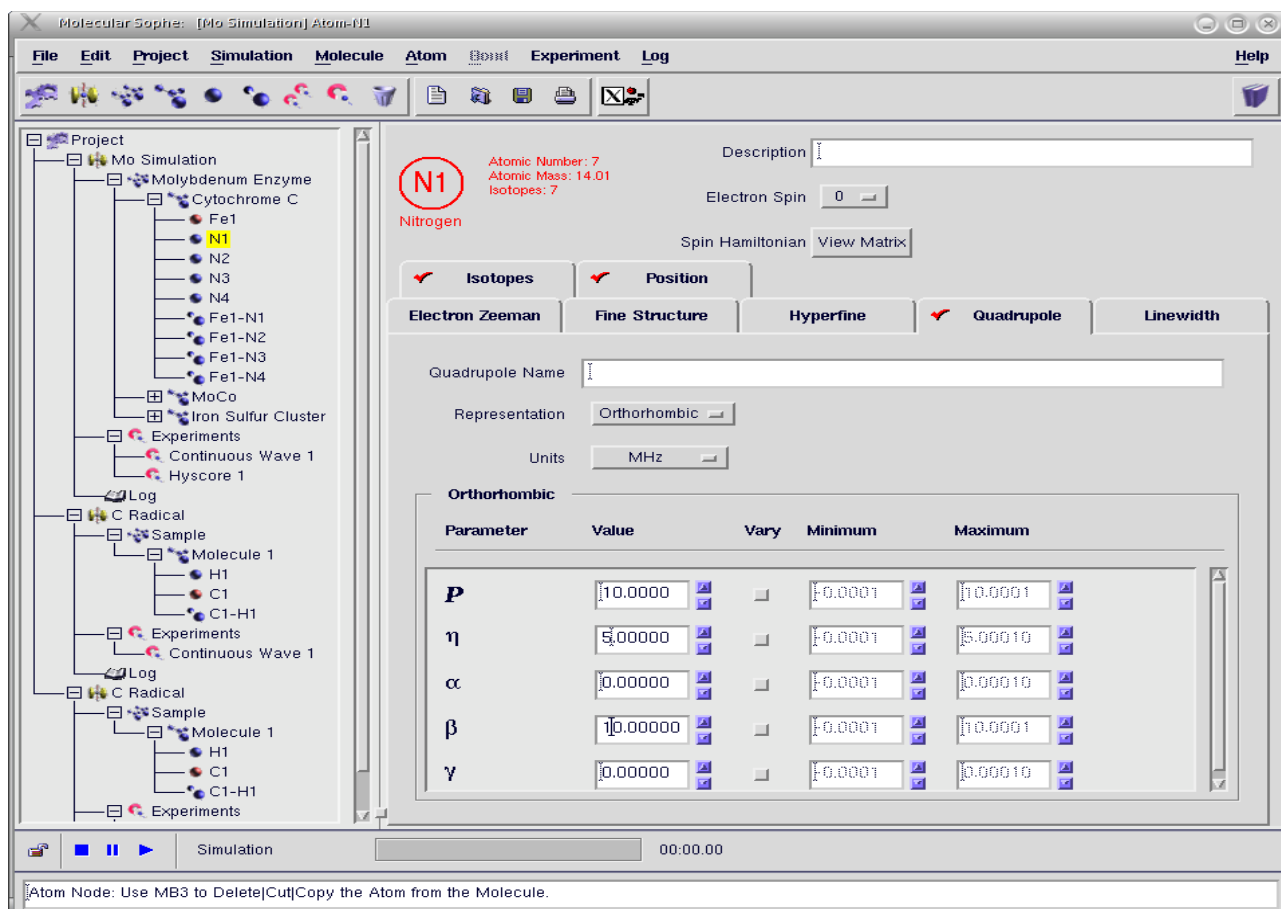


**Figure 18:** Molecular Sophe Graphical User Interface showing the Explorer Tree and the Orthorhombic Representation of the Quadrupole Interaction Form.

## 2.11 Linewidth Parameters

Molecular Sophe currently contains only a single line width model for the simulation of continuous wave EPR spectra, angular variation of  $g$  values, as described below:

$$\sigma_v^2 = (\sigma_x^2 g_x^2 l_x^2 + \sigma_y^2 g_y^2 l_y^2 + \sigma_z^2 g_z^2 l_z^2) / g^2 \quad (7)$$

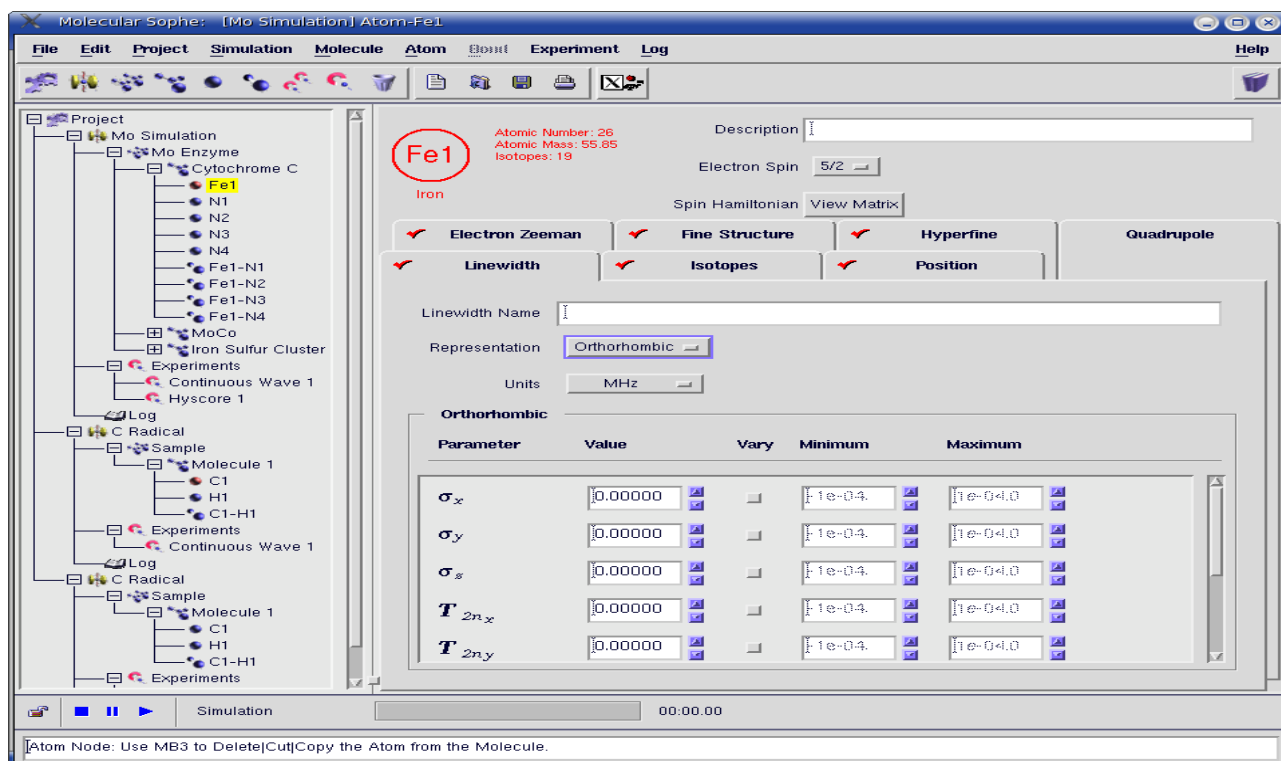


**Figure 19:** Molecular Sophe Graphical User Interface showing the Explorer Tree and the Orthorhombic Linewidth Parameter Form. Nuclear  $T_2$ 's, and Euler angles are accessible by scrolling the window..

Representations in the Linewidth Parameter Form (Figure 19) include orthorhombic, axial and isotropic symmetries. Units include MHz,  $10^{-4} \text{ cm}^{-1}$  and nanoseconds (nsec), the latter being more appropriate for pulsed EPR spectra. For pulsed EPR spectra we also include the Nuclear spin-spin relaxation time  $T_{2,N}$ . Addition of a more generalised linewidth model involving a distribution of spin Hamiltonian parameters and positional coordinates (bondlengths and orientations) is forthcoming. The approach will be similar to that employed for the D and E-strain linewidth model in the XSophe-Sophe-XeprView<sup>®</sup> computer simulation software suite.

## 2.12 Atom Isotopes

The Isotope Form (Figure 20) contains a list of the atoms isotopes and their natural abundance, nuclear spin, if known, and the quadrupole moment if the nuclear spin is greater than  $1/2$ .

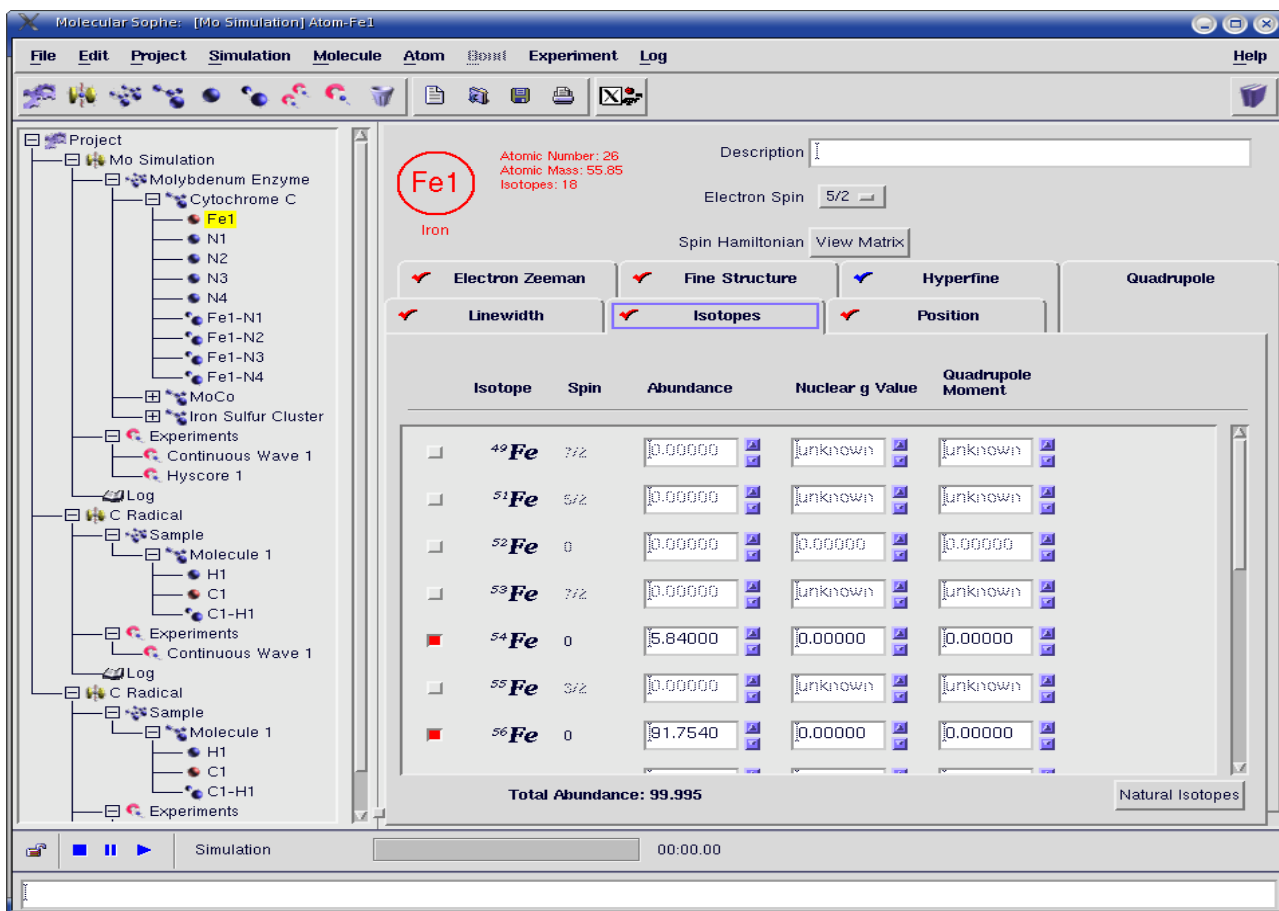


**Figure 20:** Molecular Sophie Graphical User Interface showing the Explorer Tree and the Isotope Form.

Nuclei can be chosen by selecting the check box adjacent to the isotope. The abundance of an isotope can be modified if the user requires the simulation of spectra in which the EPR active molecule contains an enriched isotope. The user should ensure that the total abundance for all isotopes corresponds to 100%. Naturally abundant isotopes can be selected by pressing the button, right hand bottom corner of the Form. A fictitious spin ( $I=0$ ) has been added to all atoms enabling a quick way of selecting an atom with ( $I=0$ ). Note that the abundance of this isotope will have to be modified in the Isotope Form.

### 2.13 Position Form

The atom's coordinates can be entered through the Position Form (Figure 21). Since it makes no sense to have mixed units for the atom's coordinates, the units for the atom's coordinates are defined in the Molecule Form (Figure 11). The atom's coordinates can be optionally used to determine the asymmetric components of either the hyperfine or exchange interaction matrices.

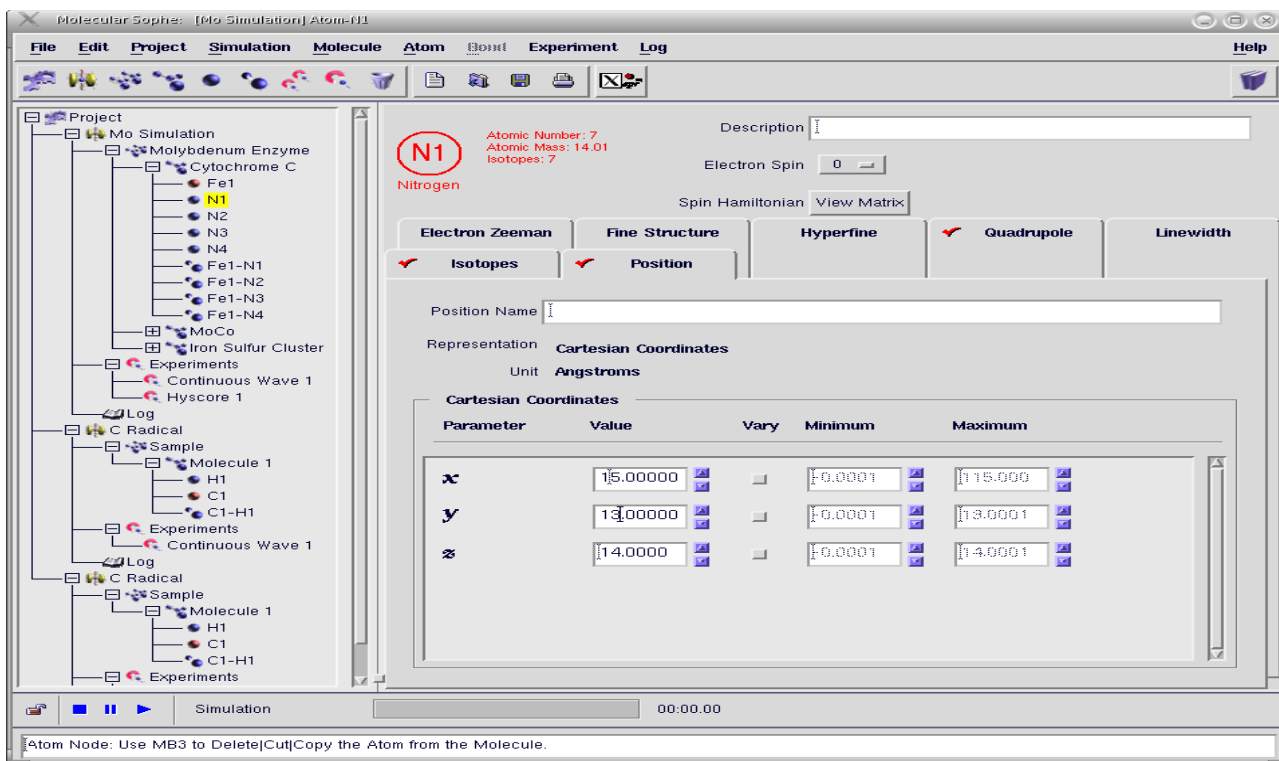


**Figure 21:** Molecular Sophe Graphical User Interface showing the Explorer Tree and the Position Coordinate Form.

## 2.14 Adding Bonds

Superhyperfine and Exchange interactions occur between an atom containing one or more unpaired electrons and the nucleus of an atom with a non zero nuclear spin or another atom containing unpaired electrons, respectively. In the graphical user interface these interactions are created through the Add Bond window (Figure 22) accessed either by a right mouse click on the Molecule Node, clicking the Bond Icon (Top menu) or through the Molecule Menu. The Add Bond window allows the user to define the interaction (bond) between the atom containing the unpaired electron(s) and the atom containing the nucleus. It is important that the atom containing the unpaired electrons is identified through the left hand combo box (Figure 22). Inclusion of the dipole dipole interaction can be chosen by selecting the check box.

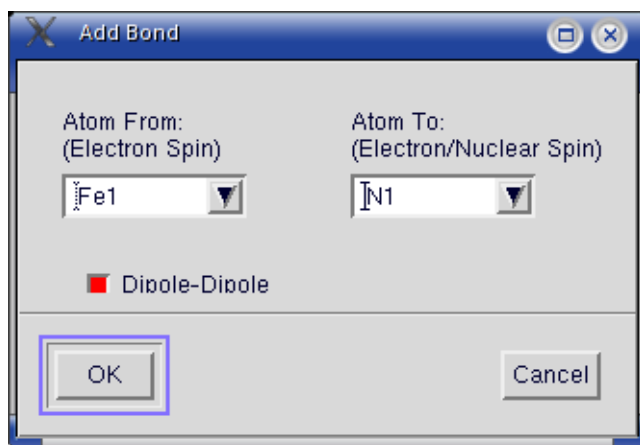


**Figure 22:** Molecular Sophe Graphical User Interface showing the Add Bond window. Note the atom containing unpaired electrons occurs in the left hand combo box. In this example **Fe1** is the atom containing unpaired electrons.

Having chosen the dipole-dipole interaction, the user should ensure that the positional coordinates are entered for each atom defined in the bond, in this case Fe1 and N1.

## 2.15 SuperHyperfine Interactions (S.A.I) (Figure 2)

Once the bond is created in the Explorer Tree then a left mouse click on the bond opens the Superhyperfine Interaction Form (Figure 23). The representations and units for the superhyperfine interaction are identical to those for the hyperfine interaction (Section 2.8).

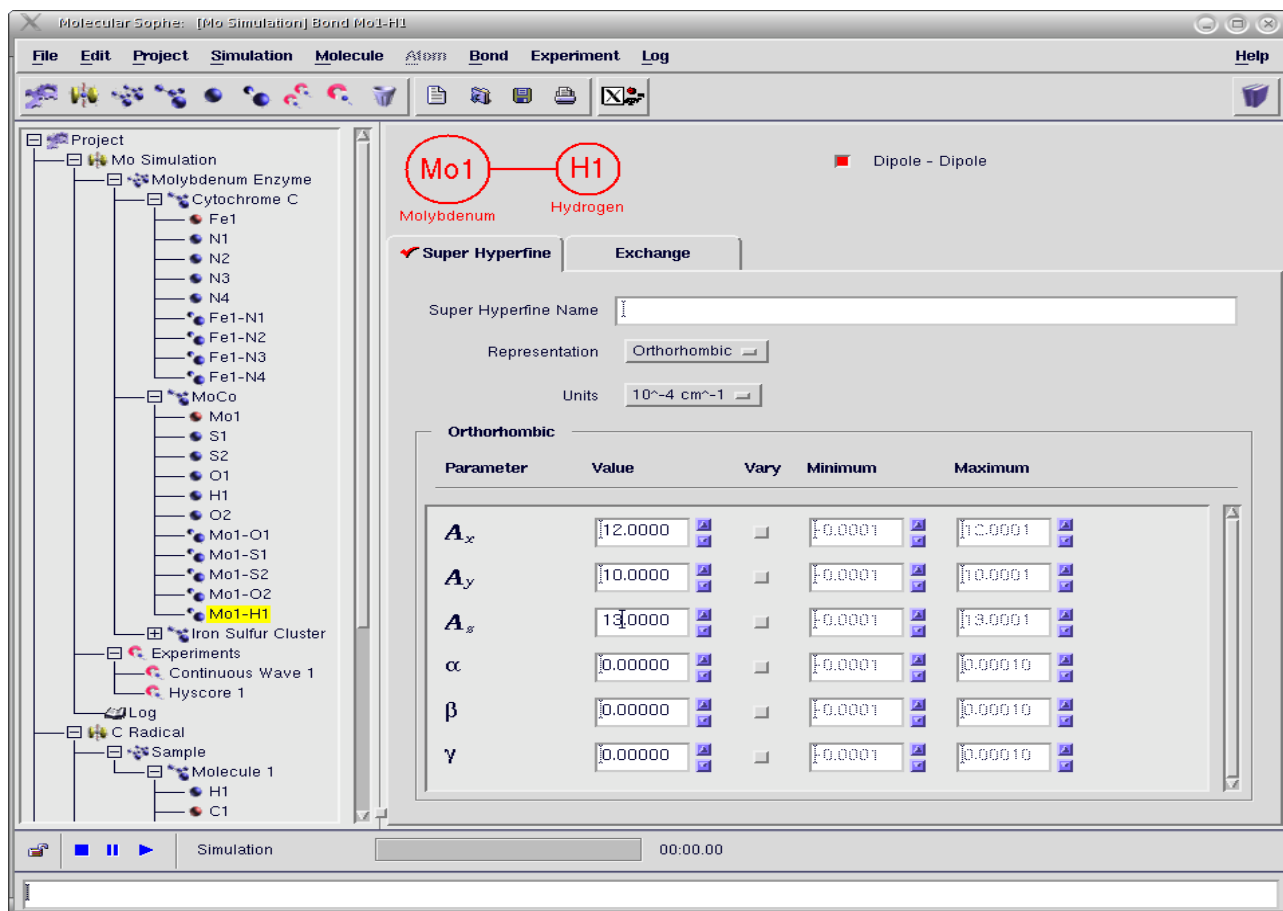


**Figure 23:** Molecular Sophie Graphical User Interface showing an orthorhombic Superhyperfine Interaction.

The only difference is that the dipole-dipole interaction can be switched off, on or from the Form by selecting the check box. If the check box is selected then the internuclear distance and orientation is calculated from the positional coordinates of both atoms and the anisotropic interaction is calculated subsequently and added to the parameters. The superhyperfine interaction can be toggled off / on by clicking (middle mouse button) on the red / blue tick radio button on the superhyperfine tab.

## 2.16 Exchange Interaction (S.J.S) (Figure 2)

The exchange interaction involves the interaction of two or more paramagnetic centres, for example the  $[\text{Fe}_2\text{S}_2]^{2+/1+}$ ,  $[\text{Fe}_3\text{S}_4]^{1+/0}$ ,  $[\text{Fe}_4\text{S}_4]^{3+/2+/1+}$  (Figure 1). The total spin Hamiltonian for an exchange coupled system is given by the sum of the individual spin Hamiltonians and the interaction Hamiltonian (Eqns 1 and 2 respectively). The isotropic exchange interaction involves the overlap of molecular orbitals, whilst the anisotropic exchange interaction (dipole-dipole coupling) is a through space interaction. In the graphical user interface, the user first adds a “bond” between two atoms containing one or more unpaired electrons (ie.  $S_1, S_2 \geq 1/2$ ). Of course, in metalloproteins, this may be an interaction and not a real bond. Once the bond has been created a left mouse click on the bond will open up the bond Form (superhyperfine and exchange interaction tabs). Clicking on the Exchange Interaction Tab opens the exchange Form (Figure 24 , b and c). Currently there are four representations (Isotropic, Anisotropic (Axial and Orthorhombic Symmetry) and Antisymmetric). Given the spin Hamiltonian in Eqn. 2, a positive value of  $J_{\text{iso}}$  corresponds to antiferromagnetic coupling between the two atoms and for inorganic chemists who are used to working with the Hamiltonian ( $H = -2J_{\text{iso}}^* S_1.S_2$ , \* is used here to distinguish the two values),  $J_{\text{iso}}^* = -J_{\text{iso}}/2$ .

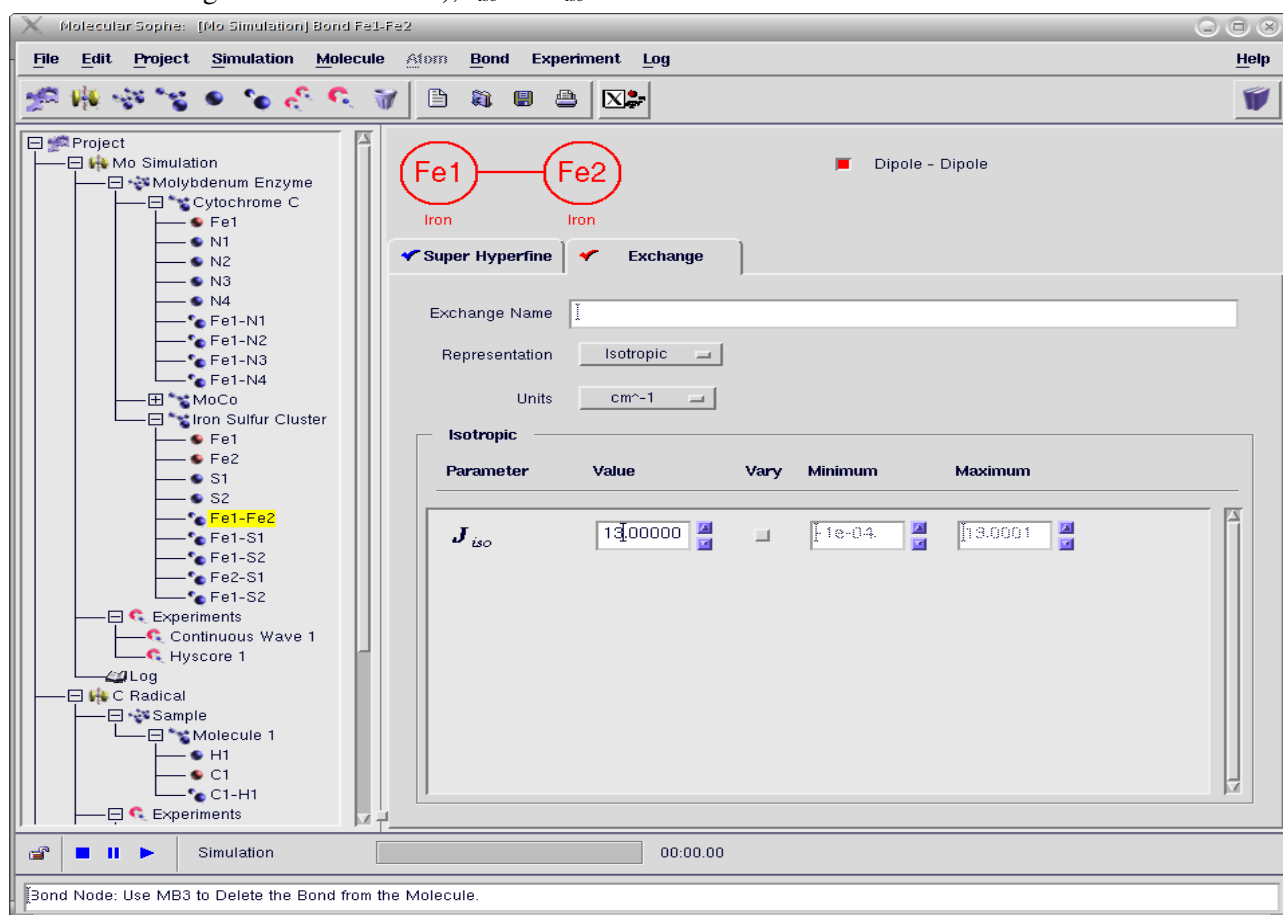


**Figure 24:** Molecular Sophe Graphical User Interface showing (a) the Isotropic Exchange Interaction.

The anisotropic exchange parameters can either be added through the Anisotropic Representation (Axial - Figure 24 or orthorhombic) or calculated from the positional coordinates of the two atoms through the dipole-dipole interaction, by toggling the Dipole-Dipole check box (red enabled).

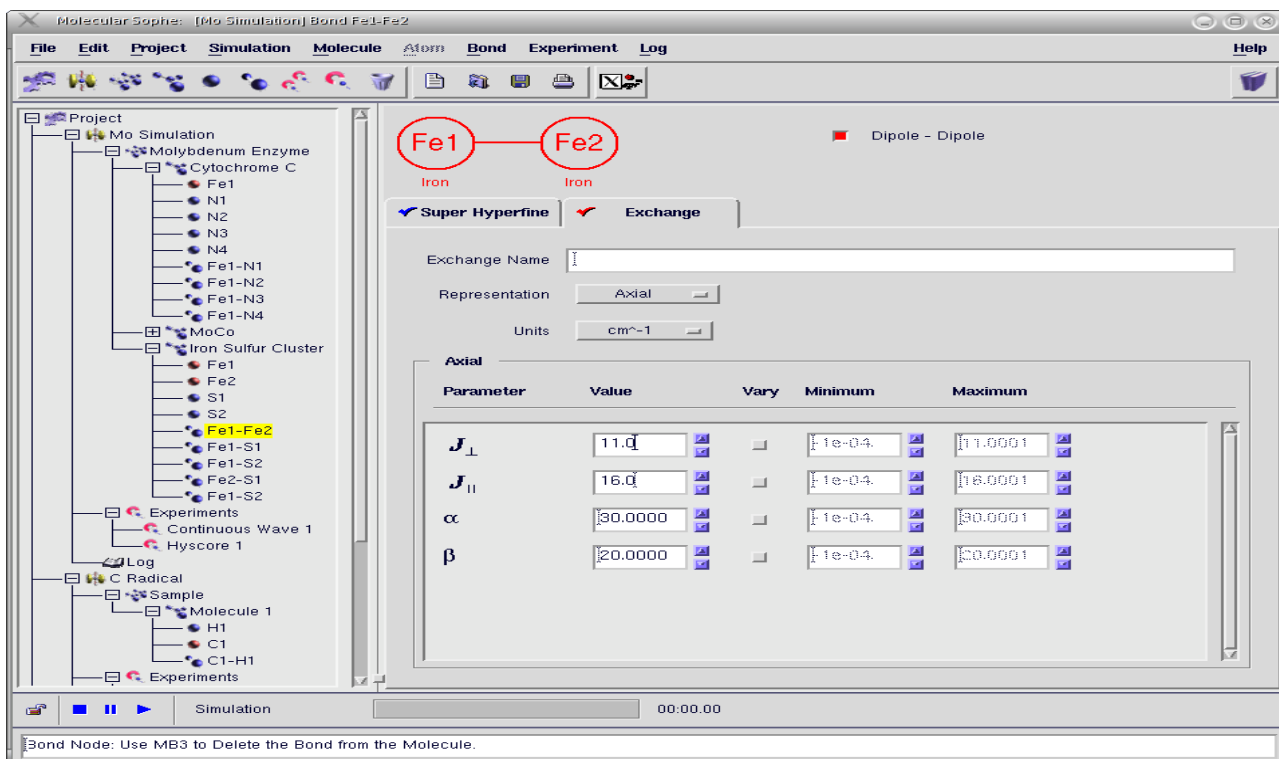


Figure 24: Molecular Sophe Graphical User Interface showing (b) the Axial Anisotropic Exchange Interaction.

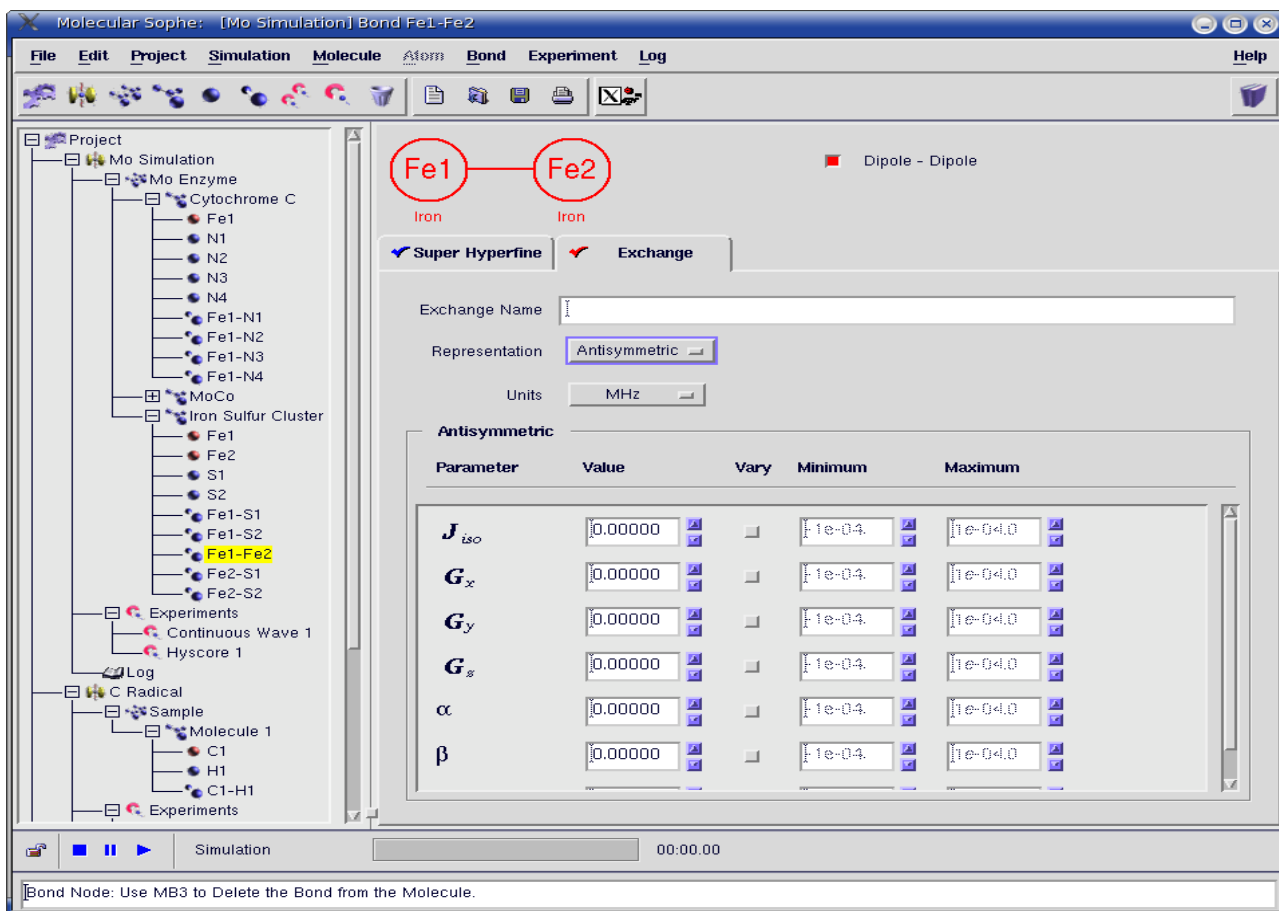
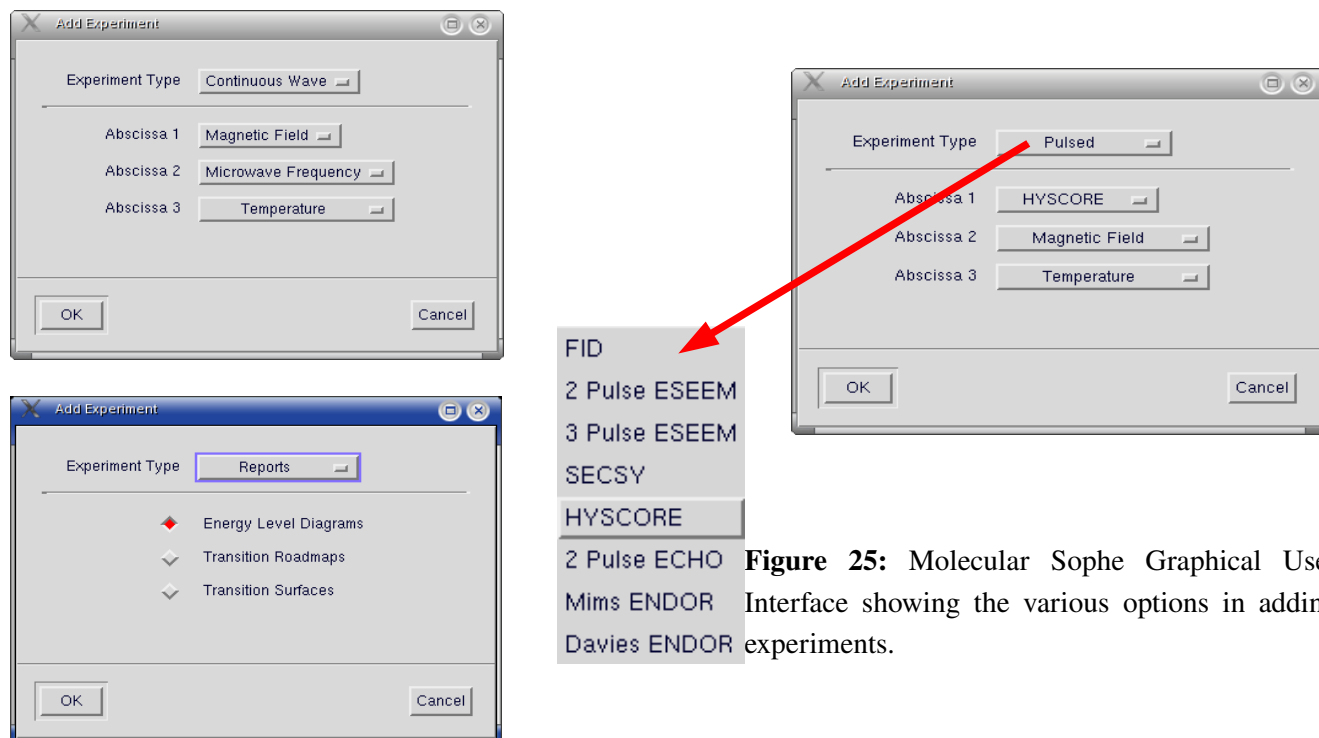


Figure 24: Molecular Sophe Graphical User Interface showing (c) the Antisymmetric Exchange Interaction.

The antisymmetric exchange term (Eqn. 2,  $G_{ab} S_a \times S_b$ ) can be included by selecting the Antisymmetric exchange representation (Figure 24 c), which includes  $J_{iso}$  and the principal components of the G matrix and three Euler angles. Dipole-Dipole terms can be also included by selecting the Dipole-Dipole radio button (red is active). This interaction has been found to be important for trinuclear copper(II) systems where the orbitals containing the unpaired electrons partially overlap.

## 2.17 Adding Experiments

Once the sample has been created, the user can now perform a range of experiments. The choice of experiment is accessed through the Experiment Menu or by a right mouse click on the Experiment Node and selecting an Experiment Type (Figure 25). As can be seen in Figure 25, the range of experiments include CW-EPR, Pulsed EPR (FID, 2 Pulse ESEEM, 3-Pulse ESEEM, SECSY, HYSCORE, 2 Pulse Echo, MIMS and Davies ENDOR) and Reports (Energy Level Diagrams, Transition Roadmaps and Transition Surfaces). The ENDOR experiments (MIMS and DAVIES) are currently being developed. Multidimensional experiments can also be performed by adding additional abscissas (Temperature, Microwave Frequency, Goniometer Angle and Magnetic Field). Currently we have no means to visualise four dimensional data sets, thus orientational selective HYSCORE measurements cannot be visualised as a single dataset. This can be overcome in the short term by duplicating the HYSCORE Experiment (right mouse click on the HYSCORE Experiment and select Copy Experiment) and adjusting the static magnetic field in the copied Experiment. This process can be repeated as often as necessary.



**Figure 25:** Molecular Sophie Graphical User Interface showing the various options in adding experiments.

## 2.18 Experiment Form

The Experiment Form (Figure 26) contains the list of experiments available for selection. Individual experiments can be included/excluded by selecting/deselecting the check box adjacent to the experiment option. Each experiment also has a weighting which will be used when optimising spin Hamiltonian parameters from multiple experiments.

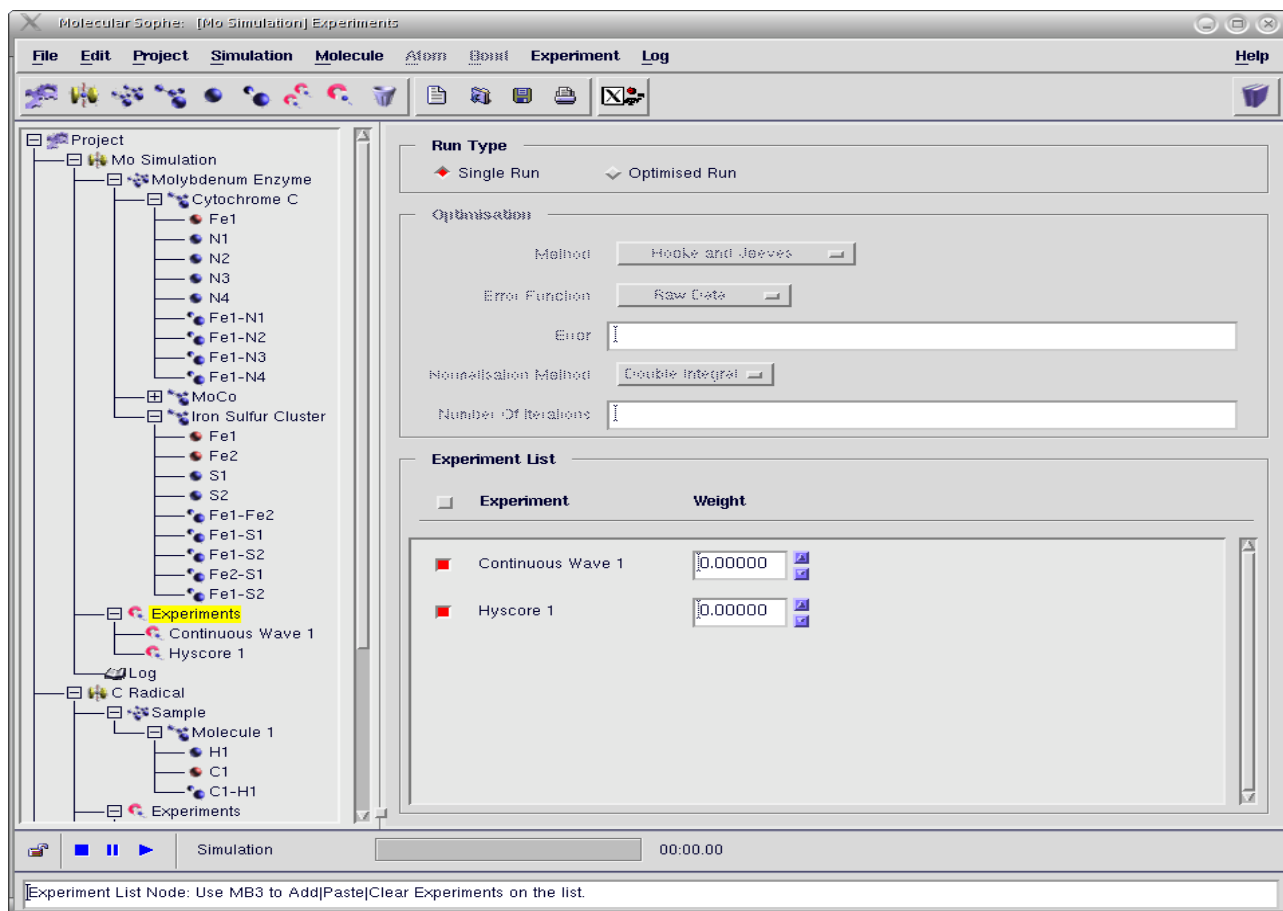


**Figure 26:** Molecular Sophe Graphical User Interface showing the Experiment Form.

The following sections describe three experiments: CW EPR, HYSOCORE and Energy level Calculations.

## 2.19 Continuous Wave (CW) EPR Experiments

Once a CW EPR Experiment has been added to the Explorer Tree, the CW-EPR Experiment forms can be viewed by a left mouse click on the CW EPR Experiment Node in the Explorer Tree. The Continuous Wave EPR Experiment Form has Continuous Wave, Sophe, Spectra and Configuration Tabs. The Sophe, Spectra and Configuration Tabs are common to all experiments and will be dealt with separately.

The Continuous Wave Form (Figure 27) allows the user to enter values concerning the field sweep (centre field, sweep width and the number of data points), microwave frequency, detection mode and temperature. The units for the field sweep parameters include Gauss, mTesla and Tesla and those for the microwave frequency are

MHz, GHz and THz. The harmonic corresponds to the  $n^{\text{th}}$  derivative spectrum, where  $n=0, 1$  and  $2$ , the first derivative being the normal mode acquired on an EPR spectrometer using phase sensitive detection. Whilst experimentally the phase of the EPR spectrum can vary anywhere between  $0^\circ$  and  $180^\circ$ , only the limits are really useful at present. Setting the phase to  $180^\circ$  inverts the spectrum. Boltzmann populations for each energy level are automatically included and consequently the temperature will affect the intensity of the EPR signal between two different energy levels. For exchange coupled systems the magnitude and sign of  $J_{iso}$  may be obtained from a variable temperature spectrum/simulation. Similarly, if the zero field splitting is larger than the microwave quantum, then a variable temperature spectrum/simulation can provide the sign and magnitude of the axial zero field splitting (D).

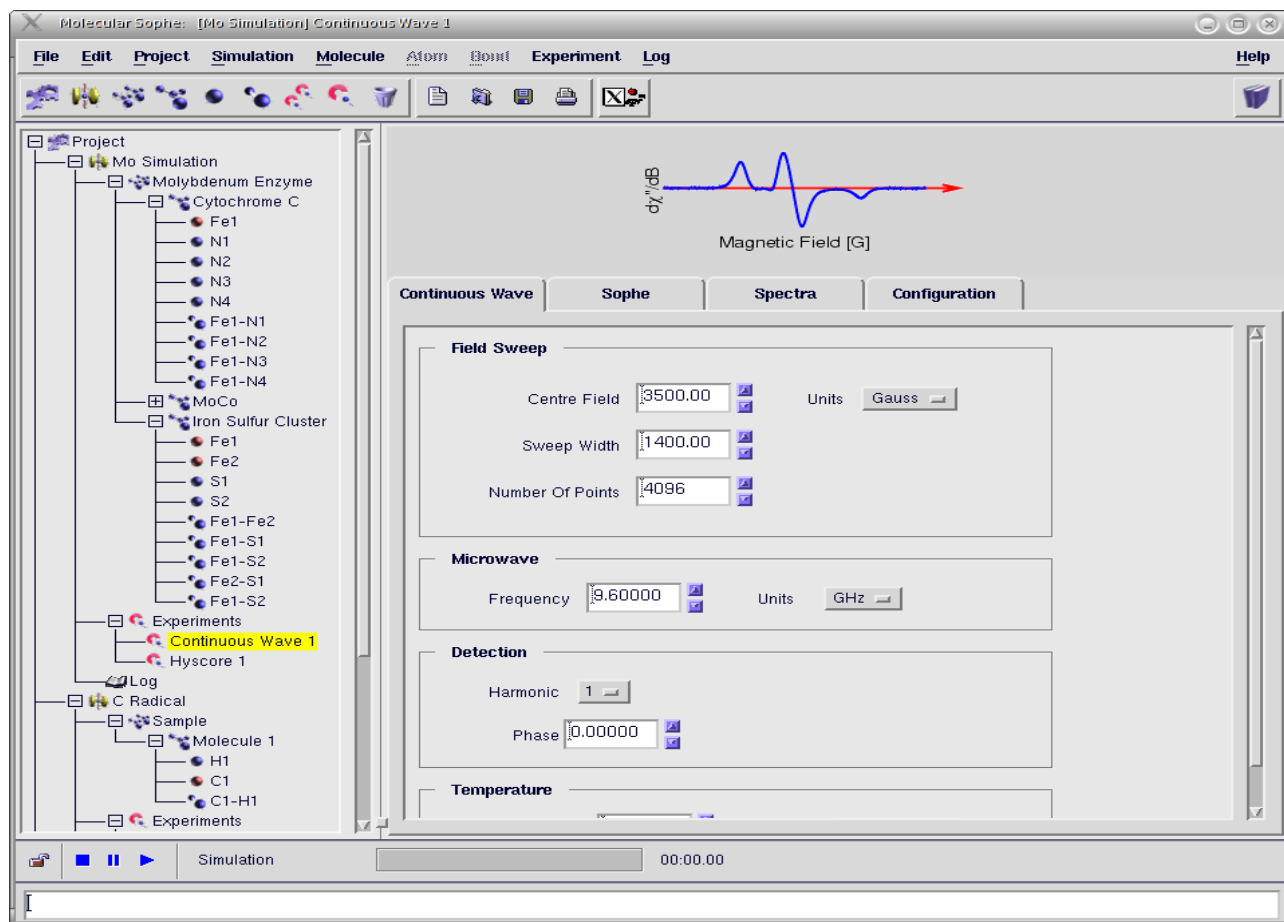


**Figure 27:** Molecular Sophe Graphical User Interface showing the Continuous Wave Experiment Form and specifically the Continuous Wave tab.

If the user selected a multidimensional CW EPR spectrum, for example multifrequency, variable temperature experiment (Figure 28) then additional tabs are added to the CW EPR Experiment Form, namely, Temperature and Frequency. These tabs allow the user to define the start and increment values for the particular parameter and the number of data points in the additional dimension. The parameters in this tab, for example the temperature tab, overrides the temperature setting in the Continuous Wave tab. This also applies to the microwave frequency and Goniometer Angle.

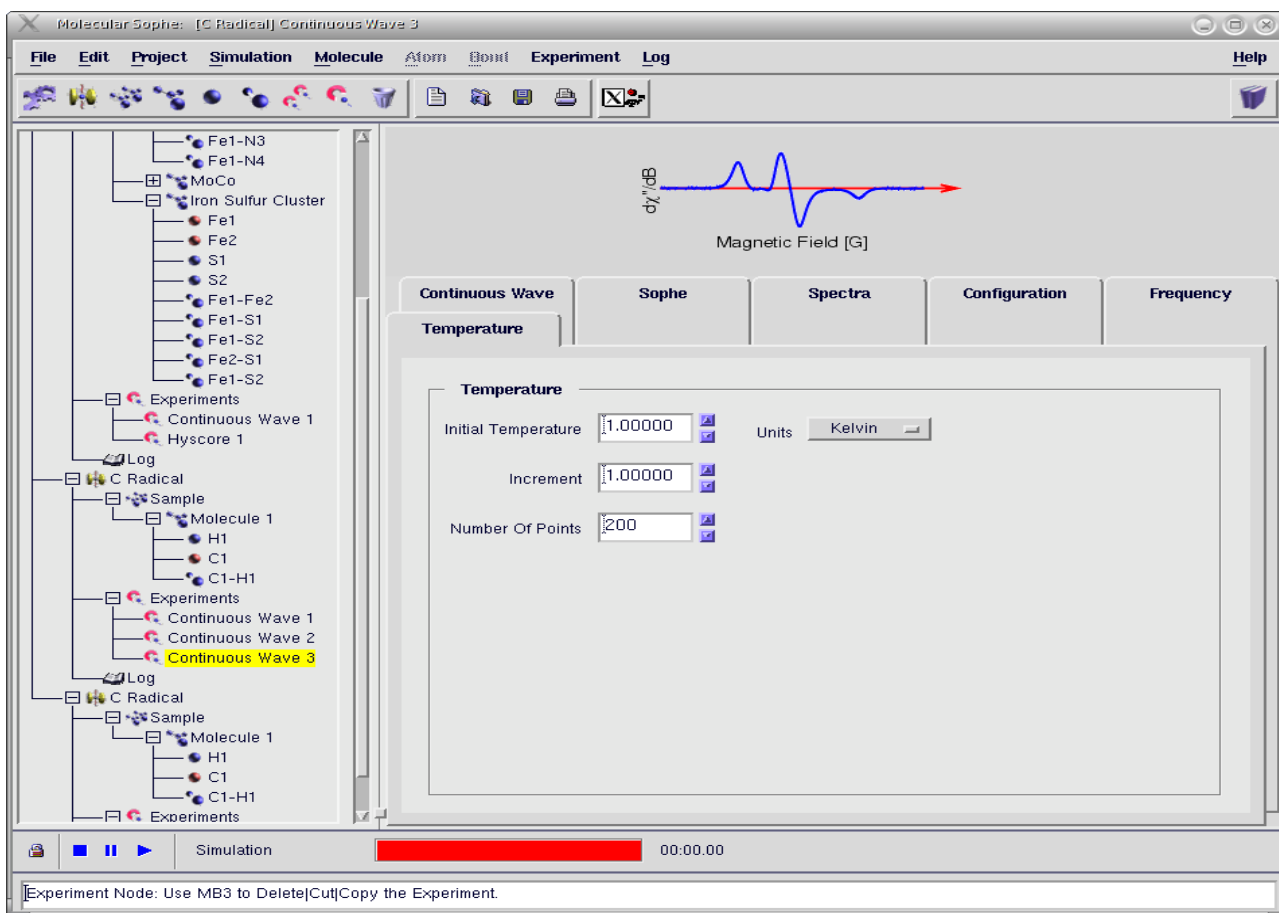


**Figure 28:** Molecular Sophe Graphical User Interface showing the Temperature Form of a Multidimensional Experiment.

## 2.20 Sophe Computational Parameters

The Sophe tab (Figures 29 and 30) allows the user to input various parameters required for the computational calculation, define the SOPHE Grid (Section 3.1) and determine the transition probability (selection rules to be used). In the Calculation Panel, matrix diagonalization is currently the only method available for performing continuous wave and pulsed EPR simulations. The field segmentation algorithm employed in the computational program (Sophe) requires the user to define the number of field segments where matrix diagonalization will be employed. Whilst the number of field segments can usually be set to one or two, sometimes sharp features (vertical lines) may be apparent in the spectrum and these arise from the presence of multiple transitions within a segment. If this occurs then the number of segments should be increased.

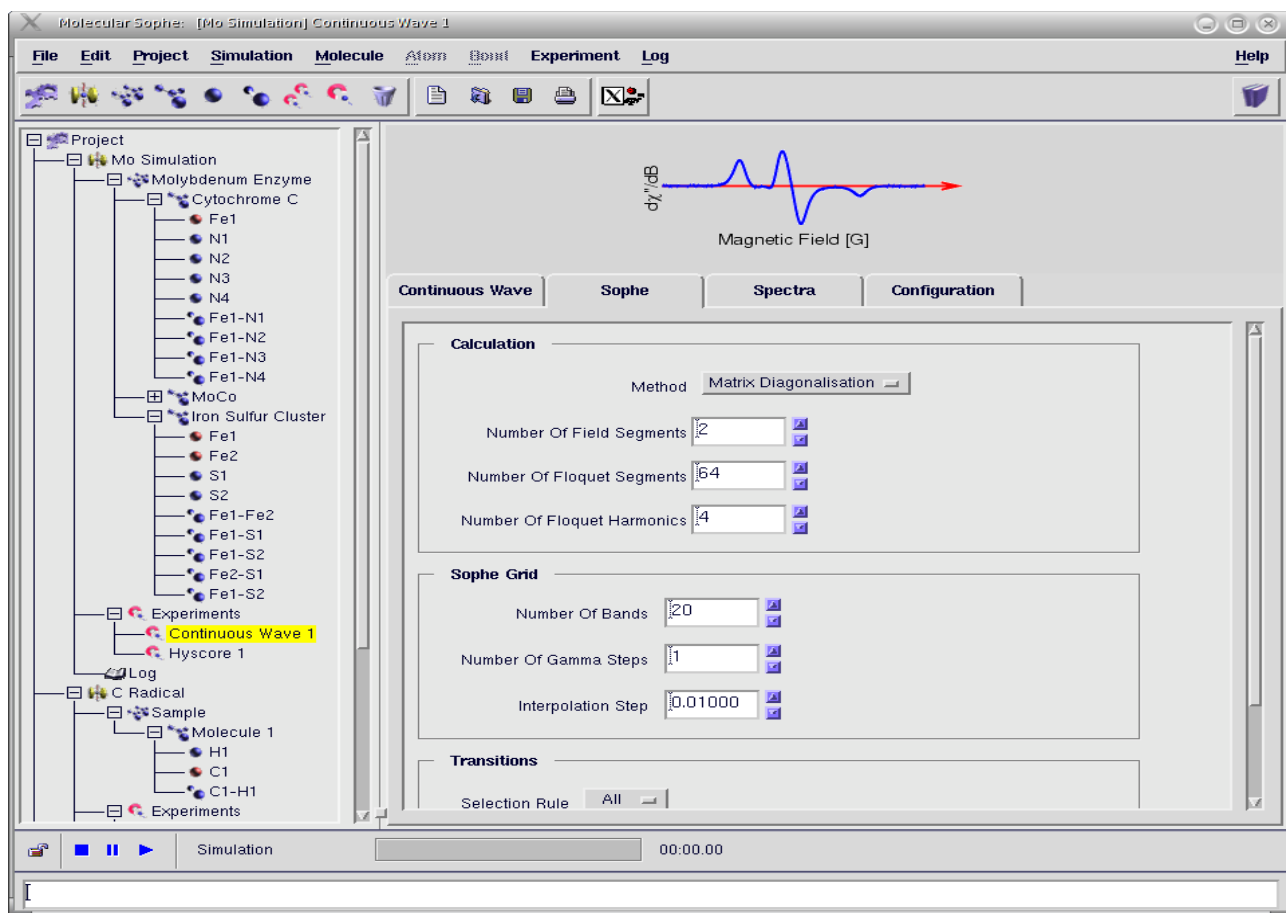


**Figure 29:** Molecular Sophe Graphical User Interface showing the upper part of the Sophe Tab within the CW EPR Experiment Form.

Floquet Theory is often used to describe the evolution of a periodic time dependent semiclassical spin Hamiltonian in magnetic resonance. The number of Floquet Segments and Floquet Harmonics are only used in the simulation of Pulsed EPR experiments. The number of Floquet Segments refers to the number of segments microwave pulses are divided into so that within each segment the time dependent spin Hamiltonian is 'assumed' to be time independent. These segments are used to calculate the average Hamiltonian for the pulse. When the number of Floquet Segments is set to zero, the representation is reduced to the rotating frame which is only appropriate for species in which there is no significant electron spin state mixing, for example species containing only a single unpaired electron. For high spin and exchange coupled molecules, the number of Floquet Segments should be greater than zero.

The SOPHE grid (Section 3.1) is defined by the number of orientations between the 'z' and 'x' global coordinate system. The number of gamma steps, used in the simulation of pulsed EPR experiments, is used to calculate the transition probabilities of the echo intensities. Since the Sophe interpolation scheme has not been implemented into Molecular Sophe, the Sophe interpolation step is not currently used.

The Selection Rules are used to define the transition threshold for inclusion of transitions in the simulation. Setting the selection rules to 'ALL' sets the transition threshold to 1.0, None sets it to zero and Some is somewhere in between, which the user can define to only observe forbidden or allowed transitions. In principle the Selection Rules should always be set to 'ALL'.

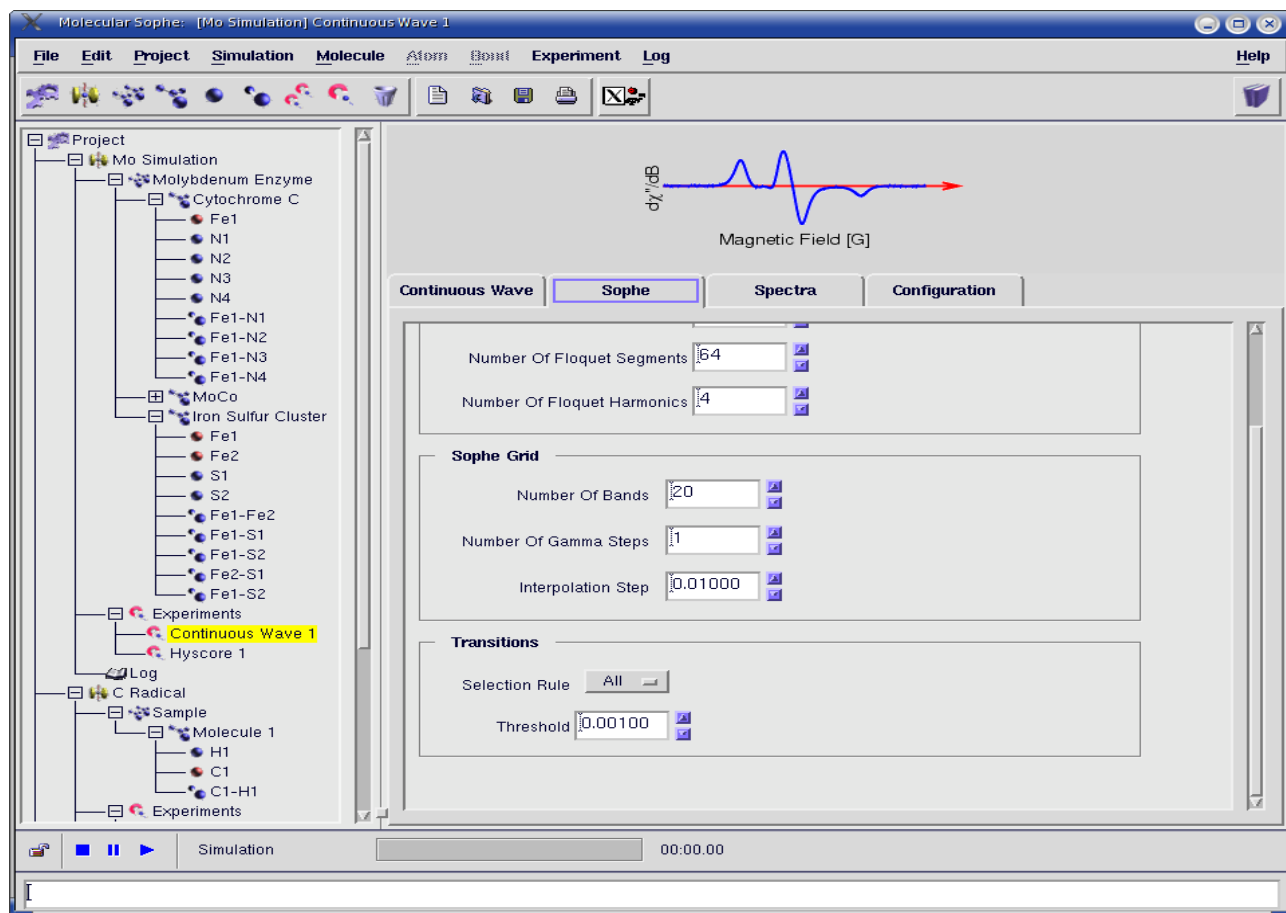


**Figure 30:** Molecular Sophe Graphical User Interface showing the (b) lower part of the Sophe Tab within the CW EPR Experiment Form.

## 2.21 Spectra Input/Output

Molecular Sophe employs a data directory to store all of the information associated with a particular simulation. Apart from the input file for the computational programme, Sophe, **ALL** of the input and output spectra are also stored in this directory. This simplifies the organization of simulations. The Spectra Form (Figure 31) allows the import of an experimental spectrum into the Molecular Sophe data directory and the export of simulated and experimental spectra from this directory. A title for the experiment can also be added which is added to the resultant simulation spectrum. The user can also choose the filetype (Be3st and ESP Bruker formats) of the spectrum to import into the data directory and the output file format (Be3st and ESP Bruker formats, GNUPlot, Image Plot, Postscript and OpenInventor).

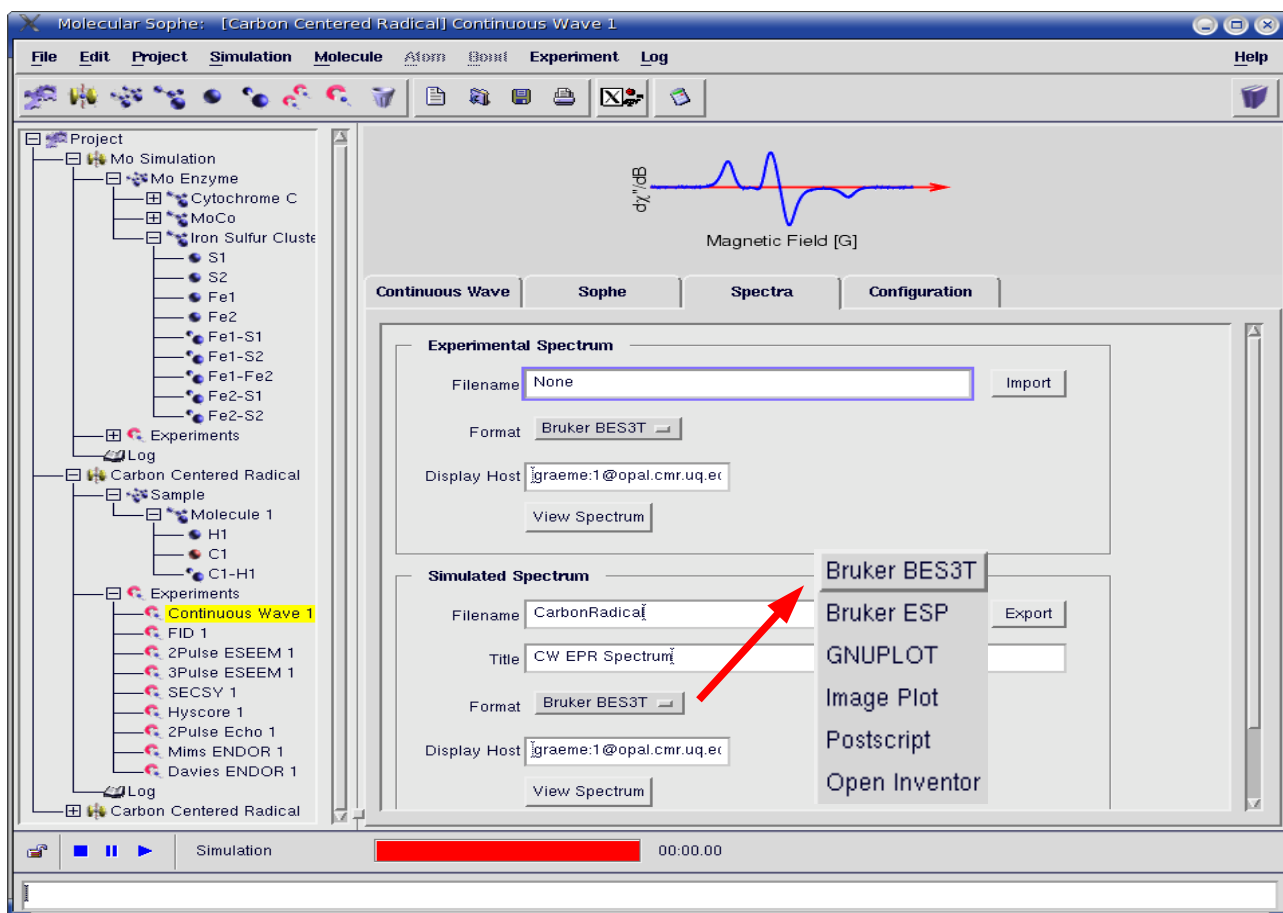
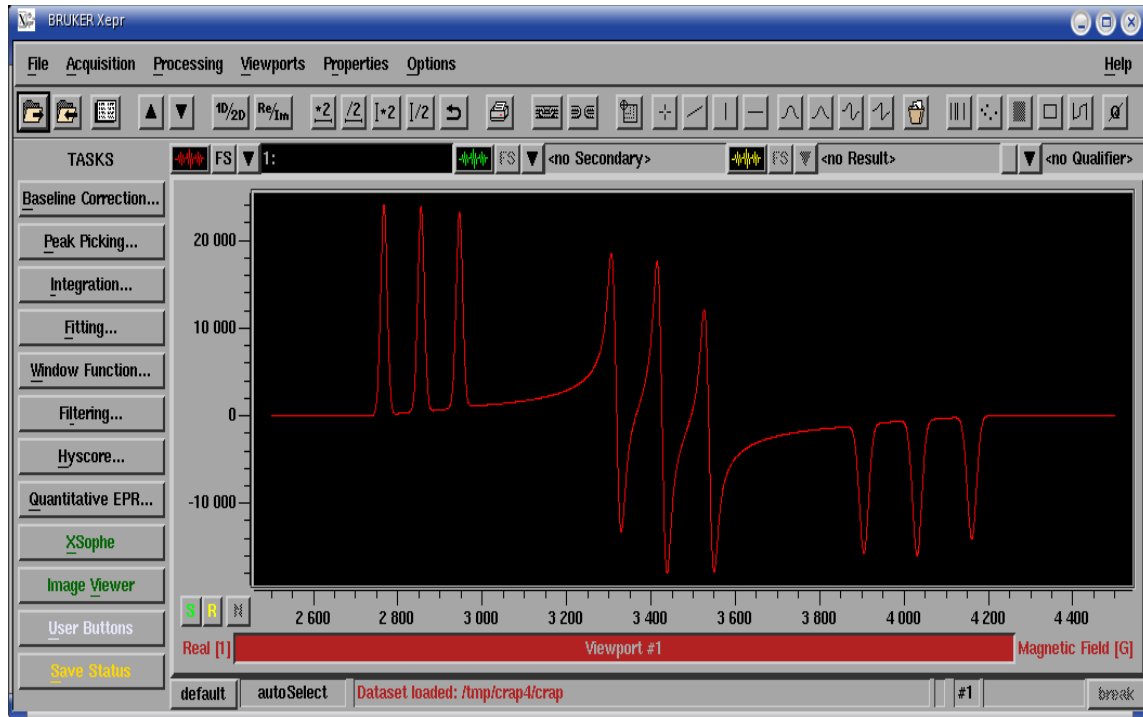


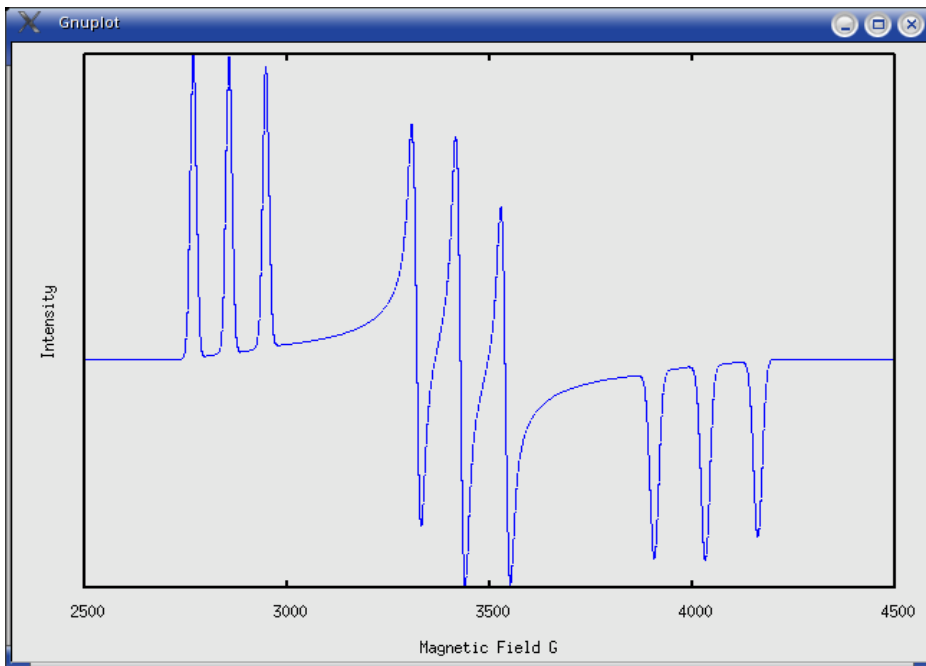
**Figure 31:** Molecular Sophe Graphical User Interface showing the Spectra Tab within the CW EPR Experiment Form.

Apart from the OpenInventor file format which is specifically used for the visualization of transition surfaces, ALL of the other file formats are generated when you run a simulation. You can change the output file type and select View spectrum to see the results in a different format. Both the Bruker Be3st and ESP format files are displayed within Bruker's XeprView<sup>®</sup> and the gnuplot file is displayed in a gnuplot X11 terminal window. The Image (portable network graphics 'xxx.png' format) and postscript files are displayed in an appropriate viewer defined in the preferences window. Typically the default viewers are the web browser mozilla/firefox and ghostview, respectively and representative examples showing all displays can be seen in Figure 32 on the next page.

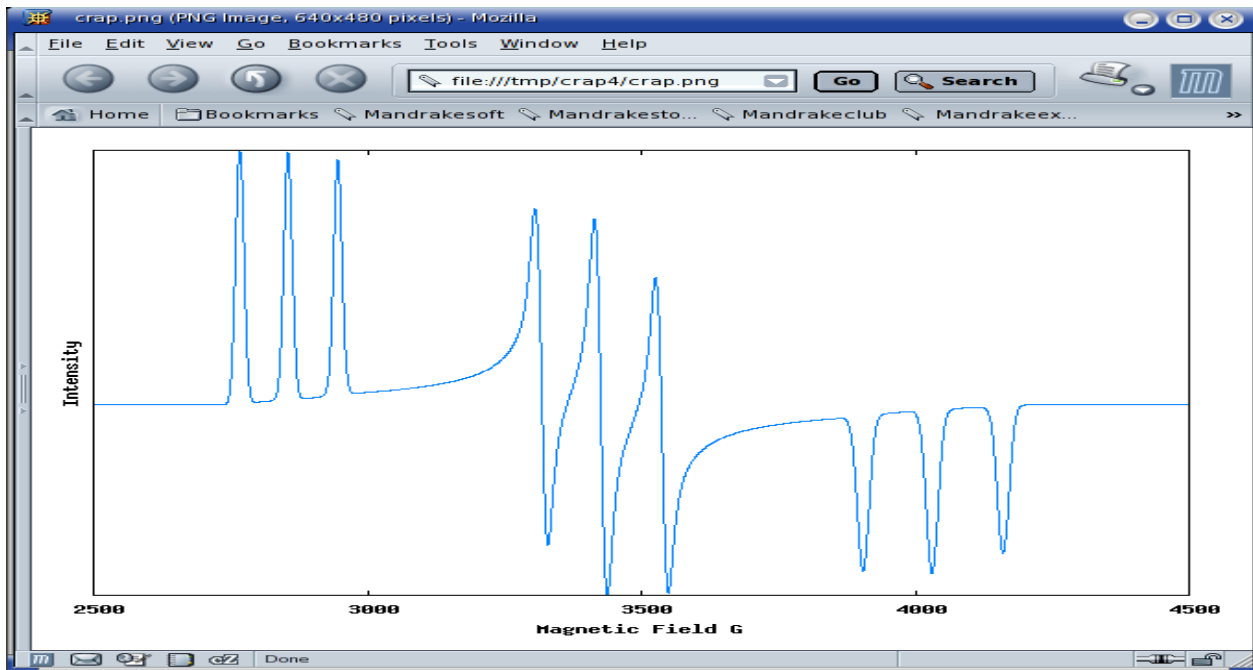
(a)



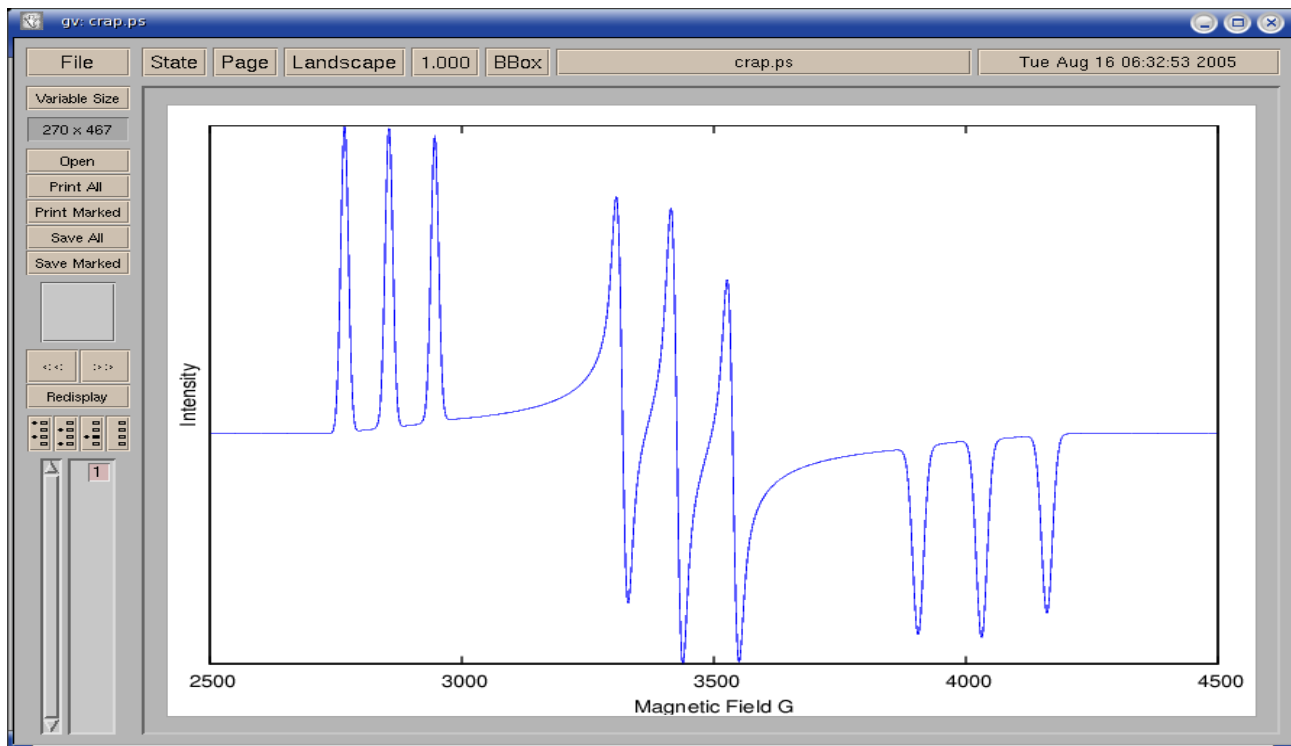
(b)



(c)



(d)



(e)

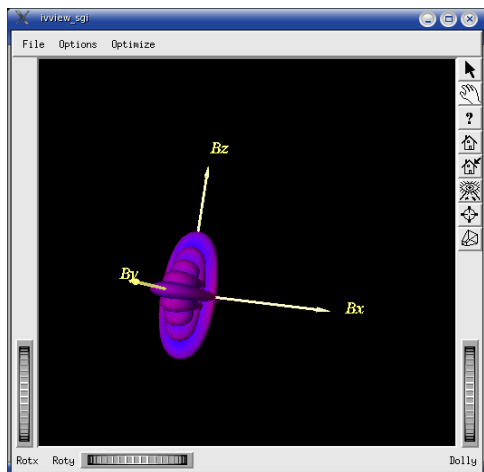


**Figure 32:** Spectral Outputs from Molecular Sophe. (a) Bruker's XeprView® (or Xepr if available), (b)Gnuplot, (c) Image plot (portable network graphics 'xxx.png'), (d) GhostView (postscript viewer) and (e) Open Inventor Viewer (ivview).

## 2.22 Resonator Configuration

The resonator Configuration Form (Figure 33) allows the user to choose: the Bruker spectrometer resonator type; the orientation of the microwave magnetic field with respect to the external applied magnetic field ( $B_0$ ); the microwave power at 0 dB; the microwave magnetic field strength ( $B_1$ ); the radio frequency (RF) power at 0 dB and the RF magnetic field strength ( $B_2$ ). Apart from the dual mode resonator (ER4116DM) which may have  $B_1$  either parallel or perpendicular to  $B_0$ , all of the other resonators have  $B_1$  perpendicular to  $B_0$ .

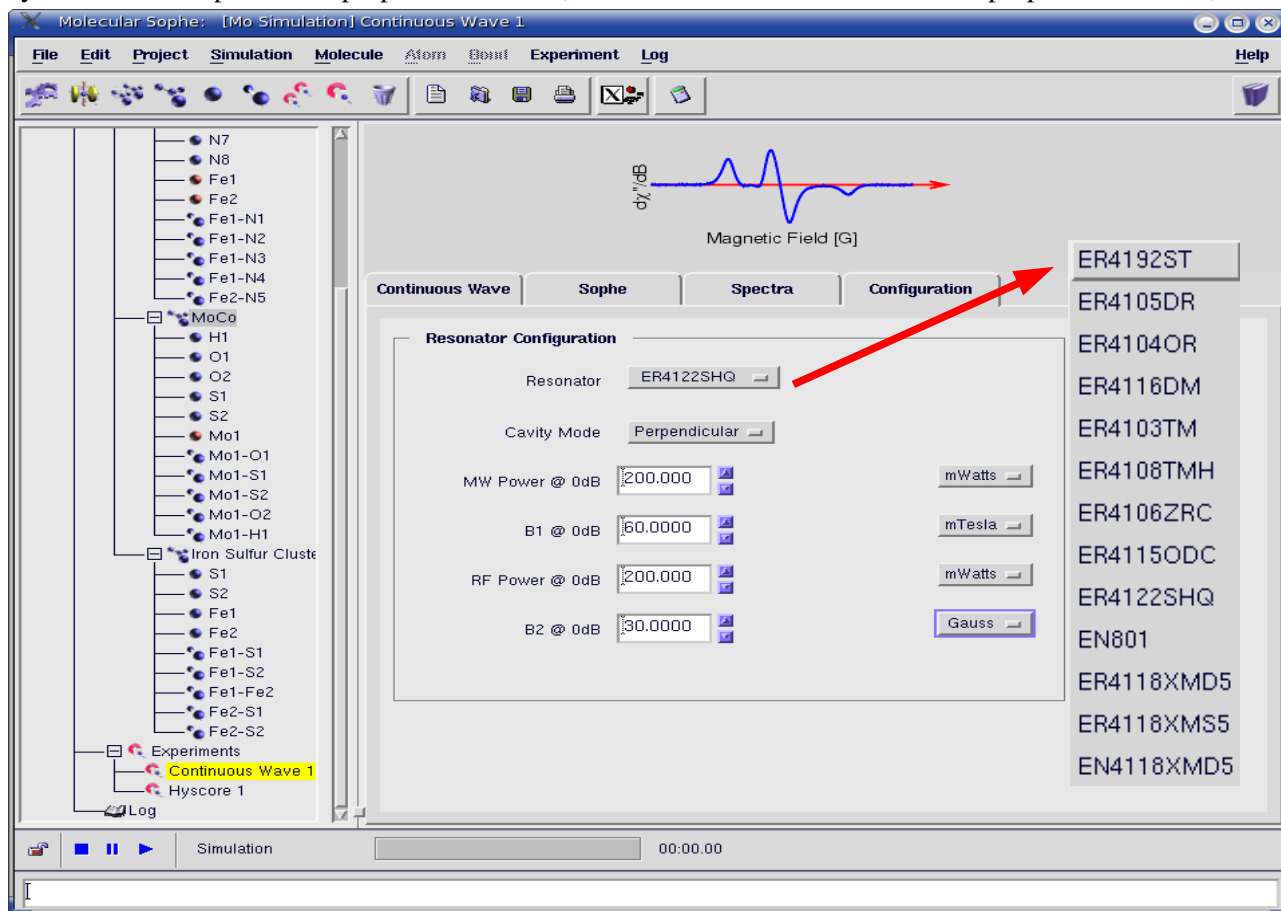


**Figure 33:** Molecular Sophe Graphical User Interface showing the Resonator Configuration Tab within the CW EPR Experiment Form.

## 2.23 Pulsed EPR Experiment – Hyperfine Sublevel Correlated Spectroscopy (HYSCORE)

The HYSCORE Experiment Form (Figure 34) is accessible after having loaded a HYSCORE Experiment (Section 2.17) and selected the HYSCORE Experiment Node from the Explorer Tree. The pulse sequence is displayed in the HYSCORE Experiment Form (Figure 34). The HYSCORE Experiment (Figure 34) contains the following tabs: HYSCORE, Sophe (Section 2.20), Spectra (Section 2.21) and Resonator Configuration (Section 2.22).

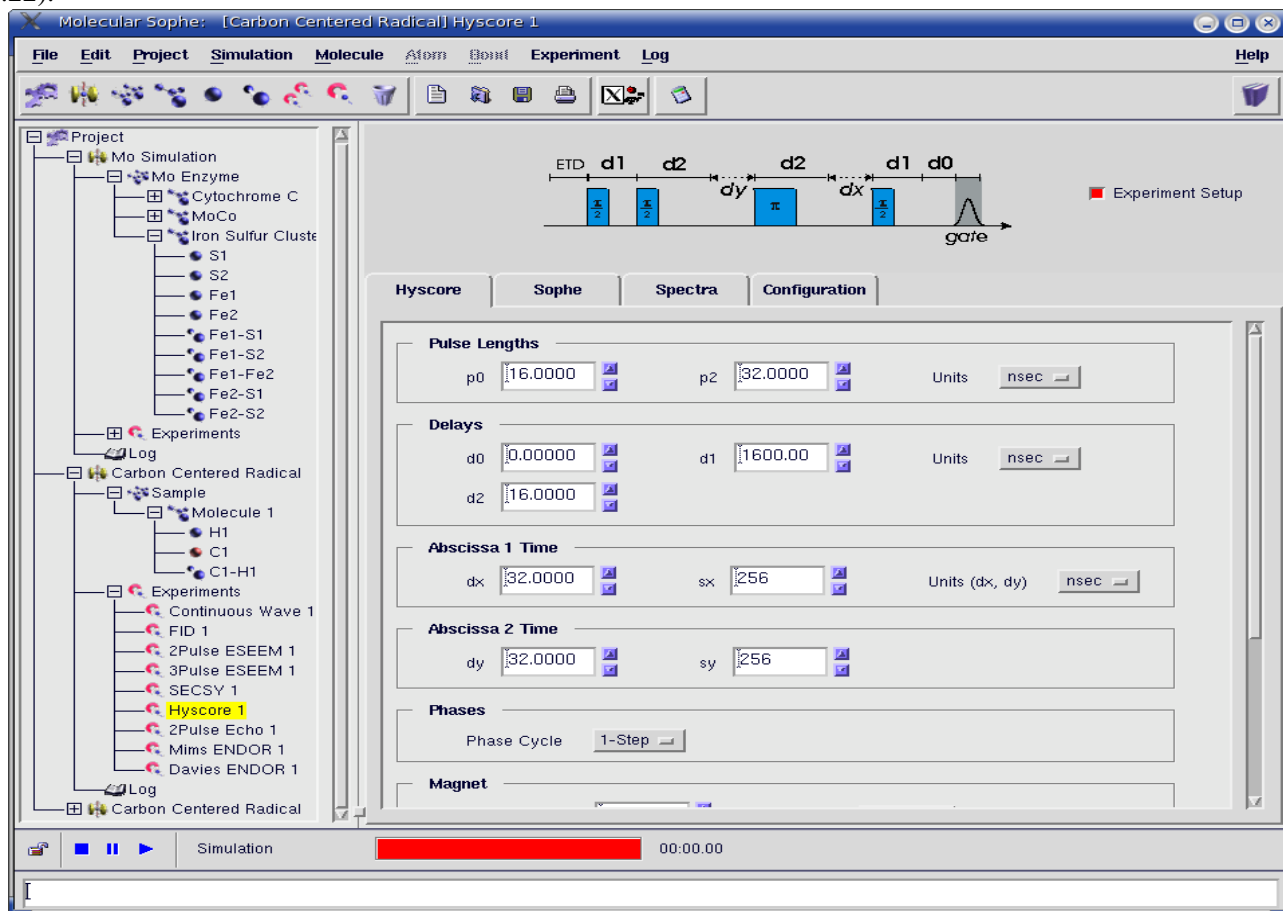


**Figure 34:** Molecular Sophe Graphical User Interface showing the HYSCORE Tab within the HYSCORE Experiment Form.

Within the HYSCORE tab the user can define the Pulse Length of the  $\pi/2$  and  $\pi$  pulses, ( $p_0$  and  $p_2$  respectively), Delay times ( $d_0$ ,  $d_1$  and  $d_2$ ), Abscissa Times, Phase cycle, static Magnetic Field, the Microwave Frequency, Attenuation and the Temperature of the experiment. Creation of the  $\pi/2$  and  $\pi$  pulses is dependent upon, the pulse length ( $p_0$  and  $p_2$ ), the microwave attenuation and the microwave magnetic field strength ( $B_1$ ) at 0dB. The latter is defined in the Resonator Configuration Tab. The attenuation required to obtain a  $\pi/2$  flip angle with the  $\pi/2$  pulse length and  $B_1$  can be obtained by selecting the Experiment Setup Toggle Button and running the experiment. This will produce a a plot of attenuation versus echo intensity (Figure 35). The Position Qualifier within XprView<sup>®</sup> or gnuplot can be used to determine the power associated with the maximum echo intensity.

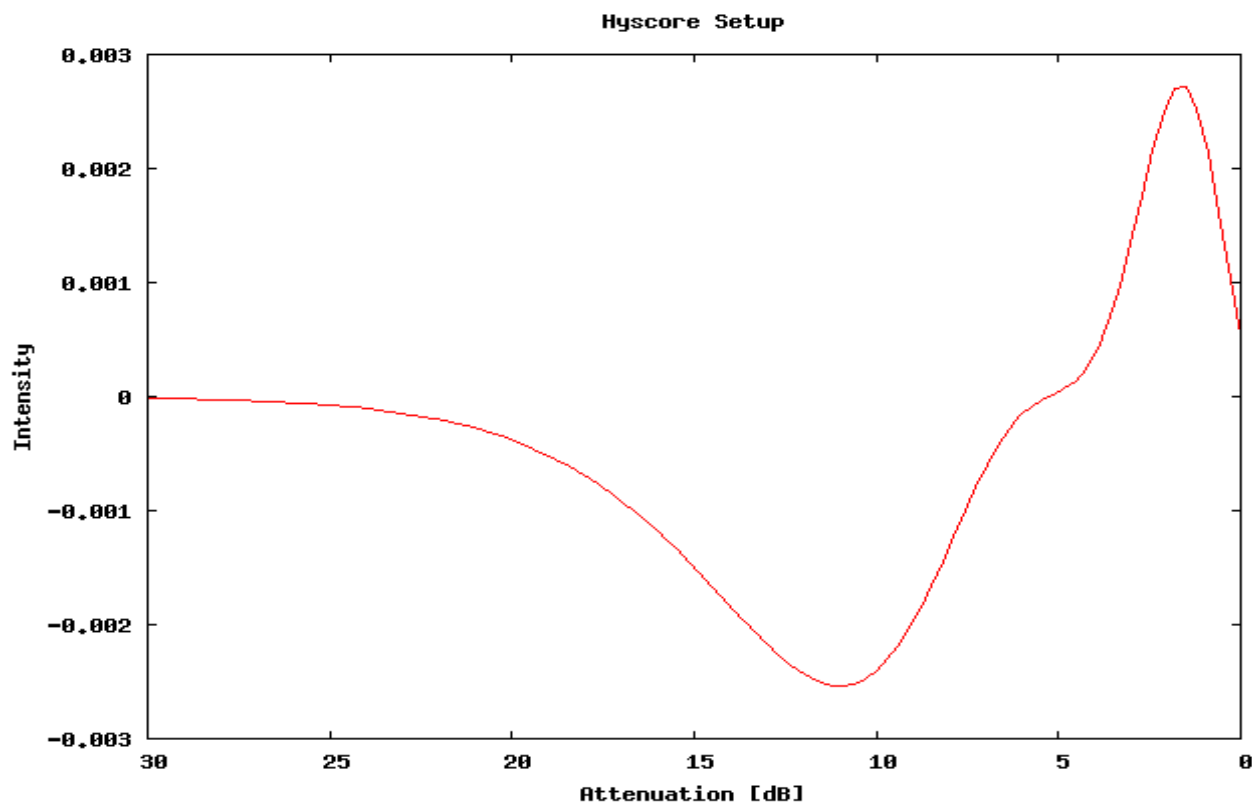


**Figure 35:** Gnuplot output showing the result from a Setup Experiment. Attenuation for  $\pi/2$  pulse = 11dB.

Currently the HYSORE is monitored at a single point (detection gate delay  $d_0$ ), rather than integrating over a detection gate. 'dx' and 'dy' define the time increments in the two dimensions and 'sx' and 'sy' correspond to the number of data (time) points calculated. Whilst the pulse sequence assumes 'dx' and 'dy' are identical as is often the case experimentally, this condition is not required in the Sophe software. The units for both 'dx' and 'dy' are selected from the Units Menu for 'dx'. The HYSORE tab is a scrollable window and as such all of the parameters may not be visible upon selecting the tab. This is the case in Figure 39 where the static magnetic field and temperature are hidden but can be entered by scrolling the window. The remaining parameters (magnetic field and temperature) and the parameters in the other tabs have been defined previously in the CW EPR Experiment Form (Sections 2.20-2.22).

## 2.24 Pulsed EPR Experiment – Orientation Selective HYSORE

Orientation selective experiments involve performing a pulsed EPR experiment, such as HYSORE as a function of orientation (magnetic field). The orientation selective HYSORE Experiment will provide a four dimensional data set from which the complete hyperfine matrix for the remote nucleus can be determined. Subsequently the internuclear distance and orientation of the nucleus from the electron spin can be determined from the anisotropic components of the hyperfine matrix. Computer simulation of an orientation selective HYSORE Experiment, or indeed any other pulsed experiment involves adding a pulsed experiment and choosing Magnetic Field as the second abscissa. Unfortunately, XepView<sup>®</sup> cannot currently visualise one or more four dimensional data sets. The Orientation Selective HYSORE Experiment Form is shown in Figure 36 and the only difference from that of the HYSORE Experiment Form is the addition of a Magnetic Field Tab which allows the initial field, increment field and the number of data points to be added (Figure 36).

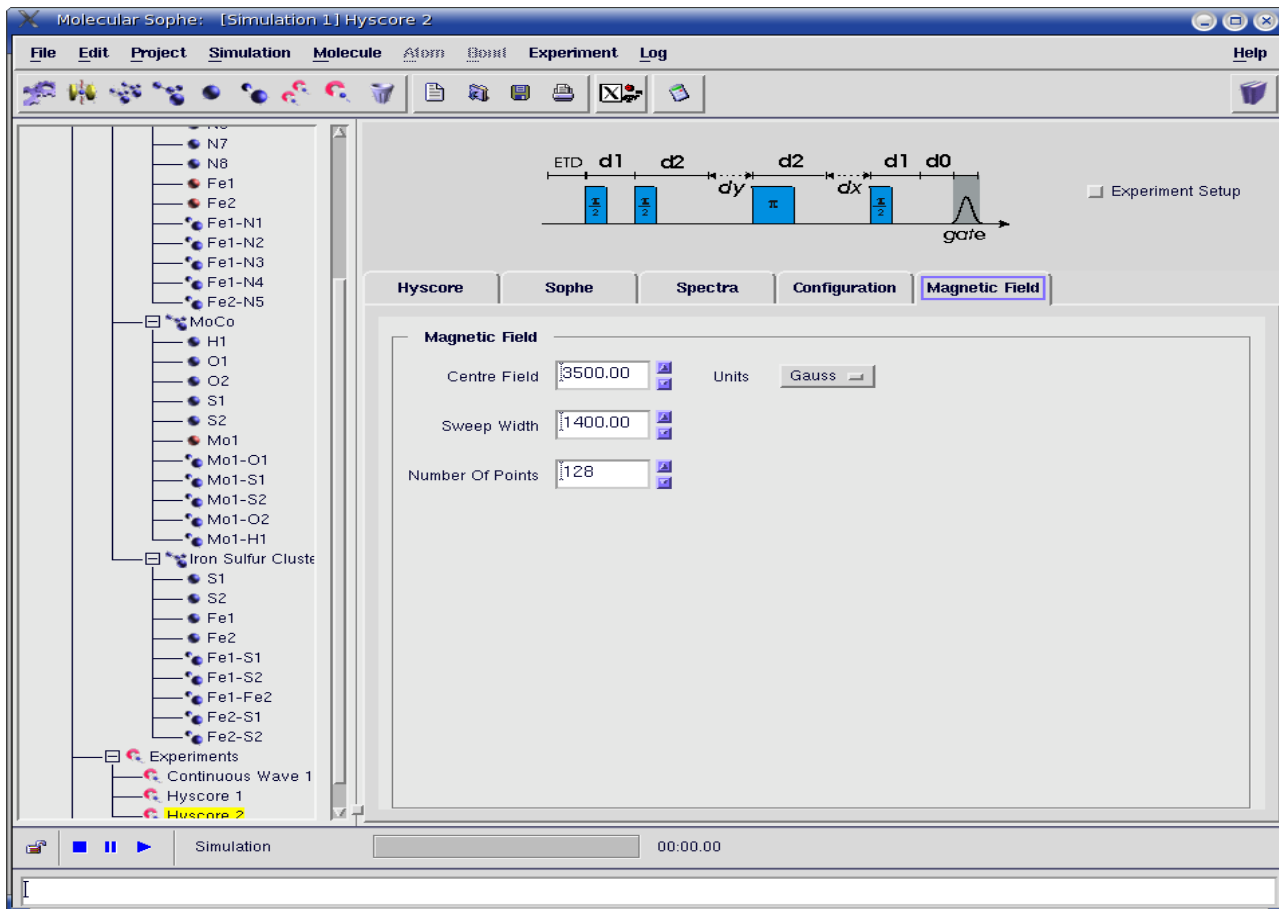


**Figure 36:** Molecular Sophe Graphical User Interface showing the Orientation Selective HYSOCORE Experiment.

## 2.25 Pulsed EPR – MIMS ENDOR

The MIMS Electron Nuclear Double Resonance (ENDOR) Experiment Form (Figure 37) is accessible after having loaded a MIMS ENDOR Experiment (Section 2.17) and selected the MIMS ENDOR Experiment Node from the Explorer Tree. The MIMS ENDOR Experiment is acquired by recording the amplitude versus the frequency of the radiofrequency (RF) pulse as shown in the pulse sequence within the MIMS ENDOR Experiment Form (Figure 37). The MIMS ENDOR Experiment (Figure 37) contains the following tabs: MIMS ENDOR, Sophe (Section 2.20), Spectra (Section 2.21) and Resonator Configuration (Section 2.22). Within the MIMS ENDOR tab the user can define the microwave Pulse Length of the  $\pi/2$  pulse ( $p_0$ ), the Pulse length of the radio frequency  $\pi$  pulse ( $rf$ ), Delays, the range of radio frequencies (Abscissa 1 Radio Frequency), Phase Cycle, the static Magnetic Field, the Microwave Frequency, Attenuation, Radio Frequency Attenuation and the Temperature of the experiment. Creation of the microwave  $\pi/2$  pulse is dependent upon the pulse length ( $p_0$ ), the microwave attenuation and the microwave magnetic field strength ( $B_1$ ) at 0dB. Creation of the radio frequency  $\pi$  pulse is dependent upon, the pulse length ( $p_0$ ), the radio frequency attenuation and the radio frequency magnetic field strength ( $B_2$ ) at 0dB.  $B_1$  and  $B_2$  are defined in the Resonator Configuration Tab.

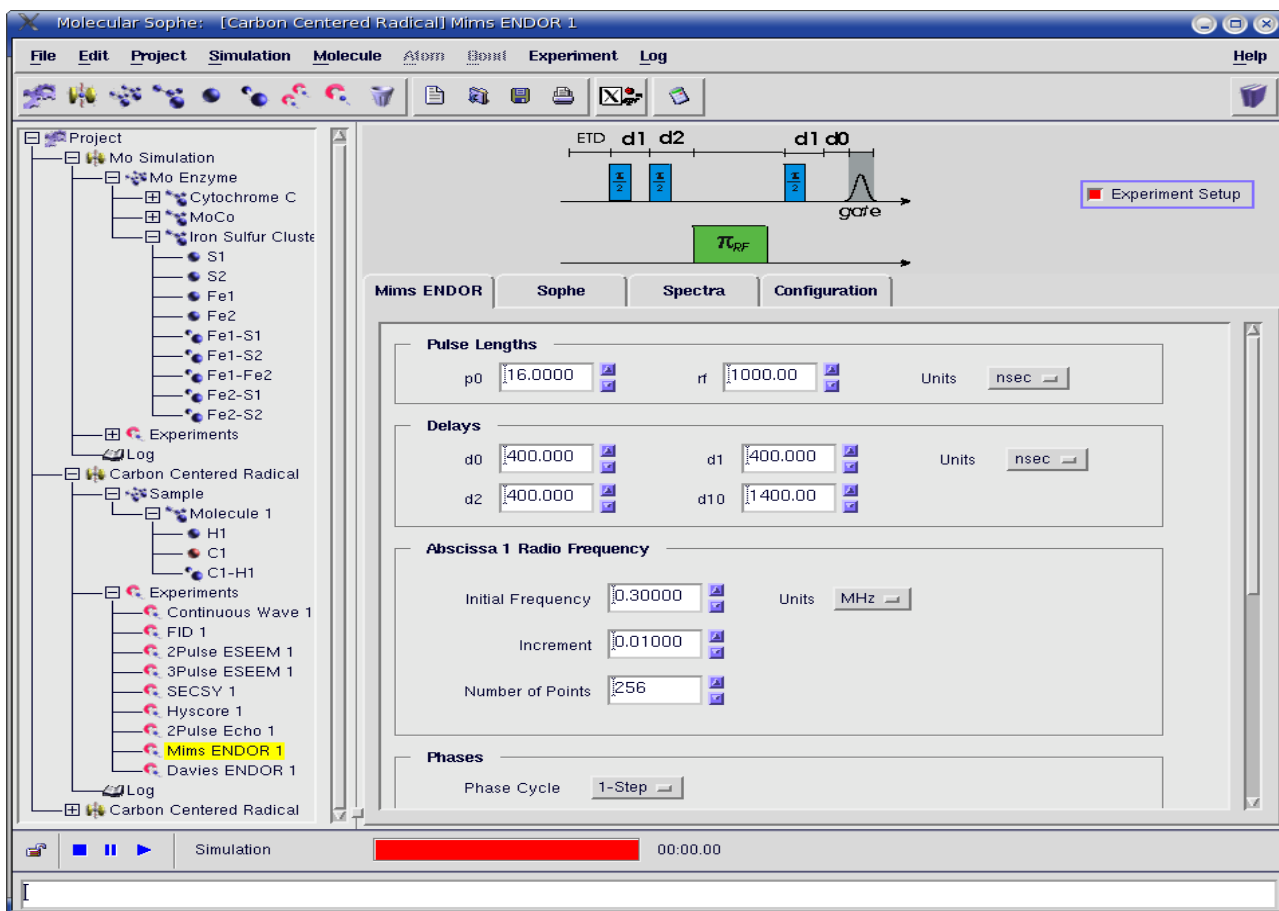


**Figure 37:** Molecular Sophie Graphical User Interface showing the MIMS ENDOR Tab within the MIMS ENDOR Experiment Form.

The microwave attenuation required to obtain a  $\pi/2$  flip angle with the  $\pi/2$  pulse length and  $B_1$  can be obtained by selecting the Experiment Setup Toggle Button and running the experiment. This will produce a plot of microwave attenuation versus echo intensity (Figure 35). The Position qualifier within XexprView<sup>®</sup> or gnuplot can be used to determine the power associated with the maximum echo intensity. Currently the MIMS ENDOR is monitored at a single point (detection gate delay d0), rather than integrating over a detection gate.

The MIMS ENDOR tab is a scrollable window and as such all of the parameters may not be visible upon selecting the tab. This is the case in Figure 37 where the magnetic field strength, microwave frequency and attenuation, radio frequency attenuation and temperature are hidden but can be entered by scrolling the window (Figure 38). The remaining parameters (magnetic field and temperature) and the parameters in the other tabs have been defined previously in the CW EPR Experiment Form (Sections 2.20-2.22).

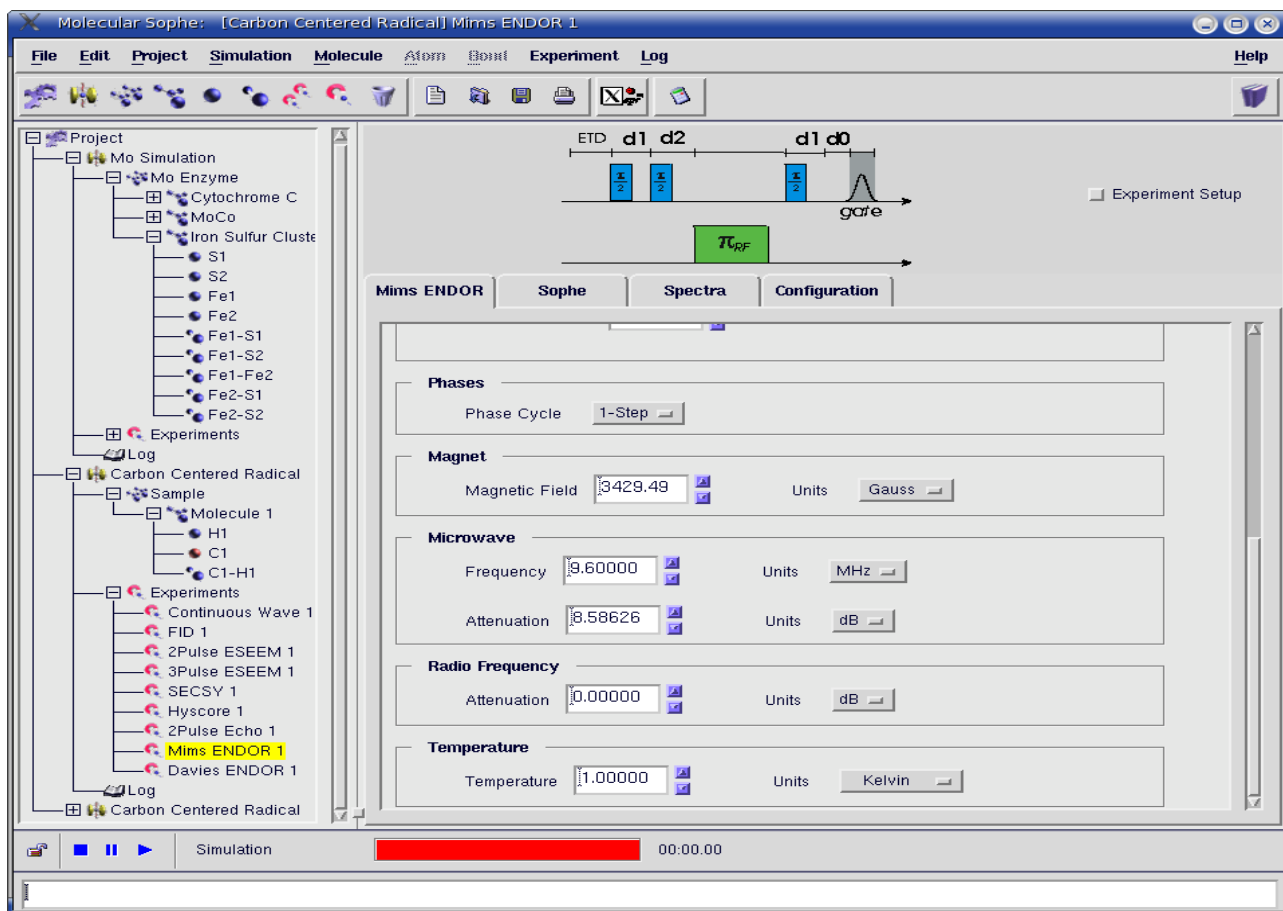


**Figure 38:** Molecular Sophe Graphical User Interface showing the MIMS ENDOR Tab (scrolled to the bottom of the window) within the MIMS ENDOR Experiment Form.

## 2.25 Reports - Energy Level Diagrams

Once an Energy Level Experiment has been added to the Explorer Tree, the Energy Level Experiment forms can be viewed by a left mouse click on the Energy Level Experiment Node in the Explorer Tree. The Energy Level Experiment Form has Energy Level, Sophe (Section 2.20), Spectra (Section 2.21) and Resonator Configuration (Section 2.22). Within the Energy Level Tab (Figure 39), the user can enter values concerning the field sweep (centre field, sweep width and the number of data points), Euler Angles (orientation of the magnetic field), microwave frequency, and temperature. The units for the field sweep parameters include Gauss, mTesla and Tesla and those for the microwave frequency are MHz, GHz and THz. Boltzmann populations for each energy level are automatically included and consequently the temperature will affect the intensity (and presence or absence) of the EPR signal between two different energy levels. The resultant energy level diagram showing energy levels (blue) as a function of magnetic field and the allowed transitions (transitions with a probability greater than the threshold) shown in red can only be viewed using Gnuplot, Image Plot or Postscript viewers. The choice of format can be chosen through in the Spectra tab. (Section 2.21).

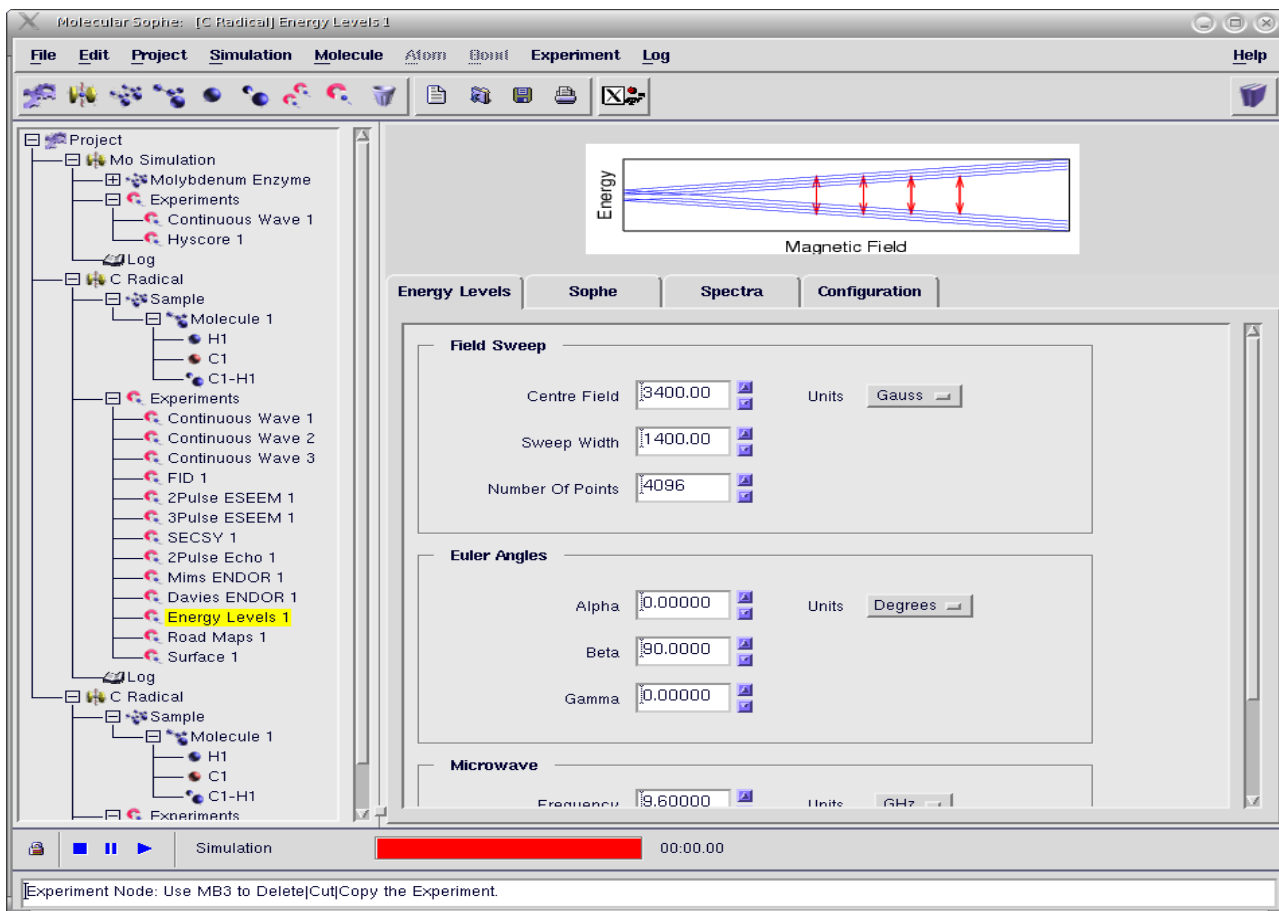


**Figure 39:** Molecular Sophe Graphical User Interface showing the Energy Level Experiment Form and specifically the Energy Level Tab.

## 2.26 Main Menus

The Main Menu is shown in Figure 40 and the following Table shows all of the Menu, Sub Menu items and explains their functions.



**Figure 40:** The main menu in the Molecular Sophe Graphical User Interface.

The Main Menu items can be accessed by placing the mouse over the particular option and performing a left click or, alternatively, pressing the <Alt> key in conjunction with the underlined letter in the Menu Item. For example the File menu can be accessed by pressing <Alt>f.

<i>Main Menu Item</i>	<i>SubMenu Item</i>	<i>Explanation</i>
<u>F</u> ile	XeprView®	Start Bruker's XeprView® Software
	Nameclean	Clean up the Orbacus Corba Nameserver
	Exit	Exit Molecular Sophe
<u>E</u> dit	Edit Preferences	Modify choice of external programs and CORBA settings
	Save Preferences	Save user preferences
	Hide Tool Bar	Hide (and show) the Tool Bar
	Hide Control Bar	Hide (and show) the Control Bar
	Hide Message Bar	Hide (and show) the Message Bar
	Load User Preferences	Load user preferences
	Load System Preferences	Load system wide preferences
<u>P</u> roject	New	Create a new project
	Save	Save the current project
	Load ...	Load a project from disk
	Delete	Delete the current project
	Add Simulation	Add a simulation to the project
	Delete Simulation	Delete a simulation from the project
<u>S</u> imulation	Add	Add a simulation
	Load	Load a simulation
	Save	Save the current simulation
	Delete	Delete the current simulation
	Copy	Duplicate the selected simulation
	Print	Print the current simulation input file
	Run	Run the current simulation
	Stop	Stop the current simulation
	Lock	Lock the current simulation
<u>M</u> olecule	Add	Add a new molecule
	Paste	Greyed out, NOT currently supported
	Clear All	Delete all molecules including all atoms and bonds
	Delete	Delete current molecule including all atoms and bonds
	Cut	Greyed out, NOT currently supported
	Copy	Duplicate Molecule
	Add Atom	Add atom to the molecule

<i>Main Menu Item</i>	<i>SubMenu Item</i>	<i>Explanation</i>
	Paste Atom	Greyed out, NOT currently supported
	Clear Atoms	Remove all atoms within the molecule
	Add Bond	Add a bond (interaction) between two atoms
	Clear Bonds	Remove all bonds between atoms
<u>A</u> tom		Only Active when the atom Node is selected
	Delete	Delete atom
	Cut	Greyed out, NOT currently supported
	Copy	Duplicate atom
<u>B</u> ond		Only Active when the bond Node is selected
	Delete	Delete bond
<u>E</u> xperiment	Add	Add an experiment
	Paste	Greyed out, NOT currently supported
	Clear All	Remove all experiments
	Delete	Delete experiment
	Cut	Greyed out, NOT currently supported
	Copy	Duplicate experiment
<u>L</u> og	Clear	Clear both Sophe and MoSophe log windows
	Print	Print both Sophe and MoSophe log windows
	Save	Save both Sophe and MoSophe log windows to disk
<u>H</u> elp	Click for Help	NOT Currently Supported
	Overview	Displays Product Information
	Index	NOT Currently Supported
	Keys	NOT Currently Supported
	Keys and Shortcuts	NOT Currently Supported
	Product Information	Displays name of the binary executable
	Manual	Manual for Molecular Sophe

## 2.27 Tool Bar

The Tool Bar (Figure 41) provides quick access to some common tasks in building the project.



**Figure 41:** The Tool Bar within the Molecular Sophe Graphical User Interface.

The buttons left to right perform the following functions:

- Load a project from disk,
- Add a simulation to the project,
- Remove the molecules, atoms and bonds from the sample,
- Add a molecule,
- Add an atom,
- Add a bond,
- Remove all experiments,
- Add an experiment,
- A Generic delete function being able to delete the currently active Node in the Explorer Tree,
- New simulation,
- Load simulation from disk,
- Save simulation to disk,
- Print the simulation using the printer defined in the preferences dialog,
- Start the XeprView® software,
- Units conversion calculator and
- The manual.

## 2.28 Control Bar

The Control Bar (Figure 42) is used to start, pause and stop simulations. Once the simulation has started the simulation is locked so that the parameters within the simulation cannot be altered.



**Figure 42:** The Control Bar within the Molecular Sophe Graphical User Interface.

The components of the control bar from left to right include a toggle button which can lock and unlock the simulation, stop, pause and start buttons and a timing bar. Upon starting the simulation, the colour of the start button changes to green. The Timing Bar (Figure 42) shows the state (grey, red and green) of the simulation. A grey timing bar indicates the simulation has not been started and a red timing bar indicates that the simulation has completed. A green timing bar indicates the percentage completion of a particular isotope combination; ie, if the simulation has atoms with multiple isotopes, the green timing bar will start multiple times.

There is a problem with threading in the X-server which can sometimes block the update of the timing bar, which can be readily seen by the timing bar stopping. If this occurs simply repress the start button and the

timing bar will be updated.

### 3.0 Sophe - Computational Code

Sophe is a sophisticated computer simulation software programme written entirely in C++ employing a number of innovative technologies including; the SOPHE partition scheme, a field segmentation algorithm, the mosaic misorientation line width model, and spectral optimisation (under development). In conjunction with the SOPHE partition scheme, the field segmentation algorithm [22-25,35] and the mosaic misorientation linewidth model [24,26] greatly increase the speed of simulations for most samples. Sophe has been completely rewritten in order to incorporate both continuous wave and pulsed EPR simulations. There are versions for both 32 bit (ix86; x=3,4,5,6) and 64 bit (x86\_64) platforms, the latter running significantly faster.

The simulation of a randomly oriented EPR spectrum involves integration over a unit sphere (Eq. (8), reproduced below) which is performed numerically by partitioning a unit sphere and calculating the resonant field positions and transition probabilities at all of the vertex points.

$$S(B, \nu_c) = C \int_{\theta=0}^{\pi} \int_{\phi=0}^{\pi} \sum_{i=0}^N \sum_{j=i+1}^N |\mu_{ij}|^2 f[\nu_c - \nu_0(B), \sigma_\nu] d\cos\theta d\phi \quad (8)$$

#### 3.1 Sophe Grid

Whilst a number of different partition schemes have been reported in the literature for performing the numerical integrations in Eqn. (9), including the igloo [36-38], triangular [39], spiral [40], and a triangular arrangement with octahedral symmetry [41], Molecular Sophe uses a partition scheme involving spherical triangles [35]. The SOPHE partition scheme [35] allows any portion of the unit sphere ( $\theta \in [0, \pi/2]$ ,  $\phi \in [\phi_1, \phi_2]$  or  $\theta \in [\pi/2, \pi]$ ,  $\phi \in [\phi_1, \phi_2]$ ) to be partitioned into triangular convexes. For a single octant ( $\theta \in [0, \pi/2]$ ,  $\phi \in [0, \pi/2]$ ) the triangular convexes can be defined by three sets of curves

$$\begin{aligned} \theta &= \frac{\pi}{2} \frac{i}{N} \\ \theta - \phi &= \frac{\pi}{2} \frac{i-1}{N} (\phi_2 - \phi_1) \\ \theta + \phi &= \theta (\phi_2 - \phi_1) - \frac{\pi}{2} \frac{i-1}{N} (\phi_2 - \phi_1), (i = 1, 2, \dots, N) \end{aligned} \quad (9)$$

where N is defined as the partition number and gives rise to N+1 values of  $\theta$ . Similar expressions can be easily obtained for  $\theta \in [\pi/2, \pi]$ ,  $\phi \in [\phi_1, \phi_2]$ . A three dimensional visualisation of the SOPHE partition scheme is given in Figure 43b. And the triangular grid resembles the roof of the famous Sydney Opera House (SOPHE).

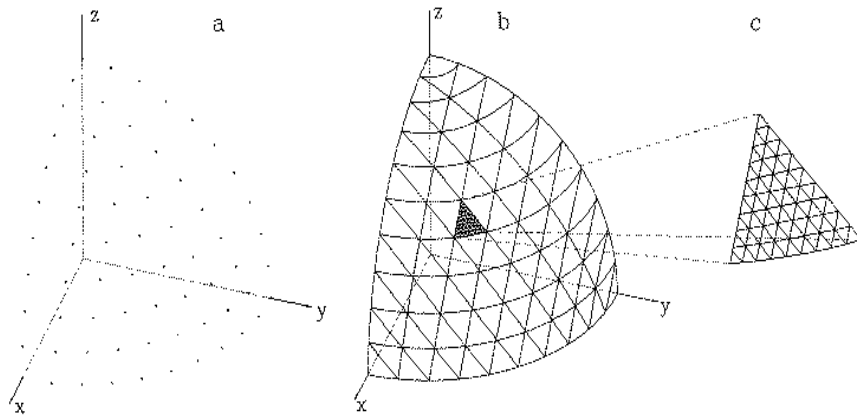


**Figure 43:** A schematic representation of the SOPHE partition scheme. (a) Vertex points with a SOPHE partition number  $N = 10$ ; (b) the SOPHE partition grid in which the three sets of curves are described by Eq. (9). (c) Subpartitioning into smaller triangles can be performed by using either Eq. (9) or alternatively the points along the edge of the triangle are interpolated by the cubic spline interpolation method [35] and each point inside the triangle is linearly interpolated three times and an average is taken.

In the SOPHE grid there are  $N$  curves in each set with the number of grid points varying from 2 to  $N+1$  in steps of 1. In order to produce simulated spectra of high quality, the unit sphere is often required to be finely partitioned, in other words, a large number of vertex points are required to reduce computational noise which is often observed when the spin Hamiltonian parameters are highly anisotropic and the linewidths are small. Each triangle in Figure 43 can be easily subpartitioned into smaller triangles, referred to as tiny triangles. In Figure 43c, a selected triangle is further partitioned into 81 tiny triangles with a subpartition number  $N=10$ . The grid formed in such a subpartition can still be described by Eq. (9). In this particular case,  $\theta$  is stepped in a smaller step of  $\pi/(2(N-1)(M-1))$  from  $\theta = 45^\circ$  to  $\theta = 54^\circ$ , the two corresponding curves which bound the triangle (Figure 43c). A similar process is applied to curves in sets 2 and 3. Alternatively, various interpolation schemes may be used to generate finer grids for simulating randomly oriented EPR spectra [39, 40, 42]. In 1995 we described the highly efficient SOPHE interpolation scheme [35].

The advantage of the SOPHE partition scheme over other schemes (igloo [36-38], triangular [39], spiral [40] and a triangular arrangement with octahedral symmetry [41]) is that it allows the implementation of interpolation schemes, such as the SOPHE interpolation scheme and the mosaic misorientation linewidth model which reduce the number of matrix diagonalizations required to eliminate computer noise. Since matrix diagonalization is an  $N^3$  process, where  $N$  is the rank of the matrix, reducing the number of matrix diagonalizations leads to significant reductions in the computational time (see below). In addition, the SOPHE grid can be described by three analytical expressions (Eqn. (9)) which are only dependent upon a single parameter, the partition number.

### 3.2 *Calculation of Resonant Field Positions*

The very nature of EPR spectroscopy as a field-swept technique imposes a computational challenge to computer simulation of randomly oriented spectra. In essence, during an EPR experiment, the spin system under investigation is constantly modified through the Zeeman interactions as the magnetic field is swept. In a general situation where two or more interactions have comparable energies, the search for resonance field positions is not a trivial task as the dependence of the energies of the spin states on field strength ( $B_0$ ) can be very complex. The complication involved is best manifested by the presence of multiple transitions between a given pair of energy levels.

### 3.3 *Brute Force - Matrix Diagonalization and Field Segmentation Algorithms*

A number of search schemes have been used in the full matrix diagonalization approach for locating resonant field positions [19, 43-46]. Generally, they can be grouped into two categories. In category I, the resonant field position is searched independently for every transition. Among the schemes belonging to this category, the so-called iterative bisection method is the safest but probably the most inefficient method [16]. Other more efficient methods such as the Newton-Raphson method have also been used [19]. In general, these search schemes are time-consuming as a large number of diagonalizations are normally required. The search schemes belonging to category II may be called segmentation methods. In these schemes, the field sweep range is divided equally into  $k$  segments and for each segment the whole energy matrix is diagonalized once for the centre field value of that segment. Thus only  $k$  diagonalizations are performed for each orientation. A perturbation theory is then employed for determining the presence of a transition in each segment. This search scheme is still limited to situations where in each segment there is no more than one possible transition. However, if  $k$  is not too large, the chance of having two resonances in a single segment is rare. Reijerse *et al.* [43] use a first-order perturbation approach for exploring transitions in each segment. However, from our experience, first-order perturbation theory cannot be guaranteed to produce resonance field positions with satisfactory precision. In Sophe we have adopted the second-order perturbation theory [47], where for each orientation on the SOPHE grid the field range is divided into a number of intervals. Matrix diagonalization [48] is performed once in each interval, and second order perturbation theory is then employed to locate the resonant field positions within the interval. We have found that this approach has proven to be efficient and reliable for locating the resonance field positions in field-swept EPR spectra and can also deal with complicated situations where multiple transitions or looping transitions are present. A saving factor in the segmentation method lies in the fact that full matrix diagonalization is only performed  $k$  times irrespective of the number of transitions involved. By contrast, in the other schemes, a few diagonalizations are required for each transition and for large spin systems this number can become very large. The precision of the resonance field positions normally depends on the segment number  $k$  as well as on the spin system. For  $S=1/2$  spin systems a value of 2 for the segment number is usually suitable, but for high spin systems where the linewidth is narrow and the magnetic field sweep is large then larger values are required. Simulations can be performed with different segmentation numbers providing an easy test of precision and also to test whether apparent resonances are noise or real.

### 3.4 *Mosaic Misorientation Linewidth Model*

When the line width is small compared to the anisotropy of the system it is necessary to integrate over a large number of orientations to avoid simulation noise in the simulated spectrum. This increases the

computational time considerably. The SOPHE grid and Interpolation schemes were developed as a way to overcome this problem. A new approach based on the mosaic misorientation linewidth model [24, 49] has recently been developed (Figure 44). In the mosaic misorientation linewidth model a Gaussian distribution of molecular geometry axes about an average crystal c-axis is assumed. In the current implementation the partial derivatives of the eigenvalues with respect to a rotation about the  $x$  and  $y$  axes are calculated using first order perturbation theory.

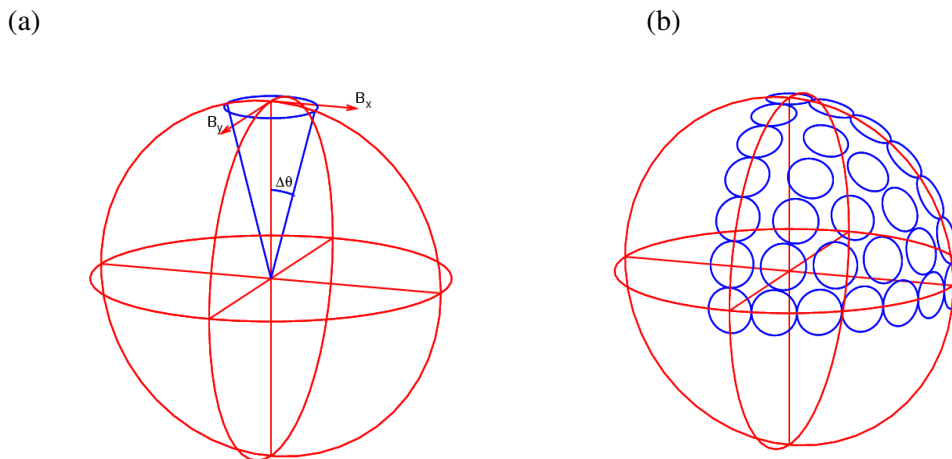


**Figure 44:** Mosaic misorientation linewidth model.

The contribution of a Gaussian distribution, of half-width  $\Delta\theta$ , to the linewidth can then be calculated with the following equation.

$$\sigma_m^2 = \left( \Delta\theta \frac{\partial E_{ij}}{\partial \theta_x} \right)^2 + \left( \Delta\theta \frac{\partial E_{ij}}{\partial \theta_y} \right)^2, E_{ij} = E_i - E_j \quad (10)$$

In the simulation of powder spectra each point in the SOPHE grid is considered to be a microcrystallite with a Gaussian distribution of orientations,  $\Delta\theta$  (Figure 44a), such that there is an overlap between adjacent grid points (Figure 44b).

$$\Delta\theta = \frac{\pi}{4(N-1)} \quad (11)$$

At turning points in the spectrum the partial derivatives of the eigenvalues and hence  $\sigma_m$  are zero and the linewidths are determined by other contributions. At other orientations where the resonant field varies strongly with orientation the line widths will be broadened (smoothed). This model simulates an EPR spectrum where the important features, the turning points, are resolved in a significantly reduced time. Increasing  $N$ , the number of bands in the SOPHE grid, will lead to a convergence to the 'true' spectrum. For a large number of spin systems,  $N$  can initially be set to 20. The mosaic misorientation linewidth model can be contrasted with interpolation schemes by considering it an extrapolation method.

### 3.5 A Comparison of Brute Force Matrix Diagonalization and Mosaic Misorientation

An example demonstrating the efficiency of the SOPHE partition scheme in conjunction with the SOPHE interpolation scheme and the mosaic misorientation linewidth model is shown in Figures 54a-d where we have calculated a randomly oriented spectrum for a high spin rhombically distorted naturally abundant Cr(III) ion for which an appropriate spin Hamiltonian is:

$$H = g_e B \cdot S + D \left[ S_z^2 - \frac{1}{3} S(S+1) \right] + E(S_x^2 - S_y^2) + S.A.I - g_n \beta B.I \quad (12)$$

The spin Hamiltonian parameters employed were  $g_e = 2.00$ ,  $D = 0.10 \text{ cm}^{-1}$ ,  $E/D = 0.25$ ,  $A_x = 120.0$ ,  $A_y = 120$ ,  $A_z = 240.0 \times 10^{-4} \text{ cm}^{-1}$ . A narrow line width was chosen (30 MHz) in order to demonstrate the high efficiency of these schemes. The unit sphere has to be partitioned very finely in order to produce simulated spectra with high signal-to-noise ratios when there is large anisotropy and the spectral linewidths are narrow.

The simulated spectra employing brute force matrix diagonalization with  $N=18$  and  $N=400$  are shown in Figures 45a and 45b respectively. Including the SOPHE interpolation scheme with a partition number  $N=18$  (Figure 45c) dramatically improves the signal to noise ratio with a considerable reduction in computational time. Application of the mosaic misorientation line width model (Figure 45d) also dramatically improves the signal to noise ratio and is computationally faster than the SOPHE interpolation method as interpolation has many overheads. Spectra in Figure 45a-d were calculated using the XSophe-Sophe-XeprView® computer simulation software suite. Clearly the mosaic misorientation linewidth model is the fastest approach and now replaces the brute force matrix diagonalization approach within the computational programme Sophe and is also preferred over SOPHE interpolation. An identical spectrum to Figure 45d is found using Molecular Sophe except the computational time was slightly longer 1.49 vs 0.79 sec. Running the same simulation on a 64bit notebook (Athlon XP3400) notebook using Mandriva Linux 2006 as the operating system produced a computational time of 0.94 sec, a factor 15 to 2 times faster on the 64 bit notebook.

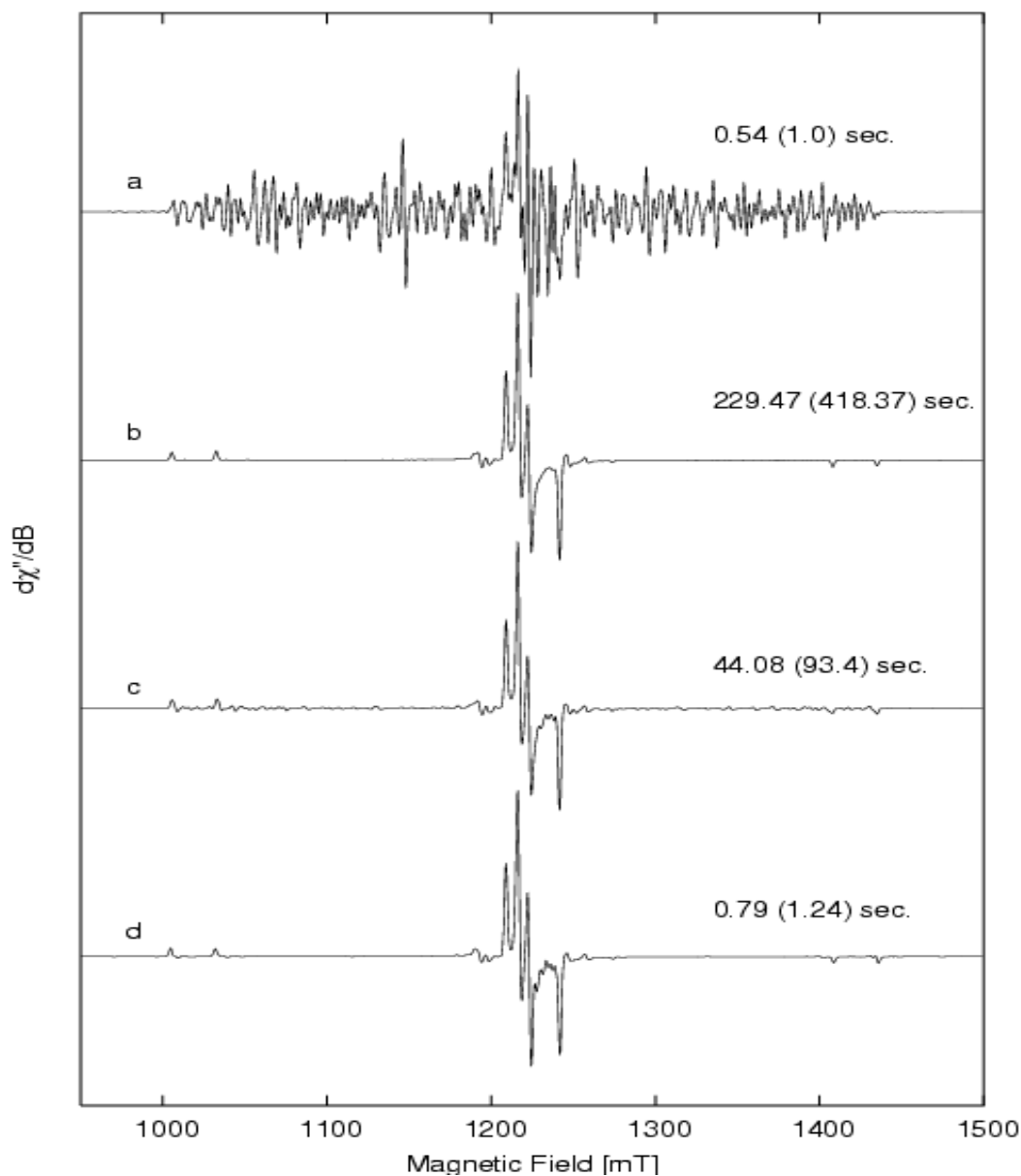


**Figure 45:** Computer simulations of the powder EPR spectrum from a naturally abundant Cr(III) spin system ( $S=3/2$ ;  $I=3/2$ ) which demonstrates the efficiency of the SOPHE interpolation scheme. (a) Without the SOPHE interpolation scheme,  $N=18$ , (b) Without the SOPHE interpolation scheme,  $N=400$ , (c) With the SOPHE interpolation scheme,  $N=18$  and (d) With the mosaic misorientation linewidth model,  $N=18$ . Computational times were obtained on both a Linux PC (AMD Athlon XP2400+ CPU with the Mandrake 9.1 operating system) and an SGI supercomputer (MIPS R14K CPU with the IRIX 6.5.20 operating system), the latter times are given in brackets.  $\nu=34$  GHz; field axis resolution: 4096 points; an isotropic Gaussian lineshape with a half width at half maximum of 30 MHz was used in the simulation.

### 3.6 Linewidth Models

At present only a single linewidth model, namely the angular variation of g-values, has been incorporated into Sophe

$$\sigma_v^2 = (\sigma_x^2 g_x^2 l_x^2 + \sigma_y^2 g_y^2 l_y^2 + \sigma_z^2 g_z^2 l_z^2) / g^2 \quad (13)$$

where  $g^2 = g_x^2 l_x^2 + g_y^2 l_y^2 + g_z^2 l_z^2$ ,  $\sigma_i$ 's (i=x,y,z) are the input linewidth parameters and  $l_i$ 's (i=x,y,z) are the direction cosines of the magnetic field with respect to the principal axes of the g matrix.

A similar approach to that used for the distribution of zero field splittings in XSophe [23,24] will be implemented for all spin Hamiltonian and structural parameters.

### 3.7 Visual Aids for Analysing Complex CW EPR Spectra

Molecular Sophe provides three tools (Energy level Diagrams, Transition Roadmaps and Transition Surfaces) for aiding the analysis of complex CW EPR spectra. The Energy Level Diagrams and Transition Roadmaps can be displayed using Gnuplot, Ghostview (postscript files) or through an image viewer (portable network graphics files) such as a web browser (Netscape or Mozilla). The transition surface scene graphs are plotted with an OpenInventor scene graph viewer (ivview) using cartesian coordinates, which is extremely useful for highly anisotropic spin systems such as high spin systems (for example Fig 4e). This requires the minimum field to be set to zero which is defined as the origin. In contrast, for nearly isotropic systems, it is important to examine a single transition at a time. The choice of transitions can be made through the Transition Labels/Probabilities window and either setting the transition threshold or defining the transitions.

### 3.8 Pulsed EPR Simulations

The simulation of pulsed EPR spectra involves calculating the evolution of an observable ( $\bar{O}$  Eq. 14) during the microwave pulses, radiofrequency pulses and free evolution periods that comprise the pulse sequence. The signal in an arbitrary pulsed EPR experiment can be simply described in superoperator notation. [8,50]

$$\langle \bar{O} \rangle = \langle \rho_0 | \hat{R}_1 \hat{R}_2 \dots \hat{R}_n | O \rangle \quad (14)$$

In most experiments the initial density matrix ( $\rho_0$ ) is the equilibrium density matrix ( $\rho$ ) with diagonal elements given by the Boltzmann population of the energy levels in the eigenbasis of the static Hamiltonian:

$$\rho_{ii} = \frac{e^{-\frac{E_i}{kT}}}{\sum_{j=1}^n e^{-\frac{E_j}{kT}}} \quad (15)$$

The density matrix for a four level spin system ( $S=1/2$ ) is :

$$\rho = \begin{bmatrix} \rho_{11} & \rho_{12} \\ \rho_{21} & \rho_{22} \end{bmatrix} \quad (16)$$

and the corresponding superbra is:

$$\langle \rho | = \left[ \rho_{11} \quad \rho_{12} \quad \rho_{21} \quad \rho_{22} \right] \quad (17)$$

The detection operator (observable) in Eqn. 14 is given by:

$$\mathcal{O} = \begin{bmatrix} \mathcal{O}_{11} & \mathcal{O}_{12} \\ \mathcal{O}_{21} & \mathcal{O}_{22} \end{bmatrix} \quad (18)$$

and the corresponding superket is:

$$| \mathcal{O} \rangle = \begin{bmatrix} \mathcal{O}_{11} \\ \mathcal{O}_{21} \\ \mathcal{O}_{12} \\ \mathcal{O}_{22} \end{bmatrix} \quad (19)$$

The transverse magnetization ( $M_x, M_y$ ) are proportional to  $S_x, S_y$ , respectively and are determined by the g value in the x-y plane, the microwave power and other experimental factors.

In general a pulse sequence is comprised of one or more microwave pulses, free evolution periods and possibly radio frequency pulses. For example the pulse sequences for the HYSORE and MIMS ENDOR experiments are shown in Figures 34 and 37, respectively. Each of these components can be mathematically described by a superpropagator ( $\hat{R}$ ) (Eqn. 14) which in turn is derived from a direct product of the propagators:

$$\hat{R} = R \otimes R^{-1} = \begin{bmatrix} R_{11} R_{11}^* & R_{11} R_{21}^* & R_{12} R_{11}^* & R_{12} R_{21}^* \\ R_{11} R_{12}^* & R_{11} R_{22}^* & R_{12} R_{12}^* & R_{12} R_{22}^* \\ R_{21} R_{11}^* & R_{21} R_{21}^* & R_{22} R_{11}^* & R_{22} R_{21}^* \\ R_{12} R_{12}^* & R_{12} R_{22}^* & R_{22} R_{12}^* & R_{22} R_{22}^* \end{bmatrix} \quad (20)$$

Coherence transfer pathways provide a way of visualising the transfer of magnetisation during a pulse sequence and in general an element of the density matrix undergoes the following transformation:

$$\rho_{ij} \rightarrow \sum_{l=0}^n \sum_{k=0}^n \mathbf{R}_{ik} \mathbf{R}_{lj}^* \rho_{kl} \quad (21)$$

In the eigenbasis of the static Hamiltonian the superpropagator for each free evolution period is diagonal. The time dependence of each element in the density matrix ( $\rho$ ) is simply given by:

$$\rho_{ij} \rightarrow e^{-2i\pi E_{ij}t} \rho_{ij} \quad (22)$$

During the microwave pulses the Hamiltonian is no longer time-independent and contains a term oscillating at the microwave frequency. Using Floquet theory [51] the superpropagators for the microwave pulses can be expressed as a Fourier series. For many spin systems the series converges rapidly and can be truncated at a low number of harmonics.

$$\hat{\mathbf{R}}(t) = \sum_{m=-n}^n \hat{\mathbf{R}}_m e^{-im\omega_{mw}t} \quad (23)$$

Pulsed EPR experiments typically involve phase cycling where the experiment is repeated with different combinations of the phases of the microwave pulses. It can be seen that for a single pulse the phase cycle  $[0, \pi]$  filters out all odd Floquet harmonics while the phase cycle  $[0, -\pi]$  filters out all even Floquet harmonics.

$$\hat{\mathbf{R}}_n e^{-in(\omega_{mw}t + \pi)} = (-1)^n \hat{\mathbf{R}}_n e^{-in\omega_{mw}t} \quad (24)$$

The use of phase cycling reduces the number of coherence pathways that must be followed. This can be further reduced if we include the condition that the initial Fourier index is 0 at equilibrium and at the time of detection must be given by  $p = \pm 1$ . This is shown in Figure 46 for a two pulse sequence. The first pulse has  $\Delta p = +1$  the second pulse  $\Delta p = -2$ . One pathway through the density matrix (in superbra notation) is shown in Figure 46. Each coherence pathway yields a peak which is then added to the spectrum. The spectrum may have one or more frequency dimensions depending on how the time periods are incremented in the experiment. The final spectrum is obtained by averaging over all pathways. For powder spectra the integration over the orientational disorder using the SOPHE grid is also performed. [35]

The above approach to the simulation of pulsed EPR spectra allows the simulation of pulsed EPR spectra from not only isolated paramagnetic samples containing a single unpaired electron but also from samples containing multiple unpaired electrons, for example high spin Fe(III) centres found in cytochromes and non heme iron proteins and coupled centres, such as the type III copper containing enzymes and the binuclear metallohydrolyases.

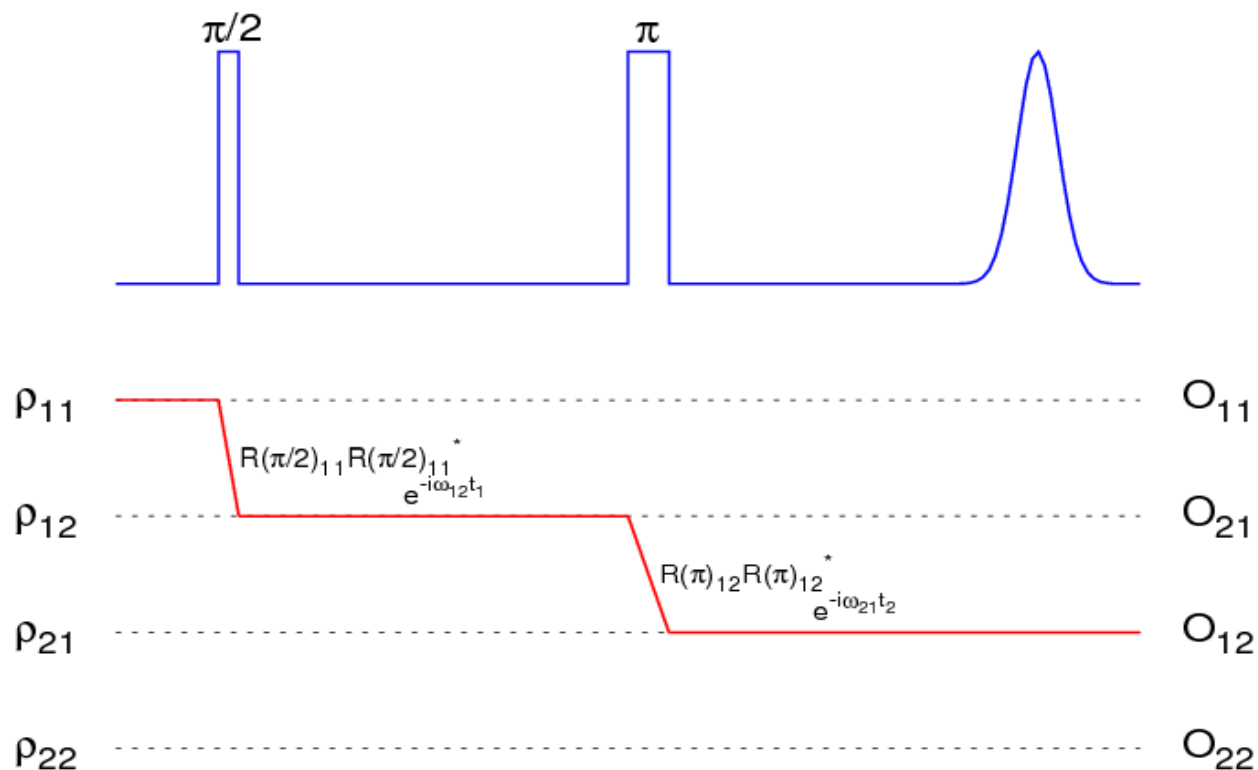


**Figure 46:** A schematic diagram of a pulsed EPR sequence and the evolution of the density matrix which is traced through each of the microwave pulses and free evolution periods. One coherence pathway from the equilibrium density matrix through to the detection operator is indicated.

#### 4.0 Molecular Sophe – Examples

##### 4.1 CW-EPR Spectroscopy

Reaction of  $\text{Tp}^*\text{Mo}^{\text{V}}\text{SCl}_2$  with a variety of phenols and thiols in the presence of triethylamine produces mononuclear, thiomolybdenyl complexes  $\text{Tp}^*\text{Mo}^{\text{V}}\text{SX}_2$  [ $\text{Tp}^*$  = hydrotris(3,5—dimethylpyrazol-1-yl)borate; X = 2-(ethylthio)phenolate (etp), 2-(n-propyl)phenolate (pp), phenolate;  $\text{X}_2$  = benzene-1,2-dithiolate (bdt), 4-methylbenzene-1,2-dithiolate (tdt), benzene-1,2-diolate (cat)] [51].

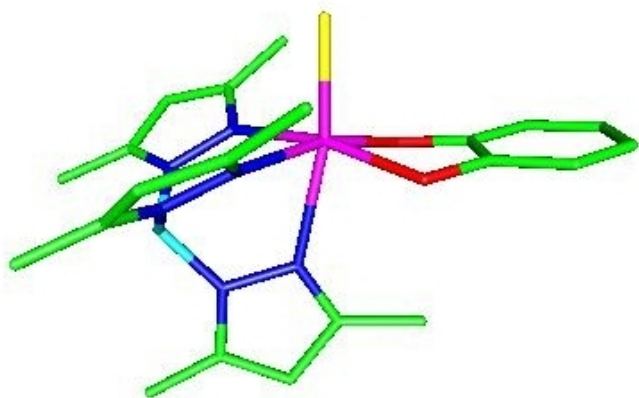


**Figure 47:** X-ray Crystal Structure of  $\text{Tp}^*\text{Mo}^{\text{V}}\text{S}(\text{cat})$

Multifrequency (S-, X-, Q-band) EPR spectra [52] of the complexes and selected molybdenyl analogues were acquired at 130K and 295K and yielded a spin Hamiltonian of  $C_s$  symmetry or lower, with  $g_{zz} < g_{yy} < g_{xx} < g_e$  and  $A_{z'z'} > A_{x'x'} \approx A_{y'y'}$ , and a non-coincidence angle in the range of  $\beta=24-39^\circ$ . The weaker  $\pi$ -donor terminal sulfido ligand yields a smaller HOMO-LUMO gap and reduced g-values for the thiomolybdenyl complexes compared with molybdenyl analogues. Multifrequency EPR, especially at S-band, was found to be particularly valuable in the unambiguous assignment of spin Hamiltonian parameters in low symmetry.

### Crystal field description of spin Hamiltonian parameters.

Large non-coincidence angles can be explained by a model in which extensive mixing among Mo 4d orbitals takes place. Although LMCT and MLCT states of appropriate symmetry may also contribute, for transition metals the dominant contribution to  $g_{ij}$  is usually  $\Delta g_{ij}^{d-d}$ , which arises from transitions within the Mo 4d manifold. In  $C_s$  symmetry with a  $\sigma^{(XZ)}$  mirror plane, in which the X axis lies between the metal-ligand bonds ( $\sigma$ ), the  $d_{x^2-y^2}$ ,  $d_{xz}$  and  $d_{z^2}$  orbitals transform as  $A'$  and the  $d_{xy}$  and  $d_{yz}$  orbitals transform as  $A''$ . The metal-based antibonding wavefunctions are therefore:

$$\begin{aligned}\psi_{X^2-Y^2}^{a'*} &= \alpha \left[ a_1 d_{X^2-Y^2} + b_1 d_{xz} + c_1 d_{z^2} \right] \\ \psi_{XZ}^{a'*} &= \beta \left[ a_2 d_{xz} + b_2 d_{X^2-Y^2} + c_2 d_{z^2} \right] \\ \psi_{Z^2}^{a'*} &= \gamma \left[ a_3 d_{z^2} + b_3 d_{X^2-Y^2} + c_3 d_{xz} \right] \\ \psi_{XY}^{a''*} &= \delta \left[ a_4 d_{xy} + b_4 d_{yz} \right] \\ \psi_{YZ}^{a''*} &= \varepsilon \left[ a_5 d_{yz} + b_5 d_{xy} \right]\end{aligned}$$

where, by definition,  $a_q > b_q, c_q$  ( $q=1,2,\dots$ ). Here covalency appears only implicitly through the metal-centered orbital coefficients  $\alpha, \dots, \varepsilon$ . Since the molecular X and Y axes are placed between the metal-ligand bonds, the ground state wavefunction is  $\psi_{X^2-Y^2}^{a'*}$ .

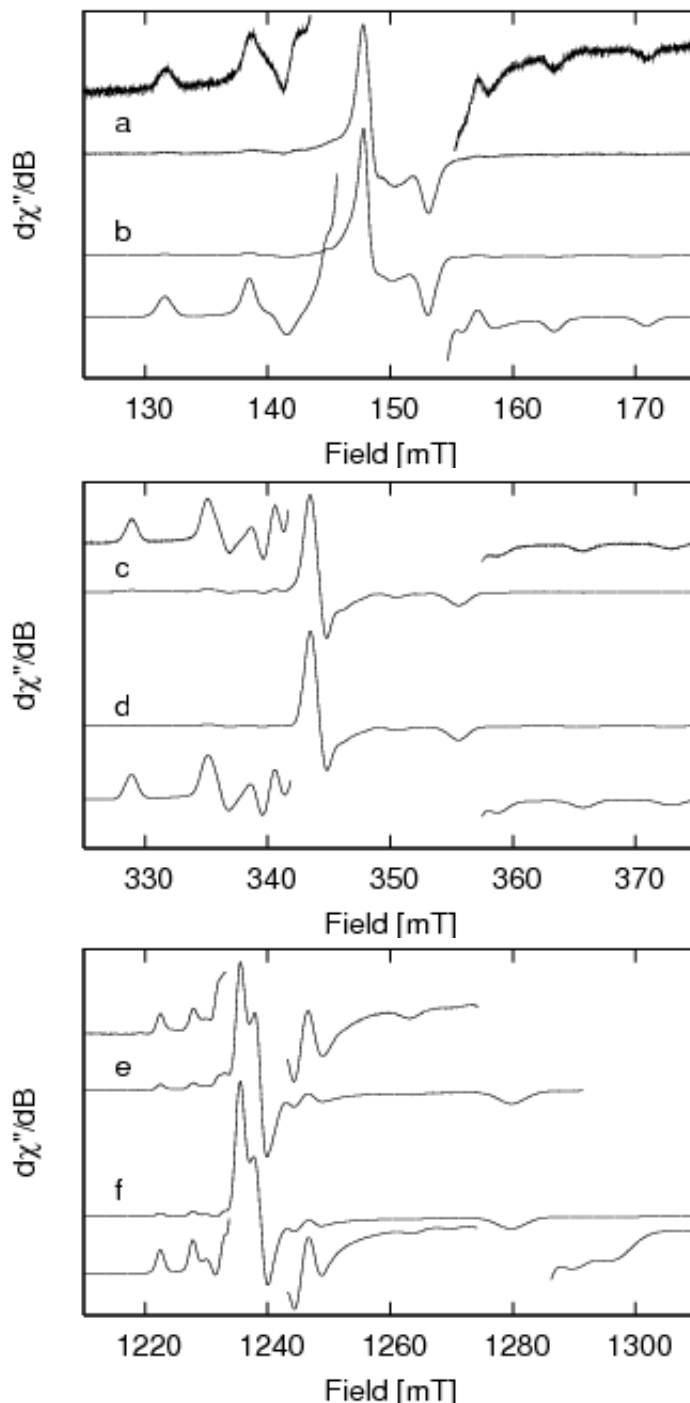


**Figure 48:** Multifrequency EPR spectra of  $Tp^*Mo^V S(cat)$  at 130K. (a) S-band, (c) X-band, (e) Q-band, (b,d,e) Computer simulated spectra.  $g_{xx}=1.9646$ ,  $g_{yy}=1.9595$ ,  $g_{zz}=1.8970$ ,  $A_{xx}=30.0$ ,  $A_{yy}=29.0$ ,  $A_{zz}=67.5 \times 10^{-4} \text{ cm}^{-1}$ ,  $\alpha=0^\circ$ ,  $\beta=34.5^\circ$ ,  $\gamma=0^\circ$

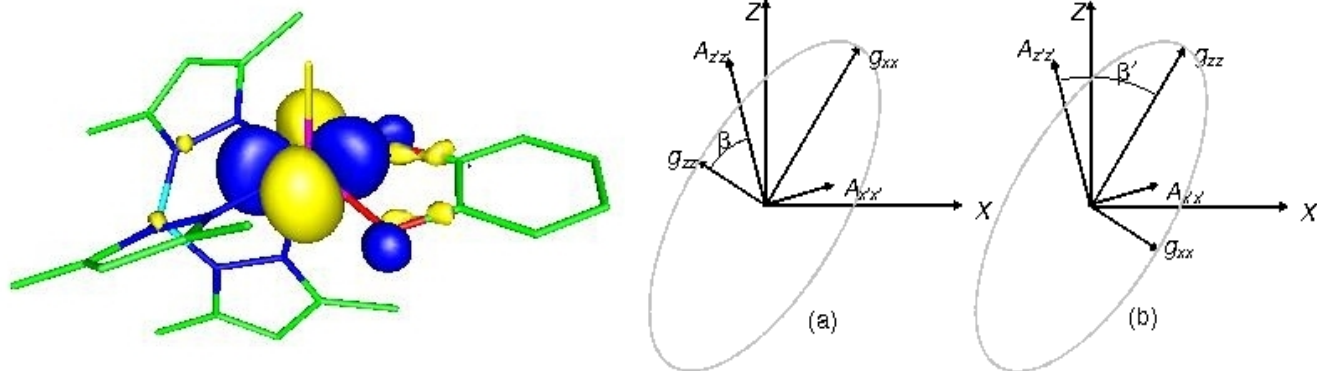


**Figure 49:** DFT Calculation (ORCA) of the LUMO for  $Tp^*Mo^V S(cat)$  and the orientation of the principal components of the  $g$  and  $A$  matrices [52].

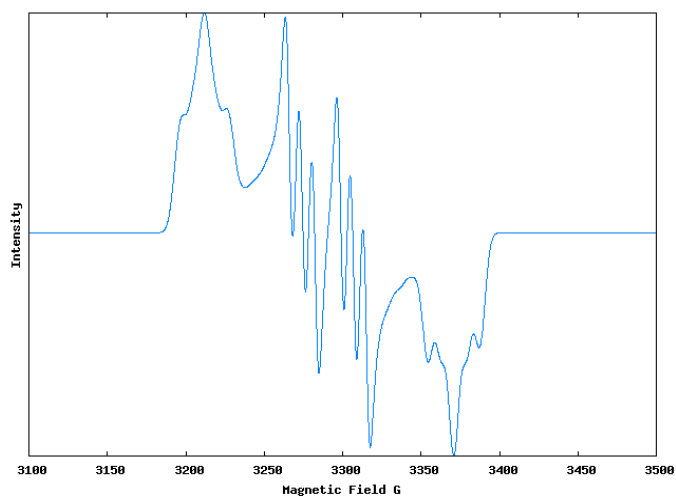
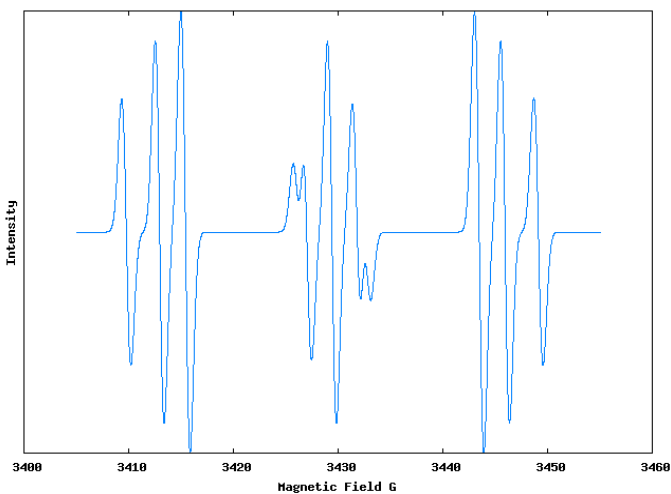


**Figure 50:** Computer simulation of the EPR spectrum of 3,4-protocatechuate dioxygenase with cyanide and  $^{15}N$ -nitric oxide [53].  $g_1 = 2.050$ ,  $g_2 = 2.001$ ,  $g_3 = 1.9535$ ;  $^{15}N$ -NO  $A_1 = 41.9$ ,  $A_2 = 91$ ,  $45$  MHz;  $^{14}N$ -protein  $A = 23$  MHz (isotropic); line widths at  $g_{1,2,3} = 4.25$ ,  $2.25$ , and  $8.77$  mT; microwave frequency =  $9.2158$  GHz; 2 field partitions; and 20 SOPHE grid segments.

**Figure 50:** Computer simulation of a nitroxide diradical.  $g_{iso} = 2.00$ ,  $A_{iso} = 15.4 \times 10^{-4} \text{ cm}^{-1}$  for each site,  $J_{iso} = 5.3 \times 10^{-4} \text{ cm}^{-1}$ ,  $9.6$  GHz, 2 field partitions; and 20 SOPHE grid segments.



## 4.2 Pulsed EPR Spectroscopy

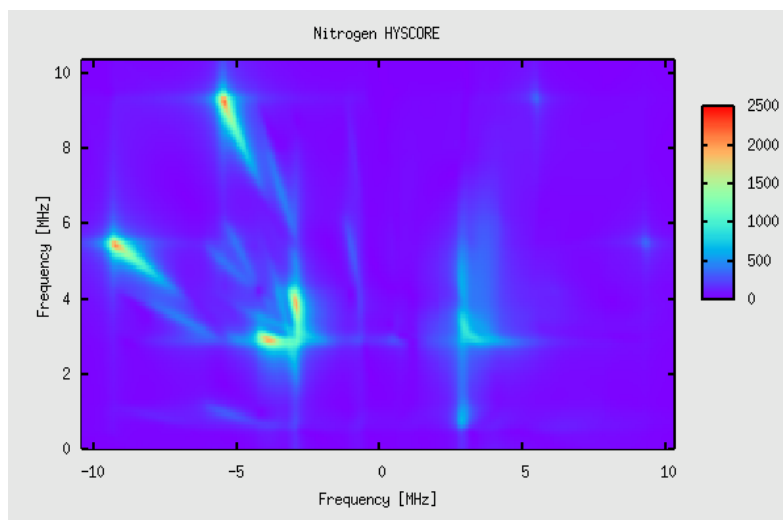
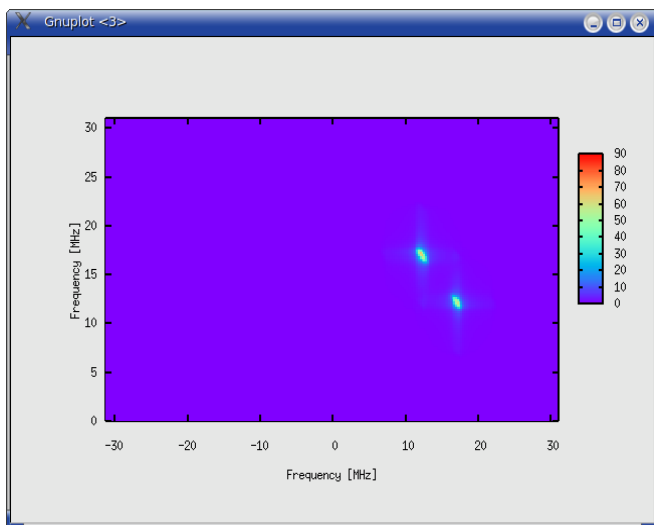
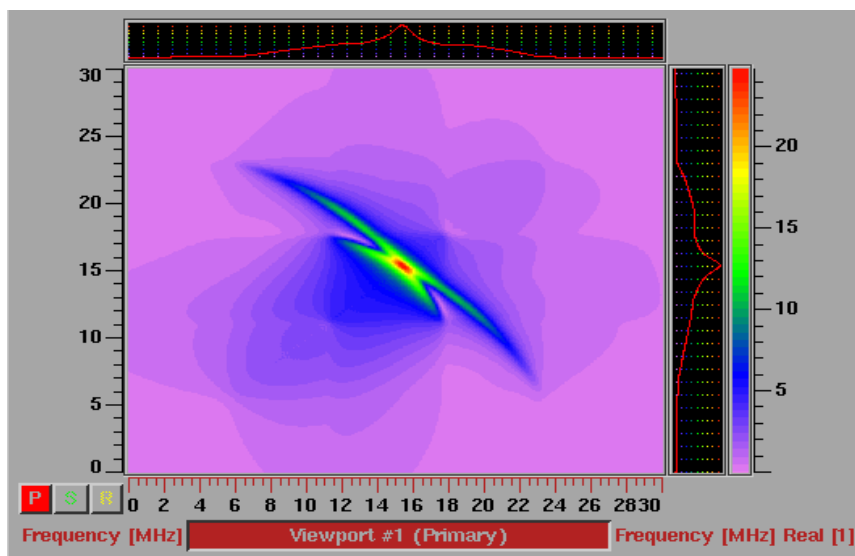


**Figure 51:** Nitrogen HYSCORE spectrum.  
 $g_{\text{iso}} = 2.0$ ,  $A_{\parallel} = 5$  MHz,  $A_{\perp} = 3$  MHz,  $P = -1$  MHz,  
 $T_{2N \text{ iso}} = 0.1$  MHz

**Figure 52:** Examples of Proton HYSCORE spectra.



## 5.0 References

- [1] J. R. Pilbrow, *Transition Ion Electron Paramagnetic Resonance*, Clarendon Press, Oxford, 1990.
- [2] F. E. Mabbs, D. C. Collison, *Electron Paramagnetic Resonance of Transition Metal Compounds*, Elsevier, Amsterdam, 1992.
- [3] R. Basosi, W.E. Antholine, J.S. Hyde, in L.J. Berliner, J. Reuben (Eds.) *Biological Magnetic Resonance*, Vol. 13, *Multifrequency ESR of Copper Biophysical Applications*, Plenum Press, New York, 1993, pp 103-150.
- [4] G.R. Hanson, A.A. Brunette, A.C. McDonell, K.S. Murray, A.G. Wedd, *J. Amer. Chem. Soc.* 103 (1981) 1953-1959.
- [5] Y.S. Lebedev, *Appl. Magn. Reson.* 7 (1994) 339-362.
- [6] L.C. Brunel, *Appl. Magn. Reson.* 11 (1996) 417-423.
- [7] E.J. Reijerse, P.J. vanDam, A.A.K. Klaassen, W.R. Hagen, P.J.M. vanBentum, G.M. Smith, *Appl. Magn. Reson.* 14 (1998) 153-167.
- [8] A. Schweiger, G. Jeschke, *Principles of Pulse Electron Paramagnetic Resonance*. Oxford University Press, Oxford, 2001.
- [9] *The Biological Chemistry of the Elements: The Inorganic Chemistry of Life*, J.J.R. Frausto, da Silva, R.J.P Williams, (Eds.), Oxford University Press, 1991, 2001.
- [10] *Metal Ions in Biological Systems*, H. Sigel. (Ed.), New York : M. Dekker, 1973-
- [11] *Biological Inorganic Chemistry : Structure and Reactivity*, I. Bertini (Ed.), Sausalito, CA : University Science Books, 2006.
- [12] A. Abragam, B. Bleaney, *Electron Paramagnetic Resonance of Transition Ions*. Clarendon Press, Oxford 1970.
- [13] A. Bencini, D. Gatteschi, *EPR of Exchange Coupled Systems*, Springer-Verlag, Berlin, 1990.
- [14] T. D. Smith, J. R. Pilbrow, *Coord. Chem. Rev.* 13 (1974) 173-278.
- [15] P. C. Taylor, J. F. Baugher, H. M. Kriz, *Chem. Rev.* 75 (1975) 203-240.
- [16] J. D. Swalen, H. M. Gladney, *IBM J. Res. Dev.* 8 (1964) 515-526.
- [17] J. D. Swalen, T. R. L. Lusebrink, D. Ziessow, *Magn. Reson. Rev.* 2 (1973) 165-184.
- [18] H. L. Vancamp, A. H. Heiss, *Magn. Reson. Rev.* 7 (1981) 1-40.
- [19] B.J. Gaffney, H.J. Silverstone, in L.J. Berliner, J. Reuben (Eds.) *Biological Magnetic Resonance*, Vol. 13, *Simulation of the EMR Spectra of the High-Spin iron in proteins*, New York, Plenum Press, 1993, pp 1-101.
- [20] S. Brumby, *J. Magn. Reson.* 39 (1980) 1-9,
- [21] S. Brumby, *J. Magn. Reson.* 40 (1980) 157-165.
- [22] D. Wang, G.R. Hanson, *Appl. Magn. Reson.* 11 (1996) 401-415.
- [23] G.R. Hanson, K.E. Gates, C.J. Noble, A. Mitchell, S. Benson, M. Griffin, K. Burrage, in M. Shiotani, A. Lund, (Eds.), *EPR of Free Radicals in Solids: Trends in Methods and Applications*, XSophe - Sophe - XexprView A Computer Simulation Software Suite for the Analysis of Continuous Wave EPR spectra, Kluwer Press. 2003, pp 197-237.
- [24] G.R. Hanson, K.E. Gates, C.J. Noble, M. Griffin, A. Mitchell, S. Benson, *J. Inorg. Biochem.*, 98 (2004) 903-916.
- [25] M. Griffin, A. Muys, C. Noble, D. Wang, C. Eldershaw, K.E. Gates, K. Burrage, G.R. Hanson, *Mol. Phys. Rep.* 26 (1999) 60-84.
- [26] M. Heichel, P. Höfer, A. Kamlowski, M. Griffin, A. Muys, C. Noble, D. Wang, G.R. Hanson, C. Eldershaw, K.E. Gates, K. Burrage, *Bruker Report* 148 (2000) 6-9.
- [27] G.R. Hanson, XSophe Release Notes, 1.1.3, Bruker Biospin, Germany, 2003, pp 1-68.

- [28] S. Stoll, A. Schweiger, *J. Magn. Res.*, 178 (2006), 42.
- [29] J. R. Pilbrow, *J. Magn. Reson.* 58 (1984) 186-203.
- [30] G. R. Sinclair, PhD Thesis, Monash University, 1988.
- [31] J.R. Pilbrow, G.R. Sinclair, D.R. Hutton, G.J. Troup, *J. Mag. Reson.* 52 (1983) 386-399.
- [32] (a) H. Kaess, J. Rautter, W. Zweggart, A. Struck, H. Scheer, W. Lubitz, *J. Phys. Chem.* 98 (1994) 354-363. (b) H. Kaess, J. Rautter, B. Boenigk, P. Hofer, W. Lubitz, *J. Phys. Chem.* 99 (1995) 436-448. (c) F. Lenzian, M. Huber, R.A. Isaacson, B. Endeward, M. Plato, B. Bonigk, K. Mobius, W. Lubitz, G. Feher, *Biochim. Biophys. Acta* 1183 (1993) 139-160. (d) H. Kä , E. Bittersmann-Weidlich, L. -E. Andréasson, B. Bönigk and W. Lubitz, *Chem. Phys.*, 194 (1995) 419-432.
- [33] H. Thomann, D. Goldfarb, M. Bernardo, P.M.H. Kroneck, V. Ullrich, *J. Inorg. Biochem.*, 59 (1995) G01.
- [34] (a) L.J. Berliner, S.S. Eaton, G.R. Eaton, (Eds) *Biological Magnetic Resonance, Distance Measurements in Biological Systems by EPR*, Vol. 19, Kluwer Academic Press, New York, 2001. (b) G. Jeschenke, M. Pannier, H.W. Spiess, *ibid*, p 493.
- [35] D. Wang, G.R. Hanson, *J. Magn. Reson. A* 117 (1995) 1-8.
- [36] R. L. Belford, M. J. Nilges, *EPR Symposium 21st Rocky Mountain Conference*, Denver, Colorado, 1979.
- [37] A. M. Maurice. PhD Thesis, University of Illinois, Urbana, Illinois, 1980.
- [38] M. J. Nilges, PhD Thesis, University of Illinois, Urbana, Illinois, 1979.
- [39] D. W. Alderman, M. S. Solum and D. M. Grant, *J. Chem. Phys.* 84 (1986) 3717-3725.
- [40] M. J. Mombourquette, J. A. Weil, *J. Magn. Reson.* 99 (1992) 37-44.
- [41] S. Stoll, Ph.D. *EPR Newsletter* 13 (2003) 24-26.
- [42] G. van Veen, *J. Magn. Reson.* 38 (1978) 91-109.
- [43] M. C. M. Gribnau, J. L. C. van Tits, E. J. Reijerse, *J. Magn. Reson.* 90 (1990) 474-485.
- [44] D. Nettar, N.I. Villafranca, *J. Magn. Reson.* 64 (1985) 61-65.
- [45] M.I. Scullane, L.K. White, N.D. Chasteen, *J. Magn. Reson.* 47 (1982) 383-397.
- [46] D.G. McGavin, M.J. Mombourquette, J.A. Weil, *EPR ENDOR User's manual*, University of Saskatchewan, Saskatchewan, Canada, 1993.
- [47] G.G. Belford, R.L. Belford, J.F. Burkhalter, *J. Magn. Reson.* 11 (1973) 251-265.
- [48] E. Anderson, Z. Bai, C. Bischof, J. Demmel, J. Dongarra, J. Du Croz, A. Greenbaum, S. Hammarling, A. McKenney, S. Ostrouchov, D. Sorensen, *LAPACK Users' Guide*, SIAM, Philadelphia, 1992.
- [49] D. Shalteil, W. Low, *Phys. Rev.*, 124 (1961), 1062-1067.
- [50] J. Jeener, *Adv. Magn. Res.* 10 (1982), 1-51.
- [51] S.C. Drew, J.P. Hill, I. Lane, G.R. Hanson, R.W. Gable, C.G. Young, *Inorg. Chem.*, 2006, Submitted.
- [52] S.C. Drew, C.G. Young, G.R. Hanson, *Inorg. Chem.*, 2006, Submitted.
- [53] A.M. Orville, Lipscomb JD. *Biochemistry*, 36 (1997) 14044.

## Acknowledgments

We would like to thank the Australian Research Council and the EPR Division of Bruker Biospin for financial support.

# VALENCY AND BONDING

A Natural Bond Orbital Donor–Acceptor Perspective

FRANK WEINHOLD AND CLARK R. LANDIS

*Department of Chemistry, University of Wisconsin-Madison, Wisconsin 53706*



CAMBRIDGE UNIVERSITY PRESS  
Cambridge, New York, Melbourne, Madrid, Cape Town, Singapore, São Paulo

CAMBRIDGE UNIVERSITY PRESS  
The Edinburgh Building, Cambridge CB2 2RU, UK

www.cambridge.org  
information on this title: www.cambridge.org/9780521831284

© Prof. F. Weinhold and Prof. C. Landis 2005

This book is in copyright. Subject to statutory exception  
and to the provisions of relevant collective licensing agreements,  
no reproduction of any part may take place without  
the written permission of Cambridge University Press.

First published 2005

Printed in the United Kingdom at the University Press, Cambridge

*A catalog record for this book is available from the British Library*

*Library of Congress Cataloging in Publication data*

ISBN-13 978-0-521-83128-4 hardback  
ISBN-10 0-521-83128-8 hardback

Cambridge University Press has no responsibility for the persistence or accuracy of URLs for external or  
third-party internet websites referred to in this book, and does not guarantee that any content on such websites is,  
or will remain, accurate or appropriate.

## Appendix A. Methods and basis sets

A quantum-mechanical calculational model can be uniquely specified by identifying (i) the method of approximation and (ii) the orbital basis set that underlies the model. The model is conventionally specified by a keyword label of the form *method/basis*, where *method* and *basis* are suitable identifying abbreviations or acronyms. Simple examples are “RHF/6-31G\*” (for the RHF restricted Hartree–Fock method and the 6-31G\* basis set) or “B3LYP/6-311+ +G\*\*” (for the B3LYP hybrid density functional method and the 6-311+ +G\*\* basis set). In this appendix we briefly describe the principal method and basis types that are now well established in the literature,<sup>1</sup> particularly as implemented in the *Gaussian* program.<sup>2</sup> Consult notes 1 and 2 for background information and original references.

### Methods

Quantum-mechanical approximation methods can be classified into three generic types: (1) variational, (2) perturbative, and (3) density functional. The first two can be systematically improved toward exactness, but a systematic correction procedure is generally lacking in the third case.

#### *Variational methods*

Variational approximation methods are identified by the form of the variational trial function, particularly by the number and types of Slater determinants.

The simplest approximation corresponds to a single-determinant wavefunction. The best possible approximation of this type is the Hartree–Fock (HF) molecular-orbital determinant. The HF wavefunction is constructed from the minimal number of occupied MOs (i.e.,  $N/2$  for an  $N$ -electron closed-shell system), each approximated as a variational linear combination of the chosen set of basis functions (*vide infra*).

To distinguish between closed-shell and open-shell configurations (and determinants), one may generally include a prefix to specify whether the starting HF wavefunction is of restricted closed-shell (R), restricted open-shell (RO), or unrestricted (U) form. (The restricted forms are total  $\hat{S}^2$  spin eigenfunctions, but the unrestricted form need not be.) Thus, the abbreviations RHF, ROHF, and UHF refer to the spin-restricted closed-shell, spin-restricted open-shell, and unrestricted HF methods, respectively.

More accurate multi-determinant “configuration-interaction” (CI) wavefunctions are described by specifying the types of substitutions (“excitations”) from the starting HF

determinant, replacing sets of occupied MOs with corresponding virtual MOs. The substitutions may include all singles (S), doubles (D), triples (T), or quadruples (Q), leading to designations such as CIS (inclusion of all single excitations), CISD (all single and double excitations), and so forth. Such wavefunctions are termed “single-reference” type, because all allowed substitutions originate from the starting HF configuration using MOs optimized for this configuration. The spin restrictions on these CI wavefunctions can be specified by prefixes analogous to those for the reference HF configuration; for example, the abbreviations RCISD, ROCISD, and UCISD specify restricted closed-shell, restricted open-shell, and unrestricted CISD, respectively.

“Multi-reference” wavefunctions can be formed by choosing two or more reference configurations and allowing the MOs to reoptimize self-consistently for the multi-configuration form. An important special case is the CASSCF (complete active-space self-consistent-field) method, in which the set of reference configurations is generated by including all excitations from a chosen “active space” of occupied and virtual MOs. Another special case is the GVB (generalized valence-bond) method, in which reference configurations are selected to match the spin-pairing pattern of a chosen valence-bond structure. Further aspects of multi-reference variational wavefunctions are beyond the scope of this appendix.

Quadratic CI (QCI) and coupled cluster (CC) exemplify more complex methods that are not strictly variational in character, but include physical corrections similar to those of higher-order perturbation theory. Keywords for these methods also include a specification of substitutions from the reference HF configuration, such as QCISD or CCSD, respectively, for QCI or CC methods with all single and double substitutions. More complete descriptions of these methods are beyond the scope of this appendix.

### *Perturbative methods*

Perturbative approximation methods are usually based on the Møller–Plesset (MP) perturbation theory for correcting the HF wavefunction. Energetic corrections may be calculated to second (MP2), third (MP3), or higher order. As usual, the open- versus closed-shell character of the wavefunction can be specified by an appropriate prefix, such as ROMP2 or UMP2 for restricted open-shell or unrestricted MP2, respectively.

An important advantage of MP2 and higher-order perturbation methods is their size-consistency at every order. This is in contrast to many variational CI methods, for which the calculated energy of two identical non-interacting systems might *not* be equal to twice that of an individual system. Size-consistent scaling is also characteristic of QCI and CC methods, which are therefore preferable to standard CI-type variational methods for many applications.

### *Density-functional methods*

Density-functional methods are based on approximating the HF exchange operator and post-HF correlation corrections by certain functionals  $\mathcal{E}_x[\rho]$ ,  $\mathcal{E}_c[\rho]$  of the electron density  $\rho$  (and possibly its gradient). A density-functional method is uniquely identified by its exchange and correlation functionals. Examples of the former include the original Becke (B), Becke one-term (B1), Becke three-term (B3), Perdew–Wang (PW), and modified one-term Perdew–Wang (mPW1) exchange functionals. Examples of the latter include the Lee–Yang–Parr (LYP) and Perdew–Wang (PW) correlation functionals.

(Note that several  $\mathcal{E}_x[\rho]$  “functionals” [such as the popular Becke three-term approximation B3] include an admixture of the true HF exchange operator with the usual

functional of electron density. Such methods are referred to as “hybrid density-functional methods” to indicate their closer connection to *ab initio* methods.)

The keyword for a given density-functional method is formed by concatenating the symbols for its exchange and correlation functionals. For example, combining the Becke three-term (B3) exchange functional with the Lee–Yang–Parr (LYP) correlation functional leads to the popular B3LYP density functional method.

As usual, a density-functional method (such as B3LYP) can be further specified as being of restricted closed-shell (RB3LYP), restricted open-shell (ROB3LYP), or unrestricted (UB3LYP) form.

### Basis sets

Contemporary basis sets are usually formed from atomic-orbital basis functions  $\chi_\mu$  of “contracted Gaussian” form,

$$\chi_\mu = \sum_{i=1}^r a_{\mu i} g_i$$

where the  $g_i$ ’s are “primitive” Gaussian-type orbitals, the  $a_{\mu i}$ ’s are fixed contraction coefficients, and  $r$  is the length of the contraction. An  $r$ -term-contracted Gaussian-type orbital (CGTO) is often denoted in the form “ $rG$ ” (e.g., “3G” for a three-term contraction).

Each CGTO  $\chi_\mu$  can be considered as an approximation to a single Slater-type orbital (STO) with effective nuclear charge  $\zeta$  (zeta). The composition of the basis set can therefore be described in terms of the number of such effective zeta values (or STOs) for each electron. A “double-zeta” (DZ) basis includes *twice* as many effective STOs per electron as a single-zeta “minimal basis” (MB) set, a “triple-zeta” (TZ) basis *three* times as many, and so forth. A popular choice, of so-called “split-valence” type, is to describe core electrons with a minimal set and valence electrons with a more flexible DZ (or higher) set.

### Pople-style basis sets

The keyword label of a standard Pople-style split-valence basis specifies the sp sets (groups of CGTOs of s and p symmetry) with distinct zeta values for each atomic shell, as well as the contraction length of each CGTO. The keyword contains the following syntactical components:

- (1) the contraction length  $n_c$  of the core-level set;
- (2) (after a hyphen) the contraction lengths  $n_v'$ ,  $n_v''$ ,  $n_v'''$ , ... of valence-level sp sets for each distinct zeta value;
- (3) (preceding the character “G”) a “+” if a *diffuse* sp set is added to each heavy (non-H) atom, or “++” if also a diffuse s function is added to each H; and
- (4) (following the “G”) a “\*” if *polarization* functions are added to each heavy atom, or “\*\*” if they are added also to H.

(“Diffuse” functions refer to extra-valent Rydberg-like functions of very small effective  $\zeta$ , which are suitable for describing anions or the very-long-range tails of electronic distributions. “Polarization” functions refer to components of higher angular momentum than required in the atomic ground configuration, e.g., an added set of five d orbitals on each C, or three p orbitals on each H.)

The generic symbol to represent a Pople-style basis set is of the form

$$n_c - n_v' n_v'' \dots (++)G(**)$$

where parenthesized (diffuse and polarization) extensions are optional. Some examples of this notation are given below, with a corresponding verbal description of the basis composition:

3-21G minimal 3G ( $n_c = 3$ ) core and double-zeta 2G ( $n_v' = 2$ ), 1G ( $n_v'' = 1$ ) valence sp sets, with no diffuse or polarization functions

6-31G\* minimal 6G ( $n_c = 6$ ) core and triple-zeta 3G ( $n_v' = 3$ ), 1G ( $n_v'' = 1$ ) valence sp sets, with polarization functions on heavy atoms

6-311++G\*\* minimal 6G ( $n_c = 6$ ) core and triple-zeta 3G ( $n_v' = 3$ ), 1G ( $n_v'' = 1$ ), 1G ( $n_v''' = 1$ ) valence sp sets, with diffuse and polarization functions on all atoms

Higher polarization functions can also be specified by replacing “\*\*” by a parenthesized list of polarization sets for heavy atoms and (after a comma) for hydrogen. For example, “(2d1f,2p)” would specify two additional d sets and one additional f set on each heavy atom, as well as two additional p sets on each H.

Some exceptions to this general syntax may be noted.

- (1) The label “STO-3G” (equivalent to 3-3G in the notation described above) denotes a minimal basis 3G set for both core and valence shells ( $n_c = 3$ ,  $n_v = 3$ ).
- (2) The label “3-21G(\*)” denotes a 3-21G set for atoms up to neon ( $Z = 10$ ), but inclusion of a d set for heavier atoms.
- (3) Polarization functions may be optionally chosen to be of “pure” or “Cartesian” form (by another keyword). In the former case, one includes the expected number of angular-momentum components (i.e., five d orbitals, seven f orbitals, etc.), whereas in the latter case some additional component(s) of lower angular momentum are included (e.g., a Cartesian “d set” includes five d orbitals plus one s orbital, a Cartesian “f set” includes seven f orbitals plus three p orbitals, and so forth).

### *Effective-core-potential (ECP) basis sets*

The ECP basis sets include basis functions only for the outermost one or two shells, whereas the remaining inner core electrons are replaced by an “effective core” or “pseudopotential.” The ECP basis keyword consists of a source identifier (such as LANL for “Los Alamos National Laboratory”), the number of outer shells retained (1 or 2), and a conventional label for the number of  $\zeta$  sets for each shell (MB, DZ, TZ, . . .). For example, “LANL1MB” denotes the minimal LANL basis with minimal basis functions for the outermost shell only, whereas “LANL2DZ” is the set with double-zeta functions for each of the two outermost shells. The ECP basis set employed throughout Chapter 4 (denoted “LACV3P” in Jaguar terminology) is also of Los Alamos type, but with full triple-zeta valence flexibility and polarization and diffuse functions on all atoms (comparable to the 6-311++G\*\* all-electron basis used elsewhere in this book).

An important advantage of ECP basis sets is their ability to incorporate approximately the physical effects of relativistic core contraction and associated changes in screening on valence orbitals, by suitable adjustments of the radius of the effective core potential. Thus, the ECP valence atomic orbitals can approximately mimic those of a fully relativistic (spinor) atomic calculation, rather than the non-relativistic all-electron orbitals they are nominally serving to replace. The partial inclusion of relativistic effects is an important physical correction for heavier atoms, particularly of the second transition series and beyond. Thus, an ECP-like treatment of heavy atoms is necessary in the non-relativistic framework of standard electronic-structure packages, even if the reduction in number of

basis orbitals obtained through neglect of atomic core electrons were of no practical importance. For this reason, all-electron basis sets (such as 6-311G and its extensions) are commonly unavailable for atoms beyond the first transition series.

### *Correlation-consistent basis sets*

Dunning has developed a series of “correlation-consistent” polarized valence  $n$ -zeta basis sets (denoted “cc-pVnZ”) in which polarization functions are systematically added to *all* atoms with each increase in  $n$ . (Corresponding diffuse sets are also added for each  $n$  if the prefix “aug-” is included.) These sets are optimized for use in correlated calculations and are chosen to insure a smooth and rapid (exponential-like) convergence pattern with increasing  $n$ . For example, the keyword label “aug-cc-pVDZ” denotes a valence double-zeta set with polarization and diffuse functions on all atoms (approximately equivalent to the 6-311++G\*\* set), whereas “aug-cc-pVQZ” is the corresponding quadruple-zeta basis which includes (3d2f1g,2p1d) polarization sets.

Related basis sets in common usage include the original Dunning full and valence double-zeta sets, denoted D95 and D95V, respectively (built from nine s-type and five p-type primitives). These sets may be augmented in the usual way with diffuse and/or polarization functions, as in the example “D95++\*\*” (diffuse and first-polarization sets on all atoms).

### **Notes for Appendix A**

1. W. J. Hehre, L. Radom, P. v. R. Schleyer, and J. A. Pople, *Ab Initio Molecular Orbital Theory* (New York, Wiley, 1986).
2. J. B. Foresman and A. Frisch, *Exploring Electronic Structure Calculations*, 2nd edn. (Pittsburgh, PA, Gaussian, Inc., 1998).